



Provided by the author(s) and University of Galway in accordance with publisher policies. Please cite the published version when available.

Title	Development and evaluation of platform-based SERS substrates for detecting cancer biomarkers at ultra-low concentrations
Author(s)	Phillipson, Nigel
Publication Date	2017-04-27
Item record	http://hdl.handle.net/10379/6508

Downloaded 2024-04-27T04:39:27Z

Some rights reserved. For more information, please see the item record link above.



Development and Evaluation of Platform-Based SERS Substrates for Detecting Cancer Biomarkers at Ultra-Low Concentrations

by

Nigel Phillipson, B.Sc.

A thesis submitted to the National University of Ireland, Galway, in partial fulfilment of the requirements for the degree of

Doctor of Philosophy

Biophotonics group,
School of Physics,
National University of Ireland, Galway



Academic Supervisor:

Professor Malini Olivo

April 2017

1 Table of Contents

Abstract.....	6
Declaration.....	7
Dissemination of work.....	8
Acronyms & Abbreviations	9
List of Figures	12
List of Tables	16
List of Equations	18
Acknowledgements.....	19
1 Introduction.....	20
1.1 General introduction; Surface Enhanced Raman Scattering (SERS).....	20
1.2 Motivation & Objectives	20
1.3 Thesis Outline	21
2 Background Theory & Literature review.....	23
2.1 Optical Processes.....	23
2.2 Raman Scattering	25
2.3 Surface Enhanced Raman Scattering	28
2.3.1 Chemical Enhancement Mechanism.....	29
2.3.2 Electromagnetic Enhancement Mechanism	30
2.3.3 Local Field Intensity & SERS Enhancement Factors	34
2.4 SERS Substrates.....	36
2.4.1 Substrate Material; Surface layers	36
2.4.2 Substrate Classifications	36
2.4.3 Metallic Nanoparticle SERS substrates	37
2.5 Platform-based Substrates	38
2.5.1 Materials & Fabrication	39
2.5.2 Immobilised MNP's substrates	40
2.5.3 Anodic Aluminium Oxide (AAO) substrates	40
2.5.4 Laser processed substrates	41
2.5.5 Lithography fabricated substrates	42
2.5.6 FIB & RIE substrate fabrication	44
2.5.7 Paper as substrate platforms.....	44
2.5.8 Oblique Angled Vapour Deposition (OAD).....	45

2.5.9	Design & Optimization	46
2.6	SERS Applications & Techniques	49
2.6.1	SERS & Biosensing	49
2.6.2	SERS & Microfluidics	53
2.6.3	Resonance Raman Scattering (RRS)	54
2.6.4	Surface Enhanced Resonance Raman Scattering (SERRS).....	54
2.6.5	Coherent Anti-Stokes Raman Spectroscopy (CARS).....	54
2.6.6	Stimulated Raman Scattering (SRS).....	56
2.6.7	Tip Enhanced Raman Spectroscopy (TERS).....	57
2.7	Novel SERS platforms	58
2.7.1	Liquid marble SERS platforms	58
2.7.2	SERS Nanoshells	58
2.7.3	Nanoshells as SERS Nanotags.....	59
2.7.4	Magnetic Nanoparticles as SERS Platforms.....	59
2.8	SERS; Novel techniques, trends & future outlook.....	60
2.8.1	Ultra-fast Raman Spectroscopy	61
2.8.2	Recent SERS sensing techniques.....	61
2.8.3	Plasmonic Metamaterials	62
3	Materials & Methods	63
3.1	Materials.....	63
3.1.1	Characterisation & Fabrication of Platform-based SERS substrates.....	63
3.1.2	SERS Biosensing of proteins	64
3.2	Methods.....	66
3.2.1	Evaluation of Platform-based SERS substrates	66
3.2.2	Design & Optimization SERS substrates.....	83
3.2.3	Application – Biosensing.....	90
4	Results 1 - Evaluation of Platform-based SERS substrates	94
4.1	SEM characterization	94
4.2	Raman analysis.....	103
4.3	FDTD analysis.....	119
4.3.1	FDTD & Raman comparisons	119
4.4	Discussion	128
4.5	Conclusions	129

5	Results 2 - Design, fabrication & optimization of SERS substrates.....	131
5.1	SCIL Substrates.....	131
5.1.1	Raman Analysis	131
5.1.2	SEM characterization.....	135
5.1.3	FDTD Analysis	141
5.2	Nanogap substrates.....	156
5.2.1	Raman Analysis; Pre-Optimized.....	156
5.2.2	SEM Characterization	156
5.2.3	FDTD Optimization	159
5.2.4	Raman Analysis; Optimized Substrates.....	165
5.3	Discussion	168
5.3.1	Tyndall SCIL substrates.....	168
5.3.2	Nanogap substrates	168
5.4	Conclusion.....	169
6	Results 3 - Application – Bioanalysis.....	171
6.1	Introduction	171
6.2	Experimental; SEM & Raman analysis.....	177
6.3	Discussion	194
6.4	Conclusions	196
7	Concluding Discussion & Future work.....	199
7.1	SERS sensing platforms	199
7.2	SERS Nanostress biosensing.....	200
8	Appendix.....	202
8.1	Commercial SERS substrates; fabrication techniques	202
8.1.1	Silmeco ltd.	202
8.1.2	Integrated optics.....	202
8.1.3	Horiba scientific.....	202
8.1.4	Diagnostic anSERS	202
8.2	SERS EF calculations.....	204
8.3	General calculations	204
8.4	Molecular structures & EDC reaction scheme.....	205
8.4.1	Molecular structures Raman reporter molecules	205
8.4.2	EDC reaction scheme.....	206

8.5	General references	207
9	Bibliography	209

Abstract

Surface Enhanced Raman Scattering (SERS) has proved to be a powerful spectroscopic tool since its discovery in 1973. Advances in nanofabrication techniques increasingly allow for the manufacture of complex nanostructured surfaces. However, an obvious constraint to developing suitable substrate topography, can be the complex and often expensive techniques required to manufacture them.

The aim of this work is to evaluate the performance of SERS substrates, and so better understand the key parameters affecting their efficiency. Then, to investigate development of novel substrates produced via state of the art nanofabrication techniques. Finally, using a suitably characterised substrate, to develop a robust method of SERS biosensing for cancer biomarkers at ultra-low concentrations.

In this study, Raman analysis was performed on commercially available, and 'in house' produced substrates functionalised with a Raman reporter; 2-Naphthalenethiol (2-NT). The substrate types investigated were fabricated via different techniques. These techniques include: Reactive Ion Etching (RIE); Inkjet printed Nanoparticles (NP); Dynamic Oblique Deposition, Laser processing and Nanoimprint lithography (NIL). The characterisation was carried out to correlate fabrication methods and the surface geometry they produce to SERS performance. The Raman response of the substrates was interpreted using SEM analysis and Finite Difference Time Domain (FDTD) modelling. The FDTD software simulates an electromagnetic wave incident on nanostructures and outputs the local electric field maxima and spatial distribution.

We discovered a number of factors that affect the SERS response of a substrate, including the size and shape of surface features, and material composition. However, the parameter that ultimately dictates the magnitude of the Raman signal enhancement is that of interstructure spacing. Substrates that achieve sub-10 nm gaps between structures cause strong interaction of adjacent electric fields and thus generate Coupled Plasmon Resonance (CPR). When CPR occurs the SERS enhancement factor is sharply increased.

Following the substrate characterisation, a high efficiency SERS substrate was chosen to investigate SERS biosensing of proteins. An indirect method to detect protein was investigated, relying on a SERS-based nanostress immunoassay. The analytes tested were the cancer biomarkers p53 and Epidermal Growth Factor Receptor (EGFR).

It was found that variation in antigen concentration influenced changes to the Raman linker spectra. This was observed in both a FWHM broadening and peak centre frequency shift for selected Raman peaks of interest. The lowest concentration measured in this work compares well with previously reported detection limits based on nanostress sensors. Not all of the linker/protein systems tested exhibited consistent and measurable peak changes. However, the differences in characteristic behaviour of linker/protein models can be exploited for multiplexed biosensing leading to better disease prognosis. With continued development, this nanostress sensing model could eventually be used in point of care clinical diagnostics.

Declaration

" Development and Evaluation of Platform-Based SERS Substrates for Detecting Cancer Biomarkers at Ultra-Low Concentrations"

Academic Supervisor:

Professor Malini Olivo

The work in this thesis is based on the research carried out at the School of Physics, National University of Ireland, Galway. I, Nigel Phillipson, hereby certify that this thesis has been written by me, that it is the record of work carried out by me, and that it has not been submitted in any previous application for a degree or qualification.

Dissemination of work

Publications

Title: *“Sensing of p53 and EGFR Biomarkers Using High Efficiency SERS Substrates”*

Journal: Biosensors;

published 2015 [1]

<http://www.mdpi.com/2079-6374/5/4/664/htm>

Conference; Oral Presentations

Title: *“Development of a Nanostructured Substrate for Surface Enhanced Raman Scattering (SERS) Biosensing”*

9th NAP Annual Scientific Workshop 2014

Tyndall National Institute, Cork.

Title: *“Biosensing of Proteins using highly sensitive SERS substrates”*

Microscopy Society of Ireland (MSI) 2016

Dublin Institute of Technology

Conference; Posters

Title: *“Development of a Stable, Reproducible and Sensitive SERS Substrate for Biological Applications”*

Science Foundation Ireland Nanoweeek Conference 2012, Trinity College Dublin.

Title: *“Development of a Stable, Reproducible and Sensitive SERS Substrate or Biological Applications”*

Photonics Ireland 2013, Queens University Belfast.

Title: *“Development of a Sensitive SERS Substrate for Biosensing of Oral Squamous Cell Carcinoma”*

European Materials Research Society (E-MRS) 2014, Lille, France.

Title: *“Indirect Sensing of Proteins using High Sensitivity SERS Substrates”*

Photonics Ireland 2015, Cork.

Acronyms & Abbreviations

2D – Two dimensional

2NT - 2-Naphthalenethiol*

3D – Three dimensional

4-ATP - 4-Aminothiophenol*

6-MP - 6-Mercaptopurine Monohydrate*

ARF - Acute renal failure

Ag – Silver

AgFON – Silver film over nanosphere

AAO – Anodic Aluminium oxide

AML – Advanced microscopy lab

Au - Gold

BC – Boundary conditions

BSE – Back scattered electrons

CA - carcinoembryonic antigen

CA125 - Cancer antigen 125

CA15-3 - Cancer antigen 15-3

CARS - Coherent Anti-Stokes Raman Spectroscopy

CMT – Conformal mesh technology

CPR – Coupled Plasmon resonance

CW - Continuous wave

DDA – Discrete dipole approximation

DUV – Deep ultraviolet

EDC - N-(3-Dimethylaminopropyl)-N'-ethylcarbodiimide hydrochloride*

EGFR – Epidermal growth factor receptor

ELISA – Enzyme-linked immunosorbent assay

EM – Electromagnetic

FEM – Finite element method

FDTD – Finite difference time domain

FIB - Focussed Ion beam

FON – Film over nanosphere

fs – Femtosecond

FSRS - Femtosecond stimulated Raman spectroscopy

FWHM – Full width half max
GUI – Graphical user interface
HGN – Hollow gold nanoshells
INRA - Immobilised Nanorod Assemblies
IPA – Isopropyl alcohol
KD - Equilibrium dissociation constant
LB - Langmuir-Blodgett
LSPR – Local surface Plasmon resonance
LFI – Local field intensity
LFIEF – Local field intensity enhancement factor
MBE - Mercaptobenzoic acid
MNP – Metallic nanoparticles
MS – Molecular sentinels
MOS - metal-organic sources
MOVPE - Metalorganic vapour phase epitaxy
MP - Mycoplasma pneumoniae
NHS - N-Hydroxysuccinimide*
NF – Near field
NIL – Nanoimprint lithography
NIR – Near infrared
NP – Nanoparticles
ns - Nanosecond
NSL – Nanosphere lithography
OAD - Oblique angled vapour deposition
PBS – Phosphate buffered saline
PDMS – Polydimethylsiloxane
PML – Perfectly matched layer
PMMA – Poly-methyl methacrylate
ps – Picosecond
PSA - Prostate specific antigen
PU – Polyurethane
PVD - physical vapour deposition
 R^2 (*R squared*) – Statistical minima for distance between fitted line through a graph data set

RCWA - Rigorous coupled wave analysis
RIE - Reactive ion etching
RF – Radio frequency
RFID – Radio frequency identification
RRS – Resonance Raman scattering
RSD – Relative standard deviation
SAM – Self-assembled monolayer
SCIL – Substrate conformal imprint lithography
SEM - Scanning electron microscope
SE-FSRS - Surface enhanced femtosecond stimulated Raman scattering
SERS – Surface enhanced Raman scattering
SERS EF – SERS enhancement factor
SERRS – Surface enhanced resonance Raman scattering
SHM – Simple harmonic oscillator
SNOM - Scanning near-field optical microscope
SRS – Stimulated Raman scattering
TERS – Tip enhanced Raman spectroscopy
TFSF – Total field scattered field (*FDTD advanced plane wave source*)
UHV-TERS - Ultra-High-Vacuum Tip enhanced Raman spectroscopy
UV-NIL -Ultraviolet nanoimprint lithography

* (for molecular structures see appendix 8.4)

List of Figures

Figure 2.1 Schematic; Optical processes	23
Figure 2.2 Schematic; Scattering processes	24
Figure 2.3 Timeline; Scattering processes	25
Figure 2.4 Schematic: Simple Harmonic Oscillator	26
Figure 2.5 Schematic; Stokes & anti-Stokes Raman scattering.....	28
Figure 2.6 Number of SERS publications.....	29
Figure 2.7 Wavelength dependence of dielectric constants of Silver & Gold.....	31
Figure 2.8 Nanosphere irradiated by incident light	32
Figure 2.9 Schematic; Nanocylinder irradiated by incident light	34
Figure 2.10 Schematic SERS substrate classifications	36
Figure 2.11 Schematic; ‘Top down’ & ‘bottom up’ processing	38
Figure 2.12 Schematic; Platform-based SERS substrate types/fabrication techniques	39
Figure 2.13 Schematic; approximate timeline - SERS substrate fabrication.....	41
Figure 2.14 Schematic; Nanosphere lithography	43
Figure 2.15 Schematic; Yee cell	47
Figure 2.16 Molecular Sentinel DNA hairpin Nanoprobe.....	53
Figure 2.17 Schematic; Coherent Anti-Stokes Raman Scattering (CARS).....	55
Figure 2.18 Schematic; Stimulated Raman Scattering (SRS).....	57
Figure 2.19 Schematic; Liquid marble SERS platform	58
Figure 2.20 Schematic; SERS Magnetic Nanoprobe fabrication.....	60
Figure 3.1 Schematic; substrate functionalisation	66
Figure 3.2 Renishaw InVia Raman Microscope	67
Figure 3.3 Wire software GUI	67
Figure 3.4 FDTD GUI.....	68
Figure 3.5 FDTD Object library	69
Figure 3.6 Selection of FDTD sources & monitors available.....	70
Figure 3.7 FDTD time monitor images; Electric field vs time; showing correct and incorrect simulations	71
Figure 3.8 FDTD Plane wave source; xz view	72
Figure 3.9 LFIEF& Reflectance at a planar Ag & Au surface	73
Figure 3.10 LFIEF response for planar and spherical simulated objects & resonance peak shift	75

Figure 3.11 FDTD generated Electric field distribution for spherical metallic nanoparticles at varying radii	76
Figure 3.12 FDTD; Electric field variation with incident polarization & spatial distribution of field about ‘sharp’ object features.....	77
Figure 3.13 Coupled Plasmon resonance for two ‘Ag’ Spheres at varying separations.....	78
Figure 3.14 FDTD set up; Ag Nanopillars.....	80
Figure 3.15 FDTD set up; Au Laser fabricated substrates.....	81
Figure 3.16 FDTD set up; Horiba substrate.....	82
Figure 3.17 FDTD set up; Inkjet substrate.....	83
Figure 3.18 Schematics and images for SCIL process	84
Figure 3.19 Flexible mask process dimensions	85
Figure 3.20 Schematic of SCIL imprinting.....	85
Figure 3.21 Schematic; nanogap substrates	87
Figure 3.22 SCIL Nanopillar; dimensions & material composition	88
Figure 3.23 FDTD set up; SCIL substrates.....	89
Figure 3.24 FDTD set up; NIL Nanogap substrates	89
Figure 3.25 Schematic for substrate functionalization	90
Figure 3.26 WiTec Confocal Raman Spectrometer.....	92
Figure 3.27 WiTec Project 4.0 software; screen shot of GUI.....	93
Figure 4.1 SEM’s - Silmeco Ag Nanopillar substrates.....	96
Figure 4.2 SEM’s - Integrated Optics Ag laser fabricated substrates.....	98
Figure 4.3 SEM’s - Horiba Au nanorod substrates.....	100
Figure 4.4 SEM’s – Diagnostic anSERS Au MNP inkjet printed substrates.....	102
Figure 4.5 Raman characterisation; substrates functionalised with 2-Napthalenethiol.....	106
Figure 4.6 Raman comparison; Au substrates functionalised with 2-NT.....	108
Figure 4.7 Comparison of Au & Ag surface layers	110
Figure 4.8 Variation to means 1066 cm^{-1} peak for Silmeco substrate and RSD for all substrates.....	114
Figure 4.9 Experimental SERS enhancement factors	116
Figure 4.10 Threshold calibration curve; Ag Silmeco substrate over 1000 to 0.01 nM concentration (mean of three substrates)	117
Figure 4.11 2-NT Raman spectra of low threshold (0.01 nM)	118
Figure 4.12 GUI images for Silmeco & Integrated Optics substrates; Table 4.4 & Table 4.5	120
Figure 4.13 GUI images for Horiba & anSERS substrates; Table 4.6 & Table 4.7	121

Figure 4.14 Raman/FDTD signal intensity comparison; all substrates	125
Figure 4.15 Variation in surface morphology; with ‘roughness factor’ σ ; Laser constructs .	126
Figure 4.16 Raman/FDTD SERS EF comparison; ALL substrates.....	127
Figure 4.17 SEM image of amorphous SERS substrate geometry with FDTD GUI set up inset	130
Figure 5.1 Tyndall substrate – 2NT spectra.....	132
Figure 5.2 Substrate comparison; Tyndall & Nanogap	134
Figure 5.3 SEM’s of post-imprint and CFF etching SCIL imprinted regions	136
Figure 5.4 SEM’s illustrating fabrication stages SCIL substrate.....	138
Figure 5.5 SEM’s final stage Au deposition; SCIL substrate.....	140
Figure 5.6 FDTD output: intensity profile showing SERS ‘hot spot’ locations.....	141
Figure 5.7 Feature geometry evaluation & FDTD/Raman comparison.....	143
Figure 5.8 FDTD comparison of material dependent SERS response for square nanopillar array with & without SiO ₂ intermediate layer	146
Figure 5.9 Nanostructured imprinted region on silicon wafer	147
Figure 5.10 FDTD simulation for a ‘contaminant’ layer on substrate surface	148
Figure 5.11 Resolution test for e-beam patterning; Tyndall substrates	150
Figure 5.12 FDTD simulation for range of structure diameters. Electric field vs wavelength	151
Figure 5.13 FDTD parameter sweep; pillar height. Electric field vs pillar height	153
Figure 5.14 FDTD Optimised structure gap & Au thickness	154
Figure 5.15 Nanogap substrates	158
Figure 5.16 Simulation region for FDTD analysis of gap parameter	160
Figure 5.17 FDTD analysis; variation of SERS EF with gap dimension	161
Figure 5.18 FDTD Electric field profiles for variation of gap dimensions	164
Figure 5.19 Optimized Nanogap substrates; 2NT spectra 1060 cm ⁻¹ peak.....	167
Figure 5.20 SEM showing uniform nanopillar array; Tyndall SCIL substrate.....	169
Figure 6.1 Schematic: Intrinsic & Extrinsic SERS biosensing.....	172
Figure 6.2 Simple nanostress response of 4-ATP conjugated SERS substrate; in the absence of any medium	174
Figure 6.3 Harmonic approximation for a two-atom system.....	175
Figure 6.4 Illustration of the energy levels associated with the CS bond.....	176
Figure 6.5 Silmeco SERS substrate functionalized with p53/antibody/4-ATP Raman linker	178
Figure 6.6 Raman Spectra for 4-ATP & 6-MP linker molecules; pre & post-functionalized	179

Figure 6.7 Frequency shift; 1080 cm^{-1} peak, 4-ATP/p53 Model.....	181
Figure 6.8 Frequency shift; 860 cm^{-1} peak, 6-MP/EGFR model.....	183
Figure 6.9 Variation in FWHM & Peak position with protein concentration for 4-ATP/p53 system	184
Figure 6.10 Variation in FWHM & Peak position with protein concentration for 4-ATP/EGFR system.....	186
Figure 6.11 Variation in FWHM & peak position for 6-MP/EGFR system.....	188
Figure 6.12 Correlation plot; FWHM & Peak centre position for 4-ATP/p53 system.....	191
Figure 6.13 Response of control substrates at FWHM for differing system configurations .	193
Figure 6.14 Schematic showing molecular weight for p53 and EGFR biomarkers	194
Figure 8.1 Molecular structure for SERS probes used in experimental work	205
Figure 8.2 EDC reaction scheme	206

List of Tables

Table 3.1 Details for commercial platform-based SERS substrates	63
Table 3.2 Details for in-house fabricated platform-based SERS substrates	64
Table 3.3 Silmeco substrate dimensions	79
Table 3.4 Horiba nanorod substrate dimensions	81
Table 3.5 Diagnostic anSERS substrate dimensions	82
Table 4.1 Mean Raman intensity & Relative deviation; all substrates	103
Table 4.2 Intra-substrate deviation of spot to spot Raman signal intensity	104
Table 4.3 Relative standard deviation values for one complete calibration curve	118
Table 4.4 Simulation parameters used for Silmeco Ag & Au substrates.....	119
Table 4.5 Simulation parameters used for Integrated Optics Ag & Au substrates	120
Table 4.6 Simulation parameters used for Horiba substrate	121
Table 4.7 Simulation parameters used for anSERS substrate	122
Table 4.8 Geometry variations for FDTD error estimation	126
Table 4.9 Maximum and minimum FDTD generated outputs for individual substrate SERS EF's	128
Table 5.1 SERS signal consistency comparison for Tyndall and commercial platform-based substrates.....	133
Table 5.2 SERS signal consistency comparison for Tyndall and Nanogap substrates	135
Table 5.3 Summary of FDTD set up parameters for Tyndall SCIL substrate	142
Table 5.4 FDTD; diameter dependent outputs.....	150
Table 5.5 FDTD optimised parameters; summary table	155
Table 5.6 Summary of FDTD set up parameters for Nanogap substrates	159
Table 5.7 FDTD generated SERS EF values for variation in interstructure spacing	160
Table 5.8 Nanogap; gap dimensions' post deposition	165
Table 5.9 Summary of FDTD optimized parameters for Tyndall SCIL substrate.....	168
Table 6.1 Raman linker/protein systems analysed.....	178
Table 6.2 Frequency shift and FWHM variation; 4-ATP/p53 model	182
Table 6.3 Frequency shift & FWHM variation; 6-MP/EGFR model	183
Table 6.4 Control system configuration.....	192
Table 6.5 Linker/Protein systems & results	194
Table 6.6 Biomarker & antibody molecular weights.....	198
Table 8.1 Summary; Platform-based substrate Raman comparison	203

Table 8.2 Reference Raman Intensities	204
Table 8.3 Laser spot size; Renishaw Raman microscope	205

List of Equations

Equation 2.1	25
Equation 2.2	25
Equation 2.3	25
Equation 2.4	26
Equation 2.5	26
Equation 2.6	26
Equation 2.7	27
Equation 2.8	27
Equation 2.9	27
Equation 2.10	30
Equation 2.11	32
Equation 2.12	32
Equation 2.13	32
Equation 2.14	33
Equation 2.15	33
Equation 2.16	33
Equation 2.17	34
Equation 2.18	35
Equation 2.19	35
Equation 2.20	48
Equation 2.21	48
Equation 2.22	48
Equation 2.23	48
Equation 2.24	49
Equation 4.1	115
Equation 6.1	174
Equation 6.2	175
Equation 6.3	176
Equation 8.1	204
Equation 8.2	204

Acknowledgements

I would like to thank the following people for their help with this PhD project.

I'm grateful to Prof. Malini Olivo, who when this research opportunity arose remembered that I had applied for a PhD 12 months earlier and was willing to take on an aging student. Also, for her input at a crucial stage of the work with advice regarding cancer biomarker sensing.

I'm especially thankful for the help and oversight provided by Dr Ger O'Connor. He has always been willing to go that extra mile in providing encouragement, advice and guidance. His continual insistence on detail and scientific rigour has played a significant part in helping me discover my potential.

I'd also like to thank Dr Peter Owens for his invaluable help as we worked together on the bioanalysis part of the project. Even after that work had been completed, he has continued to offer helpful advice and encouragement.

I'd also like to thank the many students and staff at NUIGalway. Although they are too many to mention, they have all added to what has been an interesting journey.

I'm especially indebted to my wife Ann, who has somehow coped with the many PhD stress related symptoms. We are both looking forward to the day when I will no longer need a map to find the fridge in the mornings.

Finally, I'm grateful also to the One who has been my guide in life since I was 18. He often chooses a path for me that I could never have imagined myself. Which is surely only a glimpse of the glory to come in another place.

“Your eyes will see the King in His beauty; they will behold a far-distant land”

Isaiah 33 verse 17

“This work was conducted under the framework of the Irish Government’s Programme for Research in Third Level Institutions Cycle 5, National Development Plan 2007-2013 with the assistance of the European Regional Development Fund.”



1 Introduction

1.1 General introduction; Surface Enhanced Raman Scattering (SERS)

Spectroscopy is the section of optics concerned with spectrum analysis, and investigates the interaction between light and matter. The types of interaction include, but are not limited to the following: absorption, emission and the scattering of light. The spectroscopic technique utilised in this project examines light scattering, and specifically inelastic light scattering known as Raman spectroscopy.

The usefulness of Raman scattering arises from the mechanism that produces the inelastic scattering. The interaction of an Electromagnetic wave incident at a surface produces a Plasmon Resonance effect. The free electron gas density is perturbed by the incident field, resulting in an oscillating dipole, with the collective oscillations known as Surface Plasmon Resonance (SPR). The SPR at the dielectric interface (the dielectric usually being air) generates a secondary local electric field which then acts as a scattering source. In the Raman Scattering process, a change in frequency occurs between the incident and scattered photons. The resulting frequency shift of the scattered photon is dependent upon the particular vibrational energies of the functional group involved [2]. Thus, each molecule has its own unique spectral characteristics which makes Raman scattering a powerful spectroscopic tool.

Raman scattering was first experimentally observed by C.V Raman and K.V Krishnan in 1928 [3]. However the weakness of the Raman scattered signal limited its usefulness until the discovery in 1973 of an enhancement effect now known as Surface Enhanced Raman Scattering (SERS) [4]. When light interacts with Metallic Nano Particles (MNP's) or a metallic surface containing nanostructures, the Local SPR (LSPR) strongly amplifies the secondary local electric field, and as a consequence the Raman scattered signal. The large enhancement factors involved in SERS has enabled the Raman scattering technique to realize much of its potential. In fact the sensitivity of SERS has enabled its use in single molecule detection [5].

1.2 Motivation & Objectives

The SERS effect is strongly dependent on the geometry of surface nanofeatures, and the fabrication techniques required to achieve them. Therefore, the benefits that SERS can bring to a wide variety of applications is ultimately dependent upon the suitability and performance of the substrates used. In the years following the discovery of SERS there have been many advances in nanofabrication that have enabled the production of high efficiency SERS substrates with sophisticated nanostructures. However, the difficulties of sustaining complex manufacturing processes in a low volume market remains a significant challenge.

This project begins then by examining the performance of both commercially available and novel 'in house' SERS substrates. An attempt is also made to modify another novel substrate by optimising surface nanofeatures using electric field modelling software. Then to re-evaluate the optimised substrates for performance as before.

Our **aim**, by characterising SERS substrates in this work is to relate the efficiency of a substrate's relative performance to the individual substrate topography. By understanding the

geometry dependent SERS response of a substrate, we will be able to determine what are the key fabrication parameters affecting SERS activity.

SERS is used in many research areas, it is multidisciplinary and is a marriage of Nanotechnology, Lasers and optical detection methods. The multidisciplinary nature of SERS is exemplified in SERS biosensing which is the application of this project. A high efficiency substrate is selected based on the initial characterisation work. It is then used to develop an application in SERS biosensing requiring a high level of detection sensitivity.

The SERS biosensing approach adopted in this work involves the measurement of protein concentration. There is an obvious question that arises at this point and that is: “why proteins?” Specifically, the proteins we evaluated were p53 and Epidermal Growth Factor Receptor (EGFR). Both of these are known as cancer biomarkers and have been standard benchmarks in cancer research for many years. The biomarker p53 regulates cell cycle and acts as a tumour suppressor gene; hence overexpression in the body can indicate the onset of disease.

Most of us know people who have been diagnosed with cancer and are aware that early detection is the key to patient survival. Additionally, early detection is dependent upon sensitive biosensing of cancer biomarkers at ultra-low concentrations. Our **aim** is to develop a robust and sensitive technique for the sensitive detection of cancer biomarkers, towards a future point of care clinical diagnostic method.

1.3 Thesis Outline

As a helpful guide, the structural layout for this PhD project is presented as follows.

Chapter 1

An introduction to SERS, and the project motivation and objectives are introduced in this chapter

Chapter 2

A description of SERS theory, and a review illustrating where this work lies within the field of SERS research and SERS biosensing is presented in chapter 2.

Chapter 3

Chapter 3 provides a comprehensive overview of the materials, equipment and substrates used during this research. The methodology for substrate characterisation is explained, as is the approach used to functionalise substrates for SERS biosensing. Details of substrate types and the fabrication techniques used to produce them are also included.

Chapter 4

Chapter 4 is the first results chapter, and this chapter assesses the performance of platform-based SERS substrate. The characterisation work is carried out using Raman, SEM and Finite Difference Time Domain (FDTD) analysis. The SERS response of each substrate type is evaluated by measuring signal intensity and spot to spot consistency for specific Raman peaks of interest. Using the signal from a reference sample the standard benchmark of the SERS Enhancement Factor (SERS EF) is calculated.

Chapter 4 identifies which substrate types exhibit the best SERS response. The results facilitate correlation of the key factors responsible for SERS efficiency to individual substrate geometry.

Chapter 5

Chapter 5 describes an attempt to fabricate a novel SERS sensor using a state of the art nanofabrication technique known as Substrate Conformal Imprint Lithography (SCIL). The performance of the substrates was then evaluated with the same characterisation methodology that was used in chapter 4. Following Raman and SEM analysis, detailed FDTD simulations were carried out to optimise the substrates.

A second substrate type produced by Nanoimprint lithography was characterised, optimised with FDTD analysis and then retested for SERS performance. Chapters 4 & 5 identify and confirm the key parameters influencing the efficiency of SERS performance.

Chapter 6

An investigation into SERS bioanalysis is carried out in chapter 6. Specifically, a robust technique for an indirect measurement of protein concentration is described. The Raman spectra of a linker molecule functionalised with an antibody/protein combination was examined at different protein concentrations. The resulting changes to spectral peaks of interest was related to nanomechanical stress at the linker/antibody binding site.

Chapter 7

Chapter 7 presents conclusions and principal findings from the three results chapters. It was ascertained that the parameter most affecting the signal enhancement gained from a SERS substrate is that of interstructure spacing. This is due to the Coupled Plasmon resonance (CPR) effect that can arise from nanostructures/particles in close proximity i.e. $< 10/15$ nm.

Regarding the SERS biosensing of proteins, our results demonstrated a quantitative measure of protein concentration, with a lower threshold measurement of ~ 0.25 nM achieved. This compared well with other nanomechanical stress sensor techniques.

2 Background Theory & Literature review

This chapter presents the background theory and literature review that is relevant to Surface Enhanced Raman Scattering (SERS). The theory begins with a discussion on the optical processes involved in the interaction of light with materials. The flow of the discussion then follows from Scattering to Raman Scattering and through to SERS, and investigates the mechanisms that generate the SERS effect.

In order to illustrate where this project lies within the literature, the review examines SERS substrate types and fabrication, and SERS applications and techniques. This is followed by a look at novel SERS platforms, recent trends and future challenges.

2.1 Optical Processes

Reflection, propagation and transmission are the main general classifications of optical processes involved in the interaction of light with matter. Further sub-categories that describe propagation through a material are refraction; absorption & emission; and scattering.

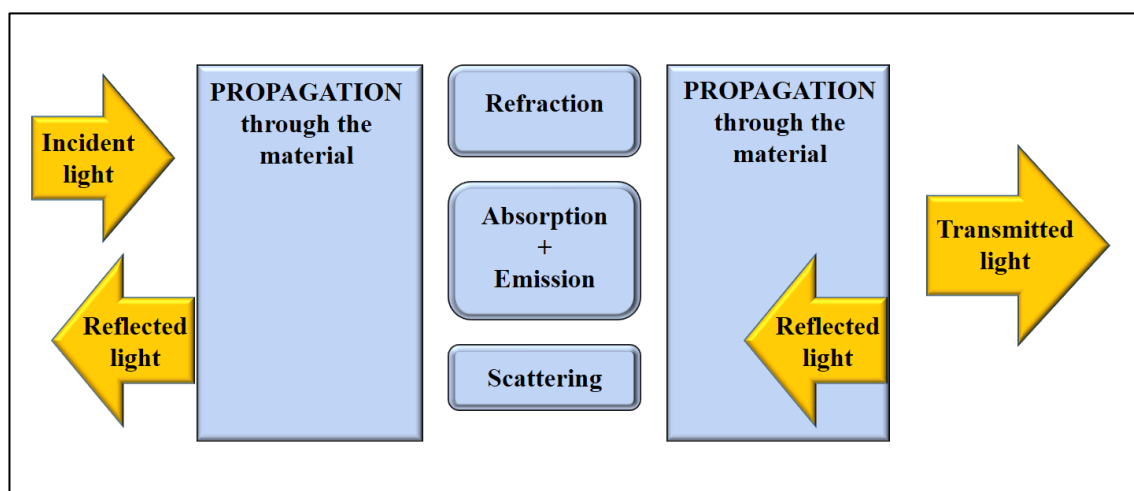


Figure 2.1 Schematic; Optical processes

Transmission is dependent on the Reflectivity which can occur at the front or back interface, and the processes occurring during propagation through the medium.

Refraction is an interfacial phenomenon where the bending of light occurs at an interface due to a change in propagation velocity. Absorption and emission are processes where energy from incident photons is either absorbed or released by a material due to the excitation of atoms.

The dual nature of light can be described as follows. Light is often thought to behave as a wave as it propagates through free space, and as a particle as it undergoes the processes of scattering, absorption, and emission. The scattering process can be described as the redirection of light as it encounters an obstacle in its path. This change in direction of the light can occur with or without a change in frequency, as either inelastic or elastic scattering respectively.

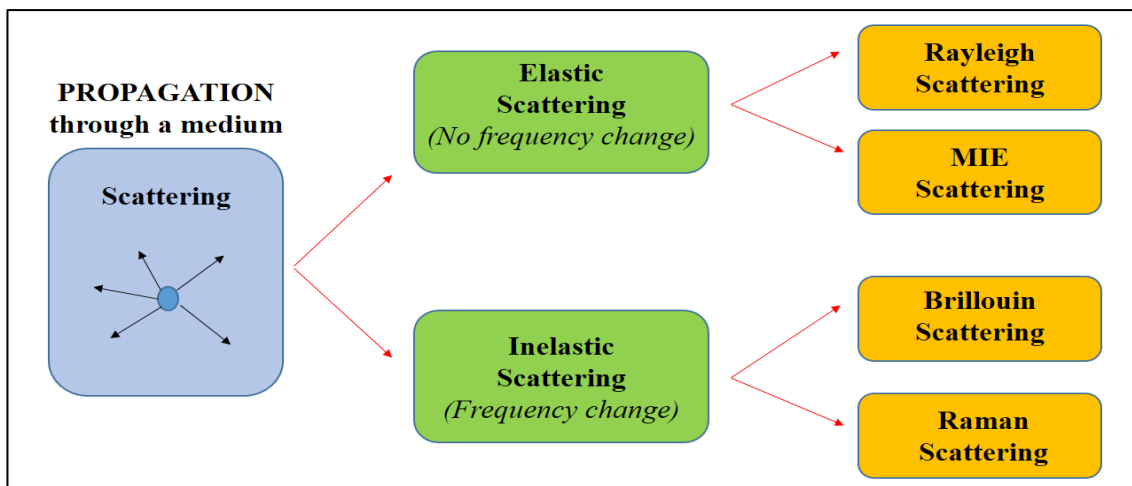


Figure 2.2 Schematic; Scattering processes

Elastic Scattering involves a change in direction; Inelastic Scattering a change in direction & frequency

As light interacts with polarisable molecules in its path, the electronic configuration of the molecules can be perturbed by the time varying electric field of the incident wave. This causes a periodic displacement of charges within the molecule and generates an induced oscillating dipole. During the elastic scattering process, a photon is absorbed and instantaneously re-emitted at the same frequency.

Rayleigh scattering involves the inelastic scattering of light from molecules that are much smaller than the incident wavelength, usually the particle size $\leq 1/10 (\lambda)$. When the particle size is similar to or greater than the incident wavelength, elastic scattering is referred to as Mie scattering, named after Gustav Mie.

Rayleigh scattering strongly depends on wavelength, with the scattered intensity being proportional to $1/\lambda^4$. However, Mie scattering is only weakly dependent on wavelength, and actually becomes independent of it once the particle size is greater than λ .

Two types of inelastic scattering mechanisms are Brillouin and Raman. Brillouin scattering is an effect resulting from the interaction of photons with acoustic phonons in a solid medium. A phonon is a quanta of molecular vibrational energy. In a solid, the collective vibrational energy exists as propagating matter waves. An acoustic phonon is an in-phase movement of lattice atoms. Whereas an optical phonon is essentially an out of phase oscillation of neighbouring atoms.

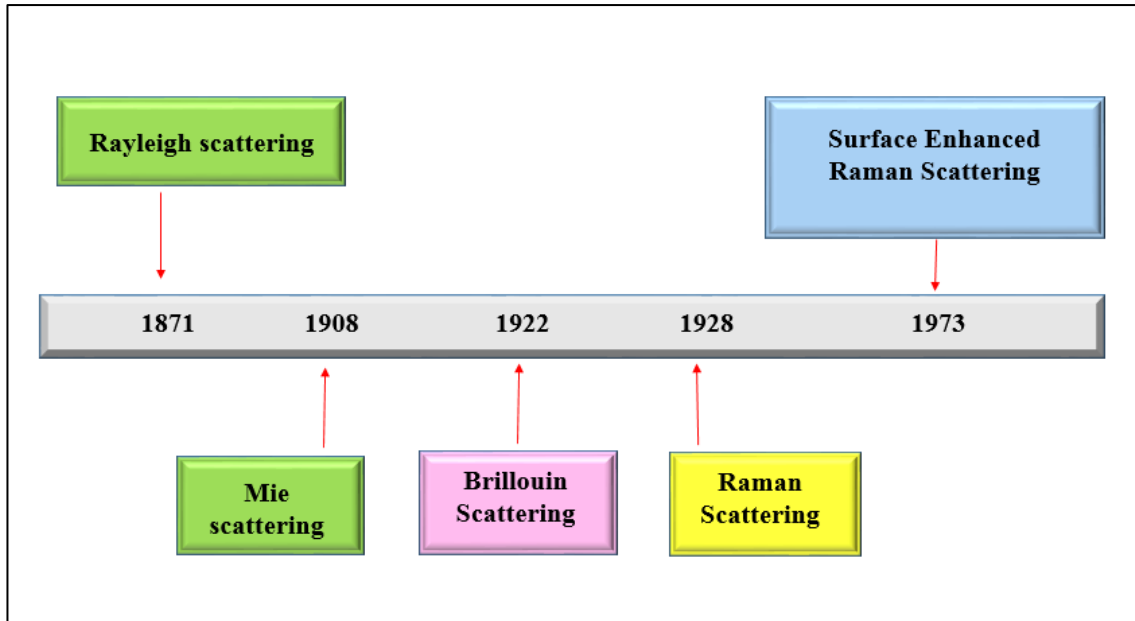


Figure 2.3 Timeline; Scattering processes

2.2 Raman Scattering

As mentioned above, the interaction of a light wave with matter induces an oscillating dipole in the electron gas cloud. The dipole moment is proportional to the incident field, and is commonly defined by the following.

$$P = \alpha E \quad \text{Equation 2.1}$$

Where P is the dipole moment; E the external field, and the constant of proportionality, ' α ' is known as the molecular polarizability.

The external electric field can be written as:

$$E = E_0 \cos(\omega_0 t) \quad \text{Equation 2.2}$$

Where E_0 is the amplitude and ω_0 is the incident angular frequency.

Combining Equation 2.1 and Equation 2.2 we can represent the time dependent induced dipole moment as:

$$P = \alpha E_0 \cos(\omega_0 t) \quad \text{Equation 2.3}$$

The molecular polarizability is a material property, and physically relates to the 'amount' by which the electron density is perturbed from equilibrium. The equilibrium 'position' is essentially the state of the molecule in the absence of the external field. We can use the classical approach to understand the process, with the example of a diatomic molecule. The molecules can be considered as two weights connected by a spring.

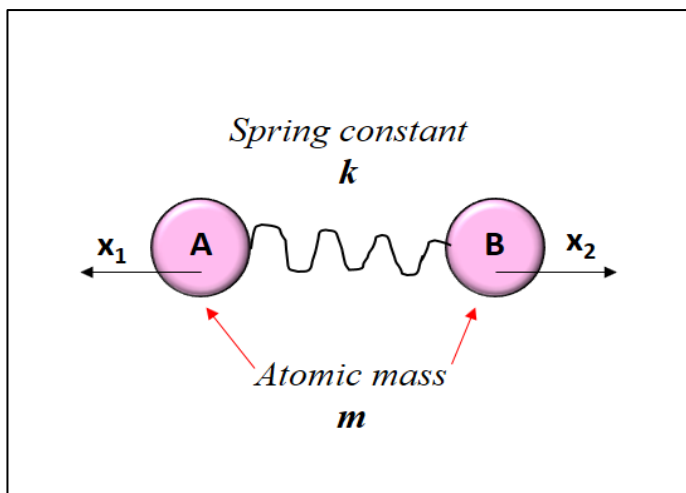


Figure 2.4 Schematic: Simple Harmonic Oscillator

Displacement from equilibrium x_1 & x_2 for weights A & B respectively; combined atomic mass of both atoms (or 'reduced mass') = m ; spring constant = k

By using Hooke's law, the equation of motion for the simple harmonic oscillator in the above schematic can be written as:

$$m \frac{d^2x}{dt^2} + kx = 0 \quad \text{Equation 2.4}$$

The total displacement is x , where $x = x_1 + x_2$

The approximation of Hooke's law works well for small displacements, and the maximum displacement is 'small', in this case; approximately 10% of the atomic bond length.[6]. For this representation, the spring constant 'k' corresponds to the atomic bond strength.

Now, we solve this second order differential equation, and replace the displacement 'x' with Q. The solution for the time dependent displacement can now be written as:

$$dQ = Q_0 \cos(\omega_{vib}t) \quad \text{Equation 2.5}$$

With dQ = the displacement from the equilibrium position; Q_0 the maximum displacement and ω_{vib} = the oscillation frequency of the SHO system - in this case the frequency of a particular vibrational mode.

Next, we develop the molecular polarizability as a function of displacement, by using a Taylor series expansion. As the maximum displacement is 'small' we can approximate the Taylor series to its first two terms and write it as:

$$\alpha = \alpha(Q) = \alpha_0 + \frac{\partial \alpha}{\partial Q} dQ + \dots \quad \text{Equation 2.6}$$

Where α_0 = the polarizability at equilibrium; i.e. no applied external field

Substituting the value for dQ from Equation 2.5 into Equation 2.6 we can now express the polarizability as:

$$\alpha = \alpha_0 + \frac{\partial \alpha}{\partial Q} Q_0 \cos(\omega_{vib} t) \quad \text{Equation 2.7}$$

Finally, we substitute the value for ‘ α ’ from Equation 2.7 into the equation for the time dependent dipole moment, P (Equation 2.3 above) to give the following:

$$P = \alpha_0 E_0 \cos(\omega_0 t) + \frac{\partial \alpha}{\partial Q} Q_0 E_0 \cos(\omega_0 t) \cos(\omega_{vib} t) \quad \text{Equation 2.8}$$

We can now apply the following trig identity to Equation 2.8 to separate the right hand side of the equation into three helpful terms.

$$\cos(x) \cos(y) = \frac{1}{2} [\cos(x - y) + \cos(x + y)]$$

$$P = \alpha E_0 \cos(\omega_0 t) + \left(\frac{\partial \alpha}{\partial Q} \frac{Q_0 E_0}{2} \right) \{ \cos[(\omega_0 - \omega_{vib})t] + \cos[(\omega_0 + \omega_{vib})t] \} \quad \text{Equation 2.9}$$

It is useful to examine the frequency dependence of each of the three terms on the right hand side of Equation 2.9. The first thing to note is that the induced dipole moments occur at three separate frequencies; ω_0 , $(\omega_0 - \omega_{vib})$ and $(\omega_0 + \omega_{vib})$.

The frequency of the first term is at ω_0 , which is the incident frequency, thus the scattering event described is elastic or Rayleigh scattering.

Both of the next two terms in the equation represent scattering events that undergo a change in frequency, i.e. inelastic scattering. The first of these describes scattering at a lower frequency and the second at a higher frequency. These are known as Stokes and anti-Stokes scattering respectively.

Moving on from the classical model, we can use quantum mechanics to understand Raman scattering. The quantum mechanical model essentially interprets Raman scattering as a three step/stage transition. Electrons in molecules occupy specific states in materials, and these states are comprised of quantized vibrational energies. An incident photon excites a molecule and is absorbed raising the system to a virtual or intermediate state. Immediately, a photon is scattered and the molecule ‘relaxes’ to a lower vibrational state.

The schematic below illustrates the difference between the Stokes and anti-Stokes scattering. Essentially, the Stokes transition relates to emission while the anti-Stokes to absorption.

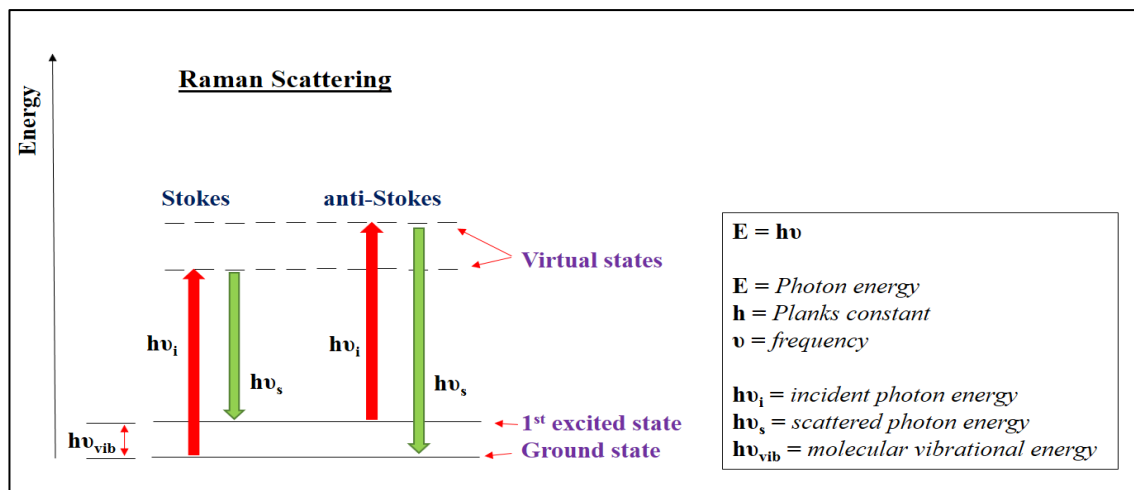


Figure 2.5 Schematic; Stokes & anti-Stokes Raman scattering

The Stokes scattering is red-shifted with respect to incident frequency and is at a lower energy. While the anti-Stokes is blue-shifted and at a higher energy with respect to the incident photon energy

The anti-Stokes intensity is much weaker than the Stokes. This is due to the lower population density of the anti-Stokes thermally excited virtual state, which is described by the Boltzmann factor.

Returning to Equation 2.9, and considering the two Raman scattering terms, it is clear that the following condition must be satisfied if Raman scattering is to occur:

$$\frac{\partial \alpha}{\partial Q} \neq 0$$

A physical interpretation of this condition, is that there must be a change in the molecular polarizability resulting from the atomic displacement. The non-zero value of ' $\delta\alpha/\delta Q$ ' is generally known as the Raman selection rule for small molecules.

2.3 Surface Enhanced Raman Scattering

Principally, when light interacts with matter it is scattered elastically by Rayleigh scattering. Subsequently the 'small' fraction of light that is inelastically scattered via Raman scattering is a weak scattering event. In 1928, C.V Raman and K.V Krishnan published their experimental findings of inelastic scattering. They reported that this scattering event was typified by "*its feebleness in comparison with ordinary scattering*" [7].

The **scattering cross section** is a useful parameter to quantify the intensity of the scattered radiation. Generally, conventional Raman scattering cross sections are much smaller than elastic cross sections (e.g. Rayleigh). Consequently, the Raman signal intensity is also much weaker. David Hahn reports the following values for diatomic Nitrogen (N₂) at 488 nm excitation:

$$\text{Scattering cross sections (cm}^2\text{/sr)} \quad \sigma_{\text{Rayleigh}} = 8.9 \text{ e}^{-28} \quad \sigma_{\text{Raman}} = 5.5 \text{ e}^{-31}$$

The resulting scattered intensities for N_2 revealed that the Rayleigh signal was more than a 1000 times greater than the Raman scattered signal [6]. In the case of a solid, the difference can be much greater, with \sim only one in $10^6 \Rightarrow 10^{10}$ photons being scattered inelastically. Additionally, Raman scattering cross sections can be up to 14 orders of magnitude lower than the effective cross sections of fluorescence.

The discovery by Martin Fleischmann in 1973 of the surface enhancement to a Raman signal has proved to be a ‘game changer’. The Surface Enhanced Raman Scattering (SERS) effect has been reported in many publications since then.

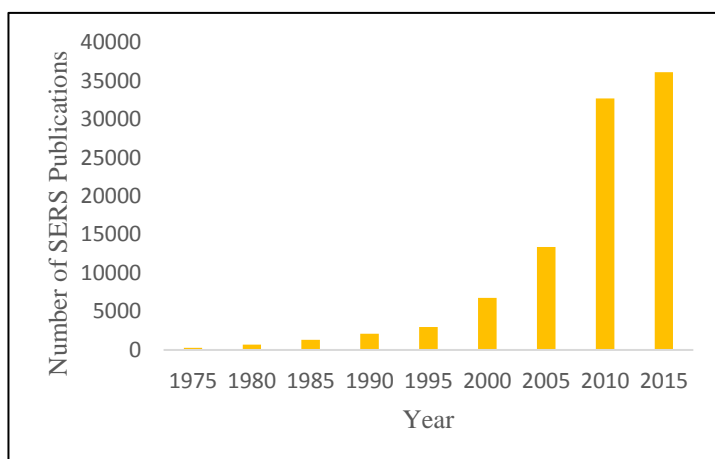


Figure 2.6 Number of SERS publications

Citation data from Google Scholar (accessed on August 29th 2016); search term - "Surface Enhanced Raman"

The initial discovery involved the observation of a strong Raman response from a monolayer of pyridine adsorbed onto a silver electrode. The electrode had been electrochemically roughened [4]. Fleischmann et al. rationalised that the enhancement arose from the increase in the surface area of the electrode. An increased surface area would lead to an increase in the number of adsorbents and hence the Raman signal. However, two separate research groups independently concluded that the signal increase was too large to be explained by an increase in surface area alone. They concluded that there must have been an actual increase of the Raman cross section leading to the enhanced signal [3].

It is generally accepted that there are two separate mechanisms that combine to generate the SERS phenomena. The first of these is electromagnetic while the other is a chemical enhancement process. It is the electromagnetic mechanism that accounts for the majority of the enhancement effect [8]. It is generally thought that these mechanisms provide average enhancement factors of \sim 100 & 10,000 for the chemical and electromagnetic respectively [2].

2.3.1 Chemical Enhancement Mechanism

When analyte molecules are absorbed onto a metal surface the molecules can interact chemically with the metal; i.e. chemisorption. This has the effect of increasing the scattering cross section and consequently the Raman intensity. From Equation 2.1, it is an increase in the magnitude of the molecular polarizability ‘ α ’ that occurs with SERS chemical enhancement.

As yet there is still much deliberation as to the mechanisms behind SERS chemical enhancement. Valley et al. describe three separate processes [9] contributing to this mechanism. These are: changes to molecular polarizability (non-resonant), molecular excitation and charge-transfer resonances. The first of these processes arises from the formation of a new chemical system between the metal and the molecule, which leads to changes in polarizability.

Whichever mechanism is responsible for chemical enhancement to the Raman signal, the molecule must be directly adsorbed onto the metallic surface. Additionally, the chemical mechanism is unique to the binding site and dependent on the specific chemical moiety of the analyte [2].

2.3.2 Electromagnetic Enhancement Mechanism

An important parameter that governs the optical (and electrical) response of a metal, is the dielectric constant ‘ ϵ ’. It is a property that is frequency dependent and is closely linked to the metal’s electronic structure. It depicts the degree of polarization that can result from an incident electric field propagating through the material, as it displaces charged particles from their equilibrium position. For metals, $\epsilon(\omega)$ and the related refractive index ‘ $n(\omega)$ ’ are complex numbers.

$$\epsilon = (\epsilon_1 \pm i\epsilon_2) = (n \pm ik)^2 \quad \text{Equation 2.10}$$

Note: ϵ_1 and ϵ_2 are the real and imaginary parts of the dielectric constant respectively; while n = refractive index and k = the extinction coefficient.

The real part of the dielectric function, ϵ_1 represents by how much a material becomes polarized as dipoles are induced by the incident EM wave. The imaginary part ϵ_2 is related to the absorption properties of the metal, i.e. vibrational energy lost as heat to the material. Thus, if $\epsilon_2 = 0$ then the material is transparent; the \pm relates to whether the dipoles oscillate in or out of phase with the incident field.

Silver and gold are two of the most useful metals for plasmonic applications. Over most of the visible spectrum, the real part of their dielectric constants is large and negative; Figure 2.7 below. The large value of ϵ_1 yields a stronger induced dipole moment, resulting in an increase to intensity related effects such as SERS. From the definition of the time dependent dipole moment, ‘P’ (Equation 2.1), an increase in the electric field naturally results in an increase to ‘P’.

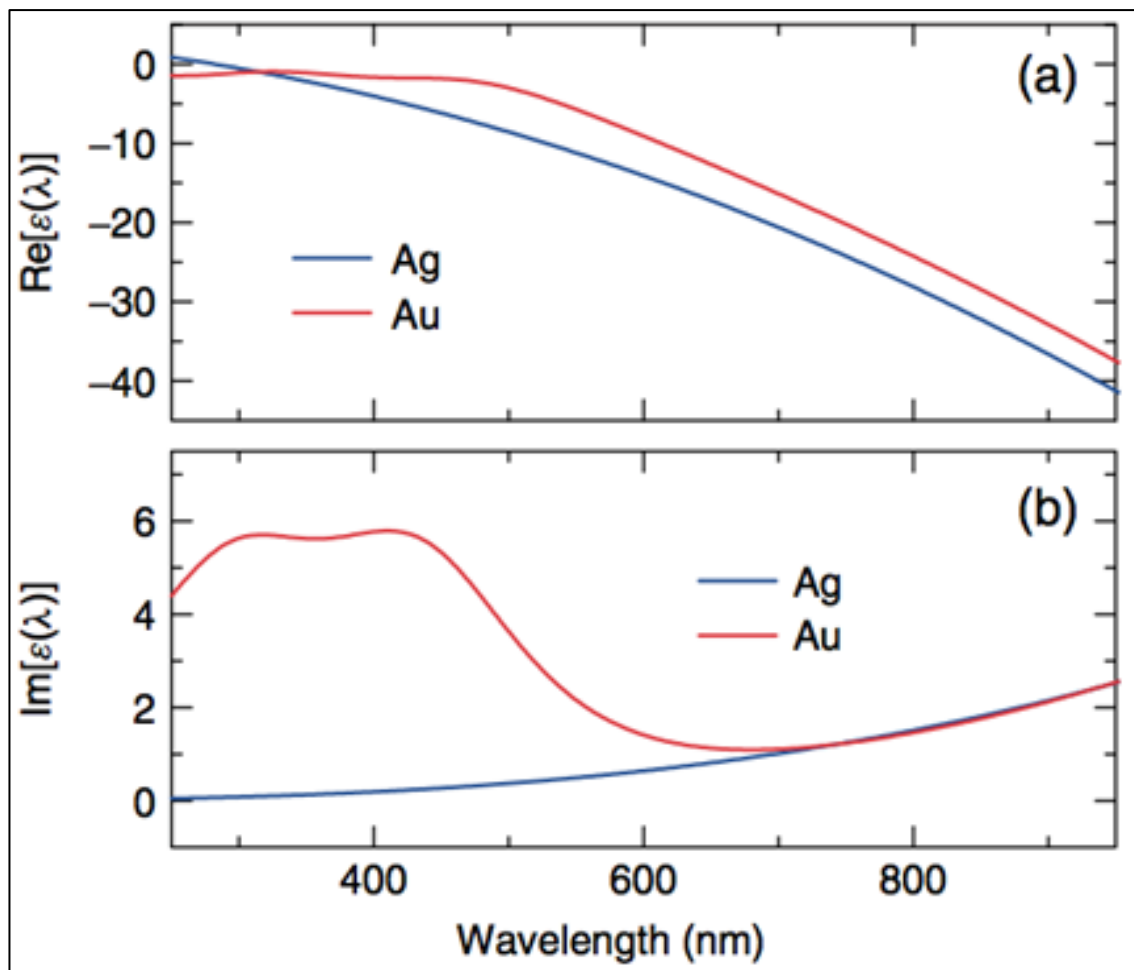


Figure 2.7 Wavelength dependence of dielectric constants of Silver & Gold

(a) The real part of the dielectric, ϵ_1 increases in magnitude with increase in λ towards the NIR for both metals (b) The imaginary part, ϵ_2 for Gold is greater than that of Silver for wavelengths ≤ 600 nm (which results in increased absorption); see General references, page 207 [10]

The electromagnetic enhancement mechanism of SERS arises from collective oscillations of electrons on the surface of noble metal nanoparticles or nanostructures. This effect is called Local Surface Plasmon Resonance (LSPR). Metallic nanoparticles or nanostructures can sustain oscillating Plasmons resulting from interaction with an incident time varying field. Surface Plasmons possess both transverse and longitudinal electric field components, while bulk Plasmons have only longitudinal. This transverse characteristic of surface Plasmons allows them to interact with light that is incident at the metal surface.

A standard model used to describe the LSPR effect of SERS, is that of a single metallic nanosphere illuminated by incident light. A key parameter for this model is that the particle size must be much smaller than the incident wavelength. When this is the case, the electric field is effectively static from the reference point of the nanoparticle. This allows the use of the electrostatic approximation of Maxwell's equations.

Two cases of a nanosphere illuminated by an electromagnetic wave are illustrated in the following schematic. The left image is of a sphere with a dimensionality of the order of the incident wavelength, λ . The right image is a sphere with radius, $a \ll \lambda$.

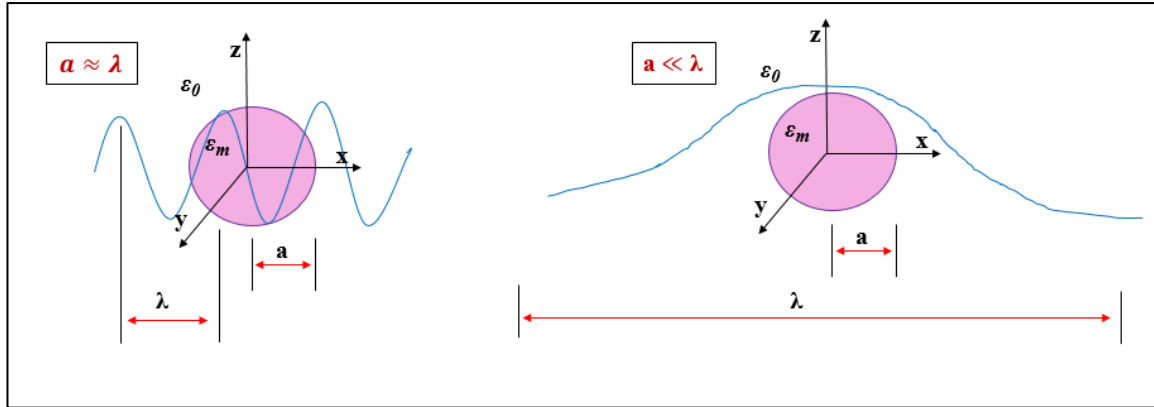


Figure 2.8 Nanosphere irradiated by incident light

Propagation along y, z-polarized light of single wavelength λ . Dielectric permittivity: metal = ϵ_m surrounding environment = ϵ_0

An expression is derived for the quasi-static electric field case (*right image above*) as follows. The perturbation of electron gas by the incident field gives rise to an induced dipole. This displacement of negative charge against the restoring force of the positive nuclei forms a stationary plasmonic oscillation.

The individual field vectors (Cartesian coordinates) are polarization dependent and for z polarized light: $E_x = E_y = 0$ with $E_z \neq 0$. Thus, the general form for the field can be written as:

$$E_z = E_z^0 \cos(kx - \omega t) \quad \text{Equation 2.11}$$

For the long wavelength approximation, i.e. $\lambda \gg a$, then $\omega t \gg kx$ and the field expression simplifies to:

$$E_z = E_z^0 \cos(\omega t) \quad \text{Equation 2.12}$$

Another consequence of $\lambda \gg a$, is that the external field can be assumed to be approximately constant in time. Thus for static charges, Maxwell's equations of electrostatics and magnetostatics describe separate effects, and the magnetostatic equations can be ignored. Further simplification can be made by replacing Maxwell's equations with Laplace's equation for the scalar potential; $\phi(x, y, z)$, given as:

$$\nabla^2 \phi = 0 \quad \text{Equation 2.13}$$

The harmonic solutions for the Laplace equation are derived via converting from Cartesian to spherical coordinates, and subsequent separation of radial and angular variables. Solving the radial equation yields two solutions which can be combined to form one general solution. The solution contains two coefficients which are determined via geometry driven boundary conditions.

These boundary conditions are as follows:

$$E_{in} \neq E_{out}$$

i.e. the field inside the sphere must be different to the field outside.

$E_{in}(x, y, z) \rightarrow \text{finite valued as } r \rightarrow 0$

The field at the sphere centre, as ($r \rightarrow 0$) is non-zero.

$E_{out}(x, y, z) \rightarrow E_0\hat{z}$ as $r \rightarrow \infty$

The incident field is unaffected by the sphere's presence in the far field region, i.e. as $r \rightarrow \infty$.

The coefficients can be determined using these boundary conditions. Thus, the analytical solution for the electric field surrounding the particle, E_{out} can be given by the following equation.

$$E_{out}(x, y, z) = E_0\hat{z} - \left[\frac{(\epsilon_m - \epsilon_0)}{(\epsilon_m + 2\epsilon_0)} \right] a^3 E_0 \left[\frac{\hat{z}}{r^3} - \frac{3z}{r^5} (x\hat{x} + y\hat{y} + z\hat{z}) \right] \quad \text{Equation 2.14}$$

Where a = sphere radius; ϵ_m & ϵ_0 are the dielectric functions for the metal and surrounding environment respectively; r = radial distance from sphere. Light is at normal incidence with E_0 magnitude of the incident electric field; x, y, z – Cartesian coordinates.

[A full derivation of Equation 2.14 is laid out by Willets and Van Duyne in the supplementary material of their 2007 publication [11] at: <http://www.annualreviews.org>]

From the small sphere, long wavelength solution above, we can see that the field around the nanosphere decays rapidly with distance from the surface. The local electric field that arises from the Plasmon resonance is a near field effect, with the decay following at least a $1/r^3$ dependence. Essentially, as $r \rightarrow \infty$ then, $E_{out} \rightarrow E_0$, generally within 2-4 nm from the surface. Within the field of SERS, these highly localised regions of intense electric field are known as 'Hot spots'.

The first bracketed term on the R.H.S (often defined as 'g') will determine the local field enhancement and the resonance conditions of the nanosphere. Note that the time dependent induced dipole moment, 'P' is $\propto g$.

$$g_{\text{sphere}} = \left[\frac{(\epsilon_m - \epsilon_0)}{(\epsilon_m + 2\epsilon_0)} \right] \quad \text{Equation 2.15}$$

The real part of the dielectric constant of the metal ' ϵ_{in} ' has a strong wavelength dependence. Consequently, the magnitude of the enhancement will also be wavelength dependent. The maximum enhancement for a nanosphere will occur when, ϵ_m is negative and: $\epsilon_m \rightarrow 2\epsilon_0$; for $a/\lambda \leq 0.1$. This condition is met for silver and gold for the visible spectrum [11]. The particle size, 'a' and the dielectric function of the surrounding environment ' ϵ_0 ' will also contribute to the enhancement.

In summary, the foremost contribution to SERS enhancement will be electromagnetic enhancement, arising from the metal nanoparticles/nanostructures. Some additional enhancement will result from an adsorbed molecule in the SERS near field region.

When 'g' is calculated for a nanocylinder, the following result is achieved [12].

$$g_{\text{cylinder}} = \left[\frac{(\epsilon_m - \epsilon_0)}{(\epsilon_m + \epsilon_0)} \right] \quad \text{Equation 2.16}$$

As per the nanosphere calculation, the field is assumed to be a static field; the approximation holds well for dimensionality much less than λ_0 i.e. $\sim 10\text{-}20$ nm. Additionally, the source wave is at normal incidence to the side of the nanocylinder as shown in the schematic below.

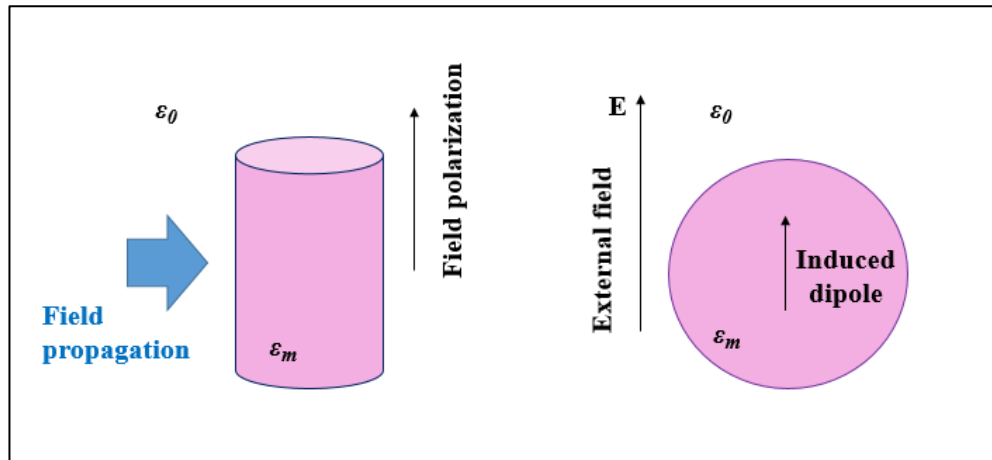


Figure 2.9 Schematic; Nanocylinder irradiated by incident light

The field is assumed constant in the direction of polarization, which is on the plane of the page – left image.

For a nanocylinder, resonance and peak enhancement is again achieved when ϵ_m is negative and: $\epsilon_m \rightarrow \epsilon_0$. By comparing the two expressions for ‘g’ (Equation 2.15 & Equation 2.16), we can see that the difference in enhancement between the two examples is principally geometry driven. Geometry induced resonance is a significant property of Local Surface Plasmon Resonance.

2.3.3 Local Field Intensity & SERS Enhancement Factors

The Local Field Intensity (LFI) is proportional to the square of the electric field amplitude at a specified point of interest. It is useful to consider changes to the LFI that result from an obstacle or inhomogeneity in the path of an electromagnetic wave. Thus, the Local Field Intensity Enhancement Factor (LFIEF) can be defined as the LFI normalised with respect to that of the incident field.

$$\text{LFIEF}(r, \omega) = \frac{|E_{loc}(r, \omega)|^2}{|E_0(r, \omega)|^2} \quad \text{Equation 2.17}$$

With E_{loc} & E_0 the magnitude of the local and incident fields respectively; the LFIEF is dependent on both the frequency, ω and the distance from the surface, r .

When $\text{LFIEF} > 1$ enhancement will occur; as per the case of nanoparticles and nanostructures interacting with light. If the $\text{LFIEF} < 1$ quenching will ensue, which is generally the case for a planar metallic surface. For a planar interface between a bulk metal and air, LFIEF quenching occurs due to the local field oscillating out of phase with the incident field.

The SERS electromagnetic enhancement mechanism causes an increase to the Raman signal because of an amplification of both the Raman and incident electric fields [3]. Thus, it is both the emission and excitation enhancements that contribute to surface enhanced Raman

scattering. As such, we can define the SERS enhancement factor (EF) as the following product:

$$\text{SERS EF} = \text{LFIEF}(\omega_L) \times \text{LFIEF}(\omega_s) \quad \text{Equation 2.18}$$

Where ω_L & ω_s are the laser (excitation) and scattered (emission) frequencies respectively.

It is important to note that the emission is directly linked to the excitation, i.e. stronger SERS signals are observed with increased laser intensity. In the majority of cases, there is only a marginal difference between ω_L & ω_s . Thus, a commonly used approximation for the SERS EF is:

$$\text{SERS EF} \sim \text{LFIEF}(r, \omega)^2 = \frac{|E_{loc}(r, \omega)|^4}{|E_0(r, \omega)|^4} \quad \text{Equation 2.19}$$

With $\omega \approx \omega_s \approx \omega_L$

This is generally referred to as the E^4 SERS EF approximation.

2.4 SERS Substrates

2.4.1 Substrate Material; Surface layers

Metallic surfaces that facilitate the Plasmonic oscillation of free electrons are essential in generating the SERS effect. The most widely used metals for the surface of SERS substrates are silver and gold and to a lesser extent copper [2], with silver and gold generating the greatest signal enhancement. The SERS enhancement from silver will be larger than from gold. This is due to the dielectric function of silver that has the effect of minimising plasmon resonance damping in the UV [13]. Other metals that can also produce the SERS effect include: aluminium [14], indium [15], platinum and palladium [16].

2.4.2 Substrate Classifications

Following Fleischman's discovery of SERS in 1973, initial SERS characterisation involved studies of pyridine on Ag electrodes [17]. This progressed to more sophisticated surface analysis, such as the work by Haynes and Van Duyne correlating spectral data to nanoparticle structure [18]. Real world applications followed with SERS sensing being used for example in the detection of glucose [19] and anthrax [20].

There are essentially two different classifications of SERS substrates which in the most general sense can be considered as random or engineered substrates. Specifically, they can be classified as either Metallic Nano Particles (MNP's) implemented as colloidal dispersions or platform-based units. Platform-based substrates comprise of noble metal surface nanofeatures acting as the SERS-active 'region' [21].

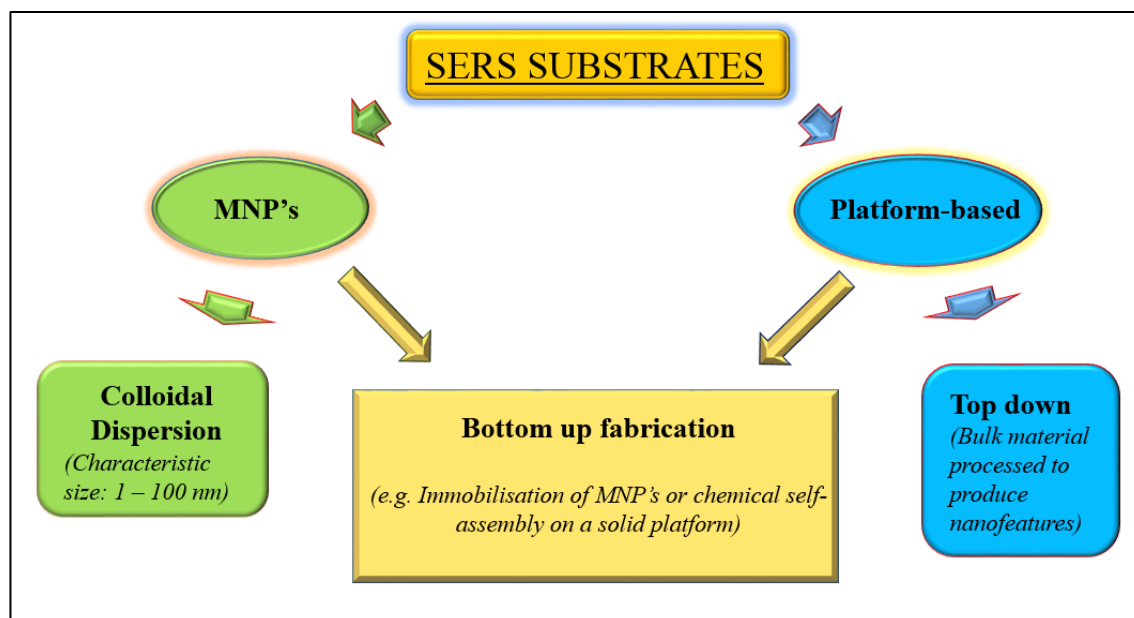


Figure 2.10 Schematic SERS substrate classifications

MNP's frequently used due to facile preparation techniques; Platform-based typically 'top down' fabrication; both categories can avail of 'bottom up' processes

2.4.3 Metallic Nanoparticle SERS substrates

MNP colloidal dispersions are arguably the most commonly used SERS substrates due to facile fabrication and high SERS enhancement [22]. SERS enhancement factors of the order of 10^{14} have been reported from colloidal Au nanoparticles which had aggregated into clusters. However, when nanoparticle clustering does not occur the SERS enhancement factor is significantly less (e.g. $\sim 10^3$) [23]. The clustering of nanoparticles can yield large enhancements, Yan et al. [24] reported an increase in the near-field coupling of adjacent particles due to increase in cluster size. Their report concludes that two factors lead to an increase in the SERS response. Firstly, that clustering leads to a reduced gap between nanoparticles with concomitant Coupled Plasmon Resonance. Additionally, there is a measurable electromagnetic interaction between clusters that increases the Raman signal of individual clusters.

Spherical nanoparticle colloids (Ag or Au) were amongst the first and are still the most widely used colloidal SERS substrates [25]. In 1974 Kreibig reported on the size dependence of the dielectric constant of spherical Ag nanoparticles [26]. While a more recent example of spherical nanoparticles and SERS is reported by Lane et al. with their use in SERS biosensing research in 2015 [27].

A comparison of the SERS response of different MNP shapes is presented by Ciou et al. [28]. Their work examined the SERS enhancements of Ag spherical and truncated prism-like MNP's, both functionalised with Rhodamine-6G in Potassium Bromide. The prism-like nanoparticles exhibited up to 20 times better enhancement factor than the spherical MNP's.

MNP's are easily prepared by chemical synthesis [29]. Generally, the synthesis involves a solvent containing the Ag or Au seed particles being mixed with acids such as Chloroauric and Ascorbic. It is believed that the organized nanofeatures that form, originate from the seed's crystal structures [30]. The development of seeded growth Au Nanorods in 2001 paved the way for more complex nanoparticle shapes. Examples of the many different nanoparticle shapes include: Nanostars, Nanocubes, and Nanotriangles [25]. Other more complex shapes have also been fabricated such as branched metal Nanoflowers [31], polyhedral nanocrystals [32] and capped dendritic Au NP's [30].

A disadvantage of colloidal MNP substrates is the random nature of MNP aggregation that can lead to poor reproducibility. In addition to random aggregation, another cause of poor reproducibility is the degrading of MNP's in solution over time or through laser exposure [13]. MNP's are generally more suited to trace analysis or solution phase SERS evaluation [2] (although the purity of the substrate must also be considered when used for trace analysis).

The poor reproducibility of Colloidal dispersions can be reduced by the immobilization of MNP's on a solid substrate. A common approach to achieve this is via the 'Bottom up' process of chemical self-assembly. Generally, this is implemented by the chemical attachment of a bifunctional molecule to the substrate surface. The molecule is bound to the surface with one functional group while the other bonds to the MNP in a self-assembly process. Freeman et al. used glass slides functionalised with amine or thiol groups, which were then incubated in a colloidal dispersion to generate MNP self-assembly [22].

Immobilising MNP on a surface or solid substrate base through self-assembly can be classified as a ‘bottom up’ process. ‘Top down’ and ‘bottom up’ describe the two fundamental techniques used in Nano technology. ‘Bottom up’ nanosynthesis essentially involves the creation of nanostructures from smaller building units such as molecules or nanoparticles. ‘Top down’ fabrication begins with a bulk material and produces nanostructures through processes such as lithography, milling or etching.

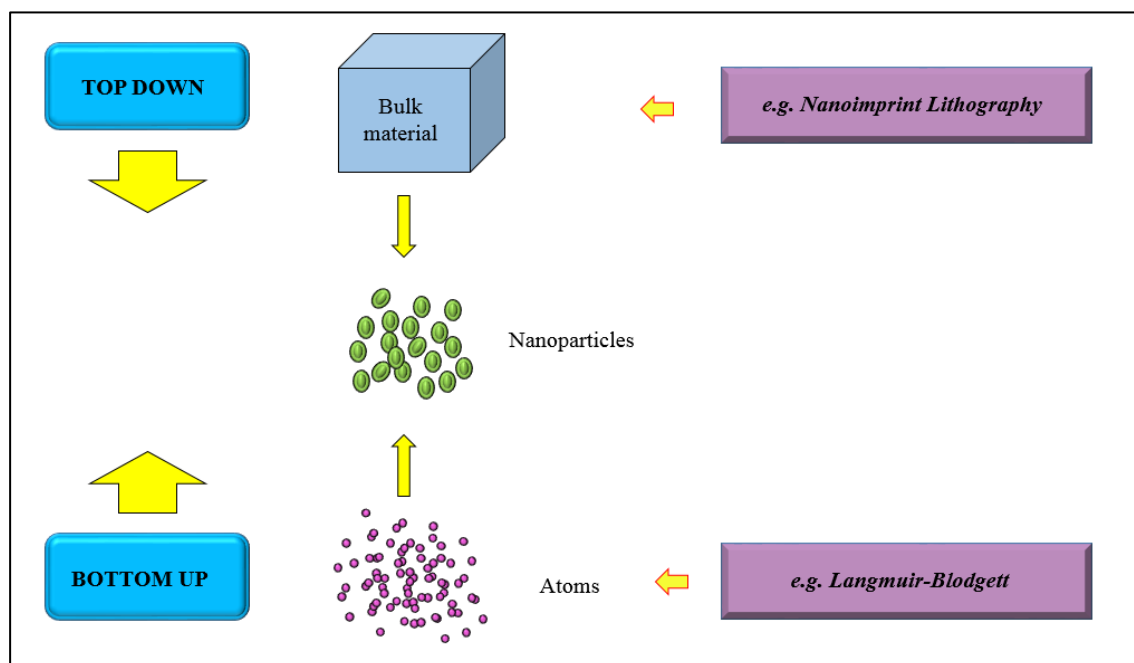


Figure 2.11 Schematic; ‘Top down’ & ‘bottom up’ processing

In summary, MNP SERS substrates can be fabricated with relatively simple techniques and offer good SERS enhancements, however, they often exhibit poor reproducibility.

2.5 Platform-based Substrates

Regarding SERS substrates of any type, there are a number of performance related issues that need to be considered, the main points are described as follows:

The obvious requirement for any SERS substrate is that of **high sensitivity** arising from a strong signal enhancement. There should also be a good **reproducibility** of the SERS signal from spot to spot and substrate to substrate. Finally, a substrate should also possess a ‘reasonable’ shelf life stability. A substrate that degrades immediately after fabrication is of limited usefulness. A signal variation of $\leq 20\%$ measured weekly over a month post fabrication was suggested by Natan [33] at the Faraday Discussion Meeting in Imperial College, London. A value of $\leq 20\%$ was also suggested by him for the deviation of the SERS signal from spot to spot and substrate to substrate.

The SERS enhancement factor is a fundamental qualifier for any SERS application. However, for quantitative sensing a consistent and reproducible substrate is also required. Platform-based SERS substrates potentially offer far greater substrate uniformity than MNP’s and are the substrates used in our study. Advances in Nanofabrication techniques have enabled the development of diverse and sophisticated SERS chips. Techniques such as Nano

Imprint Lithography (NIL) can yield highly uniform surface features, and thus low signal variation.

2.5.1 Materials & Fabrication

Silicon is the most commonly used material for the substrate platform, often used as wafers [34] or in other forms such as Silica particles [35]. Various types of processed Silicon are also used for SERS substrates such as Black Silicon [36, 37] and Porous Silicon [38, 39]. Black Silicon was originally discovered as an ‘unwanted’ side-effect of Reactive Ion Etching (RIE) of Silicon. While Porous Silicon was also inadvertently discovered, during an attempt to polish Silicon via electrochemical etching in 1956 at Bell Laboratories.

The name of Black Silicon is derived from the optical properties of the nanostructures formed by RIE. Arrays of needle-like nanostructures are produced that reduce the Reflectivity to ~ 5% over a broad wavenumber range [40]. Talian et al. [41]. report on black silicon with a 400 nm Au surface film yielding a SERS enhancement factor of $\sim 10^7$, the analyte used was Rhodamine 6G. The enhancement factor was calculated from a reference signal gained from a planar gold coated silicon wafer.

Porous Silicon consists of an array of nanoholes with a large surface to volume ratio, which can be up to three orders of magnitude greater than a polished Silicon surface. The dimensions of the nanoholes can be optimized by varying fabrication parameters such as etchant composition and time. The surface geometry of the porous silicon contains a high density of nucleation sites for the growth of silver nanocrystals during immersion plating [38]. The resulting closely packed Ag nanocrystals yield a strong SERS enhancement. Chan et al. report an enhancement of $\sim 10^7$ from Rhodamine 6G functionalised Ag porous silicon substrates [39].

There are many fabrication techniques that have been used to produce platform-based SERS substrates, some key methods are illustrated in the following schematic.

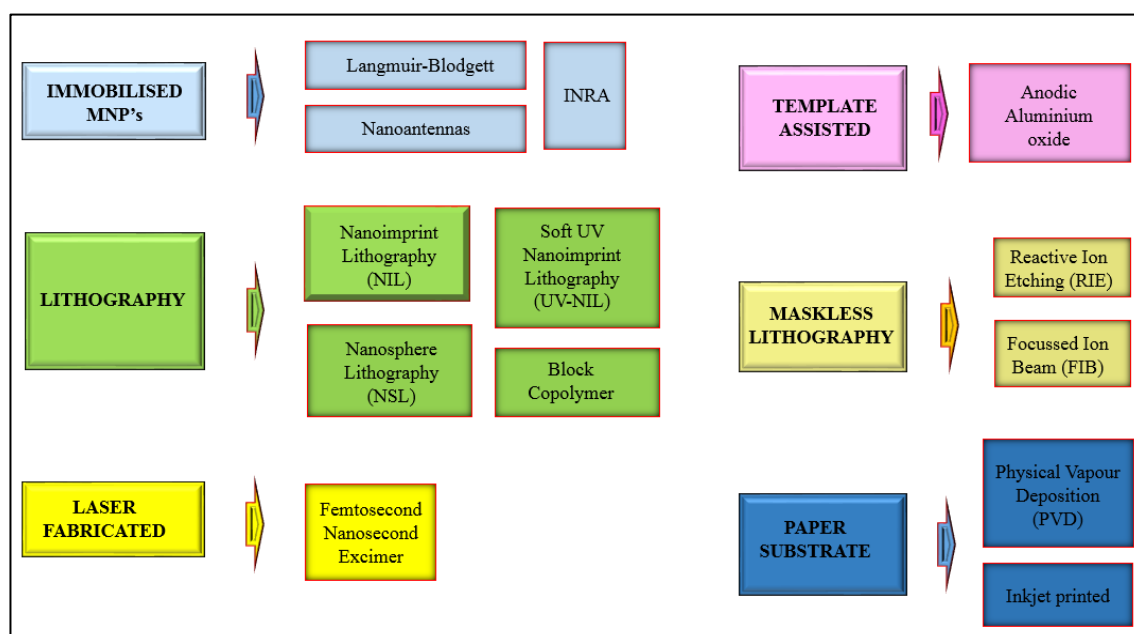


Figure 2.12 Schematic; Platform-based SERS substrate types/fabrication techniques

2.5.2 Immobilised MNP's substrates

A 'top down' approach to immobilising MNP's on a platform is used to fabricate Immobilised Nanorod Assemblies (INRA) substrates [13]. The INRA substrates are produced by depositing a noble metal film onto an array of nanospheres. Nanopillars form in the gaps between spheres during the deposition.

One of the 'bottom up' techniques used to immobilise MNP's on a solid platform is the Langmuir-Blodgett (LB) method. The LB process was developed by Irving Langmuir and Katherine Blodgett in the 1930's. An LB film usually comprises of amphiphilic molecules; i.e. a combination of hydrophilic and hydrophobic components. The method involves the formation of a film of organic monolayers onto a water/surface interface which can then be deposited onto a solid surface [42].

In order to use the LB method for immobilising nanoparticles onto a platform, a nanoparticle film is first prepared by conjugation with hydrophobic molecules. Next, the nanoparticles are mixed in a solution that is immiscible in water, and then dispersed in the water. After the solvent evaporates, a layer of randomly distributed nanoparticles forms at the water interface. The remainder of the LB process involves a compressive transfer of the film onto a solid surface. During this compression, the inter-particle spacing reduces with formation of an ordered closely packed film [43]. Tao et al. [44] report a SERS enhancement factor of $\sim 10^5$ and 10^9 for LB prepared substrates from 2,4-Dinitrotoluene and Rhodamine 6G respectively.

2.5.3 Anodic Aluminium Oxide (AAO) substrates

'Bottom up' synthesis can also be used to produce SERS Nanoantennas. Seed mediated growth of nanoparticles, followed by various stabilisation and purification stages can produce aggregation of strongly SERS-active nanoparticles on a solid platform [13]. Kleinman et al. [45] reported an enhancement factor of $\sim 10^8$ using SERS Nanoantennas functionalised with BPE.

Electrochemical oxidation of Aluminium foil can be used to produce an Anodic Aluminium Oxide layer comprising of nanopores. The layer of nanopores is then used as a template for the deposition of metallic nanowires or rods using electroplating. Using this type of template-assisted fabrication, Du et al. [46] reported enhancement factors of $\sim 10^6$ from 4-Mercaptopyridine. Additionally, they found that the strength of the SERS signal could be 'tuned' by altering the aspect ratio of the nanowires.

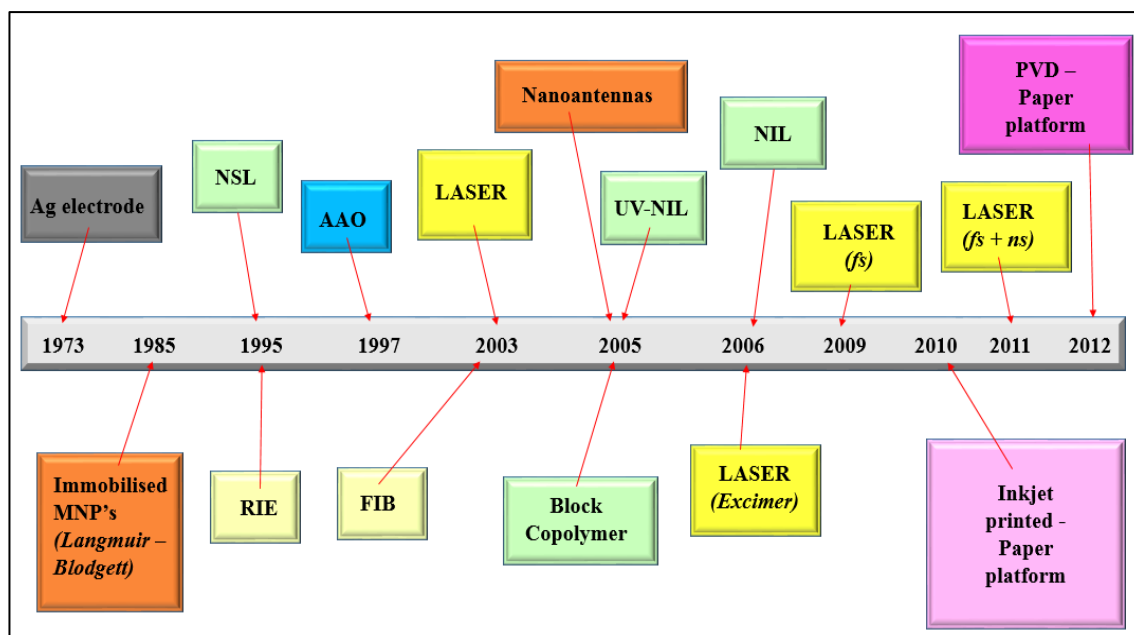


Figure 2.13 Schematic; approximate timeline - SERS substrate fabrication
Approximate timeline for main SERS substrate types

2.5.4 Laser processed substrates

Traditionally laser processing has been used to produce sub-micron surface features of a similar dimension to the incident laser wavelength. However, the development of short pulsed lasers has led to laser processing being used to fabricate nanostructures [47] and SERS substrates. One of the earliest attempts using lasers to fabricate SERS substrates was carried out by Bjerneld et al. [48] in 2003. Laser processing can be used for deposition, etching or ablation patterning. However, Bjernelds group used lasers to induce the growth and deposition of noble metal nanoparticles. Visible laser irradiation ($\lambda = 514$ & 647 nm) was directed onto an aqueous solution of Ag ions containing a reducing agent which resulted in a photoinduced growth of Ag nanoparticles. It was found that the nanoparticle size could be controlled by adjustments to the laser power. Also, ordinary cover glass could be used rather than specialised photoactive surfaces for the platform.

Another laser processing technique to fabricate SERS substrates was carried out by Agarwal et al. [49] using Pulsed Laser Deposition (PLD). Gold thin films were deposited from a 'pure gold target' by PLD with an Excimer laser ($\lambda = 248$ nm) onto silicon wafers. The gold targets were rotated during the PLD in the presence of an Argon atmosphere. Formation of metallic nanoparticle clusters was achieved by control of the gas pressure during the PLD process. The SERS performance of the substrates was assessed by concentration threshold Raman measurements. The lower threshold values obtained were $\sim 10^{-10}$ & 10^{-6} Molar for Rhodamine 6G & Apomorphine respectively; Apomorphine is a pharmaceutical drug used to treat Parkinson's disease.

A two-step process involving a short pulsed femto second (fs) laser followed by thermal evaporation was performed by Diebold et al. [50]. The surface of a silicon wafer was nanostructured using an 800 nm centre wavelength fs laser. Using frequency doubling of the pulse train, the centre wavelength was reduced to 400 nm. A silver thin film was then

thermally evaporated onto the nanostructured surface. The surface then covered with silver nanoparticles with diameters ranging from 50 – 100 nm. Using the Raman reporter Benzene-thiol, SERS enhancement factors of $\sim 10^7$ were calculated; the calculation was performed using a liquid sample as a reference measurement.

Yet another variation to laser fabricated substrates was carried out by Hamdorf et al. using a three-step procedure [51]. The surface of a silicon wafer was nanostructured with a fs laser; this was followed by metallic thin film deposition. An additional third step of nanosecond (ns) laser annealing was performed. The centre wavelength of the fs laser was 800 nm, and generated periodic ‘trenches’ on the wafer surface the gold layer was ~ 50 nm thick and was put down on the nanostructured silicon surface via a sputter coater. The ns laser was used to fabricate nanoparticles by partially melting the gold film. Adjustment of the laser fluence was required to avoid ablation and create melting of the gold film. SERS enhancements of $\sim 10^7$ were gained from Rhodamine 6G by calculations using measurements from a reference sample. The trenches produced by fs nanostructuring, generate an increase in surface area which leads to an increase in the number of nanoparticles deposited from the ns annealing.

2.5.5 Lithography fabricated substrates

Lithography techniques are a ‘top down’ approach to fabrication, where nanoarchitecture is constructed onto the ‘bulk’ material. Uniform periodic arrays of nanostructures can be produced using Nanoimprint Lithography (NIL). During NIL, a ridged mask or mold is first patterned using Electron beam patterning. The mask is then used to ‘mechanically’ imprint the pattern onto a resist coated surface. To generate a SERS response, the patterned substrates are further processed with etching and metallic film deposition. Increased output can be achieved using NIL in comparison to Electron beam lithography, because with NIL the electron beam writing is only used to produce the mask.

Alvarez-Puebla et al. [52] have used NIL to fabricate silver SERS substrates. A Polystyrene imprint resist was used to produce an array of nanostructures. In addition to a substrate with a planar surface, structured surfaces included: nanopillars of varying dimensions and a nanograting. All surfaces were coated with a SERS-active silver film by Physical vapour deposition (PVD). The relative SERS response between different substrates was assessed by calculating their relative enhancement factor. This was gained from the ratio of Raman intensity to number of analyte molecules within the laser spot with respect to the comparison substrate. The Raman reporter used was 2-Napthalene thiol. Their work correlated the relative SERS enhancements to surface topography. The advantages of NIL techniques are: large scale reproducible nanofeatures with optical tunability.

A variation to NIL that circumvents damage to surface structures arising from the use of ridged imprint masks is to use soft UV-NIL. Soft UV-NIL utilises a soft/flexible polymer mask for the imprint process [53]. The general process flow is as follows. A flexible polymer stamp with the desired nanofeatures is produced using electron beam writing. A silicon wafer is spin coated with a suitable resist, and imprinted with the flexible stamp. The resist is cured by exposure to UV light and the stamp is removed. RIE is then used to complete the pattern transfer into the silicon wafer [54].

Lithography techniques traditionally use a ‘mask’ to transfer a pattern onto a surface. An alternative lithography technique is Nanosphere lithography (NSL) which uses an array of nanospheres as a form of template assisted lithography. A 2D colloidal deposition mask can be fashioned by using either spin coating, drop coating or thermoelectrically cooled angle coating [55]. The nanospheres would typically comprise of either polystyrene or silica.

A general process flow for NSL begins with the self-assembly of a monolayer of nanospheres onto a platform such as a glass cover slip. Next a metallic film is deposited onto the colloidal mask. Different approaches can be followed for the next stage of the process which yield different structure types [29]; three methods are mostly used. The first uses Physical Vapour Deposition (PVD) to form a film over the nanosphere template; these substrates are known as Film over Nanosphere (FON) substrates. The second technique processes the FON substrate further by removing the nanosphere template, resulting in triangular or tetrahedral shaped nanoparticles. The nanospheres can be removed using a suitable solvent in an ultrasonic bath. The final method is to use electrochemical deposition and also remove the nanospheres, the resulting structures tend to be hexagonal metal Nanoislands. In each case the nanostructure array produced is uniform and periodic.

Sweetenham and Notinger performed NSL using a polystyrene nanosphere template [56]. After deposition, the polystyrene nanospheres were removed to form an array of silver truncated tetrahedral nanostructures. They reported a SERS enhancement factor of $\sim 10^5$ from NSL substrates functionalised with Rhodamine 6G.

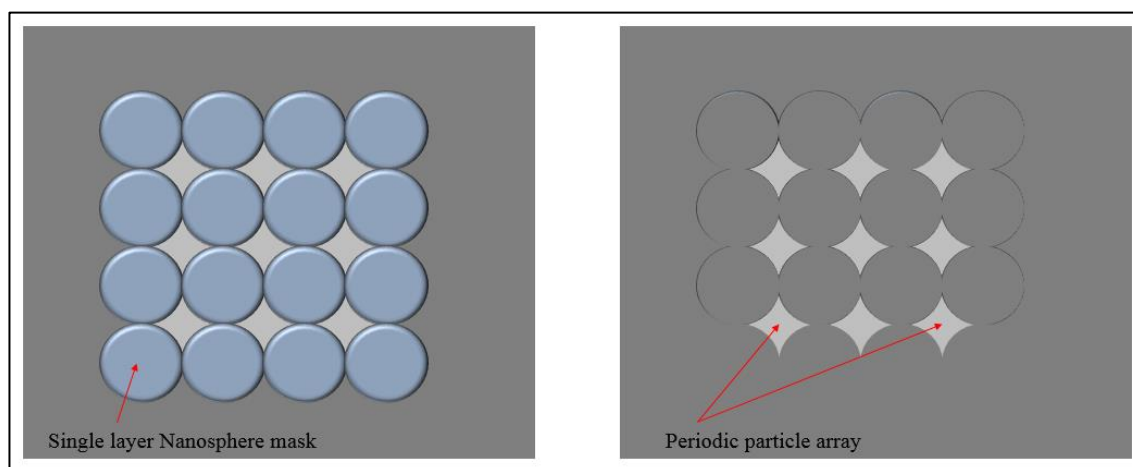


Figure 2.14 Schematic; Nanosphere lithography

Single layer nanosphere mask left image; Periodic particle array remains after removal of nanospheres right image; height of features dictated by etching parameters

Another variation of lithography methodologies is Block Copolymer Lithography, which is a marriage of ‘bottom up’ and ‘top down’ nanofabrication [57]. The process involves two or more Block Copolymers that are covalently bound at one end. As the Polymer chains are different chemically, they are immiscible, and easily self-assemble into complex nanostructures. The dimensionality is restricted only by the size of the polymer chains. The chains are linked together and phase-separation restricts the size of the features to $\sim 5\text{-}20$ nm [58]. The ‘bottom up’ self-assembly of the polymers, is then combined with ‘top down’ deposition of a metallic film to create a SERS-active coating.

Zhang et al. fabricated gold octahedral shaped nanostructures on a silicon wafer using the Block Copolymer method [59]. Measurements from their substrates functionalised with 2-Naphthalene thiol were compared to gold-citrate nanosphere substrates. The gold octahedral substrates yielded a three times greater Raman signal intensity than gold-citrate units.

2.5.6 FIB & RIE substrate fabrication

Focussed Ion Beam (FIB) and Reactive Ion Etching (RIE) are two popular methods used in Maskless lithography.

Lin et al. used FIB to fabricate gold nanostructured substrates of varying geometries [60]. Using electron beam evaporation, a 500 nm gold film was deposited onto a silicon wafer. Processing of the gold film via FIB produced arrays of nanostructures with different topographies, generated by adjustment of FIB parameters. Structure shapes included: hexagon, pentagon, shield and kite-like features. Interstructure spacing of ~ 22 nm was achieved. A similar process was carried out by Sivashanmugan et al. but was also combined with an extra step of nanoparticle deposition [61]. A gold film exposed to FIB produced a uniform array of gold nanorods. Deposition of silver nanoparticles was then performed to further enhance the SERS response, which demonstrated a significant increase over the gold nanorods.

Maskless Reactive Ion Etching (RIE) has been used to produce high efficiency SERS substrates [1]. RIE of a silicon wafer is used to produce a large area array of silicon nanopillars of uniform height [62]. Metallic deposition is then used to create a SERS-active surface. The high aspect ratio nanopillars have a tendency to 'lean' towards adjacent pillars creating efficient 'hot spots' that generate strong SERS enhancements [63].

2.5.7 Paper as substrate platforms

The topography of paper contains micro and nanofibers which has led to investigating its suitability for use as a solid platform for plasmonic nanostructures. A number of different fabrication techniques and different types of paper have been used. Zhang et al. examined six different paper types [64], and used Physical vapour deposition (PVD) of silver to produce SERS substrates. Testing with Rhodamine 6G demonstrated that the SERS test strips could detect ultra-low concentrations of 10^{-10} Molar. Other reported techniques for fabricating SERS paper substrates include: spray application; brushing; laser treatment and inkjet printing.

The paper substrates fabricated by spray application were first prepared with a wax printer [65]. The printed design yielded separate hydrophilic and hydrophobic (waxed) regions. A solution of glycerol/Ag colloids was sprayed onto the hydrophilic region using a hand spray applicator. A SERS enhancement of $\sim 10^7$ (based on a reference signal) enabled detection of Rhodamine 6G at concentrations of 10^{-9} Molar. The spray technique produces an even dispersal of nanoparticles across the paper fibres. Applying the MNP solution with a dipping technique can also result in uniform distribution of particles, but has the disadvantage of lengthy process time; up to two days. Direct dropping is also a facile method for application of the MNP solution, however it produces irregular nanoparticle deposition.

Another facile approach to fabricate paper SERS substrates is to use brushing to achieve nanoparticle coverage; this method was reported by Zhang et al. [66] in 2014. Application with gentle brushing, followed by drying and a repeat application of brushing from the opposite direction produced a uniform nanoparticle deposition. An enhancement factor of $\sim 10^7$ for Rhodamine 6G was calculated and a relative standard deviation of $\sim 15\%$. The enhancement factor was calculated by comparison with a reference signal from a paper substrate without MNP's.

Yu et al. [67] report on a technique to fabricate SERS substrates from a paper platform using deposition of a metal film, and subsequent laser processing. The first step of their process involves a noble metal film being deposited onto filter paper. The fibril topography of the paper encourages formation of a metal layer that is discontinuous in nature. Silver and gold are strong absorbers in the deep-UV, and a KrF Excimer ($\lambda = 248$ nm) is used to maximise thermal conductivity in the metal film. Additionally, the low thermal conductivity of the paper leads to highly efficient conversion of the laser power to heat within the metal film. Yu et al discovered that a single laser pulse with a power density of 125 Jcm^{-2} could generate the formation of highly concentrated nanoparticle arrays. Investigation of this technique with other platforms such as silicon and glass revealed that paper produced the best SERS substrate. Fabrication with the silicon and glass platforms required several laser pulses, leading to ablation and a decreased yield of nanoparticles. A concentration detection limit of 10^{-18} Molar was achieved when testing the paper substrate with the Raman reporter 4-ATP, which is within the regime of single molecule detection.

In order to fabricate SERS test strips, Wu and White utilised an inkjet printer to apply 'nanoparticle ink' to cellulose chromatography paper. The test strips were used in conjunction with a portable Raman spectrometer for trace detection of analytes. Repeated printing, achieves a SERS-active region on the test strips that contains a high density of nanoparticles. The strips are used as swab's or dipsticks to detect target analytes. The porous nature of the paper encourages lateral flow to focus the liquid and analytes towards the SERS-active region. In addition to characterisation of the test strips with Rhodamine 6G (at $5 \mu\text{M}$ concentration) they also tested for residues of heroin, cocaine and the pesticide malathion.

2.5.8 Oblique Angled Vapour Deposition (OAD)

Deposition processes of various kinds are generally used to form surface metallic layers for SERS substrates. However these techniques can also be used to directly fabricate SERS-active nanostructures, for example via Oblique Angled Vapour Deposition (OAD) [22]. A substrate prepared via OAD is 'tilted' during a physical vapour deposition process. This enables the deposition to be directed onto the substrate surface at an oblique angle. An array of Nanorod structures form when the deposition glancing angle $> 70^\circ$ to the surface normal [68]. As metallic nucleation sites form, they create a 'shadowing effect' that encourages preferential formation of nanorods in the deposition direction [69].

2.5.9 Design & Optimization

Computational modelling that examines Electric field behaviour around nanostructures, is a convenient tool for optimizing SERS substrates. Simulation techniques used in substrate design include: Finite Difference Time Domain (FDTD) [70]; Finite Element Method (FEM) [71] and Rigorous Coupled Wave Analysis (RCWA) [72]. A disadvantage of FEM and discrete dipole approximation (DDA) methods is that they are generally restricted to 2D models [70]. This is due to the requirement that each simulation object must be included in the computation frame.

The FDTD method that is used in this project is a numerical/computational method for solving the time dependent Maxwell's equations. It is used to model the electric field behaviour of electromagnetic radiation as it interacts with physical structures of nanoscale dimensions; i.e. smaller than the incident wavelength. FDTD analysis has been widely reported in many research publications on SERS [73-78]. The efforts of some other research groups using FDTD analysis to simulate plasmonic fields of nanostructures are described as follows.

Grimault et al. used 3D FDTD to investigate the Plasmonic behaviour of Au cylindrical and ellipsoidal NP's [70]. They were able to simulate infinite arrays of particles via the use of periodic boundary conditions (BC); periodic BC's were frequently used in this project. The main simulation outputs they presented were the position of the LSPR peak and the SERS EF. Their FDTD results were in good agreement with experimental data. Furthermore, the FDTD computations could predict with confidence the geometrical dependence of the LSPR peak position. This could then allow for 'tuning' of fabrication parameters to yield maximum SERS gain.

Xu et al. fabricated Au coated arrays of pyramid-like polymer submicron structures, these structures were produced as both positive and inverse pyramids. From the complementary FDTD simulations performed, they were able to investigate the difference in SERS EF achieved from both structure array types [79]. The periodic nature of their substrates allowed for the use of periodic BC's in x, and y, and perfectly match layer (PML) layer in z. As mentioned above, Grimault et al. had used the FDTD modelling to allow LSPR 'tuning' for differing geometries. Xu et al. also found that FDTD can be used to optimize structure geometries to achieve maximum SERS EF.

FDTD analysis can be used to determine the optical response of nanostructures or particles by calculation of extinction, absorption and scattering spectra, and transmittance and reflection. However, as noted by Grimault et al, extinction spectra cannot accurately predict optimum SERS near-field enhancement. In the 2016 review by Zeng, Liu and Wei, they report that the 3D FDTD method is especially of value when calculating EM field maxima, spatial distribution, and SERS EF [78]. They state that FDTD analysis enables a better understanding of the underlying mechanisms that generate the SERS effect. Thus, the true benefit of FDTD is realized by relating this understanding of the underlying physics to substrate design and optimization.

As mentioned above, other computational methods have been used to investigate SERS performance. The FEM method was used by Wu et al. [63] to analyse the Ag Silmeco substrates that were reported on in chapters 4 & 6 (pages 94 & 171 respectively). They used 3D FEM to calculate scattering spectra, EM field maxima and distribution for a single Ag

pillar structure. Based on their computational modelling, they were able to optimize fabrication parameters. A second publication by Wu et al. also investigated 3D FEM analysis [71], however this time additional simulations were performed for dimer structures. The FEM analysis was performed using the commercially available COMSOL Multiphysics software.

The RCWA method has also been used to simulate SERS behaviour about nanostructures. Oo et al. modelled Plasmon dispersion of inverted pyramid nanostructures [72]. Simulations were performed to investigate the EM field within the indented regions on the substrate. Simulation outputs were obtained over a wavelength range of 400 – 1500 nm, and for varying incident field polarization and ‘surface-contact’ angles. They discovered that the SERS EF’s could be increased by optimizing the aspect ratio of the inverted pyramid structures.

The use of FDTD or other corresponding simulation techniques to analyse SERS substrates enables a clearer understanding of the underlying mechanisms involved. In conjunction with these insights, the geometric dependent nature of SERS can then be related to design, fabrication and optimization of substrates.

2.5.9.1 Finite Difference Time Domain (FDTD)

Electric and magnetic (E & H) fields are essentially continuous. However, they can be made discrete by sampling at different time intervals and different spatial locations. The simulation region is made discrete spatially by the use of a 3-D mesh of unit cells first proposed by K.Yee in 1966 [80]. Each vector component of the E & H-fields is located at a different position within the cell, which are sensibly chosen for convenient calculations of the Maxwell curl equations.

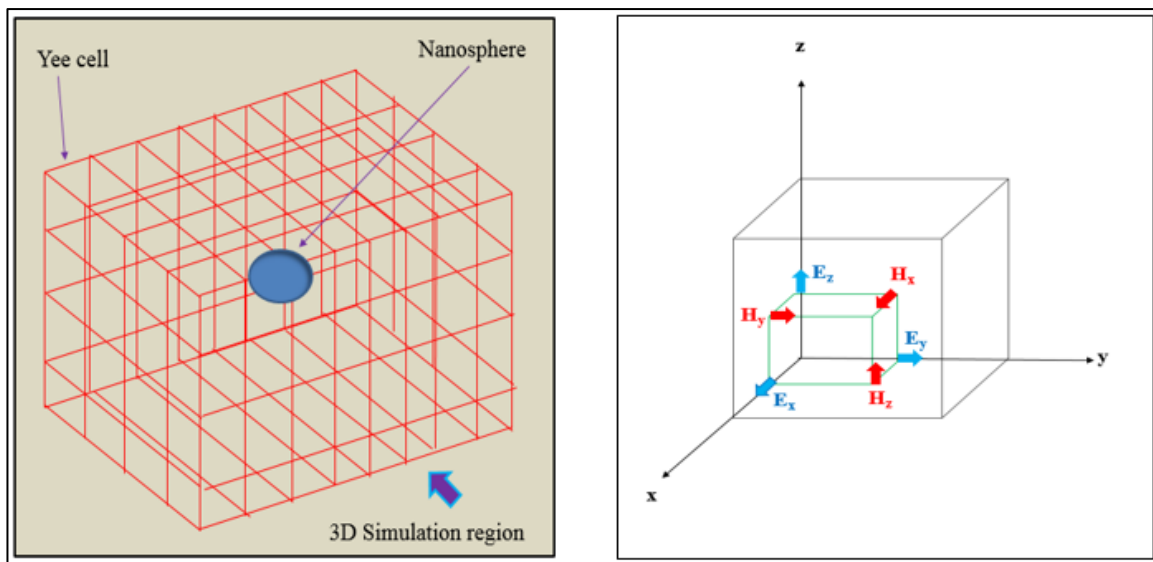


Figure 2.15 Schematic; Yee cell

(a) 3D simulation region of interest constructed from adjacent Yee cells; encompassing a nano object (b) A single Cartesian Yee cell showing ‘staggered’ positions of vector components for E & H fields

The resolution of the FDTD calculations is limited to the size of the Yee mesh cells used. This resolution effects the simulation run time which is strongly dependent on mesh grading.

The time domain method for calculating the discretised E and H fields, involves alternate calculations at staggered time steps. Where each calculation is offset by one half step.

$$\vec{E}(t) \rightarrow \vec{E}^{n\Delta t} \qquad \vec{H}(t) \rightarrow \vec{H}^{(n+\frac{1}{2})\Delta t} \qquad \text{Equation 2.20}$$

Thus the general flow of the time-stepping calculations is:

$$\vec{E}^0 \rightarrow \vec{H}^{\frac{1}{2}} \rightarrow \vec{E}^1 \rightarrow \vec{H}^{\frac{3}{2}} \rightarrow \dots$$

While the field calculations are carried out using:

$$\vec{E}^{(n+1)} = \vec{E}^n + \frac{\Delta t}{\epsilon} \nabla \times \vec{H}^{(n+\frac{1}{2})} \qquad \text{Equation 2.21}$$

$$\vec{H}^{(n+\frac{3}{2})} = \vec{H}^{(n+\frac{1}{2})} - \frac{\Delta t}{\mu} \nabla \times \vec{E}^{(n+1)} \qquad \text{Equation 2.22}$$

Note, the fields are calculated for each individual Yee cell, and so we consider $\vec{E}^{(n+1)}$ and $\vec{H}^{(n+\frac{3}{2})}$ as incorporating $\vec{E}_{(x,y,z)}$ and $\vec{H}_{(x,y,z)}$.

The E-field at a given time step is equal to the E-field at the previous step plus a term proportional to the curl of the H-field. Similarly, the H-field (a half time step later) is equal to the previous H-field minus a term proportional to the curl of the E-field.

Although the E and H field time-stepping calculations are at different time intervals, they are calculated for the same spatial region. The field calculations are for each unit cell within the simulation region. These finite difference or centred difference calculations do not require solving simultaneous equations. This avoids the necessity of large computational requirements, and achieves 2nd order accuracy (for both spatial and temporal intervals) [81].

The alternate calculations are continued until a steady state or continuous wave electric field is achieved in each lattice cell throughout the simulation volume. The FDTD output required by most users will be as a function of frequency. A Fourier transform is used to output the continuous wave (CW) electric field as a function of frequency.

$$\vec{E}(\omega) = \int_0^{T_{sim}} e^{i\omega t} \vec{E}(t) dt \qquad \text{Equation 2.23}$$

T_{sim} = the simulation time

A variety of excitation sources can be used in the time domain simulation, e.g. plane wave, dipole, Gaussian etc. The time stepping iterations are calculated from an initial time when all fields are assumed to be zero, Thus, regardless of the type of source used, the time signal will be a pulse, s(t). The impulse response of the system can be calculated by normalising the CW field with respect to the source input pulse.

$$\vec{E}_{impulse}(\omega) = \frac{1}{s(\omega)} \int_0^{T_{sim}} e^{i\omega t} \vec{E}(t) dt \quad \text{Equation 2.24}$$

$E_{impulse}(\omega)$ = the system impulse response

There are two advantages in obtaining the impulse response. Firstly, the field output will be independent of the source used. Secondly, for $s(\omega) \approx 1$ the value for $E_{impulse} \equiv$ the CW response of the system. In the case of $s(\omega) = 1$, then $s(t)$ would be a delta function. The ‘real world’ equivalent to $s(t)$ as a delta function, is to use an ultra-short pulse. The use of a suitably short pulse approximates to a delta function; a typical simulation run time ~ 1500 fs. A benefit of using a short pulse is that a broad range of frequency outputs can be obtained from one simulation.

2.6 SERS Applications & Techniques

The high sensitivity and molecular specificity of SERS sensing have seen the technique being used in many and varied applications. These include use in the food industry [82]; drug detection [83] and forensic science [84]. SERS has also been used in the detection of environmental pollutants [85]. As water yields a ‘neutral’ SERS signal (due to its low polarizability), SERS analysis has proved especially beneficial to detect waterborne contaminants [86].

The rise of global terrorism has generated the need for improved detection of chemical threats with simpler methods and at lower thresholds. SERS has been used to meet such threats by the use of portable Raman spectrometers [87].

Due to the non-destructive nature of SERS analysis it has been utilized in both Art [88] and Archaeology [89]. Yet another application has been in anti-counterfeiting detection. An example of this is the use of security labels containing Ag nanostructures that exhibit a polarization dependent SERS signal [90].

2.6.1 SERS & Biosensing

The unique characteristics of SERS makes it ideal for important applications such as Biosensing [91]. There are numerous advantages that SERS brings to this field of research. These advantages include: low sample volume requirements [92]; ability to distinguish spectra from similar molecules; low detection thresholds [93] and rapid label free identification [94]. It has also been reported that changes to Raman spectral intensity will occur as a disease developments [95]. As such, SERS could also be used to monitor the progress of disease during treatment. Additional advantages that SERS brings to bioanalysis are as follows.

The presence of additional and unwanted analytes in a sample volume can easily be distinguished in SERS spectra, and so exert minimal interference to the desired target signal [96]. Additionally, a strong SERS enhancement will reduce/suppress fluorescence [96, 97] which would otherwise decrease sensitivity.

A promising application of SERS lies in the field of DNA sensing [94] SERS has been used in the detection of DNA sequencing [98]. molecular biosensing is an application that is useful in both disease detection [99] and forensics [100].

Chemical mapping or imaging involves the combination of a visual image with a spectral readout. In addition to mid and near infrared imaging, Raman spectroscopy has also been used for bioimaging. SERS has been successful in both in vitro and in vivo investigation.

In vitro SERS imaging has been extensively reported [101-105]. In 2006 Schlucker et al. utilized SERS in vitro bioimaging for the detection of prostate specific agent (PSA) from patient tissue samples.

SERS in vivo imaging was first reported by Stuart et al. [106] who successfully measured the glucose concentration of rodent interstitial fluid. With suitable further development, this technique may prove useful in diabetes care.

Some important biosensing applications of SERS include: diagnosing diabetes [107]; detection of renal failure [108]; respiratory disease [109] and cancer diagnostics [95]. These applications are described in more detail as follows.

A difficulty in using Raman spectroscopy for diabetes detection arises from the inherently weak Raman signal generated by glucose [110]. Sharma et al. report on a sensitive SERS technique for the detection of glucose in vivo [111]. Using a self-assembled monolayer (SAM) on a silver film over nanosphere (AgFON) substrate they demonstrated limits of detection lower than currently accepted standards.

Problems of poor kidney health can be connected to a number of various diseases which makes the diagnosis of renal health issues of strong importance. The customary approach in acute renal failure (ARF) detection is to measure serum creatinine as a bioindicator of kidney malfunction; the sensing of serum creatinine is a blood based technique. However, increased levels of creatinine are often a late indication of the presence of kidney disease. As such, current difficulties in the diagnosis of ARF lie especially in the area of early detection. SERS offers highly sensitive, multiplexed bioanalysis, and also a rapid detection time (< 10 seconds). Thus, making the technique especially suited to the monitoring of creatinine levels which denote the rate of metabolic breakdown and disposal of creatine phosphate.

SERS bioanalysis has been investigated for sampling of urine to measure creatinine levels, often with the use of Au colloids [112, 113]. Also, Kho et al. have used a SERS microfluidic platform to analyse urine [92]. While Wang et al. addressed the issue of substrate reproducibility by using platform-based SERS substrates [108].

The bacterium *Mycoplasma pneumoniae* (MP) is a key source of human respiratory illness, and according to Waites et al. may be the cause of up to 40% of pneumonia related respiratory complaints [114]. Hennigan et al. [109] utilized a SERS platform-based Ag nanorod array to successfully differentiate between three strains of MP with a sensitivity comparable to existing methods. An additional control was carried out where 10 previously identified clinical samples were correctly classified using the SERS platform.

Cancer is largely recognized as the primary fatal disease worldwide [110]. While early detection is of primary concern for any disease treatment it is especially significant in cancer care. For all cancers, patient survival is strongly dependant on treatment being administered at early stage of the disease.

As has previously been mentioned, SERS bioanalytical techniques in general possess a number of significant advantages to the use of existing methods. An example of this is provided by the work reported on by Domenici et al. in their studies on SERS based nanobiosensing of p53 [115]. Techniques commonly used for p53 sensing are mostly fluorescence-labelled immunosorbent assays. However, these methods require several preparation steps and lengthy incubation times but deliver only partially quantitative outputs.

The work undertaken by Domenici et al. involved the use of Au nanoparticles functionalized with various Raman reporter molecules, followed by conjugation with p53. The binding event between the Raman reporter 4-ATP and p53 resulted in a Raman band at $\sim 1328 \text{ cm}^{-1}$, and this was found to vary in intensity with changing p53 concentration. Measurements at a lower threshold of $5 \times 10^{-13} \text{ M}$ concentration of p53 were reported.

SERS has also been used to detect cancers in blood plasma. Feng et al. [95]. report on the non-invasive detection of nasopharyngeal cancer (a rare form of head/neck cancer) from a facile blood test. Samples were obtained from patients with nasopharyngeal cancer and healthy volunteers. Their method involved Raman spectra being obtained from a mixture of Ag NP's and blood plasma with a 1:1 ratio. Principal component analysis (PCA) was then used to determine spectral differences between the two sample groups, with a high degree of sensitivity ($\sim 90\%$). However, some unavoidable overlap of data sets was also present in the spectral data.

A technique that largely circumvents an unwanted overlap of spectral data sets is reported by Lin et al. who have also investigated SERS analysis of blood plasma [116]. Their novel approach involved combining SERS analysis with a membrane electrophoresis plasma purification step. The component ratio and configuration of blood plasma will alter due to the presence and progression of disease. Spectroscopic analysis of these changes is challenging due to the complicated mixture within the tested sample.

The purification step undertaken by Lin et al. served to separate the blood plasma from serum proteins. The separated serum proteins were then analysed using SERS biosensing which avoided spectral interference that would otherwise arise from the presence of the plasma. The SERS sensing was carried out using Ag NP's and the analysis was enabled via PCA. Lin et al. reported a 100% sensitivity between healthy and patient sample groups in the detection of gastric cancer.

Multiplexed sensing of cancer biomarkers is a key advantage that SERS brings to clinical research. Jun et al. [117] describe SERS based multiplex immunoassays. Ag NP's embedded in polystyrene microbeads were functionalized with different Raman reporters, which were then coated in silica for the detection of p53.

Other SERS techniques and novel sensing platforms used for cancer research include the following.

Chon et al. report on magnetic beads combined with antibody conjugated metallic NP's used in SERS immunoassays [118] to detect carcinoembryonic antigen (CA). The molecular marker CA is present in lung, pancreas, breast and ovary cancers [119]. Improvements to SERS immunoassays include the use of hollow metallic NP's [120].

Microfluidic SERS chips have also been used in cancer research [121]; for further details on SERS microfluidics see section 2.6.2.

SERS has also been employed for cancer imaging. Imaging of the regions between cells for the detection of cancer biomarkers has been reported by Lee et al. [122]. While tissue imaging has been being by Jokerst et al. [123] and colloidal Au NP's have been used to successfully image tumours in vivo in small animals [124].

2.6.1.1 Intrinsic biosensing

Intrinsic or direct spectral measurement of complex biomolecules is challenging even with the use of SERS. An intrinsic approach that circumvents this limitation, is to directly measure spectra from biomolecules and then use multivariate statistical analysis to analyse the data.

It is problematical to apply statistical methods to analyse multivariate data, as generally there is a high correlation between the large number of variables present [125]. A method that avoids these issues is Principal Component Analysis (PCA). PCA deconstructs the data into uncorrelated variables, enabling the identification and quantification of trends/components within complex data sets. Statistical analysis generally investigates deviation about a mean. However, PCA is generally applied directly to raw data, and is especially suited to examining variation above a spectroscopic baseline.

Virkler et al. made use of PCA of multiple samples, to attempt differentiation of the spectral components of dry saliva [126]. From the statistical analysis they concluded that the complex spectra consisted of three individual spectral components along with a fluorescence background. The successful use of multivariate statistical analysis to distinguish spectral components of other biofluids has also been reported [127].

2.6.1.2 Extrinsic biosensing

An example of extrinsic SERS biosensing is reported by Ni et al. [128] where an immunoassay containing two separate antibody/antigen combinations was used. Their first step was to functionalize an Au coated substrate with two separate 'capture' antibodies, and then to incubate with a mixture of the two corresponding antigens. This procedure is also followed separately to prepare an immunoassay consisting of two different Raman reporter labelled Au colloids. This immunoassay is then pipetted onto the functionalized substrate and the relative concentrations of the assay components were then determined from the resulting Raman Spectra.

Extrinsic SERS biosensing can also involve the use of MNP's. Chen et al report on generating MNP aggregation via a reaction between a 'MNP/Raman reporter/anti-body' conjugate and its corresponding antigen [129].

Another extrinsic approach that uses MNP's is reported by Wang and Vo-Dinh [130]. Their approach uses what are known as molecular beacons or Molecular Sentinels (MS). The MS Nanoprobe comprises of a 'DNA hairpin + Raman tag + Ag MNP' combination. The DNA is Thiol-conjugated which encourages the DNA to covalently bond with the Ag MNP. The Raman tag is attached to the 'shorter' end of the DNA strand; 3'-end, while the 5'-end is attached to the MNP surface.

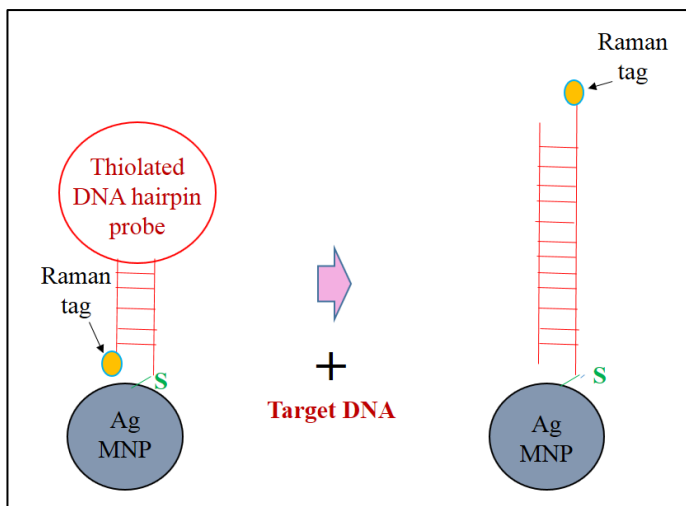


Figure 2.16 Molecular Sentinel DNA hairpin Nanoprobe

Raman tag attached to 3'-end of hairpin Nanoprobe bringing it into the SERS Plasmonic region

In the left image, the DNA probe is immobilised onto the Ag MNP surface while also bringing the Raman tag into the SERS active region. The addition of a target DNA causes the probe to be reconfigured due to hybridization, removing the Raman tag from the Plasmonic region; right image. The resulting Raman outputted intensities were found to exhibit inverse DNA concentration dependence for the target DNA.

2.6.2 SERS & Microfluidics

The combination of SERS, Microfluidics and biosensing is commonly referred to as ‘Lab-on-a-chip’ biosensing. Amongst the many advantages of ‘Lab-on-a-chip’ biosensing are ‘closed analysis system’ and low sample volume requirements [131].

Microfluidics involves the manipulation of small volumes of fluids (10^{-9} to 10^{-18} litres) in a micro or nanochannel, and is generally regarded as an enabling technology [132]. Over the past number of years, its partnership with SERS, has resulted in the production of SERS-based optofluidic platforms. A generally accepted definition for a SERS-based optofluidic platform, is that of a ‘lab-on-a-chip’ device, comprising of a microfluidic component and a Raman Spectrometer [133].

A common truism that is applicable to all forms of nanotechnology, is quoted by Chakraborty [134] as follows "As a system reduces in size, its surface area to volume ratio increases". Thus, as a system scales down to nanometre dimensions, the surface effects dominate over volumetric ones, and fluid properties can differ from those of a bulk material. In microchannels, reduced flow resistance/lower pumping effort, and laminar flow are often observed. Thus, microfluidics can lead to the manipulation and transportation of fluidic samples in a rapid and controllable way. These characteristics lend themselves to optical characterization methods, which can provide both short analysis time and sensitive measurement capability. Techniques such as absorbance [135] and fluorescence spectroscopy [136] were initially used in conjunction with microfluidics. However, SERS has an advantage over fluorescence techniques, in that it offers label-free detection capabilities [133].

Most microfluidic systems are characterized by a low Reynolds number, and so exhibit laminar flow with concomitant diffusion limited mixing [137]. As such, mixing is a significant challenge facing the development of microfluidic SERS-based platforms. Many techniques exist to increase microfluidic mixing; one of the most commonly used is that of chaotic advection [138]. Increased mixing efficiency in microchannel flow cells can be beneficial to SERS-based microfluidics analysis as it can reduce spot-to-spot signal variations, which are often associated with static SERS measurements [139]. Both metallic nanoparticle colloids and platform-based SERS substrates are used in microfluidics [133].

2.6.3 Resonance Raman Scattering (RRS)

If the incident excitation wavelength used in Raman scattering is matched to an electronic transition, an increase in the Raman intensity is observed. This resonance condition is known as Resonance Raman Scattering (RRS), and it was first observed in 1946. The closer the frequency matching between incident and electronic transitions the larger the signal enhancement [140].

A disadvantage of RRS is that the excitation is normally in the UV-visible range, and fluorescence background ‘noise’ can be an issue. An advantage of RRS arises in the analysis of organic molecules. The RRS peaks of interest are more readily distinguishable than the complex spectra generated from conventional Raman sampling of organic samples [141, 142].

Resonance Raman Spectroscopy can be performed with a standard Raman spectrometer in conjunction with a tunable laser for resonance matching.

2.6.4 Surface Enhanced Resonance Raman Scattering (SERRS)

Surface Enhanced Resonance Raman Scattering (SERRS) combines the enhancement from RRS with SERS using a SERS substrate. In addition to amplifying the SERS signal, SERRS also provides additional molecular specificity [141, 143]. The main advantage of SERRS over RRS is that the fluorescence background is suppressed by the SERS signal.

2.6.5 Coherent Anti-Stokes Raman Spectroscopy (CARS)

Coherent anti-Stokes Raman Spectroscopy (CARS) utilizes two ‘pump’ lasers, the pump and Stokes beams shown in the schematic below. The energy to the pump beam is set to a value less than the difference between the Ground and 1st excited state. The interaction with a third ‘probe’ laser results in the generation of a coherent Raman signal. The CARS signal arises from the frequency difference between the pump and Stokes beams. To achieve coherence, this difference is ‘tuned’ to match a particular molecular vibration.

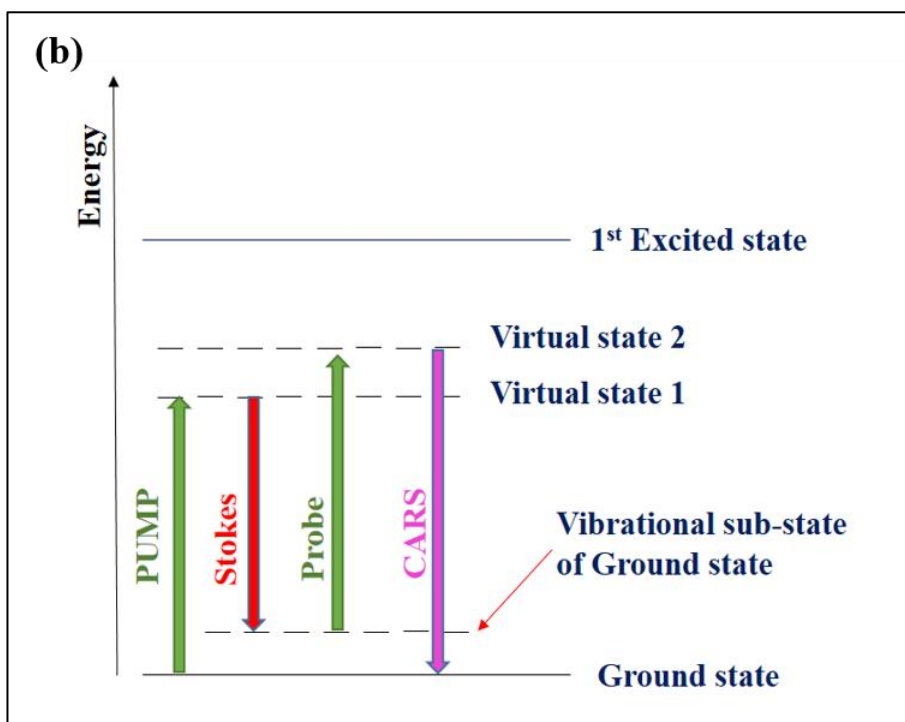
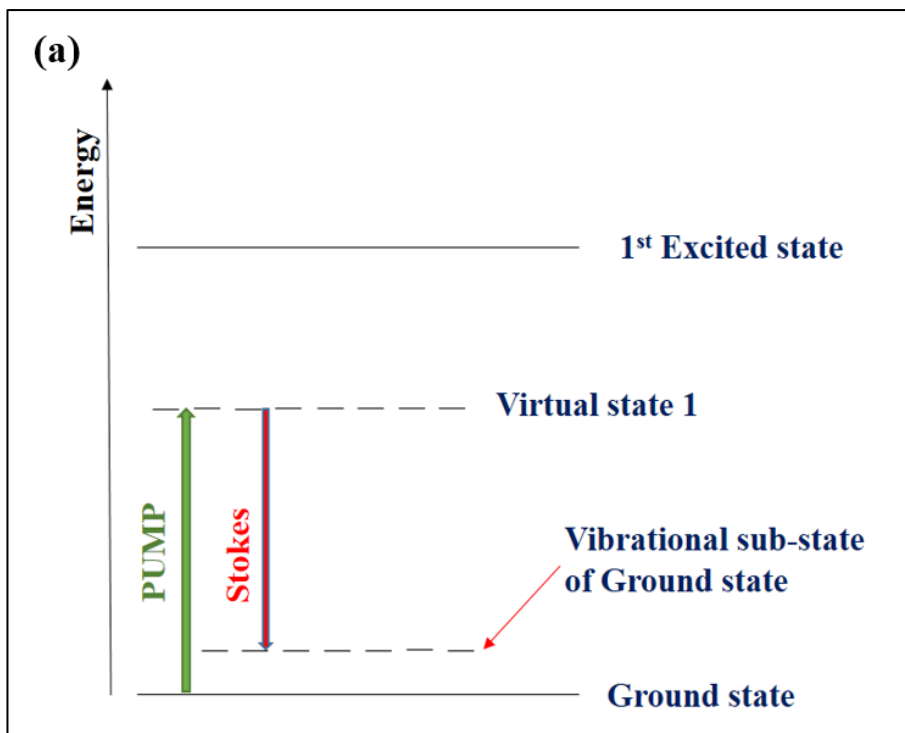


Figure 2.17 Schematic; Coherent Anti-Stokes Raman Scattering (CARS)

Energy level schematic illustrating the CARS effect (a) Pump laser excitation excites molecule to a virtual state (b) Pump acting as third probe beam to stimulate vibrational sub-state and create 'electronic' conditions for CARS

The pump laser excites molecules to populate a virtual state (marked **Virtual state 1** – left image above). This virtual state has less energy than the 1st excited state, and by adjusting the frequency of the Stokes laser, virtual state 1 is depopulated. This double stimulation results in a densely populated sub-state of Ground. The pump beam acting as a third probe, now

stimulates the sub-state to populate a new virtual state (marked *Virtual state 2 – right image above*). The molecules relax from Virtual state 2 back to Ground generating the CARS signal. The CARS signal has a higher energy than the pump, and is the anti-Stokes detected signal.

The Raman signal produced by CARS is greater than that produced via spontaneous Raman scattering. Although sensitive and enhanced signal strength are two of the main advantages of CARS, the high-power requirement leads to the disadvantage of sample or material damage. Other disadvantages arising from the use of CARS are high background interference and fluorescence.

Some of the unique characteristics of CARS lead to its use in applications such as gas-phase Spectroscopy [144]. A particularly beneficial characteristic of CARS is its sensitivity at certain temperatures. Automotive fuel injection processes typically operate over the temperature range of 300-700 K. As CARS is highly sensitive at these temperatures it has been successfully used for low temperature sensing of spray fuel injection for the automotive industry [145].

CARS have been used to detect organic molecules such as Lipids. Lipids are organic molecules contained in fats, and contain large numbers of C-H bonds, which are easily detected using CARS. Renia et al. report on the use of CARS for the detection of Lipids in liquid droplets [146].

2.6.6 Stimulated Raman Scattering (SRS)

Stimulated Raman Scattering (SRS) was first observed in 1962 [147], and is similar to CARS, and uses both pump and Stokes lasers. When the frequency difference between the two lasers matches a molecular vibration then stimulated excitation occurs.

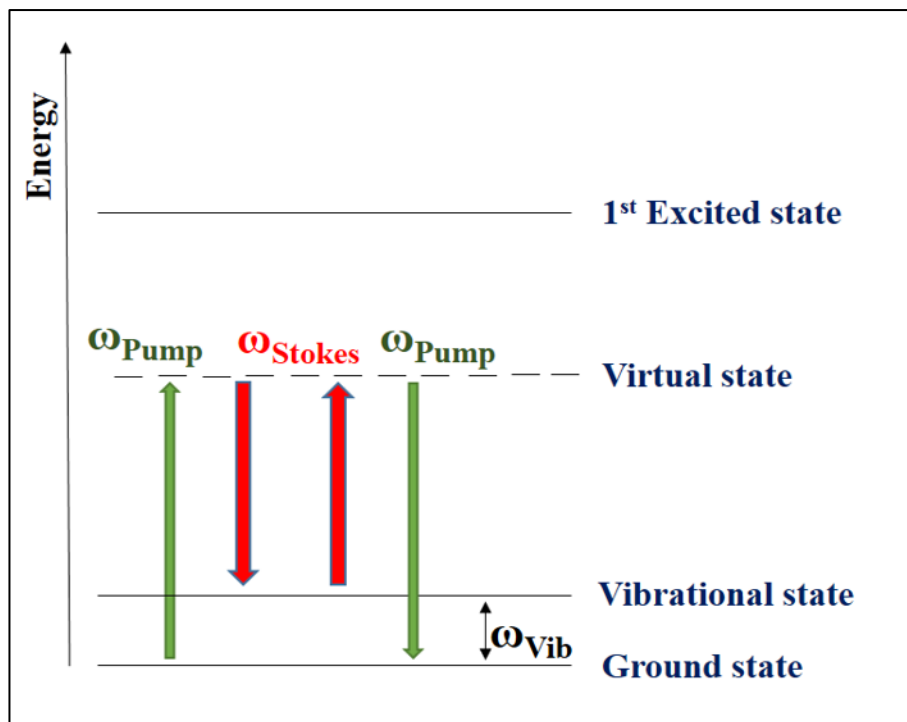


Figure 2.18 Schematic; Stimulated Raman Scattering (SRS)

Schematic illustrating SRS, frequency differential between pump and Stokes matched to ω_{Vib} with resulting stimulated amplification of Raman signal.

When the frequency difference between the beams matches ω_{Vib} there is loss of intensity at the pump wavelength and a gain at the Stokes wavelength. This stimulated molecular excitation serves to amplify the Raman signal. SRS delivers low background interference and greater chemical specificity, and is extensively used in bio-imaging [148-150].

2.6.7 Tip Enhanced Raman Spectroscopy (TERS)

The combination of SERS with other types of sensing has improved many existing characterisation techniques such as gas chromatography [151]. Tip-Enhanced Raman Spectroscopy (TERS) has combined SERS with scanning probe techniques to enable spectral characterisation of surface analytes [152]. The TERS method involves the use of an AFM where the tip has been constructed with a noble metal nanostructured surface (usually silver or gold). Incident laser excitation generates plasmon resonance at the tip apex. One advantage of TERS is that the technique isn't restricted to the use of metallic or SERS substrates, and is commonly used with a planar surface [153].

The spatial resolution of optical microscopy is diffraction limited and dependent on the incident wavelength, and is described by the Rayleigh criteria. With the development of Scanning near field microscopes (SNOM) spatial resolution was reduced to limits dependent on the size of an aperture. However, the TERS technique is effectively an aperture-less optical probe, and can achieve a spatial resolution in the range 3-20 nm [154, 155]. Nevertheless, in order for TERS to be used for single molecule detection, a resolution of < 1 nm is required. Zhang et al. have demonstrated nanometre resolution capability with TERS by availing of the fine-tuning potential of scanning tunnelling microscopy [156]. Their

method involved matching the plasmon resonance of the probe to molecular vibrational transitions.

2.7 Novel SERS platforms

2.7.1 Liquid marble SERS platforms

In 2016 a ‘liquid marble’ novel SERS platform, comprising of an oleic acid core coated with silver nanoparticles was reported by Zhang et al. [157]. Oleic is an oil-like fatty acid and is immiscible in water. When two immiscible liquids undergo sonication, micro/nanospheres are generated at the liquid/liquid interface. The method employed by Zhang et al. involved adding oleic acid and silver nanoparticles to distilled water. After sonication, microspheres of oleic acid were produced at the water acid interface which were coated with the silver NP’s.

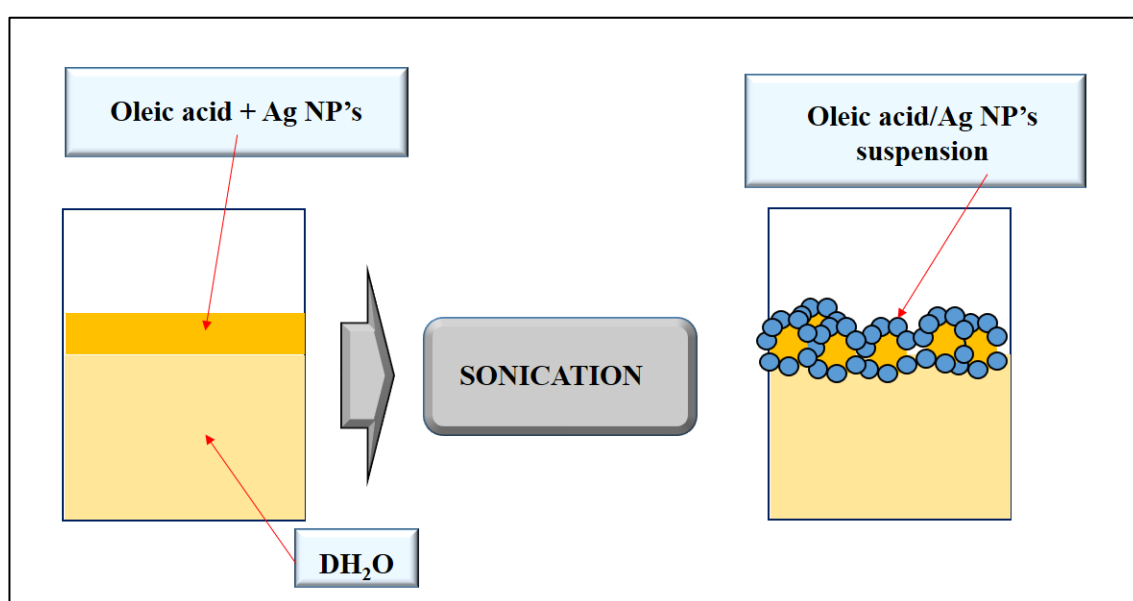


Figure 2.19 Schematic; Liquid marble SERS platform

Oleic acid & Ag NP’s added to DI water (left image) after sonication Ag NP’s encapsulate micro-sized oleic acid spheres aggregated at water interface

The liquid marbles were used by the group as a SERS platform for thiolate sensing. In addition, they reported another possible application. The liquid marbles were also able to absorb solar energy, and it is suggested they could be used as solar/thermal absorbers.

2.7.2 SERS Nanoshells

Metallic shell nanoparticles have been produced which effectively have ‘built-in’ SERS hotspots. Yang et al. report on SERS Nanoshells with a diameter of ~ 100 nm comprising of a dendritic network of branches [158]. Their approach used waterborne Polyurethane (PU) to synthesise gold nanoparticles. The PU’s act as a surfactant lowering the surface tension at the water/metal interface, during chemical reduction. The gold NP’s that form has gold ‘fingers’ 3-5 nm wide with gaps of just 1-3 nm. The PU’s act as a template that encourages the NP’s to grow around them. These types of shell-like nanoparticles can be used as drug delivery agents and also for spectral imaging of intracellular activities.

The MNP structure and SERS performance of Nanoshells can be ‘designed’ by the choice of polymer and tuning of fabrication parameters. Song et al. produced SERS Nanoshells with internal nanogaps of ~ 1.5 nm using block copolymers [159]. The Nanoshells contained a Raman tag within the interior shell gaps, and can be used for ultra-sensitive SERS sensing of cancer biomarkers.

Yim et al. are another group who have used MNP Nanoshells for SERS-biosensing [160]. A silver Nanoshell is functionalised with Graphene oxide, which is an ultra-sensitive Raman reporter. This high sensitivity enabled the Nanoshells to be used for SERS biosensing of cancer cells. The Nanoshells were conjugated with a one-atom thickness film of Graphene oxide which possesses strong Raman peaks of interest. Additionally, the Nanoshell probes were used with the Surface Enhanced Resonance Raman Scattering technique, which produced strong enhancement and also exhibited simple Raman spectra.

2.7.3 Nanoshells as SERS Nanotags

Bedics et al. demonstrated that Nanoshells functionalised with chalcogenopyrylium dyes can exhibit superior performance over conventional nanoparticles and Raman reporters [161], especially in the NIR.

Generally, SERS activity tends to be weaker in the NIR region, as Raman scattering is dependent on the 4th power of the excitation frequency. However, these Nanotags exhibited strong SERS activity at 1280 nm excitation. The Nanotags consisted of Hollow gold nanoshells (HGN) and strongly bound chalcogenopyrylium dyes. The SERS response in the NIR arises from the unique chemistry of the chalcogenopyrylium dyes. The dyes strongly bind to the gold surface of the HGN’s with multiple functional groups, ‘trapping’ the molecules within the Near-field SERS region. Thus, the SERS enhancement is dependent on the surface Plasmons rather than just the incident frequency, which would be weaker in the NIR.

The strong SERS activity at 1280 nm excitation exhibited by these Nanotags is advantageous for biosensing. Longer excitation wavelengths allow for greater penetration of bio-samples such as tissue.

2.7.4 Magnetic Nanoparticles as SERS Platforms

Novel SERS substrates have been developed by combining SERS platforms with magnetic materials. Jun et al. fabricated magnetic SERS Nanoprobes with silver NP’s surrounded by a silica coated shell [162]. The shell is then embedded with silver NP’s which are then functionalised with Raman reporters. Another silica layer is overlaid and conjugated with a specific antibody. The silica layers deliver chemical and material stability to the Nanoprobes.

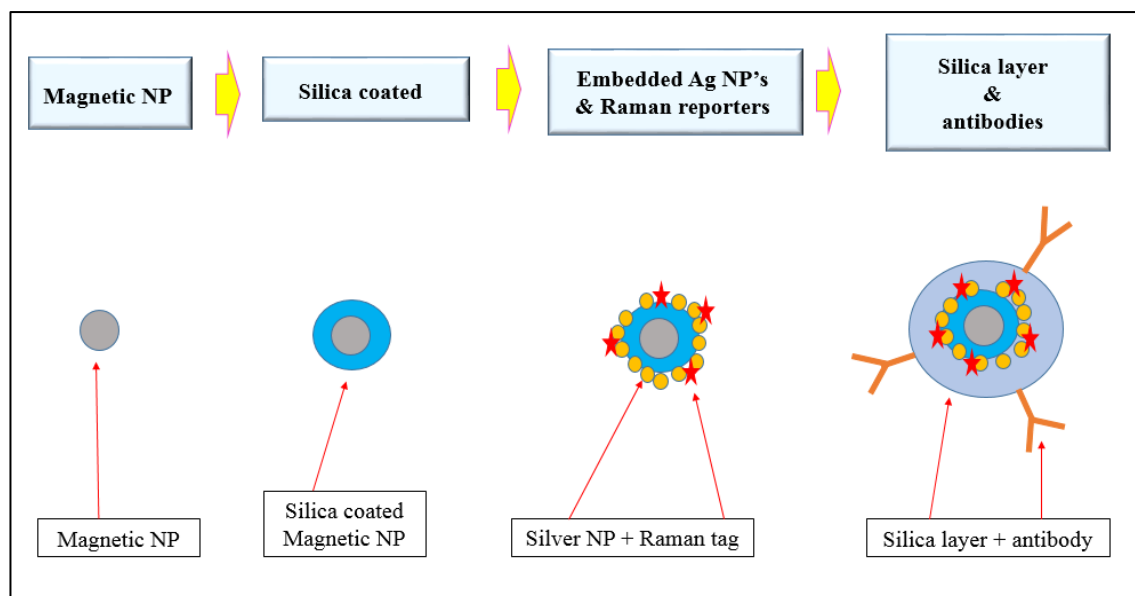


Figure 2.20 Schematic; SERS Magnetic Nanoprobe fabrication

The magnetic Nanoprobes generate a large SERS enhancement, but also exhibit magnetic properties. The probes have been used for the biosensing of breast-cancer and floating leukaemia cells. The targeted cells can be readily separated from non-target ones by using an external magnetic field. Additionally, the applied magnetic field leads to NP aggregation which further enhances the SERS signal.

The use of magnetic materials in SERS platforms has also been used to control ‘hot spots’. Guo et al. achieved this by influencing the interparticle spacing of paramagnetic nanoparticles by the application of an external magnetic field [163]. Their first step was to fabricate Fe_3O_4 NP’s which were then linked to gold NP’s. During further chemical processing, the gold NP’s initiated seed-growth to form an outer gold shell on the Fe_3O_4 NP’s. When added to a Hexane/water mixture the magnetic NP’s formed a monolayer at the Hexane/water interface. The monolayer was functionalised with the Raman active Mercaptobenzoic acid (MBE). The monolayer comprised of particles with ‘large’ interparticle spacing and generated a weak SERS signal.

When an external magnetic field was applied parallel to the monolayer, the interparticle gap was reduced with subsequent increase in SERS response. As the material is paramagnetic, the SERS response of the particles was reversible when the magnetic field was removed. This technique used by Guo et al. offers an alternative to achieving reduced gap dimensions via direct fabrication.

2.8 SERS; Novel techniques, trends & future outlook

In the years following the discovery of SERS, considerable progress has been made in developing robust and sensitive substrates. Research groups will continue to fabricate and optimise these substrates. However, in the future, key advances in the field of SERS may lie in SERS-augmented techniques such as Ultra-fast Raman spectroscopy and SERS sensing applications e.g. TERS [13]. Additionally, the development of new metamaterials for use in SERS substrates may provide innovative substrates with enhanced levels of performance.

2.8.1 Ultra-fast Raman Spectroscopy

Femtosecond Stimulated Raman Spectroscopy (FSRS) is an ultra-fast spectroscopic technique which enables the measurement of spectra as a function of time. Molecular vibrations occur on ultra-short time scales; atomic motions can range from 10 femtosecond (fs) to 1 picosecond (ps) [164]. Providing time resolved data at such a time scale can give a valuable insight into the underlying mechanisms and dynamics of chemical and biological reactions. This is especially valuable for applications involving plasmon induced reactions, e.g. H₂ dissociation or solar steam production.

The mechanism of FSRS initialises with an ultra-short fs pulse (A) to photo-activate a desired chemical reaction, resulting in the molecules being in an excited state. After a controlled delay, a narrow bandwidth picosecond Raman pulse (B), and a broadband femtosecond probe pulse (C) are used to illuminate the sample. When the frequency difference between the second and third beams matches a molecular vibration, stimulated Raman scattering occurs. Typical parameter values for the probe and pump beams are: (A) ≤ 30 fs; (B) ~ 3 ps; (C) ~ 20 fs, with wavelengths at: (B) $\lambda \sim 800$ nm; (C) ~ 830 -960 nm [165]. The broadband parameters of Raman pulse (C) enable measurement over a wide spectral range of > 1500 cm⁻¹.

Combining FSRS with SERS as Surface Enhanced Femtosecond Stimulated Raman Scattering (SE-FSRS) has proved challenging. This is primarily due to sample damage arising from the high peak intensity of the fs laser pulses. However, colloidal Nanoantennas SERS substrates have proved to be robust enough to be used with FSRS [13]. In 2011, Frontiera et al. reported on the first successful attempt at SE-FSRS using gold Nanoantennas substrates [166].

Ultra-fast SERS techniques such as FSRS and SE-FSRS have the potential to revolutionise the field of Raman spectroscopy [166]. A stimulated Raman process uses multiple pulses and produces a coherent signal, which in turn yields a greater photon collection efficiency. As such, ultra-fast stimulated Raman techniques can bring greater sensitivity to SERS characterisation. Keller et al. suggest that stimulated Raman techniques may yield greater enhancements than the E⁴ dependence observed from spontaneous SERS. However, this order of enhancement is still only a theoretical consideration and has yet to be observed experimentally [167].

2.8.2 Recent SERS sensing techniques

A useful technique that limits laser damage of samples is that of Remote SERS sensing. The method involves the propagation of Surface Plasmon Polaritons along a metal film towards a SERS-active region rather than direct laser excitation of the sample [168].

A disadvantage with Tip Enhanced Raman Spectroscopy (TERS) can arise from the ambient atmosphere in the environment of the tip and sample. A method that avoids this difficulty is Ultra-High-Vacuum TERS (UHV-TERS). Unwanted scattering can occur from small molecules in the air and 'mask' the spectra of the target analyte. This could be especially problematical in the case of an unknown target species, e.g. Plasmon driven chemical reactions [169].

Pozzi et al. reported on the use of UHV-TERS in conjunction with pico second excitation and noted that irreversible signal degradation can be avoided [170].

2.8.3 Plasmonic Metamaterials

A metamaterial is generally defined as an engineered material with ‘nanofeatures’ less than the excitation wavelength of the particular application in question. The incident wave interacts with the engineered morphology ‘as if it is a continuous surface’. Thus, the material response is heavily dependent on the nanofeatures and can be ‘tuned’ to meet specific requirements.

The development of Metamaterials suitable for use with nanoscale photonics has great potential in the field of SERS. An important example of such a material is Graphene oxide, which is emerging as an important material for SERS research due to its unique properties. These properties include: strong chemical enhancement; fluorescence quenching; and material properties such as high molecular absorption and water dispersibility [171]. These important properties of Graphene oxide arise from its unique chemical structure. Graphene oxide comprises of many oxygen functional groups that enable it to strongly bind to both metal and analyte molecules.

It is well established in the field of SERS that the mechanisms producing enhancement are electromagnetic and chemical, with the electromagnetic process being mostly responsible for the effect. While the electromagnetic enhancement has been thoroughly investigated, there is still much deliberation on the mechanism that produces chemical enhancement. Furthermore, investigation into the mechanism producing chemical enhancement has been hindered by the difficulty to separate the two enhancement mechanisms. This is where Graphene oxide is of special interest to SERS research as it doesn’t generate an electromagnetic enhancement, but does exhibit a strong chemical enhancement. The chemical enhancement is thought to result from the highly planar nature of the material surface, which is atomically flat. This property allows for a diminished separation between the material and analyte molecules which leads to a more efficient charge transfer.

As a SERS substrate material, Graphene oxide is used in both chemical and biosensing applications. Fan et al. report on sub-nanomolar detection of aromatic molecules using a silver/Graphene oxide composite nanomaterial used for single particle SERS sensing [171].

The key challenge facing the future of Plasmonic Metamaterials is to avoid resistive losses that dampen Plasmonic excitation at optical frequencies [172]. Various strategies have been suggested to combat this, such as doping or alloying that allow for band structure engineering [173]. Another promising technique involves the use of organic molecules such as DNA for the seed-mediated growth of nanostructures on planar surfaces [174]. DNA-mediated assembly allows for tunable arrays of nanostructures with controlled interstructure spacing [175].

3 Materials & Methods

This chapter gives details of the experimental methods and materials used in this project. The methods include the use of Raman spectrometers and Finite Difference Time Domain (FDTD) computational modelling. A description is presented of the platform-based SERS substrates used including details of their material composition. Additionally, for the SERS biosensing application details are provided for the cancer protein biomarkers used. This includes a description of the functionalisation technique used to prepare the substrates for bioanalysis.

3.1 Materials

3.1.1 Characterisation & Fabrication of Platform-based SERS substrates

The coinage metals Ag and Au are the most commonly used in SERS applications and these are the materials present on the outer surface layers of substrates evaluated in this work. Characterisation is carried out on a number of commercially available platform-based SERS substrates. A list of the substrates obtained for this work is given in Table 3.1.

Table 3.1 Details for commercial platform-based SERS substrates

Supplier	Substrate features	Metallic surface layer	Subsurface dielectric material
Silmeco Ltd., Denmark	‘Leaning’ Nanopillar	Ag	Silicon
Silmeco Ltd., Denmark	‘Leaning’ Nanopillar	Au	Silicon
Integrated Optics, Lithuania	Amorphous surface features	Ag	Soda lime glass
Integrated Optics, Lithuania	Amorphous surface features	Au	Soda lime glass
Horiba	Nanorod array	Au	SiO ₂
Diagnostic anSERS Inc., U.S.	Aggregated MNP’s	Au	Chromatography paper

In addition, two novel ‘in house’ substrates were fabricated using Nanolithography techniques. Novel substrates produced using Substrate Conformal Imprint Lithography (SCIL) were fabricated at the Tyndall National Institute, Cork under National Access Programme (NAP) funding. Bi-metallic Nanogap substrates were fabricated in Singapore, at the Agency for Science, Technology and Research (A* STAR) facility.

Table 3.2 Details for in-house fabricated platform-based SERS substrates

Substrate source & type	Substrate features	Metallic surface layer	Subsurface dielectric material
Tyndall; SCIL imprinted wafer	Nanopillar array	Au	SiO ₂
A*STAR; deep UV-NIL	Nanogap array	Au/Ag bimetallic layer	SiO ₂

There are a number of Raman active molecules used in SERS research including: Rhodamine 6G [176], 4-Aminothiophenol (4-ATP) [177], Crystal Violet [5], 6-Mercaptopurine Monohydrate (6MP) [178], and 2-Naphthalenethiol (2-NT) [179]. The characterisation of the substrates was carried out using 2-Naphthalenethiol. The 2-NT and Spectral Grade Ethanol were obtained from *Sigma Aldrich* and used as received.

Renishaw Wire 3.4 software was used to perform background subtraction on all Raman spectra, and Igor Pro 5.0B used for all plots.

Finite Difference Time Domain (FDTD) analysis was carried out with software purchased from Lumerical solutions Ltd., Vancouver, Canada.

3.1.2 SERS Biosensing of proteins

For SERS analysis of proteins, synthetic biomarkers with their antibodies were used, which enabled accurate control over concentration and purity levels.

The following were purchased from *Becton Dickinson*:

Wildtype recombinant human p53 protein in aqueous buffered solution (556439, 53kDa), Purified mouse anti human p53 antibody (554294, 0.5 mg/ml). The concentration of the stock solution was 1.890 μ M.

The following were purchased from *Abcam*:

Active human EGFR protein fragment (ab 155726, 95 kDa) and Anti-EGFR antibody (ab 2430, 0.2 mg/ml); stock solution was at 10.53 μ M concentration.

The biomaterials obtained from both Becton Dickinson and Abcam were used according to the manufacturer's guidelines and without further purification steps being performed.

The following materials were obtained from *Sigma Aldrich* and used as received:

4- Aminothiophenol (4-ATP), Phosphate Buffered Saline (PBS), N-Hydroxysuccinimide (NHS), (N-(3-Dimethylaminopropyl)-N'-ethylcarbodiimide hydrochloride (EDC), 6-Mercaptopurine Monohydrate (6MP), Glycine and Spectral Grade Ethanol.

High efficiency SERS substrates were obtained from the Danish company Silmeco. Substrates were received packaged in batches of 5 and in a nitrogen atmosphere to prevent early oxidation. A collaboration with Silmeco was undertaken and a non-disclosure agreement set up between NUIG and Silmeco. This involved characterization data from platform-based substrates (page 103-117) being shared with the company in exchange for large numbers of free samples.

3.2 Methods

3.2.1 Evaluation of Platform-based SERS substrates

The first stage of the project was to characterise a number of commercially available platform-based SERS substrates. These had been fabricated by different techniques and contain varied surface morphologies. A brief description of the manufacturing techniques is given in Appendix 8.1.

3.2.1.1 Raman Analysis

Evaluation of the commercial and non-commercial SERS substrates was performed by examining the Raman spectra of substrates functionalized with 2-Napthalenethiol (2-NT).

The SERS substrates were prepared for Raman analysis using the following protocol:

A stock solution of 2-NT was prepared. A molarity of 1×10^{-4} M was gained with '0.0016' g 2-NT diluted in 100 mL of Spectral Grade Ethanol. A 100 mL volumetric flask was used - measuring to the bottom of the meniscus yielding (100 ± 0.08) mL, and a working solution of 10 μ M 2-NT was then diluted from stock.

Substrates were then gently rinsed with the 100% pure Spectral Grade Ethanol using a plastic weighing boat and allowed to air dry.

After cleaning, the substrates were then placed in a 25 mm glass beaker and covered with the 10 μ M solution of 2-NT. The top of the beaker was sealed with parafilm to prevent evaporation.

The substrates were allowed to incubate in the 2-NT for 2 hours [180, 181] allowing the 2-NT to covalently form a monolayer on the substrate surface.

After incubation, the substrates were taken out and gently rinsed in Ethanol to remove any unbound/excess molecules and air dried.

The functionalised substrates were placed on glass slides prepared with double sided tape and removed to the Raman lab for spectral measurements.

All incubation steps of the protocol were performed at room temperature.

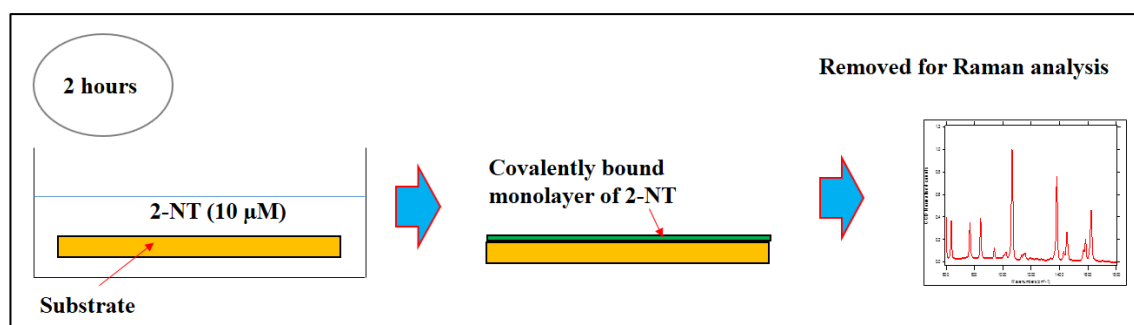


Figure 3.1 Schematic; substrate functionalisation

All substrates functionalised to same protocol described above

Raman measurements were performed using a Renishaw InVia Raman microscope at 785 nm laser excitation and 600 lines/mm grating, with a system resolution of ± 0.25 cm^{-1} . A 50x objective lens (NA 0.75) delivered the laser beam and collected the back scattered light.

Instrument alignment and calibration procedures (including use of an internal silicon reference sample at 520 cm^{-1}) were carried out before each set of experiments. The laser power used was 0.006 mW with a spot diameter of $\sim 1.3\text{ }\mu\text{m}$.

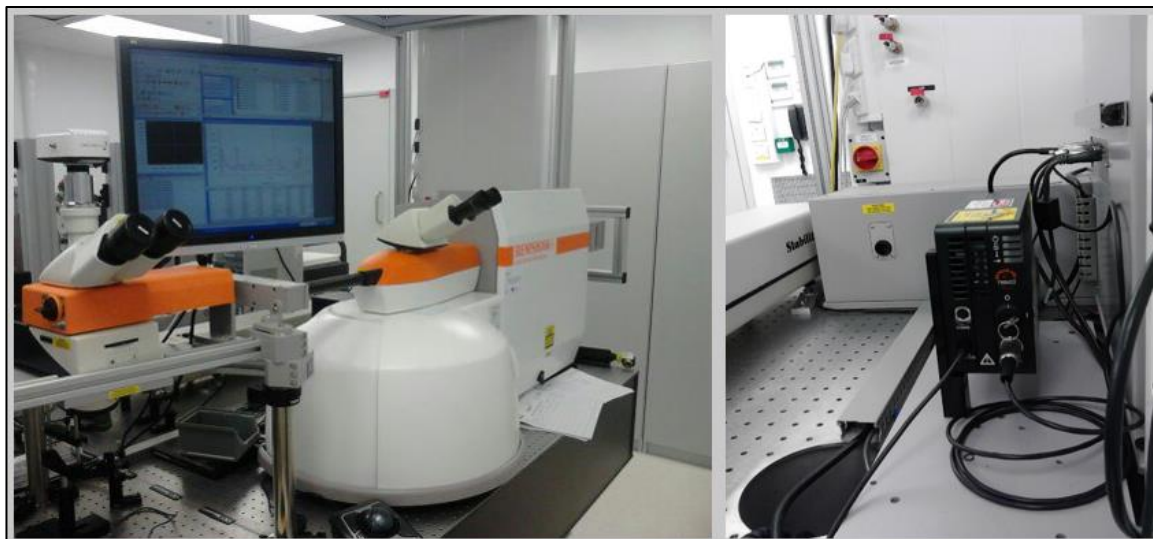


Figure 3.2 Renishaw InVia Raman Microscope

Raman Spectrometer & clean room location

Three substrates of each type were tested. For each individual substrate, spectral acquisitions were recorded at 10 random locations across the SERS active region at a minimum separation of $10\text{ }\mu\text{m}$.

Spectra were recorded over the range $600 - 1800\text{ cm}^{-1}$ with a 10 second integration time, 4 acquisitions and Cosmic Ray Removal.

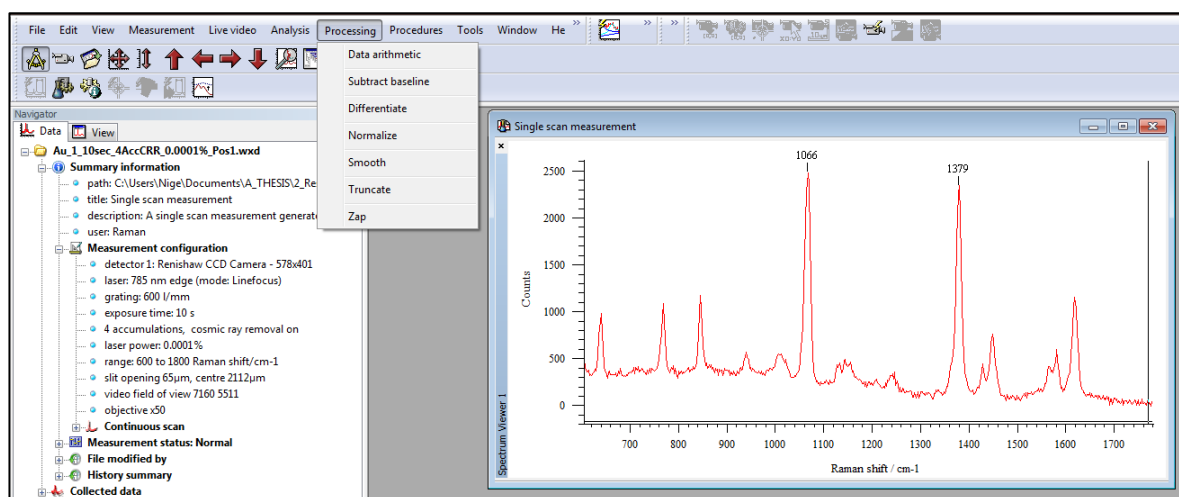


Figure 3.3 Wire software GUI

Baseline subtraction & Cosmic ray removal performed using Wire 3.4 software

Cosmic Ray removal was applied during the Raman acquisitions. The baseline subtraction was carried out using the Wire software and the spectral data sets were then removed to graphing software for further processing.

3.2.1.2 Finite Difference Time Domain (FDTD) Analysis

In this project the **FDTD** tool is used for analysis and optimization of SERS substrates. Essentially the software models electric field behaviour around nanostructures. It is accurate for features that have dimensions less than the incident wavelength. A description of FDTD theory is provided above; page 47.

The simulations are set up in the CAD environment of the GUI. There are four basic simulation object types, these are: The simulation region; structures; sources and monitors.

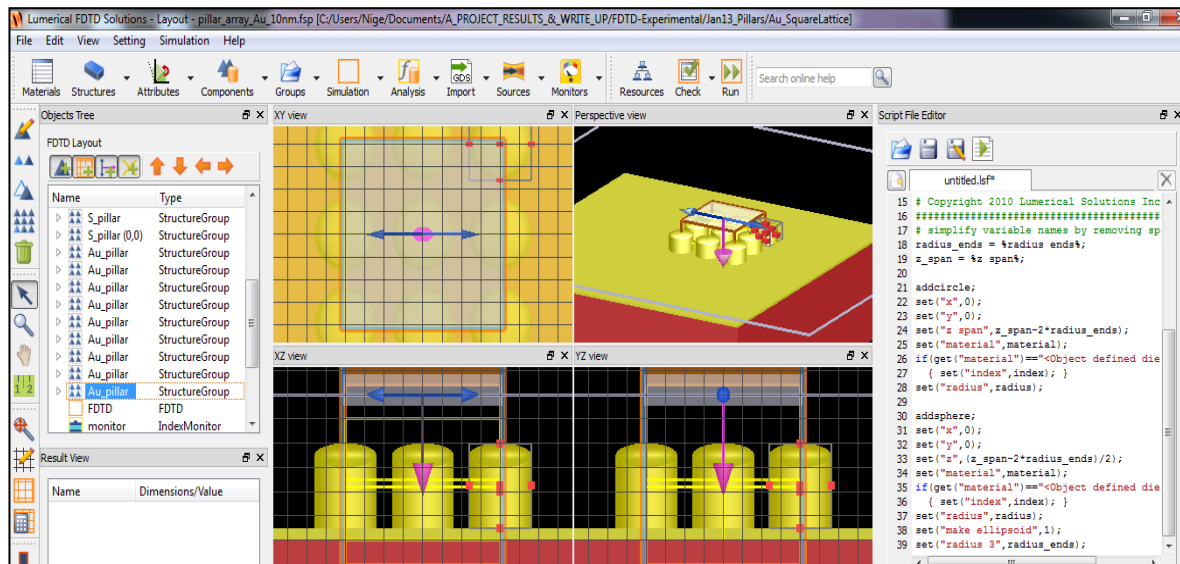


Figure 3.4 FDTD GUI

The CAD environment (centre) reveals XY, XZ, YZ and Perspective views of simulation. A scripting option (right) allows for alteration of simulation objects to specific requirements

A typical work flow for simulation set up is as follows:

1. Create structures
2. Set simulation region & boundary conditions
3. Add suitable source
4. Add monitors
5. Check memory requirements => *Run simulation*
6. Analyse results & export data sets

Objects can be selected from the basic structures or from the object library which contains many complex structure and analysis objects, illustrated below in Figure 3.5. Any object outside the simulation region will not be included in the simulation. Selecting the correct boundary conditions is crucial to avoid spurious results such as non-physical reflections. A useful boundary condition is the Perfectly Matched Layer (PML) which absorbs incident fields. The PML allows for simulation of fields propagating away from the simulation region, without reflections occurring at the simulation boundary.

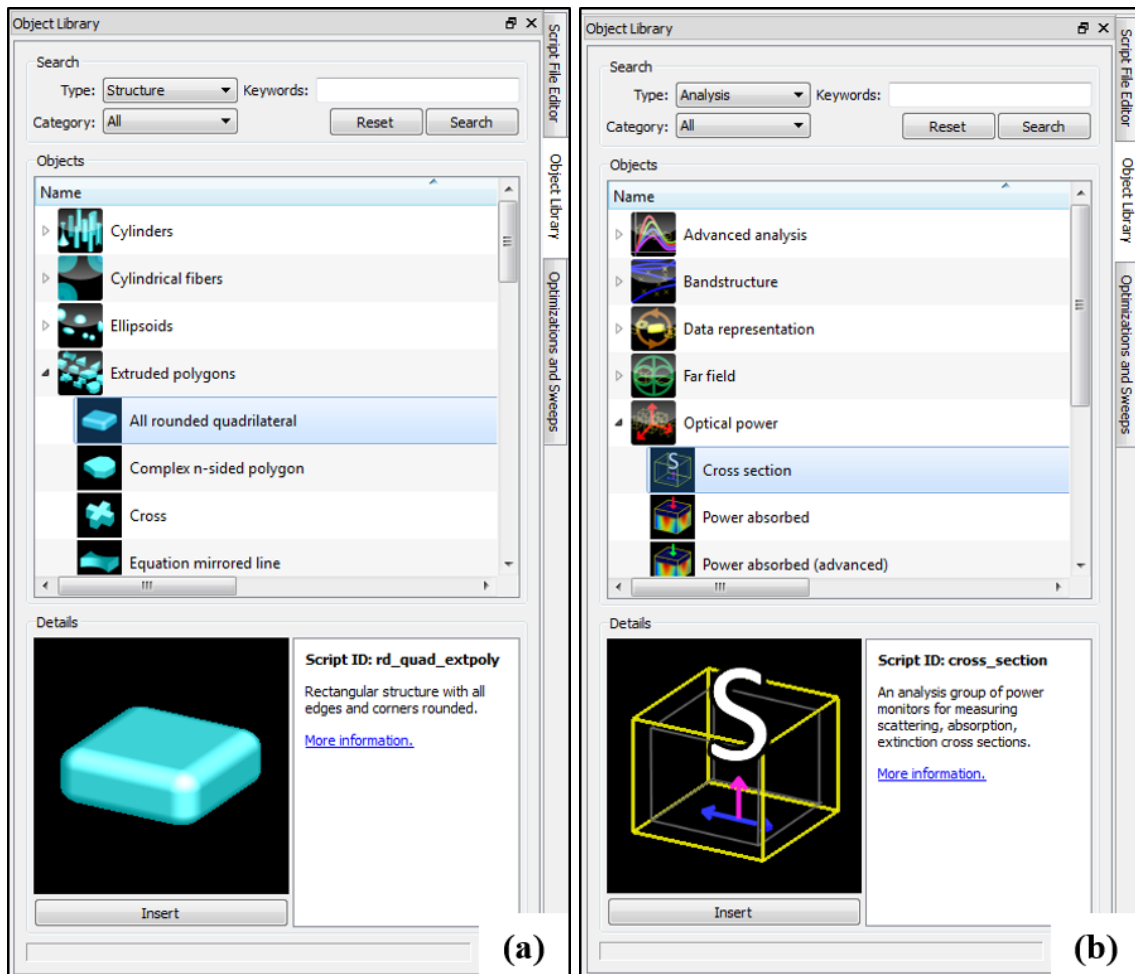


Figure 3.5 FDTD Object library

(a) Structure objects (b) Analysis groups. From these default objects/groups the desired simulation entities can be optimized

The source defines how the incident field is introduced into the simulation, sources include Plane, Gaussian and Dipole. The correct choice for combination of source and boundary conditions is also important; for example, a Gaussian source should not be used with periodic boundary conditions. Monitors record quantitative data from the simulation for field, time, refractive index etc.

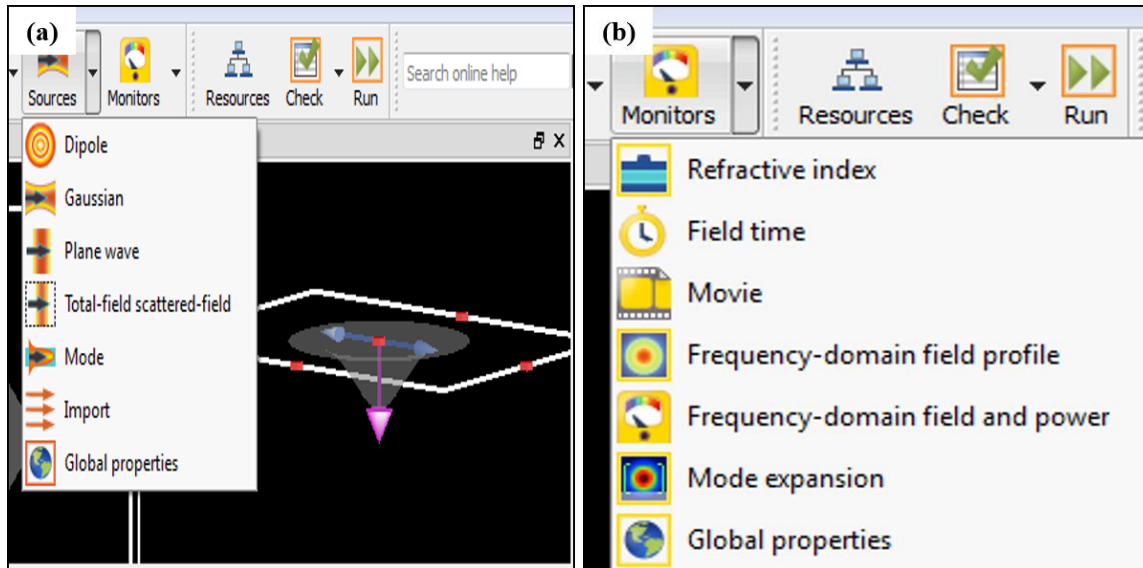


Figure 3.6 Selection of FDTD sources & monitors available

(a) List of monitors, including FDTD GUI image of Gaussian source; pink arrow propagation direction, blue arrow polarization (b) List of available monitors. Refractive index monitor can be used prior to running a simulation to check correct choice of material etc.

Finally, it is important to check memory requirements in the available drop down menu. The simulation time is significantly affected by mesh size (dx), as the simulation time scales as $(\lambda/dx)^4$ for 3D simulations. A course mesh is usually selected at first, then gradually decreased in size for subsequent simulations. When the outputs converge, there is no necessity to reduce the mesh further. The $(\lambda/dx)^4$ dependence arises from the following considerations.

The speed of light in a finite mesh cell is different to that of real space, and is dependent on the mesh dimensions. The simulation time is dependent on the propagation time through each mesh cell. For a 3D simulation, the time is dependent on dx , dy and dz to give approximately a $(\lambda/dx)^3$ relation. However, there is an additional dependence on dt which means that the simulation time has approximately a $(\lambda/dx)^4$ relation.

In addition to the simulation time dependence on mesh size, there is also an issue regarding numerical errors associated with finite mesh size. This problem is addressed using conformal mesh technology (CMT), which is included in the Lumerical software package used on this project. Essentially, the CMT adjusts the mesh size to the refractive index of the material, with a smaller mesh size being used for higher refractive indices. This ensures that numerical errors arising from finite mesh cells are kept below a certain threshold value.

An additional option provided by the software is to use mesh override regions to manually select smaller mesh size for a region of interest such as material interfaces.

The pulsed source used in the simulations begin at an initial time when fields are assumed to be zero. The algorithms require the energy in the FDTD region to reach zero by the end of the simulation run. Time monitors plot fields as a function of time, and are generally used to check that the system energy has sufficiently decayed, see sample FDTD generated plots below, Figure 3.7.

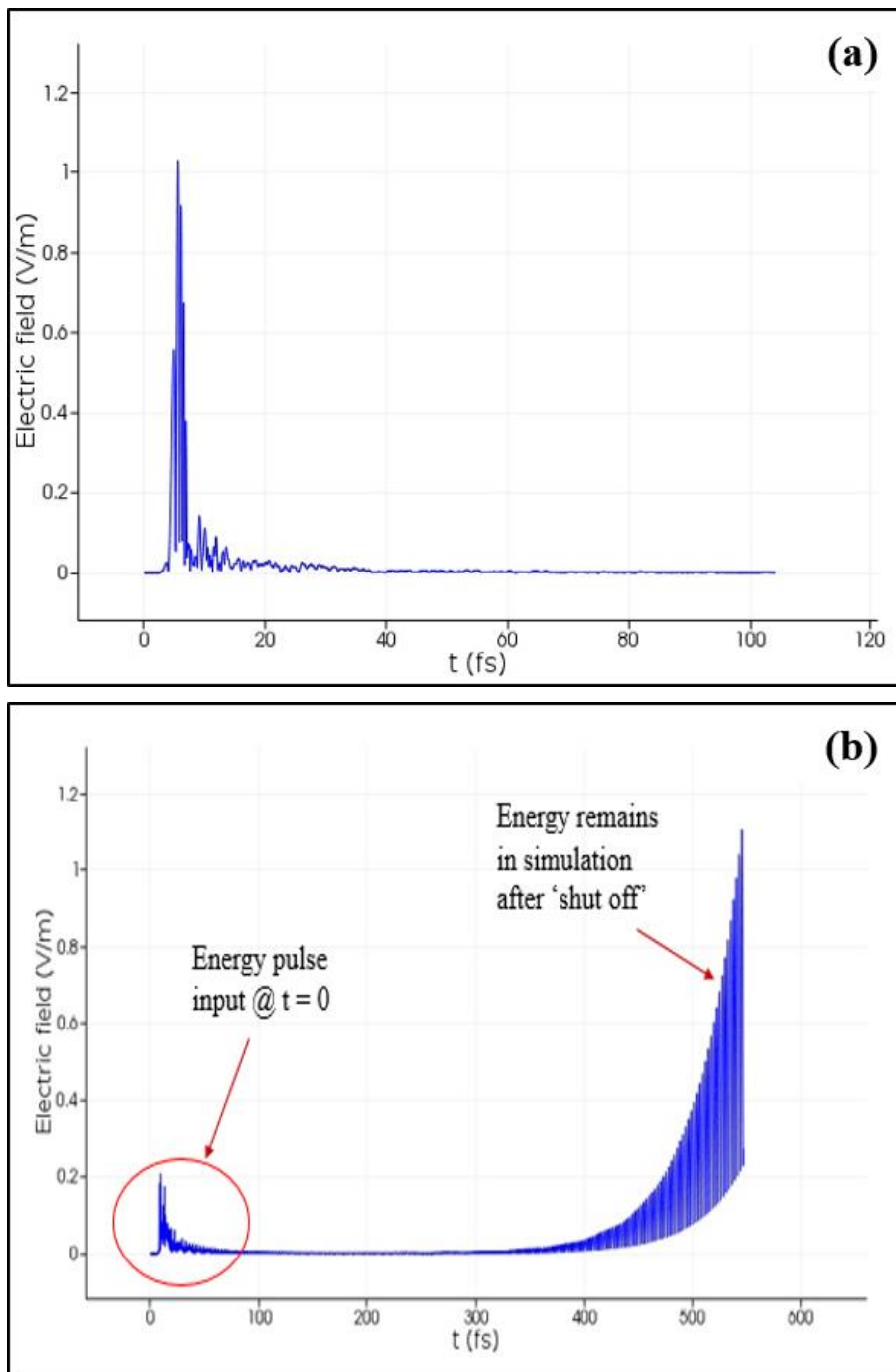


Figure 3.7 FDTD time monitor images; Electric field vs time; showing correct and incorrect simulations

(a) Correct simulation parameters. The energy in the system has sufficiently decayed by the end of the simulation, and the system has reached CW state (b) Image shows diverging simulation arising from incorrect simulation parameters. Incorrect boundary conditions were used to achieve this illustrated result. In this case, the simulation records non-physical reflections.

In order to avoid spurious outputs arising from energy remaining in the simulation as illustrated in Figure 3.7 (b) two or three 'point' time monitors are used on all simulations.

Initial simulation work is performed to compare FDTD simulations with expected theoretical results. These are carried out to better understand how the FDTD analysis relates to the mechanism that generates SERS, and to gain proficiency in the use of FDTD software. A plane wave source is used for these simulations; the simulation objects used were a planar metallic surface and a metallic nanosphere of varying radii.

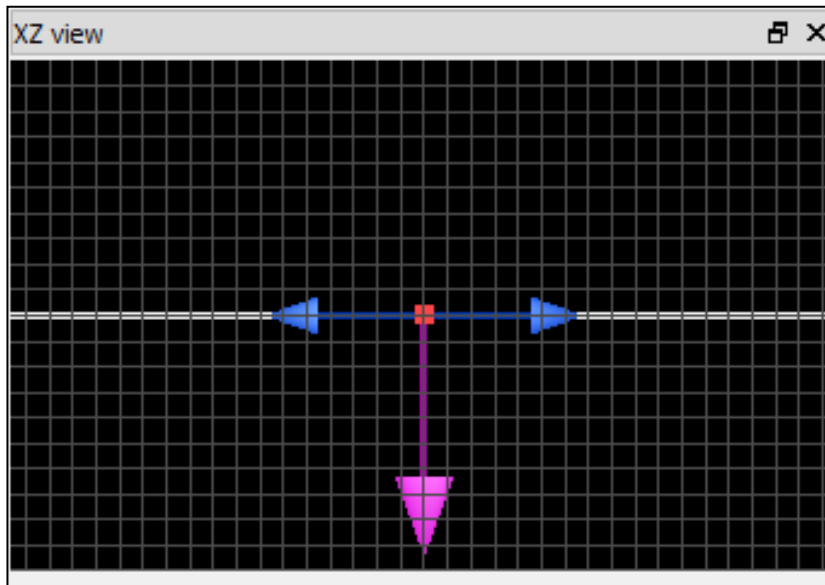


Figure 3.8 FDTD Plane wave source; xz view

Propagation Normal to x, y and downward, polarization along x

The SERS response of nanoscale features are simulated for the following:

1. Local Field Intensity Enhancement Factor (LFIEF) & Reflectance at a metallic planar surface
2. Size dependant SERS response of a nanosphere surface
3. Polarization dependence & ‘Lightning rod effect’
4. Coupled Plasmon Resonance (CPR) arising from variation of interstructure spacing

Note: The expected theoretical outputs are sourced from: “Surface Enhanced Raman Spectroscopy” edited: Sebastian Schlucker [12].

1. LFIEF & Reflectance at a planar metallic surface

The Local Field Intensity Enhancement Factor (LFIEF) is essentially the Local Field Intensity normalized with respect to the incident intensity. For a flat Ag or Au surface over most of the visible range, the LFIEF should be < 1 with a correspondingly high reflectance; for Ag $\sim 100\%$ and for Au $\sim 50\%$ below 600 nm.

The simulation region contained a flat metallic rectangular object with the surface irradiated by a plane wave source at normal incidence. The simulations are carried out over a wavelength range of 200-1000 nm and the outputs are shown in Figure 3.9 below.

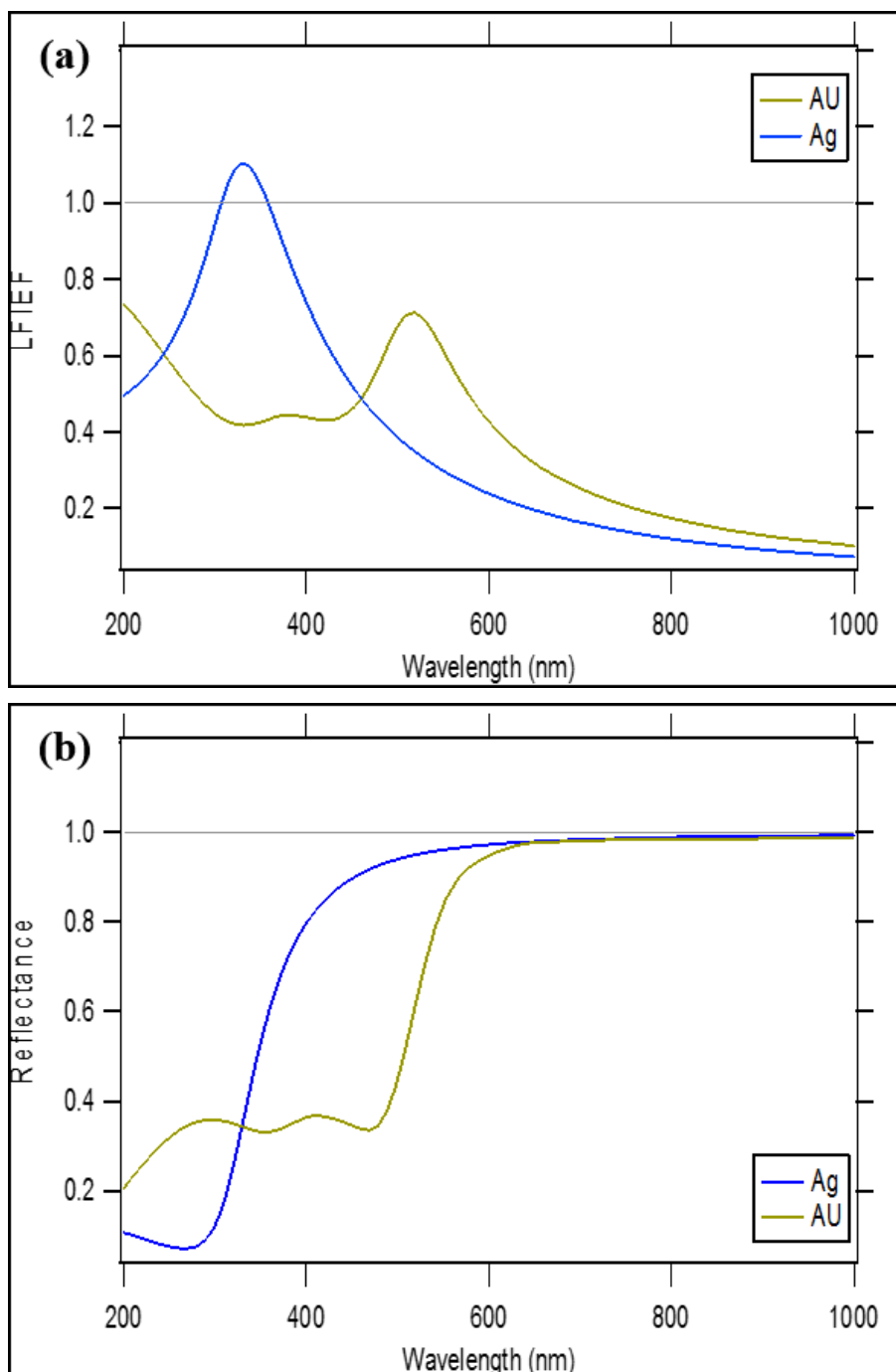


Figure 3.9 LFIEF & Reflectance at a planar Ag & Au surface

(a) LFIEF response illustrating the 'quenching of the LFI at the metal surface (b) The reflectance as a function of wavelength is shown for both Ag & Au. High reflectance is observed for Ag over most of the visible range and from ~ 600 nm for the Au surface.

The outputs generated illustrate the expected behaviour. In (a) the response from the planar surface is a quenching of the LFI for both silver and gold. Additionally, both metals exhibit a concomitant high reflectance (b). The quenching to LFI and hence SERS response, for a planar metallic surface demonstrates the importance of the importance of surface features in the fabrication of SERS-active substrates. The shape, and especially the Nano-dimensionality of the surface features is of particular importance. This is examined in the next series of simulations.

2. Size dependant SERS response of a nanosphere surface

Next we will examine the SERS response of a non-planar metallic surface by introducing an object with nano-dimensionality into the path of the incident electromagnetic wave.

Simulations were carried out for a silver nanosphere with varying radii of 30-120 nm, using a plane wave source at normal incidence.

LFI quenching occurs at a planar metallic surface, the response now expected is that of field enhancement. It is also expected that both the magnitude of the local electric field, and the position of the resonance peak, will vary with the size of the nano object.

In Figure 3.10 difference in LFIEF response, of a planar and nanosphere surface is illustrated. Note that 'quenching' occurs at the planar surface; see also Figure 3.9 (a). However, replacing the planar surface with a MNP, now results in an enhancement to the LFI. In tandem with the change in strength of the field maxima, there is also a frequency shift of the resonance peak position; Figure 3.10 (a) & (b) respectively.

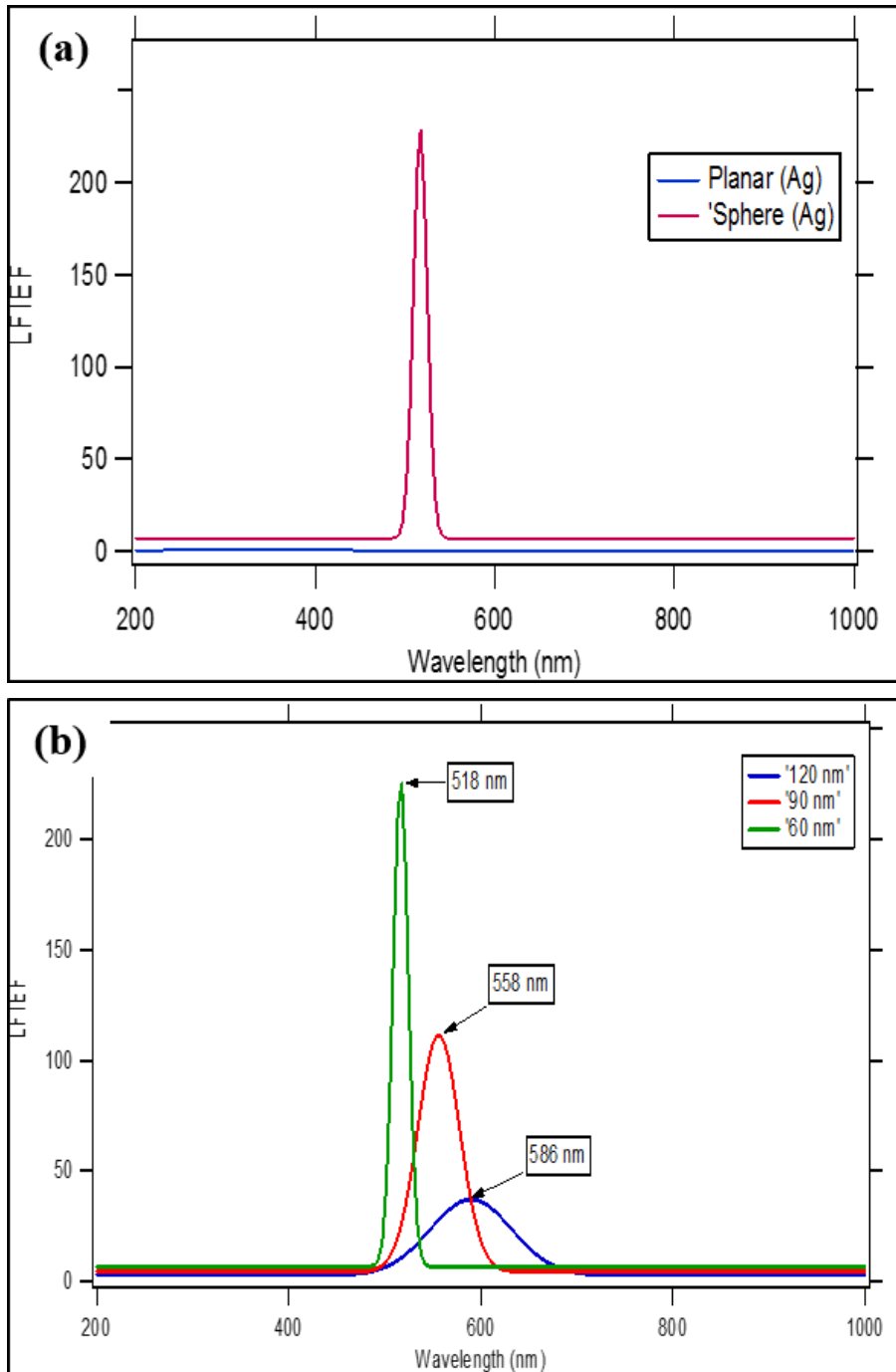


Figure 3.10 LFIEF response for planar and spherical simulated objects & resonance peak shift

(a) LFIEF comparison of a planar and 60 nm radius nanosphere; both Ag. Quenching occurs at planar surface while LFI enhancement is observed for the nanosphere (b) As the radius of sphere is varied, a red-shift is noticed with increasing radius. Simulations using plane wave source at normal incidence.

In order to illustrate the variation of Electric field maxima and spatial distribution with sphere radius, 2D plots for Electric field are presented next in Figure 3.11.

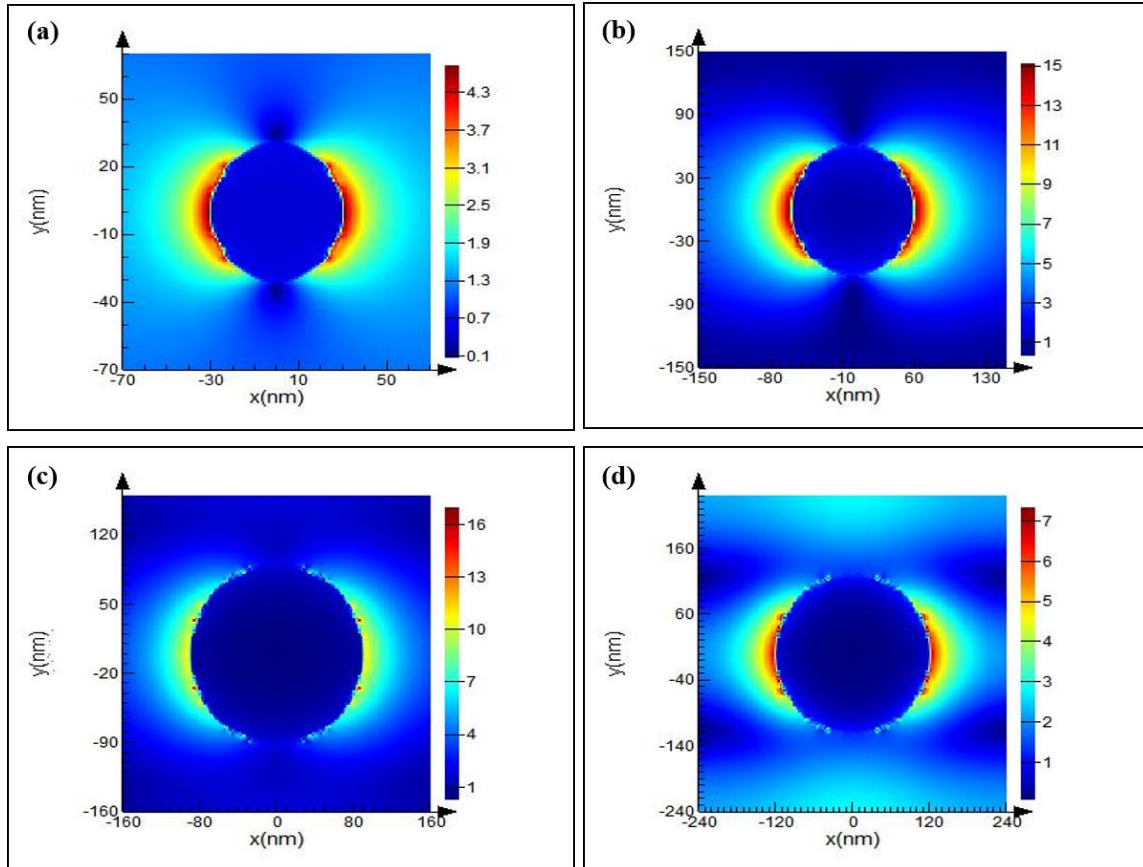


Figure 3.11 FDTD generated Electric field distribution for spherical metallic nanoparticles at varying radii

2D images showing Electric field maxima and spatial distribution about nanospheres of varying radii (a) through to (d) 30, 60, 90, 120 nm radius respectively. Plane wave source at normal incidence and polarization along 'x'. Scale bar; Electric field (V/m)

In Figure 3.11, both the Electric field maxima and spatial distribution change with variation of the nanosphere radius. However, in each case the local field maxima occur on the edges of the sphere that are parallel to the incident polarisation (*i.e.* along 'x'). The effect on the local electric field of varying the incident polarisation is examined in the next simulation.

3. Polarization dependence & 'Lighting rod effect'

In order to examine how the spatial distribution of electric field is affected by incident polarisation, the following simulation is carried out. A silver nanosphere of 60 nm radius is 'illuminated' by a plane wave source at normal incidence. The outputs were examined for incident polarization along both the 'x' and 'y' axes, with all other parameters remaining the same.

An additional simulation is carried out to examine how objects with 'sharp' edges can intensify the local electric field in what is known as the 'lightening rod effect'. In order to illustrate the 'lightening rod effect', the nanosphere in the previous simulation is replaced with a nano-square.

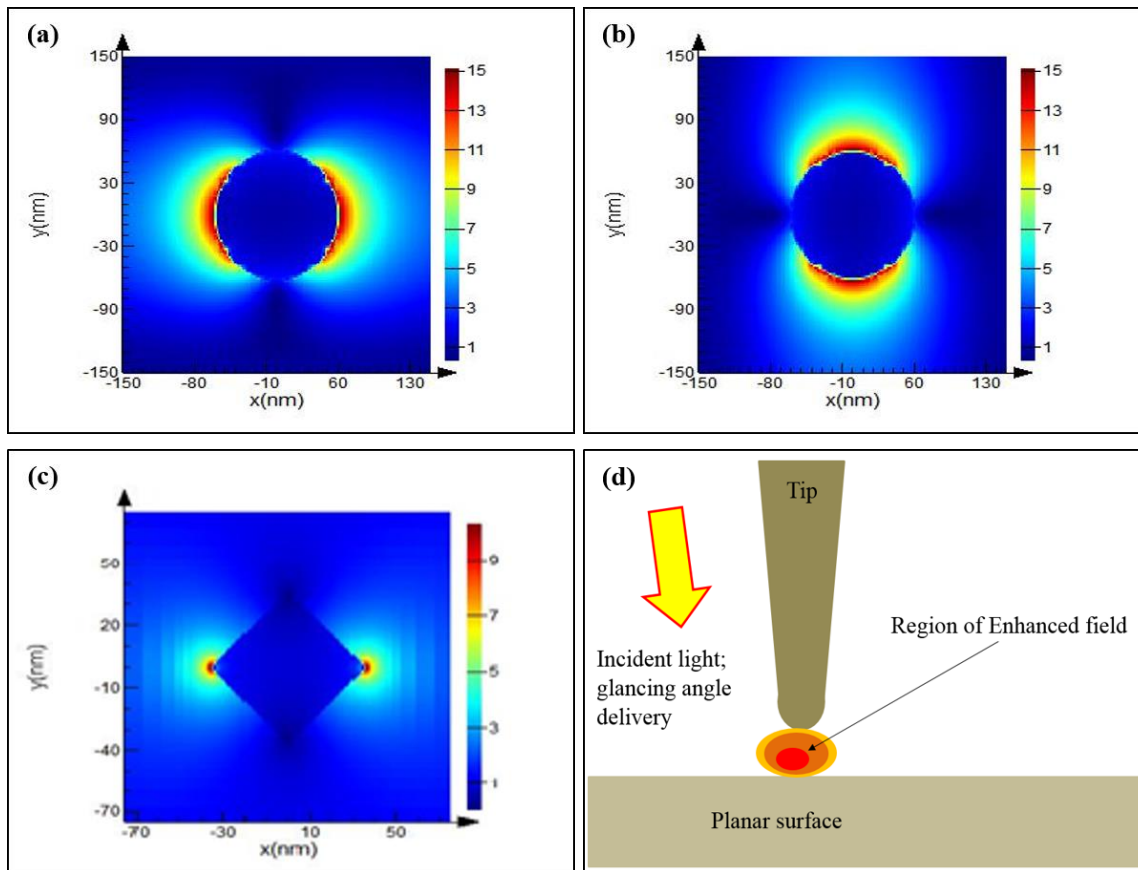


Figure 3.12 FDTD; Electric field variation with incident polarization & spatial distribution of field about ‘sharp’ object features

Incident polarization along ‘x’ & ‘y’ shown in (a) & (b) respectively (c) Incident polarization along ‘x’ for a nanosquare, 60 nm sides. (a) through to (c) plane wave source at normal incidence. Scale bar Electric field (V/m) (d) Schematic; showing application of SERS edge or ‘lightning rod’ effect as utilised in TERS

From Figure 3.12 (a) & (b) it can be seen that the field maxima occur parallel to the incident polarization, while the strength of the field remains the same. For a SERS substrate with antistrophic topography, suitable alignment of the sensor, and with due consideration to the polarization should be observed. Image (c) illustrates the lightning rod effect. The spatial distribution of the field is strongly localized around the apex of the square that is parallel to the incident polarization. The ‘lightening rod effect’ can be utilized in SERS applications such as TERS; shown in the schematic of (d).

4. Coupled Plasmon Resonance (CPR)

Having already considered the SPR of a single object (sphere), we now look at two neighbouring objects and the effect on the electric field as they are brought closer together.

Just as for the above simulations, a plane wave source is used at normal incidence.

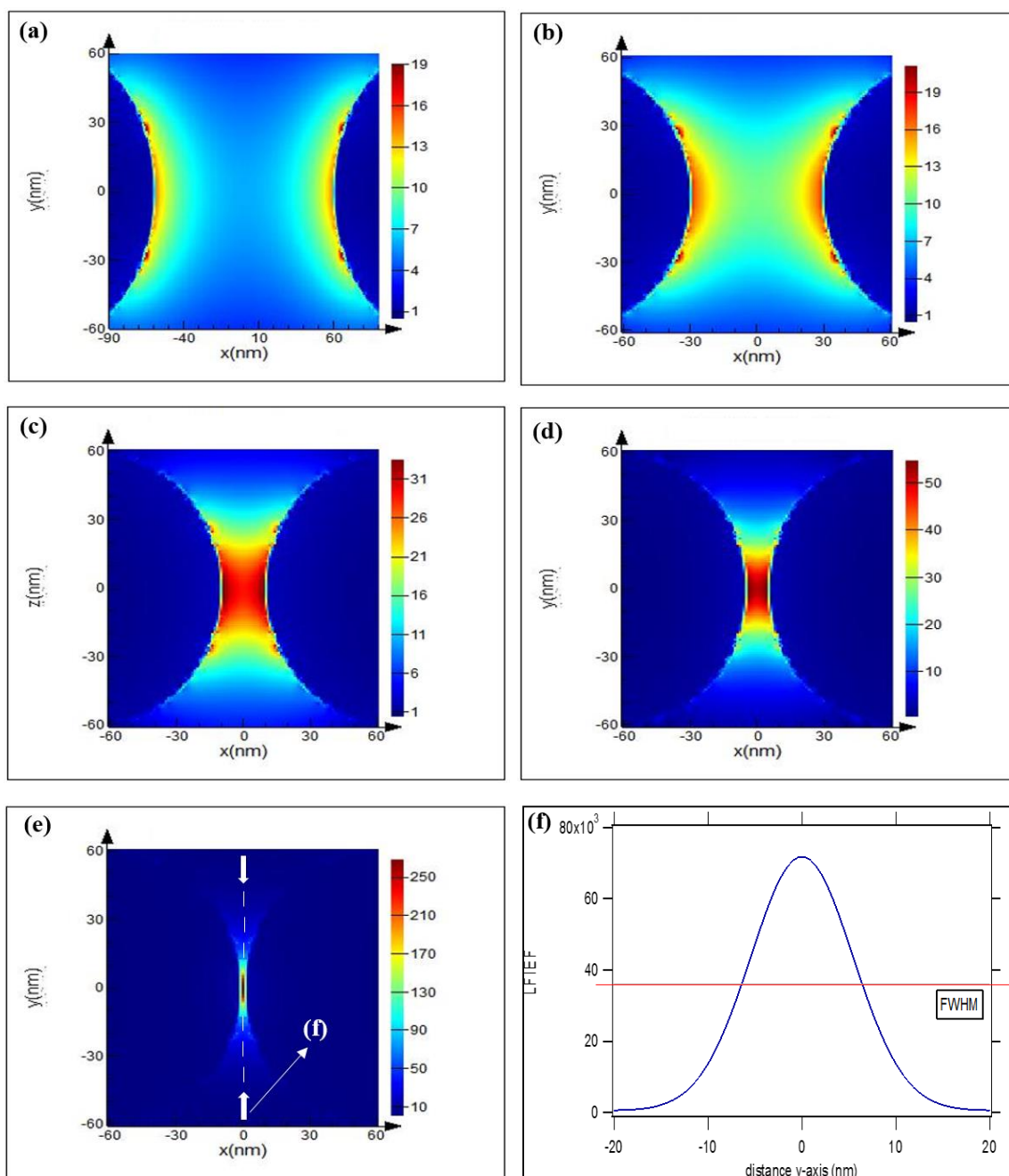


Figure 3.13 Coupled Plasmon resonance for two ‘Ag’ Spheres at varying separations
 Images (a) to (e) Electric field between nanospheres. Distance between spheres: initially at 120 nm, decreasing through 60, 20, 10 and 2 nm (a) to (e) respectively, radius 60 nm (f) Local Field Intensity Enhancement Factor (LFIEF) vs Sphere separation along ‘y’ at $x=0$ (line profile marked on (e) for visual purposes). ALL simulations - Plane wave source, Polarization along ‘x’ and normal to x, y (downward). Scale bar Electric field (V/m).

In Figure 3.13 above, when the spheres are far apart (twice their radius), there is essentially no interaction between the individual local electric fields, shown in (a). Thus, from the standpoint of SERS activity, they can be considered as two separate objects. However, as the structures are brought closer together, their fields begin to interact, with concomitant increase in the strength of the field maxima; especially noticeable in (c) & (d); gaps of 20 and 10 nm respectively. As the gap is further decreased, the strength of the field maxima strongly

increases, with the eventual formation of a SERS ‘hot spot’ (e). SERS ‘Hot spots’ are highly localized regions of intense electric field.

To illustrate the near field characteristics of a SERS hot spot, the LFIEF is plotted against distance from ‘hot spot’ centre along the y axis at $x = 0$; (f). Hot spots are characterised by the presence of a large LFIEF at their centre [12] Normally this is also accompanied by a strong localisation of CPR. Both of these characteristics are seen in the image. The LFIEF is seen to rapidly fall off with distance from the hot spot centre; reaching FWHM value at ~ 6 nm from centre along ‘y’.

Secondly, the platform-based substrates were modelled and comparisons made to the experimental Raman outputs. For individual simulations, a range of parameter dependent FDTD outputs is also generated to gain an approximate ‘uncertainty’ value. The individual simulation ‘set up’ is described as follows.

Silmeco substrates

The simulation set up for Silmeco Capped Silicon Nanopillar substrates is shown below in Figure 3.14, the same geometry is used for simulating both Ag & Au Nanopillars. The SERS enhancement mainly arises from the ‘leaning’ of adjacent pillars and the Coupled Plasmon Resonance between them. As such the simulation was set up for a dimer rather than a single pillar. The dimensions of the metallic pillar cap and general substrate geometry were gained from a publication by Wu et al. [71]. The separation between pillar caps was set to 1 & 4 nm. The 1 nm gap accounts for the leaning effect of the nanopillars, and the 4 nm to give a ‘sense’ of the uncertainty of the simulations.

Table 3.3 Silmeco substrate dimensions

Material	Structure spacing (nm)	Material	Structure spacing (nm)
<i>Ag</i>	1	<i>Au</i>	1
	4		4

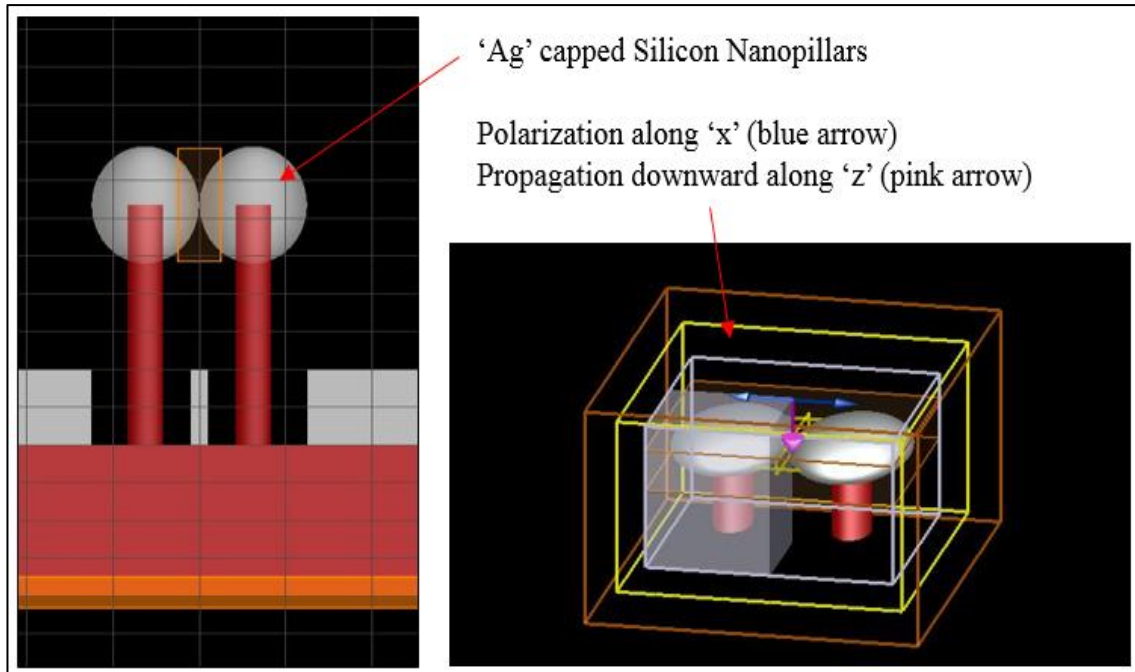


Figure 3.14 FDTD set up; Ag Nanopillars

The shaded rectangle between the two pillar caps is a mesh override region (left image). Plane wave source, propagation normal to x, y (downward) Polarization along x .

A mesh override region is used for the area between the two pillar caps where the field maxima and field enhancement occur. This allows for a reduction in simulation memory requirements and brings the benefit of accuracy to the ROI.

In the perspective view (*right image*) there is a 'shaded' area in the bottom left quadrant. This is due to the use of symmetric boundary conditions. These conditions can be applied when the structure and fields are both symmetric and periodic, i.e. when the electromagnetic fields have a plane of symmetry through the middle of the simulation region. The main advantage is that the simulation run time is reduced by a factor of 4, thus allowing for a finer mesh to be used. Here a PML layer is used along the 'z' axis.

Integrated Optics substrates

These substrates were simulated using a 'roughened surface' object from the object library in order to simulate an amorphous surface. The simulation geometry used for Au and Ag surfaces was the same in both cases. The substrate soda lime glass base was introduced first into the simulation region as a roughened surface object. Then adjustments to the object roughness were made to achieve the desired topography. The object was then copied and moved upwards in 'z' to create a surface layer which also had the amorphous features and the material changed to Au. The interface between the soda lime glass platform and metallic surface layer is defined by selecting suitable mesh order priority for both objects. Selecting the correct priority setting 'instructs' the software to ignore the metal below the interface. This can be seen clearly in the x, z view of Figure 3.15 (a) below.

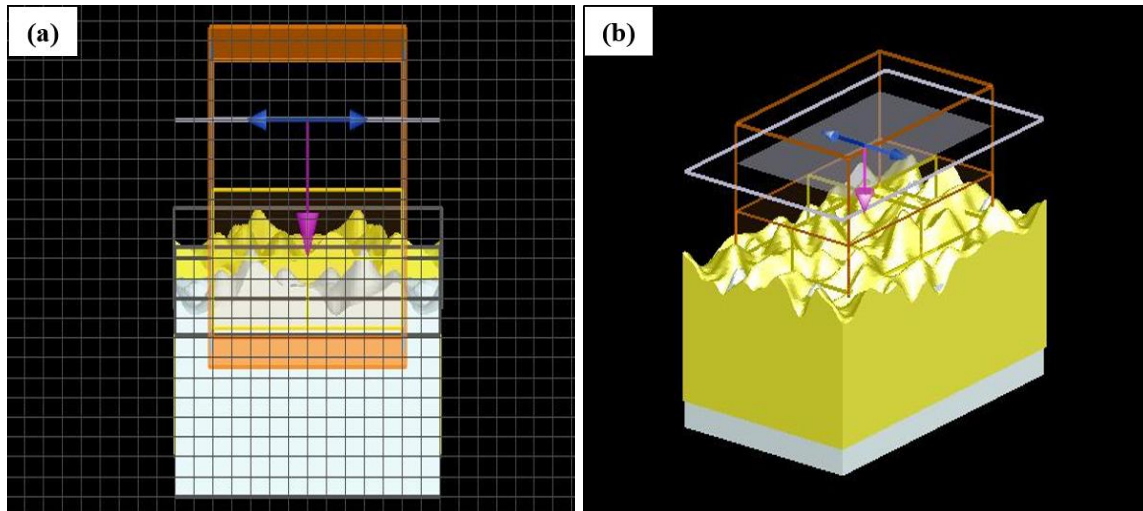


Figure 3.15 FDTD set up; Au Laser fabricated substrates

(a) *x, z view, Au surface coating thickness = 200 nm* (b) *Perspective view showing amorphous features. Plane wave source, propagation normal to x, y and downward, polarization along x.*

PML boundary conditions were used on all boundaries. Although the structures extend through the PML boundaries only the structures within the bounded region are simulated. Extending the objects through the boundaries in this way ensures that material properties at the boundary are clearly defined. FDTD calculates the fields propagating through the PML layer. However, if a structure has an interface within the PML layer it will generate non-physical reflections.

Horiba substrates

The Au Nanorods were also simulated as a dimer, and simulations carried out for structure separations relating to the long and short axes presented in the following table.

Table 3.4 Horiba nanorod substrate dimensions

Height	550	
Diameter	80	
All measurements (nm)	Minimum separation	Maximum separation
Axis 1 – long axis	60	80
Axis 2 – short axis	10	20

The Au Nanorods were simulated as illustrated in the figure below.

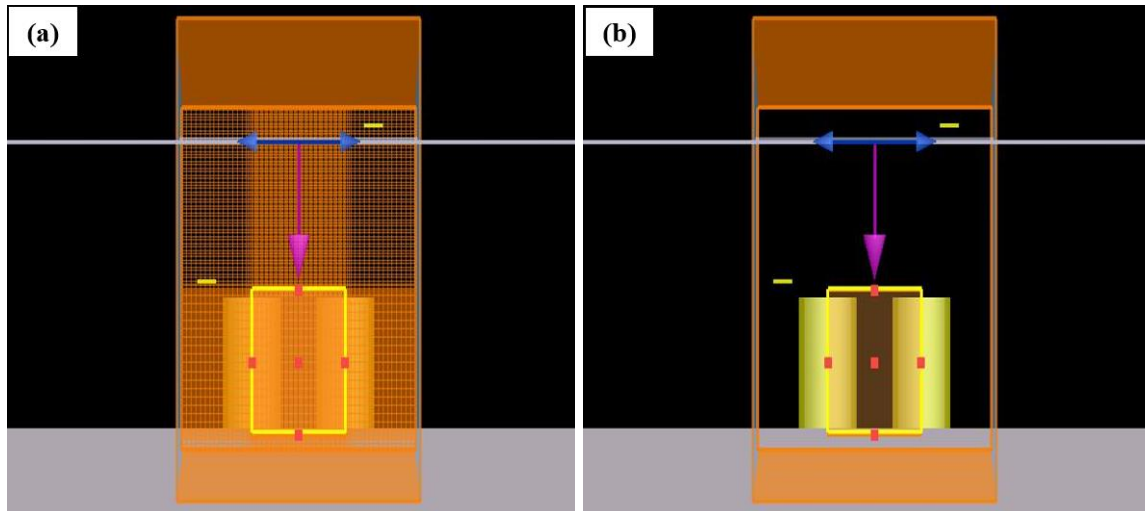


Figure 3.16 FDTD set up; Horiba substrate

x, z view (a) shows standard graded mesh region (b) graded mesh disabled for visual purposes; mesh override region visible between nanorods. Plane wave source; propagation normal to x, y and downward, polarization along x .

The standard FDTD mesh applies a finer mesh near to the edge of objects. However, a mesh override region allows for manual setting of finer mesh over desired regions; illustrated in (b) above. The two short yellow lines visible middle left and top right are point time monitors.

Diagnostic anSERS substrates

For this simulation, two Au nanoparticles on a paper substrate were introduced into an FDTD region.

Table 3.5 Diagnostic anSERS substrate dimensions

Sphere diameter (nm)	Structure spacing - along 'x' (nm)
50	10
50	30

The platform base was chromatography paper and refractive index data was gained from the publication by Fabritius et al. [182]. A mean refractive index based on the literature was selected and uploaded to the FDTD material data base.

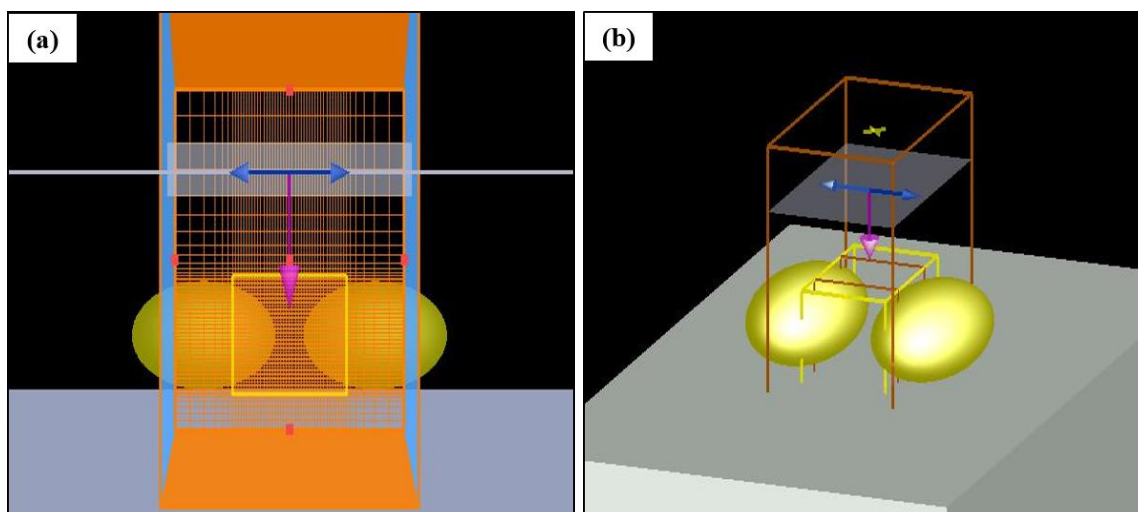


Figure 3.17 FDTD set up; Inkjet substrate

(a) *x, z view; mesh override across region between Au nanoparticles* (b) *perspective view. Plane wave source; propagation normal to x, y and downward. Polarization along x.*

The FDTD generated SERS Enhancement Factor is calculated as an approximation based on field maxima measured during the simulation. Two ‘profile’ monitors are used to measure the spatial distribution and magnitude of the local electric field across 50 frequency points. One monitor records values across ‘x, z’ while the other across the ‘y, z’ plane. A MATLAB script then selects the maximum electric field value, and applies the E^4 enhancement approximation.

Following these simulations, the model is then further developed in Results chapter 2 to both optimize and analyse the Nanolithography substrates, page 141 & 159.

3.2.2 Design & Optimization SERS substrates

3.2.2.1 Fabrication techniques; SCIL substrates

The substrates from the **Tyndall National Institute** were delivered under National Access Programme (NAP) funding, using Substrate Conformal Imprint Lithography (SCIL).

The fabrication process is described as follows:

1. e-beam patterning onto Silicon wafer to produce Master mold
2. Fabrication of Flexible Mask & stamp
3. SCIL imprinting
4. Etching
5. Deposition of noble metal film to achieve SERS response

The ‘patterning sequence’ of the imprint process involves three basic steps which are detailed in Figure 3.18 and explained briefly as follows:

Firstly, a Master mold is made by e-beam patterning of a wafer that is spin coated with Hydrogen Silsesquioxane (HSQ) resist. HSQ is a negative resist allowing the e-beam patterned regions to remain post developing. The Master is realized with structures ~ 50 nm in height.

Next, a flexible mask is made from the Master using a bilayer of Hard-PDMS and PDMS which yields topography that is ‘indented’ from the Master.

Finally, the SCIL process generates an imprinted wafer with a morphology comparable to the design on the Master. Subsequent etching produces nanostructures of the desired height ~ 450 nm.

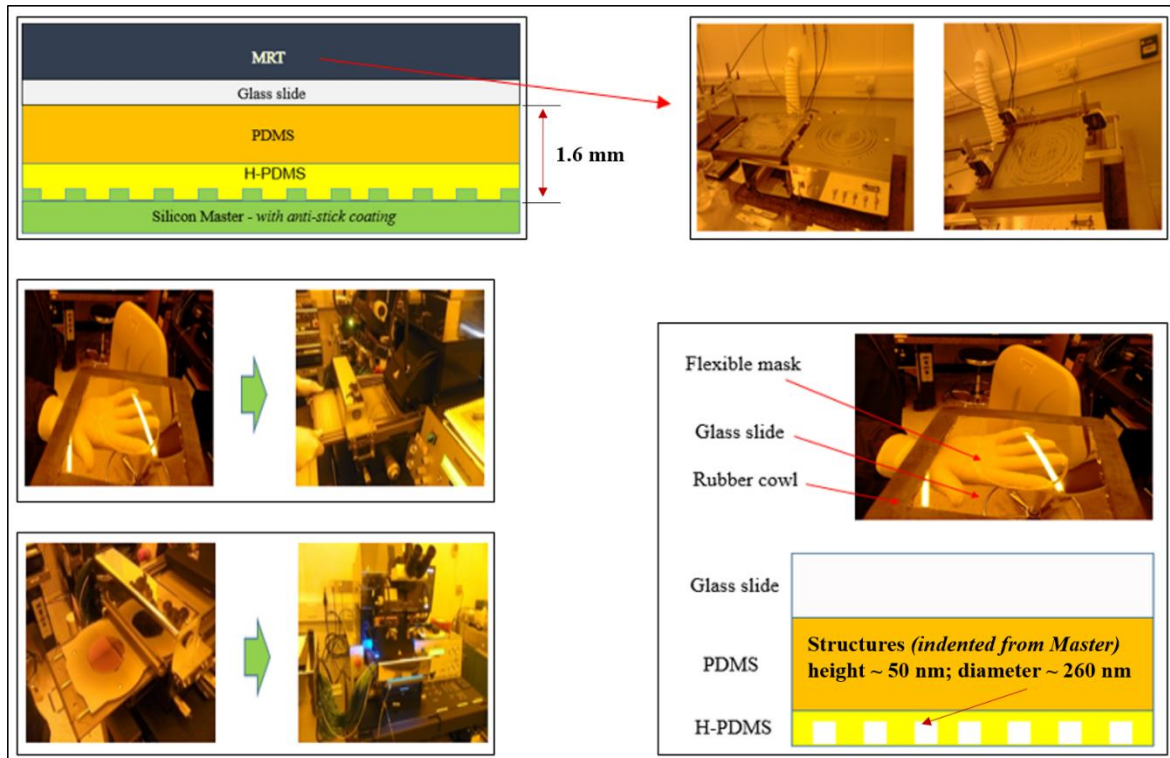


Figure 3.18 Schematics and images for SCIL process

Silicon Master with attached: biopolymer layer (H-PDMS/PDMS) process depth ~ 1.6 mm; glass carrier slide; Mask Replicator Machine (MRT) – upper left schematic. MRT tool – upper right image. Glass carrier & flexible mask inserted into SCIL machine for imprinting of silicon wafer – left middle image. Aminol resist coated silicon wafer loaded to SCIL MA6 mask aligner, ready for conformal imprint – left lower image

The flexible mask process dimensions are shown in Figure 3.19.

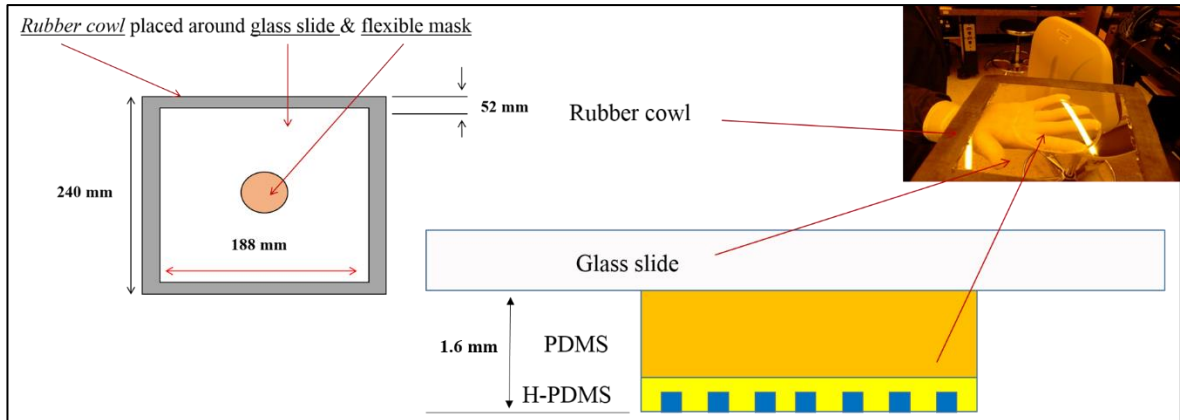


Figure 3.19 Flexible mask process dimensions

The diameter of the flexible mask is the same as the silicon wafer (100 mm wafer diameter)

Substrate Conformal Imprint Lithography can produce nanostructures with better feature resolution and quality in comparison to other nanolithography methods. Improved quality is achieved using the flexible stamp and sequential ‘roll on/roll off’ imprinting described in Figure 3.20. Capillary action ‘pulls’ the stamp into the liquid resist and so minimizes air inclusion that would otherwise cause surface damage and poor feature resolution.

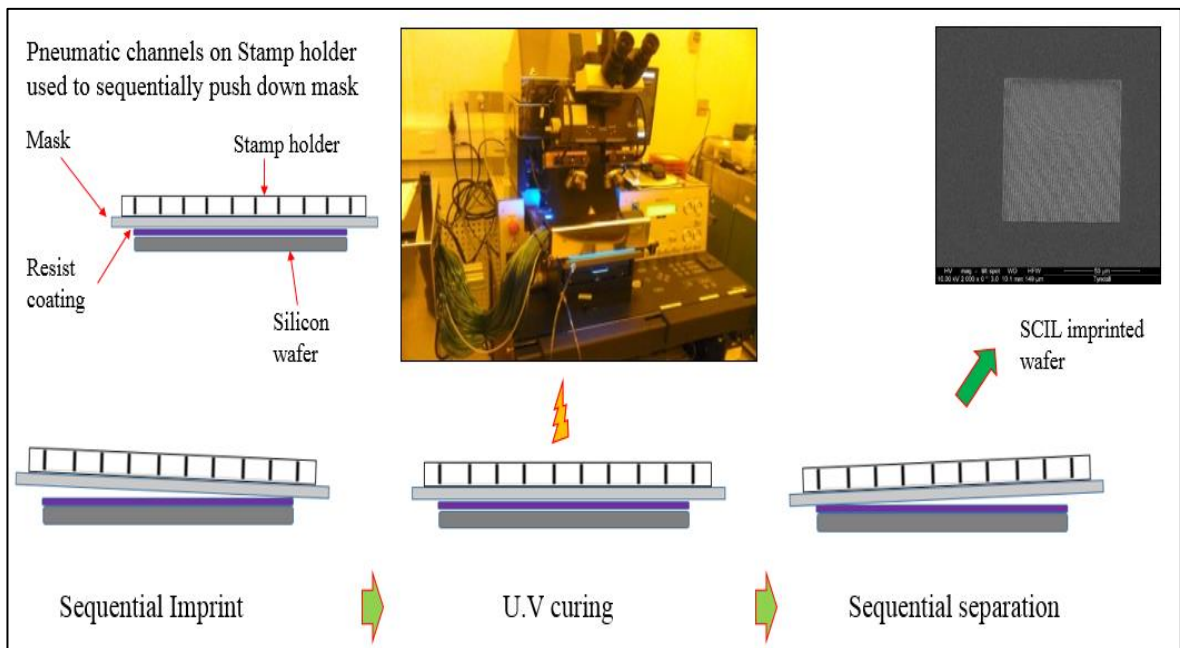


Figure 3.20 Schematic of SCIL imprinting

Vacuum holds Mask in place, series of pneumatic channels in stamp holder activate & deactivate sequentially to produce ‘roll on/roll off’ imprint sequence. UV curing ~ 15 minutes

The imprinted wafer is then removed. Any residual organics are removed by O₂ cleaning, the wafer is then etched to ‘punch’ through the Silicon and leave structures of the desired height.

A SiO₂ layer is ‘sputtered’ onto the nanostructures to initially ‘bulk out’ the structures prior to deposition of metal layer. A nanolayer of Titanium (~ 5 nm) is deposited onto the SiO₂ surface, also by sputtering; in order to provide adhesion for the noble metal layer.

The sputtering technique is a type of physical vapour deposition (PVD). Argon gas is injected into a vacuum chamber which is ionized by a radio frequency (RF) source. A target is placed on a cathode and the substrate/sample to be sputtered is placed above the target. The Oxford Sputterer used at Tyndall contains a Magnetron source, where magnets are located behind the cathode. Electrons from the Argon plasma are captured in the magnetic field which increases the rate of collision with Argon atoms. Resulting positive ions are accelerated towards the target and charge-neutral material is ejected. This material flux is deposited onto the sample, coating it in a thin film of the target material.

A thin metallic film is then applied via metalorganic vapour phase epitaxy (MOVPE). MOVPE is a type of chemical vapour deposition method. Thin film growth is via a chemical reaction rather than PVD. MOVPE utilises metal-organic sources (MOS) which are injected into a gas chamber reactor (not vacuum). A carrier gas transports the MOS across a heated substrate/sample, where a surface chemical reaction ensues, resulting in an epitaxial thin film growth.

3.2.2.2 Fabrication techniques; Nanogap substrates

Nanogap substrates were designed and fabricated at the **A* STAR** facility in Singapore. These substrates comprise of a nanohole array on a Silicon wafer with a bimetallic surface coating. The bimetal film consists of a silver layer of 35 nm thickness and a gold outermost layer 10 nm thick. Gold provides a more stable outer layer than Ag, while a bimetal Ag/Au layer yields a greater SERS response than Au only [183, 184]

Fabrication of the Nanogap substrates on a Silicon wafer essentially involves a four step process which is detailed in the publications by Dinish et al. [180] & Fang et al. [185]. A brief overview of the process is described as follows.

1. Firstly, deep UV (DUV) Photolithography is used to create a mask patterned with an array of circles. The Lithography was performed using a DUV excimer laser (248 nm) and a positive resist, i.e. the written structures are removed during development.
 - a. Positive resist; commonly poly-methyl methacrylate (PMMA)
 - b. Developer; (commonly: acetone; sometimes chlorinated solvents such as methylene chloride) – removes written area’s i.e. circles array.
2. Etching of the Silicon is achieved with RIE to a depth of ~ 150 nm.
3. Dry oxidation of SiO₂ – to ‘bulk out’ structures
4. physical vapour deposition via e-beam evaporation is used to form a bimetallic layer; Ag followed by Au outer layer.

The use of a positive resist yields an array of closely packed nanoholes with the regions between the holes remaining as raised structures, illustrated in the following schematic; Figure 3.21.

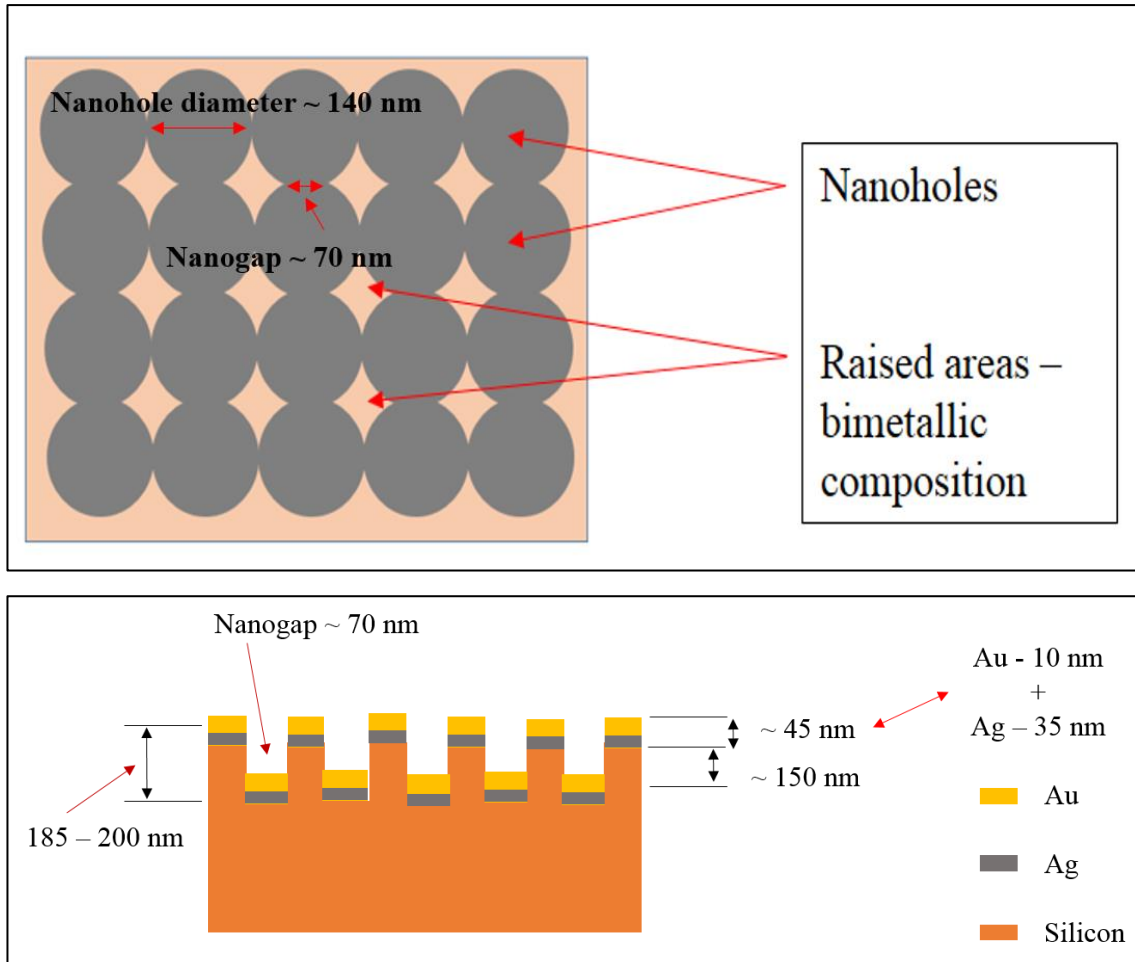


Figure 3.21 Schematic; nanogap substrates

Upper image - x, y view showing raised bimetallic areas between nanohole array post developing
 Lower image x, z side profile; bimetallic layer ~ 45 nm which consists of - 35 & 10 nm layers of Ag & Au respectively

3.2.2.3 Raman Analysis; SCIL & Nanogap substrates

The procedure used for substrate functionalisation and Raman analysis of the platform-based units above was also used for the SCIL and Nanogap substrates.

3.2.2.4 FDTD analysis; SCIL fabricated substrates

The dimensions used for simulating the SCIL substrates are shown in Figure 3.22 below. The simulation consisted of two pillars with periodic boundary conditions used along 'x' and 'y', with a plane wave source and PML along the 'z' boundary. Note the structure array and the substrate base extend through the boundaries in x, y – this is to prevent non-physical reflections between the edge of the substrate and the simulation boundary.

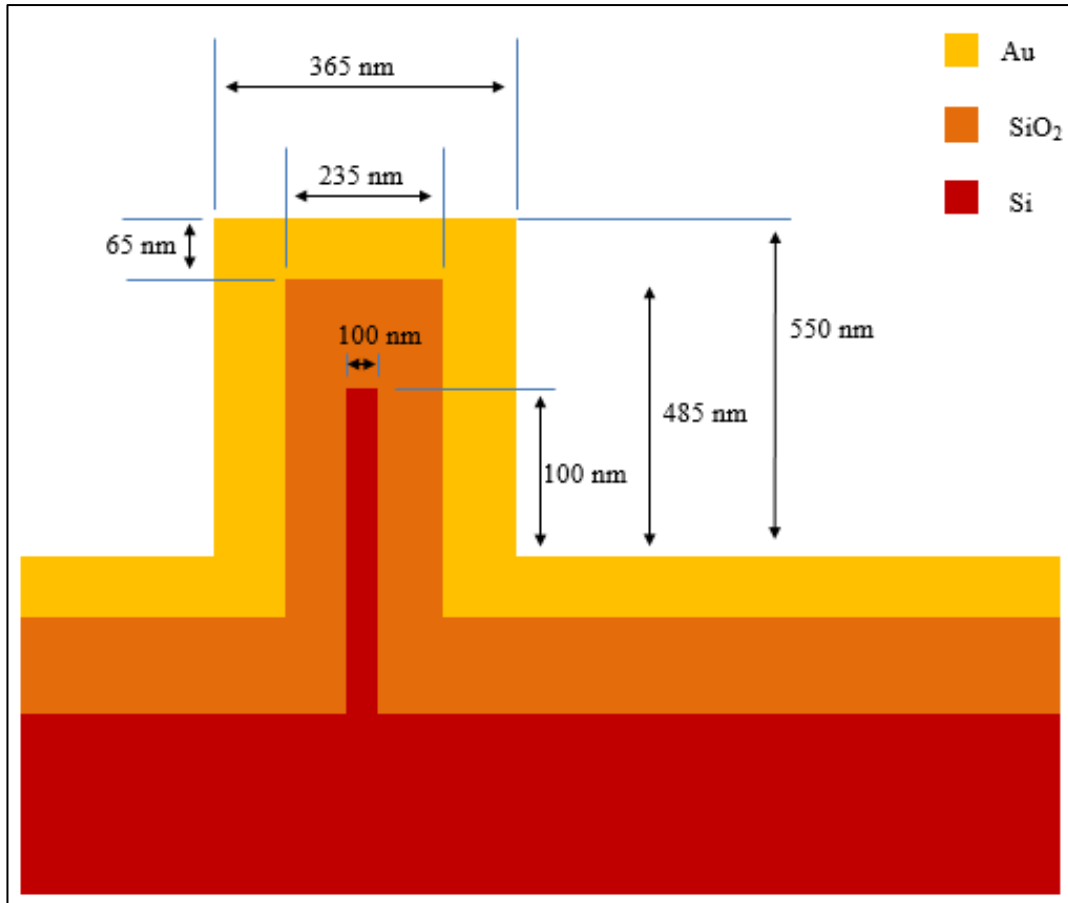


Figure 3.22 SCIL Nanopillar; dimensions & material composition

Schematic showing Silicon imprinted Nanopillar with SiO₂ buffer layer and Au surface layer

As shown above, the simulation objects consisted of an inner Silicon pillar overlaid with SiO₂ with an Au outer layer, the pillar tops are 'rounded' as shown in the GUI image below.

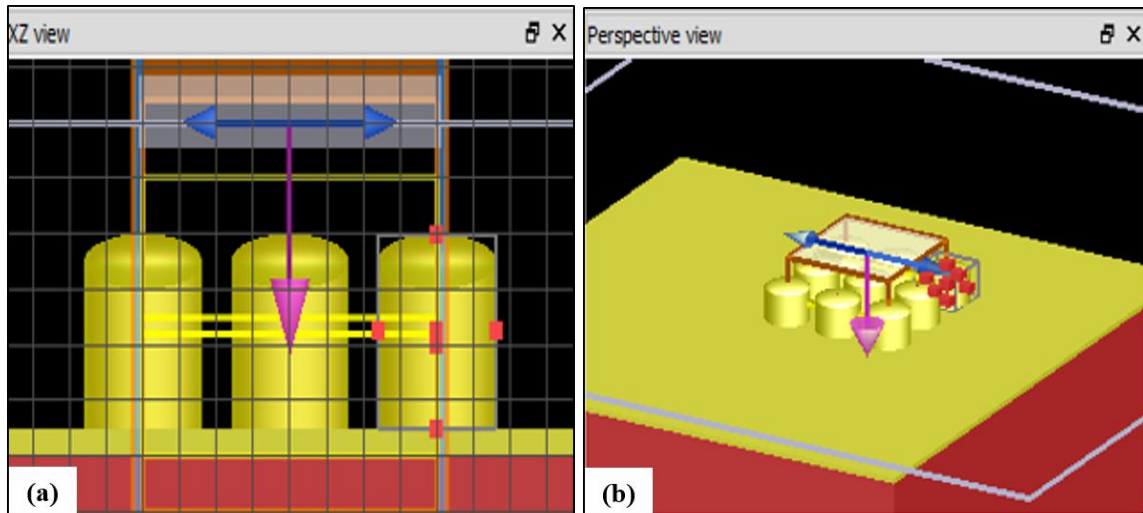


Figure 3.23 FDTD set up; SCIL substrates

(a) x, z view (b) perspective view. Plane wave source, propagation normal to x, y (downward) polarization along 'x'. Structure array and substrate base continue through FDTD simulation boundaries in x, y

3.2.2.5 FDTD analysis; Nanogap substrates

The dimensions used for simulation of the NIL Nanogap substrates are shown in Figure 3.21 above (i.e. height – 185-200 nm; diameter – 140 nm; nanogap ~ 70 nm)

The schematic shows a cross-section view of the features. The x, y view below shows that the 'raised' structures essentially resemble a rounded cross shaped feature.

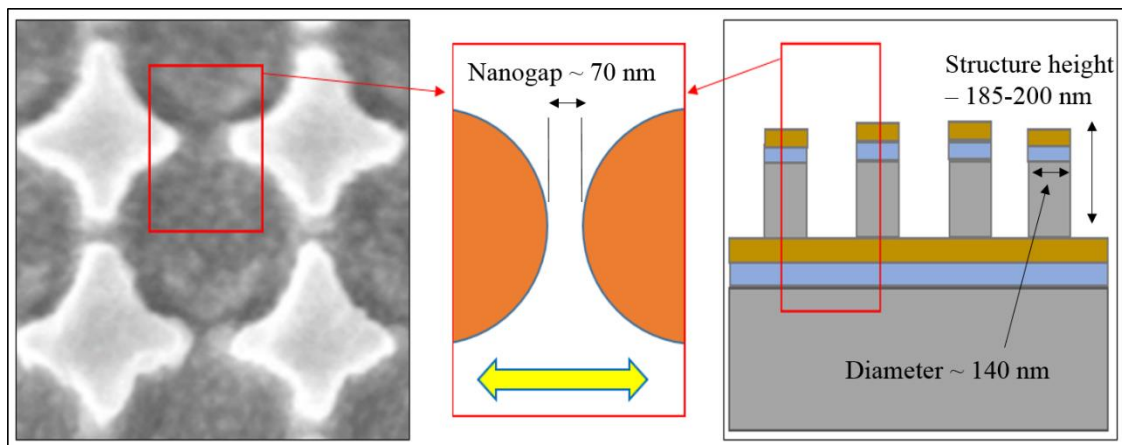


Figure 3.24 FDTD set up; NIL Nanogap substrates

SEM image; x, y view shows cross shaped raised structures and FDTD simulation region - left image. Schematic cross-section displays x, z FDTD region – right image. Zoom schematic (center image) shows view x, y for simulation objects required for FDTD analysis of 'hot spot' between adjacent cross edges, polarization (marked) along x. Plane wave source, propagation normal to x, y and downward

The hot spot regions occur at the edges of the cross-shape structures as shown in the zoom image above (lower left). The simulation set up is to simulate two pillars as shown in the lower left image, with incident polarization along 'x'.

3.2.3 Application – Biosensing

The sensitive measurement of protein concentration in this work utilises an indirect approach. The effect on the Raman linker spectra caused by changes to p53 and EGFR concentration are examined.

3.2.3.1 Substrate functionalisation

The procedure for functionalisation of the substrates is illustrated below in Figure 3.25.

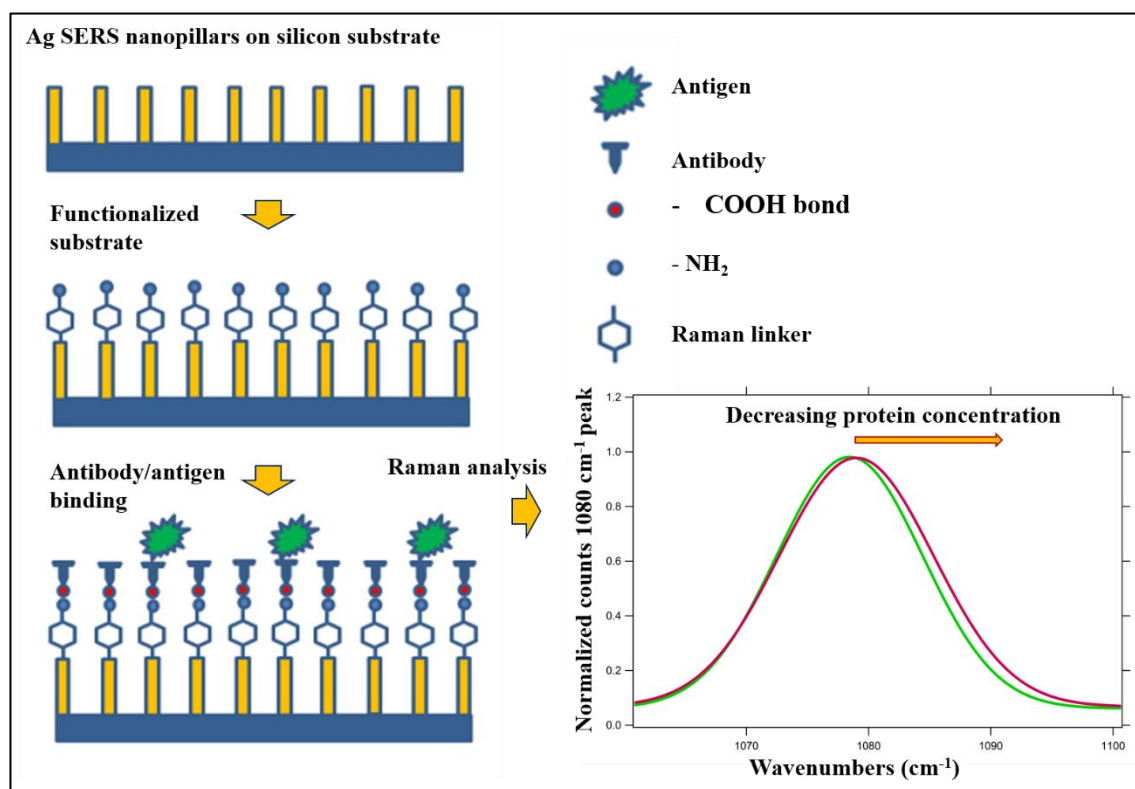


Figure 3.25 Schematic for substrate functionalization

Functionalization of Ag Nanopillar substrate, with covalently bound Raman linker and antibody. With increasing antigen concentration, observed shift in CS peak to higher wavenumbers with corresponding decrease in FWHM; lower right image.

As an initial cleaning step the Silmeco substrates were gently rinsed with the 100% pure Spectral Grade Ethanol.

For this and subsequent cleaning steps a clean plastic weighing boat was used. As liquid was carefully poured out of the boat, surface tension held the substrates to the boat surface, allowing safe removal of waste between rinses. Substrates were allowed to dry briefly in air after cleaning.

The cleaned substrates were then placed in a 25 mm glass beaker and incubated for a period of one hour in either 4-ATP or 6-MP. The top of the beaker was covered with parafilm to prevent evaporation during the incubation. Both linkers were prepared with Ethanol to 10 mM concentrations.

During incubation, the linker molecules covalently bonded to the substrate to form a monolayer. After one hour, substrates were removed and gently rinsed five times with Ethanol, to remove any unbound/excess linker molecules.

One substrate conjugated with the linker molecule only, was set aside at this point.

EDC and NHS solutions (171 mM & 427.5 mM respectively) were prepared separately in 0.01 M PBS. Next 20 μ l of anti-p53 was mixed with 0.5 ml (171 nM) EDC & 0.5 mM (427.5 mM) NHS and placed under vortex for 5 minutes.

The linker bonded substrates were then placed in a 25 mm glass beaker and incubated for two hours in the EDC/NHS/anti-p53 mixture.

After the two-hour incubation, the bioconjugated substrates were gently rinsed with PBS (0.01 M) in order to remove any unbound antibody solution.

A 10 mM Glycine solution was prepared separately in 0.01 M PBS. Then 1 ml of the Glycine was added to 9 ml EDC/NHS (50:50 by volume mixture).

The purpose of the EDC was to activate the carboxyl terminal on the surface of the antibody structure, while the NHS greatly improves the coupling efficiency of the reaction. It should be noted that the use of EDC/NHS to functionalize both 4-ATP & 6-MP for binding with antibodies is supported in the literature. The same protocol was used by Kho et al. to functionalize 4-ATP & 6-MP Raman linker molecules with the H1 & p53 biomarkers respectively [186]

In order to block (*stop*) the reaction, the substrates were left in a glass beaker in the Glycine activated EDC/NHS mixture overnight.

The next morning the substrates were then gently rinsed with PBS. One antibody bound substrate (i.e. substrate + Antibody) was set aside from the rest at this point.

A number of desired protein concentrations were prepared by serial dilution; 20 μ l of each protein concentration was placed on top of the substrate with a pipette and left to incubate for 1 hour. After 1 hour, the substrates were gently rinsed in PBS buffer to remove any excess unbound protein.

The functionalised substrates were placed on glass slides prepared with double sided tape and removed to the Raman lab for spectral measurements.

All incubation steps of the protocol were performed at room temperature.

3.2.3.2 Raman measurements

Raman measurements were performed using a WiTec Confocal Raman Spectrometer @ 785 nm excitation wavelength - using 600 & 1200 lines/mm gratings.

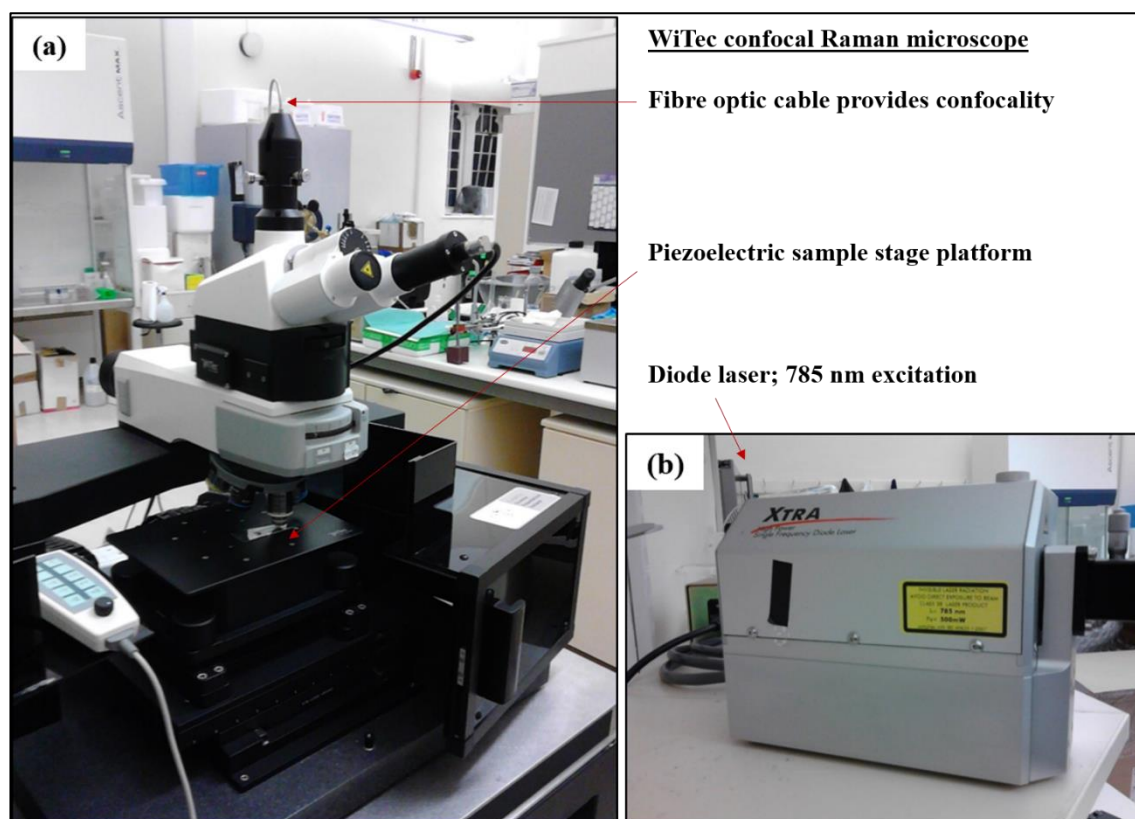


Figure 3.26 WiTec Confocal Raman Spectrometer

WiTec Confocal Raman Microscope & 'XTRA' 500 mW, 785 nm Diode Laser – providing narrow spectral linewidth (typically < 10 MHz)

Spectra were collected using an Andor Ixus cooled charge coupled device (-60°C) with a 100x objective lens to deliver the laser beam and collect the back-scattered light. Rayleigh scattering was blocked with the appropriate notch filter. The laser spot diameter was $\sim 1\ \mu\text{m}$ with a laser power of 0.05 mW. The Instrument calibration was verified using the maximum signal from a silicon standard at $520\ \text{cm}^{-1}$.

Measurements were performed using a 25-point area scan over a $10 \times 10\ \mu\text{m}$ region of interest using a 1 second acquisition time. We expect that, post-functionalisation, the substrate surface, will comprise both free linker and protein-bound linker molecules. The average spectra from the area scan, will yield an average response of these free linker and protein-bound linker molecules.

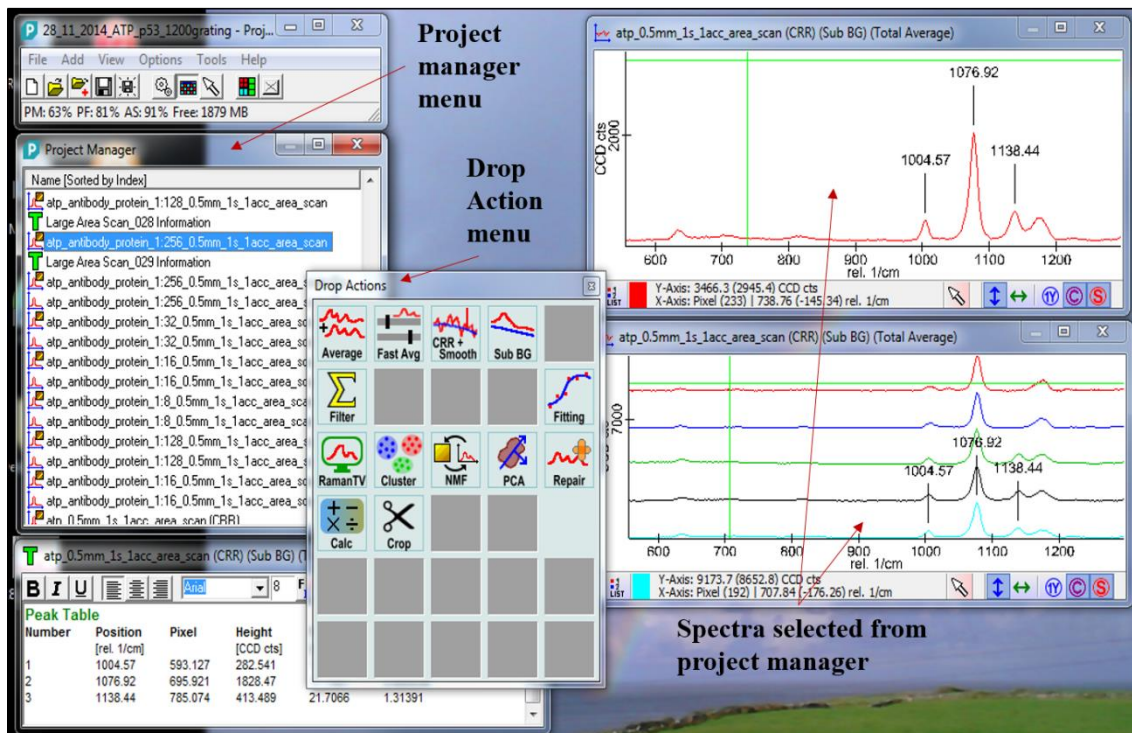


Figure 3.27 WiTec Project 4.0 software; screen shot of GUI

Spectral data from the Project manager window processed via the drop action menu option (inset); Project manager used to select single or group spectra prior to exporting data sets.

Spectral data was processed using the WiTec Project 4.0 software. The process flow for the 25-point area scan was as follows. First to apply Background subtraction then Cosmic ray removal followed by total average of the 25 spectra data set. Further processing was performed in Excel and Igor Pro 5.0B software, i.e. Normalisation to peak of interest and Gaussian curve fitting.

4 Results 1 - Evaluation of Platform-based SERS substrates

Characterization of the platform-based SERS substrates was carried out by measuring the Raman signal intensity from the substrates, after functionalization with a 10 μ M solution of 2-Napthalenethiol (2-NT). SEM and FDTD analysis was then carried out to correlate substrate surface features with SERS performance.

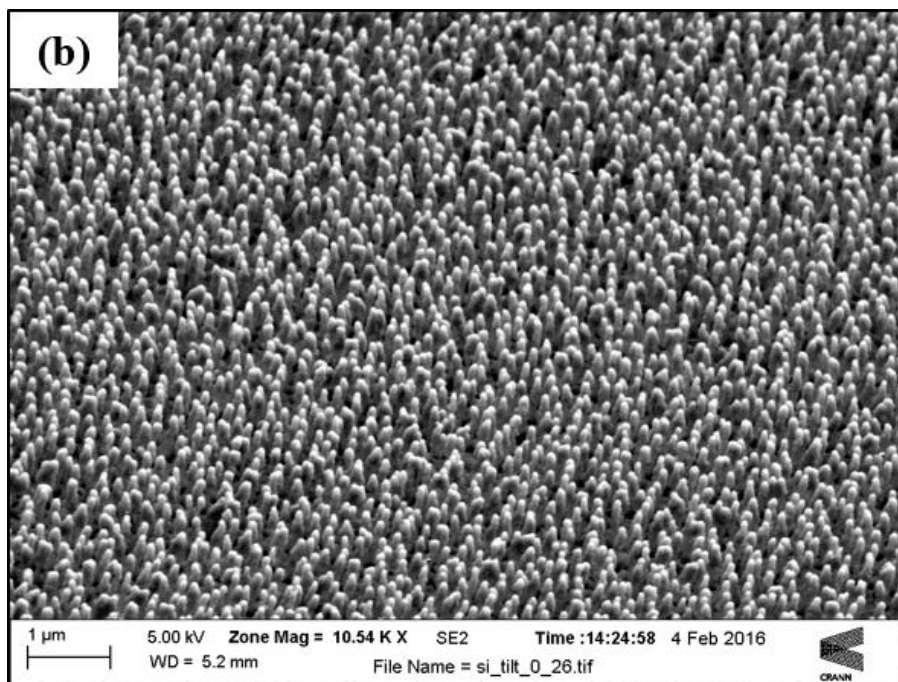
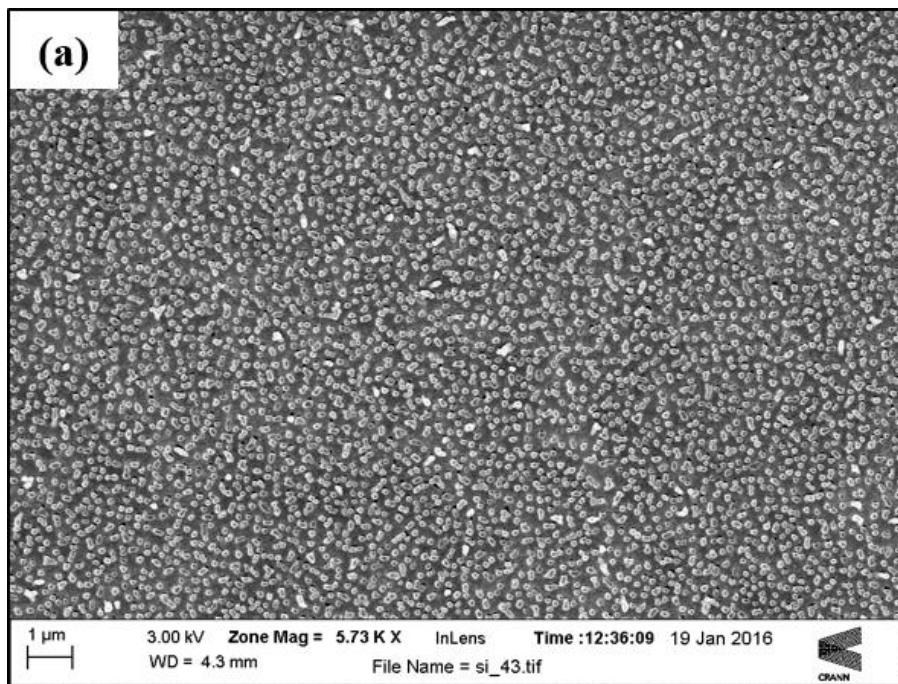
4.1 SEM characterization

SEM imaging of the commercial substrates was carried out at the CRANN Advanced Microscopy Lab (AML), Dublin. The SEM system was fitted with the following detectors:

A high efficiency **In-Lens** detector is utilised for detecting Secondary Electrons (SE) directly in the beam path for surface imaging. The **SE2** detector is used to detect both SE's and Back Scattered Electrons (BSE). This allows for greater penetration depth and gives a more distinct topography of the sample. The other detector is the Energy Selective Backscattered (**ESB**) detector, and is used primarily to detect BSE's and give a material composition image. Heavier atoms appear brighter on this contrast image.

Images for the following platform-based substrates are shown below: Silmeco (Ag), Integrated Optics (Ag), Horiba and anSERS.

Silmeco Ag Nanopillar substrates



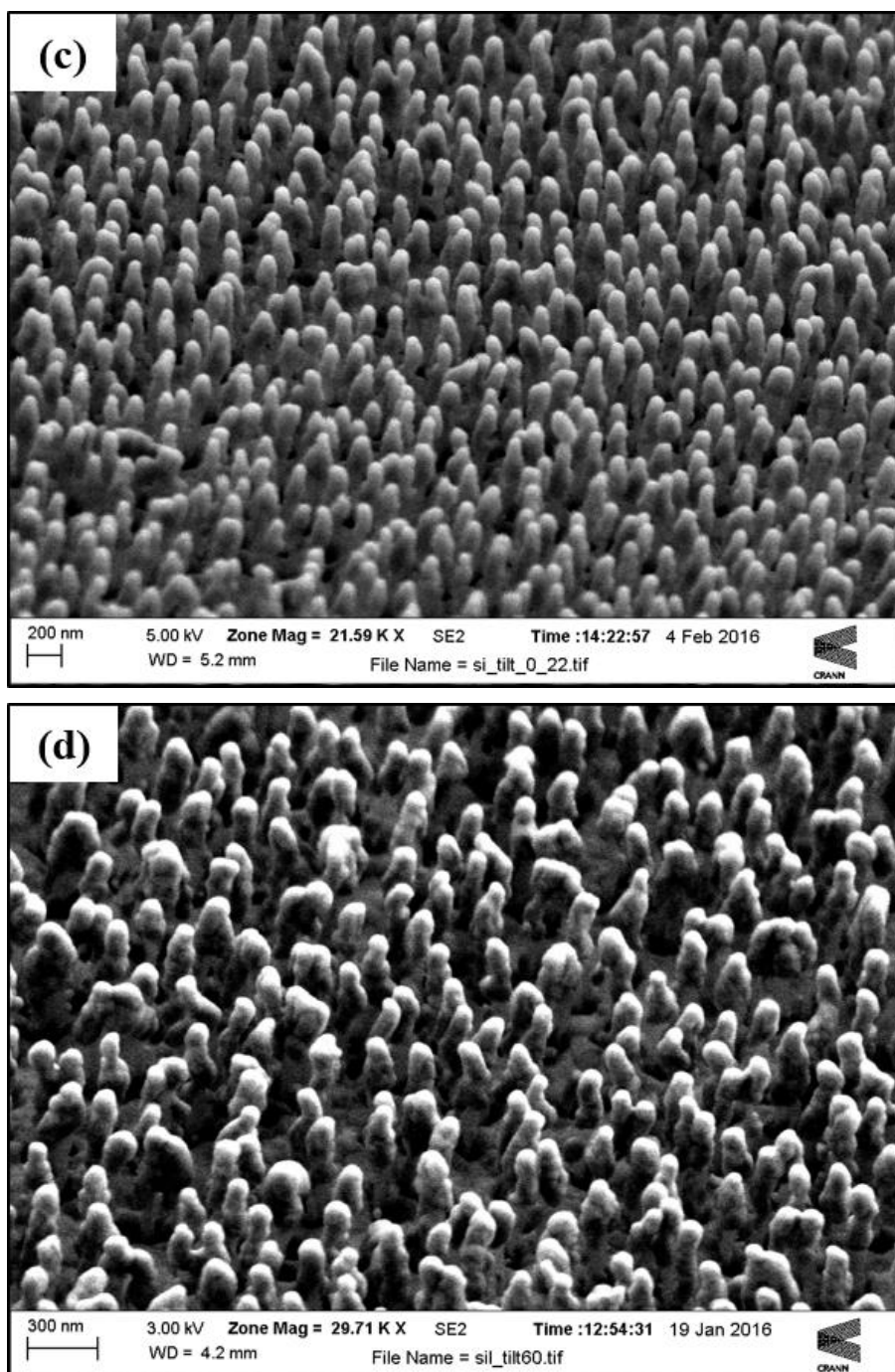
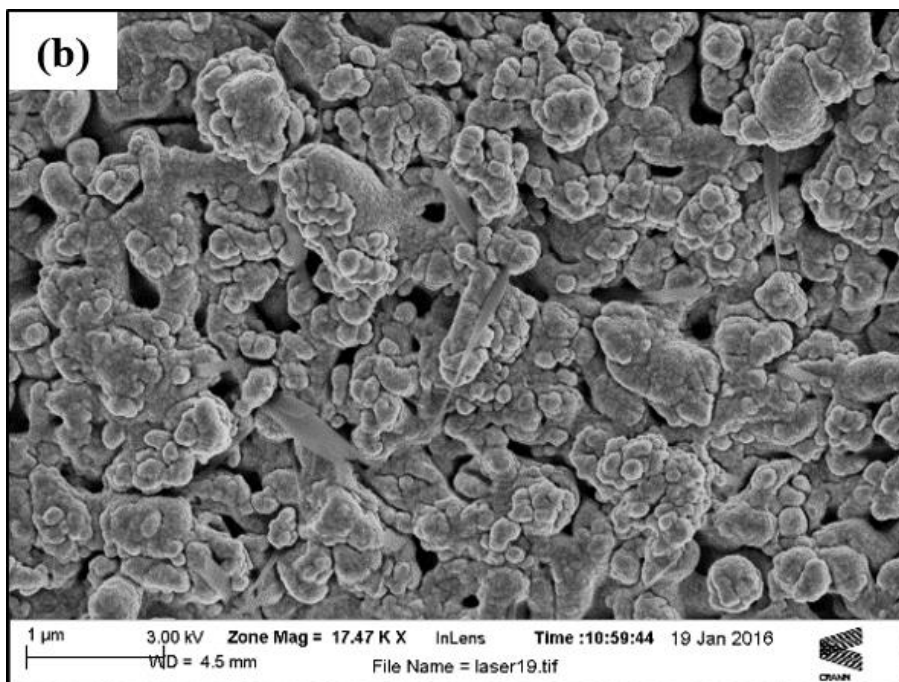
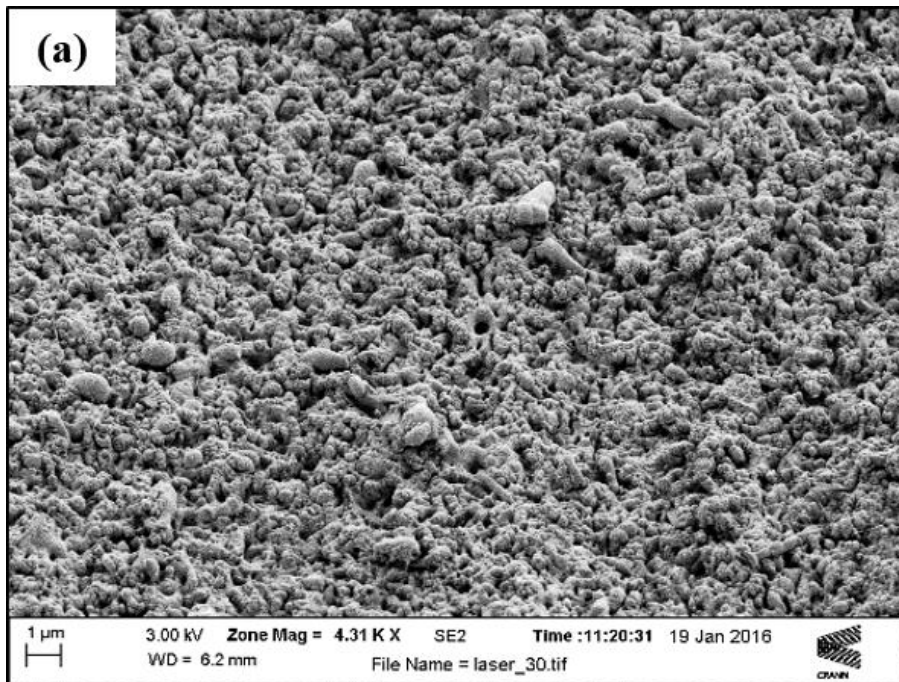


Figure 4.1 SEM's - Silmeco Ag Nanopillar substrates

(a) InLens surface view of nanopillars; Magnification 5.73 KX, 1 μ m scale bar (b) SE2 detector; Magnification 10.54 KX; 1 μ m scale bar; (c) SE2; Magnification 21.59 KX; 200 nm scale bar (d) SE2; Magnification 29.71 KX; 300 nm scale bar. Acceleration voltages: (a) to (c) 5 KV & (d) 3 KV

The nanopillars are fabricated to have a high aspect ratio, and have a tendency to 'lean in' towards adjacent pillars, creating nanogaps of < 4 nm. When a liquid analyte is deposited onto the substrate surface, this leaning effect becomes more pronounced. However, some leaning of nanopillars is visible in (d) from a pristine substrate.

Integrated Optics; laser fabricated substrates



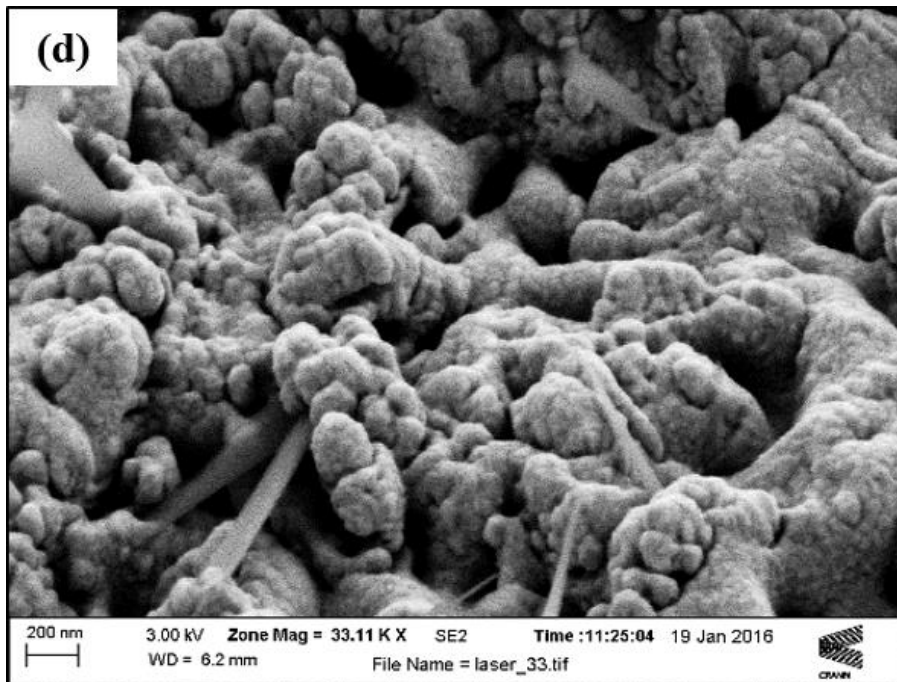
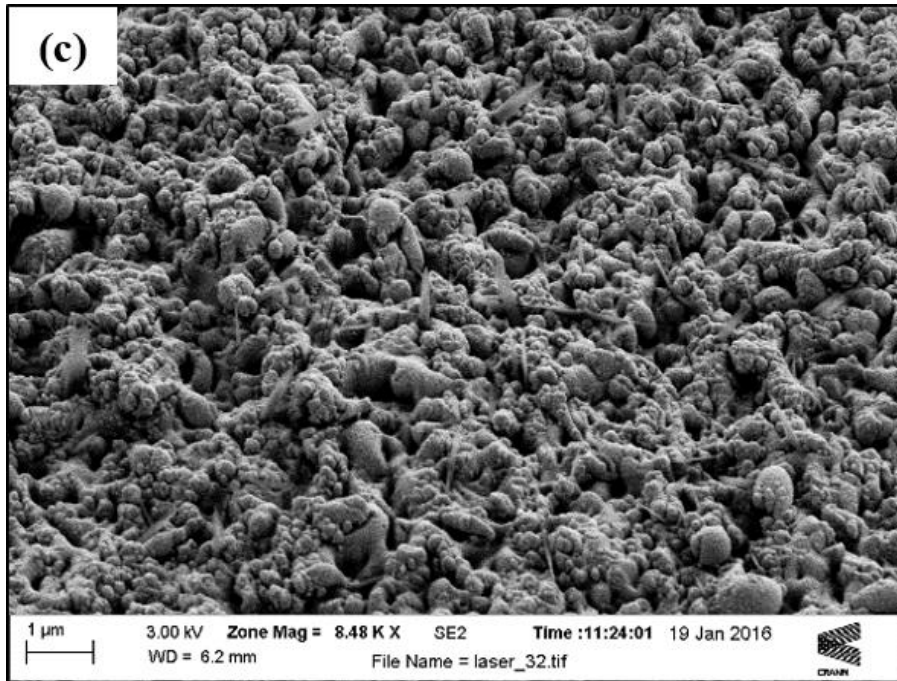
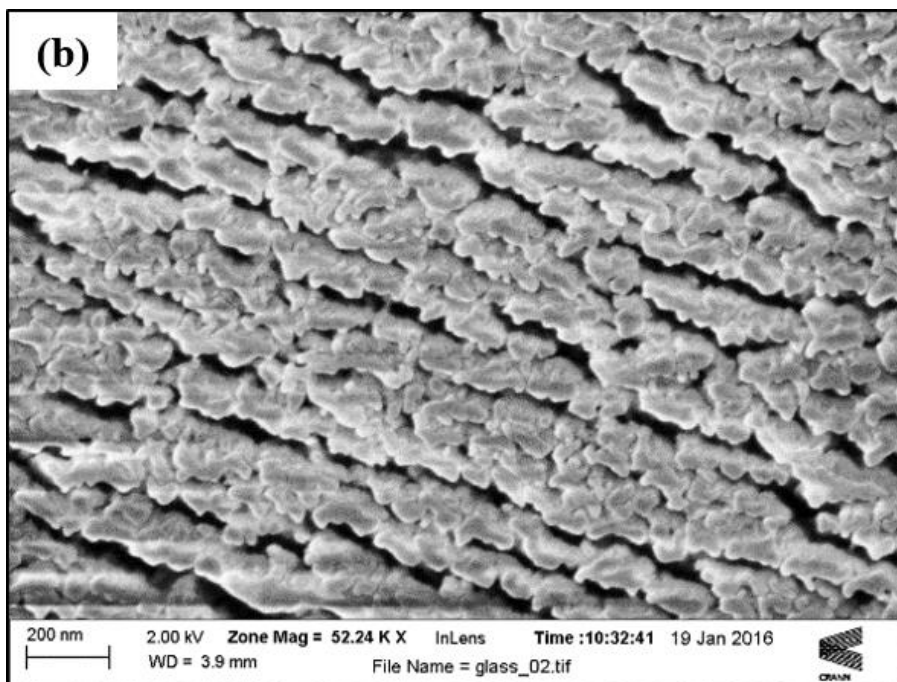
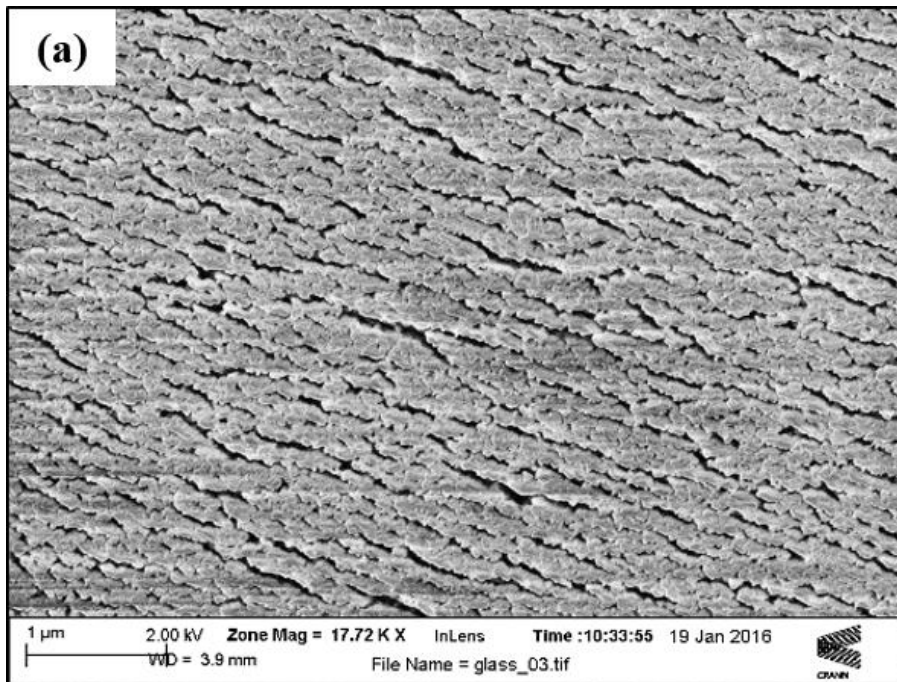


Figure 4.2 SEM's - Integrated Optics Ag laser fabricated substrates

(a) SE2; Magnification 4.31 KX; 1 μm scale bar (b) InLens view of surface features; Magnification 17.47 KX; 1 μm scale bar (c) SE2; Magnification 8.48 KX; 1 μm scale bar (d) SE2 zoom of amorphous features; Magnification 33.11 KX; 200 nm scale bar. Acceleration voltages (ALL) 3 kV

The substrates shown in Figure 4.2 clearly show the amorphous nature of the laser fabricated substrates, produced via short pulsed lasers at ablation threshold. The higher mag image in (d) shows the random nature of the surface features.

Horiba Au Nanorod substrates



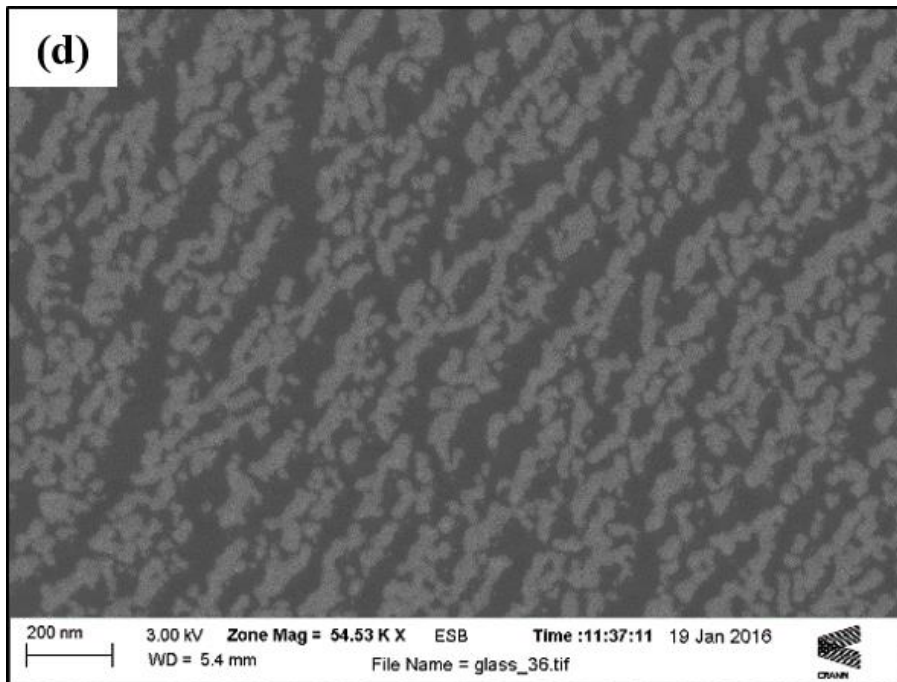
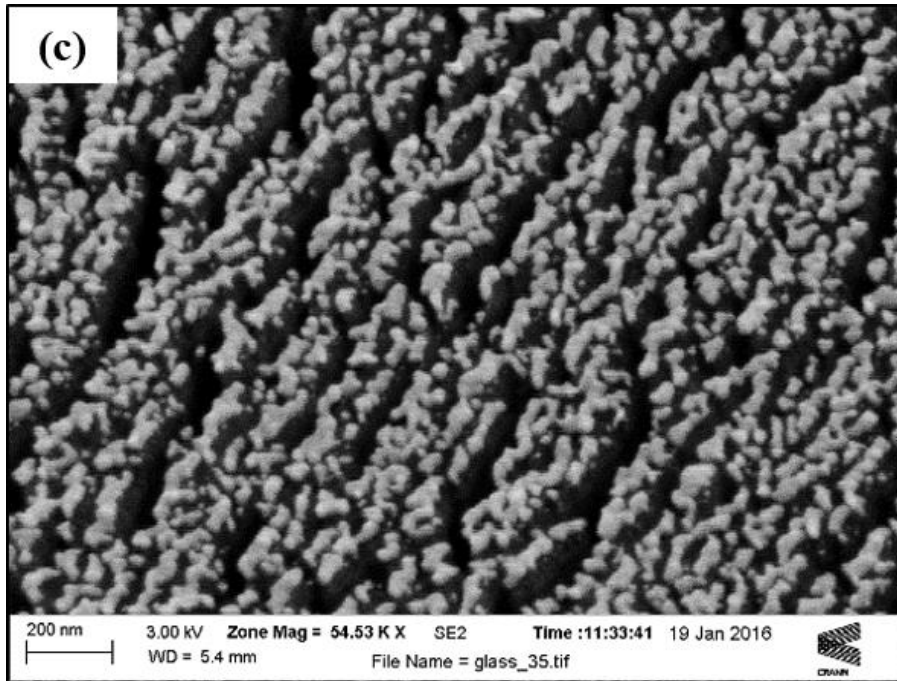
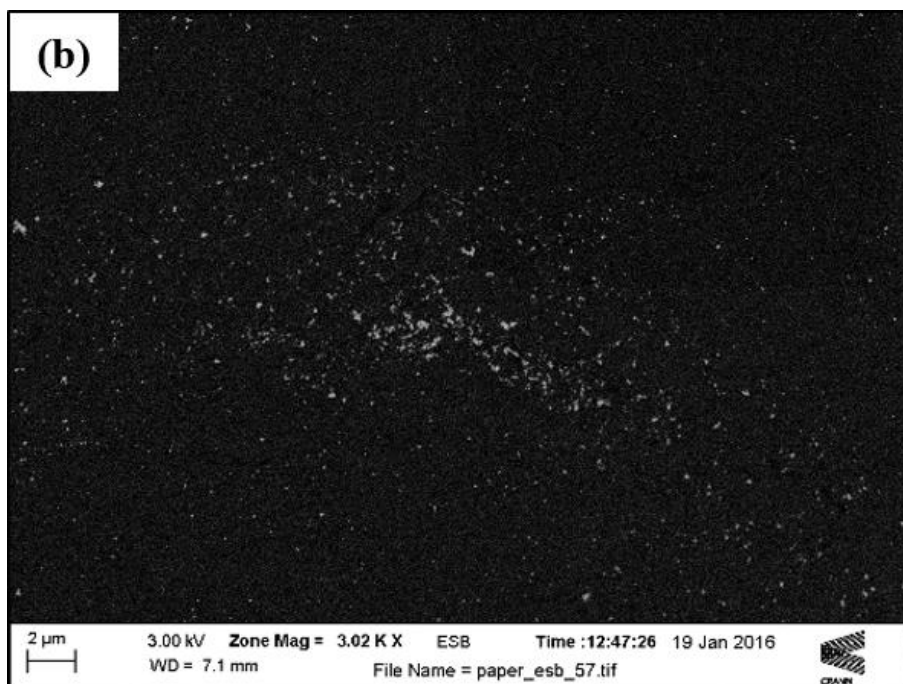
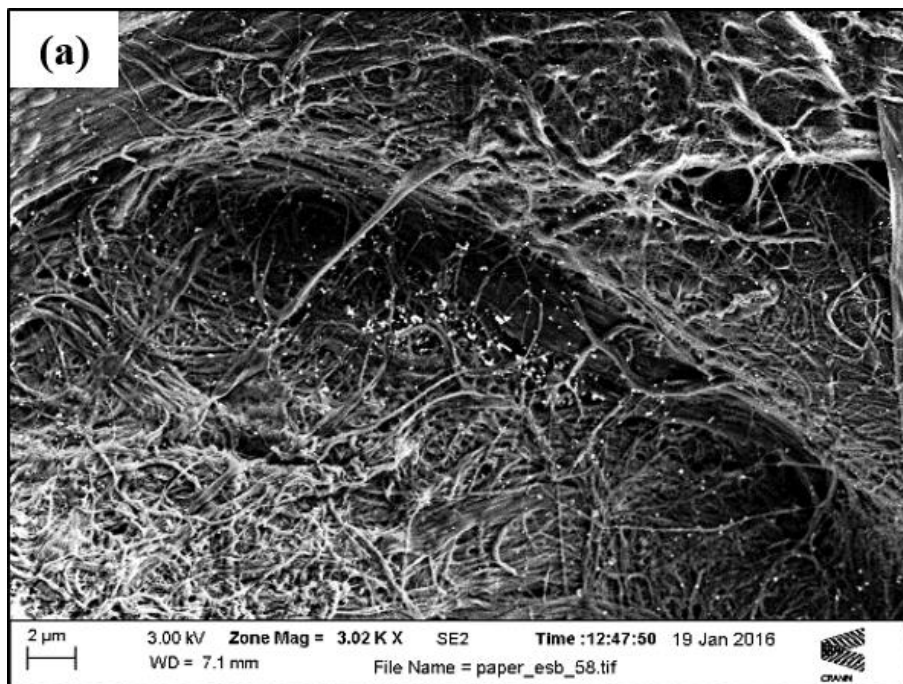


Figure 4.3 SEM's - Horiba Au nanorod substrates

(a) InLens; Magnification 17.72 KX; 1 μ m scale bar (b) InLens; Magnification 52.24 KX; 200 nm scale bar (c) SE2; Magnification 54.53 KX; 200 nm scale bar (d) ESB; Magnification 54.53 KX; 200 nm scale bar. Acceleration voltages (a) & (b) 2 kV (c) & (d) 3 kV.

In Figure 4.3 (a) and (b), the anisotropic nature of the nanorods produced by ‘shadowed’ deposition can be clearly seen. The SE2 image in (c) shows the ‘gaps’ between rods with a clearer sense of the topography. While the backscattered electron image in (d) at the same mag, shows the Au outer layer present on upper layer of the nanorods; the heavier Au atoms appears brighter.

Diagnostic anSERS inkjet printed substrates



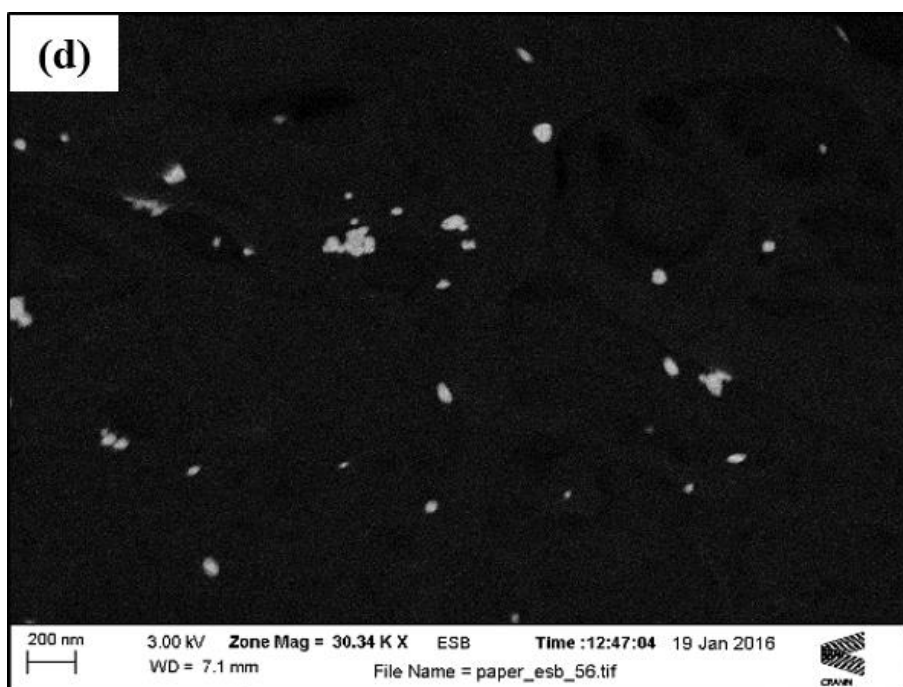
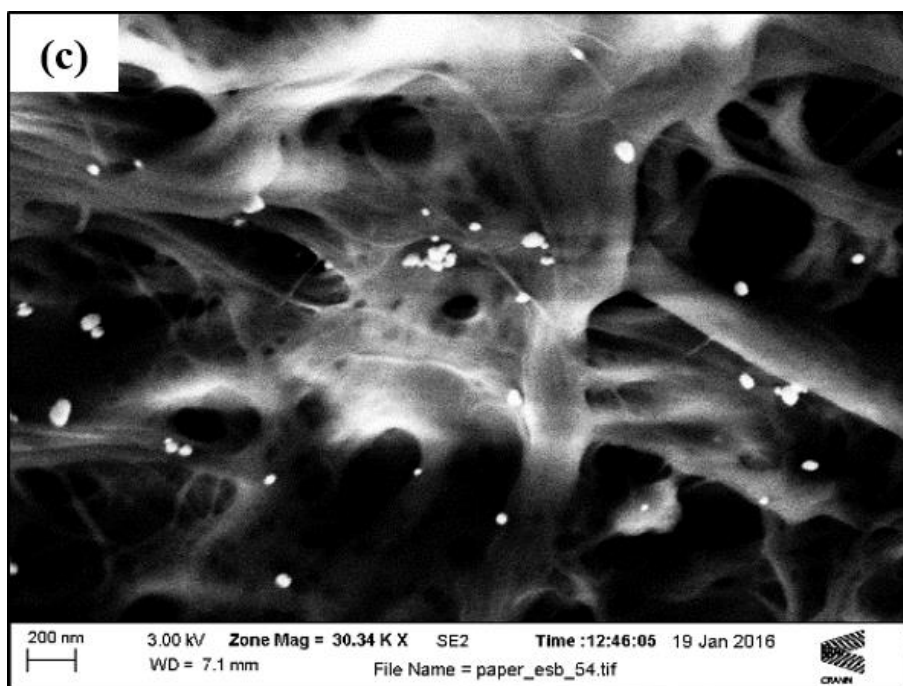


Figure 4.4 SEM's – Diagnostic anSERS Au MNP inkjet printed substrates

(a) SE2; Au MNP's embedded in cellulose paper; Magnification 3.02 KX; 2 μ m scale bar (b) ESB; Magnification 3.02 KX; 2 μ m scale bar (c) SE2 zoom; Magnification 30.34 KX; 200 nm scale bar (d) ESB zoom; Magnification 30.34 KX; 200 nm scale bar. Acceleration voltages (ALL) 3 kV

The SEM's of Figure 4.4 show the inkjet substrates with the MNP's embedded into cellulose chromatographic paper. The clustering of Au MNP's is clearly visible; aggregated via repeated printing to increase MNP density and reduce particle spacing. In the ESB images of (b) & (d) the heavier Au atoms appear brighter than the background of the paper substrate.

4.2 Raman analysis

The 2-NT Raman Spectra has dominant peaks at 1066 & 1380 cm^{-1} . The 1066 peak results from the symmetric C-H bending vibration, while the 1380 peak cm^{-1} corresponds to a stretching of the hydrocarbon ring. The relative response of these two peaks, for each substrate type was examined. The Raman microscope parameters were maintained at the same values for each substrate type and each experiment.

Three substrates of each type were tested. Spectral acquisitions were recorded at 10 random locations across each substrate at a minimum separation of 10 μM to avoid oversampling. Maximum CCD counts, and relative standard deviation for the peak of interest were obtained, and displayed in Table 4.1 below.

Table 4.1 Mean Raman intensity & Relative deviation; all substrates

Relative standard deviation (RSD) is given for the mean signal deviation across three substrates tested for each substrate type. RSD calculated as per Equation 8.1

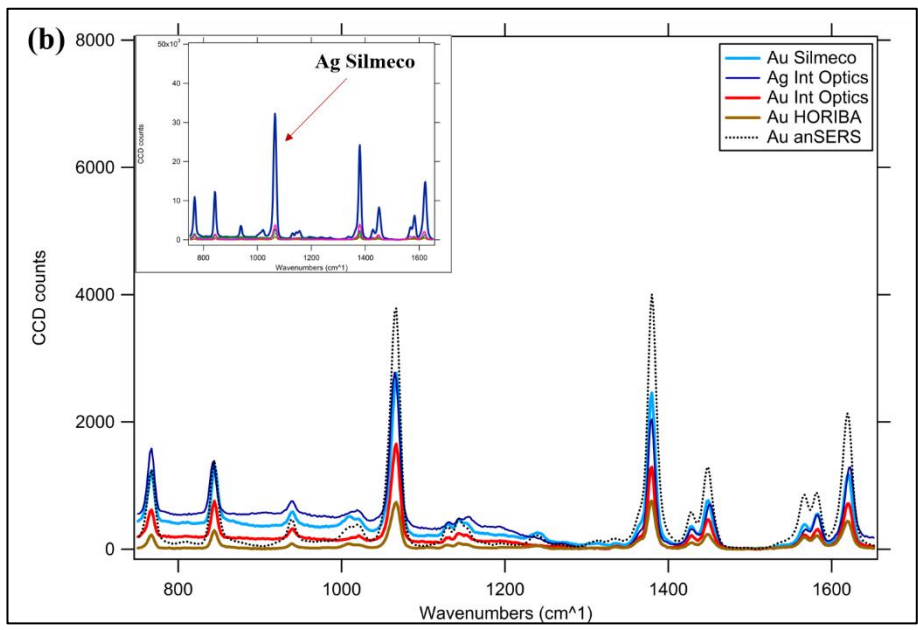
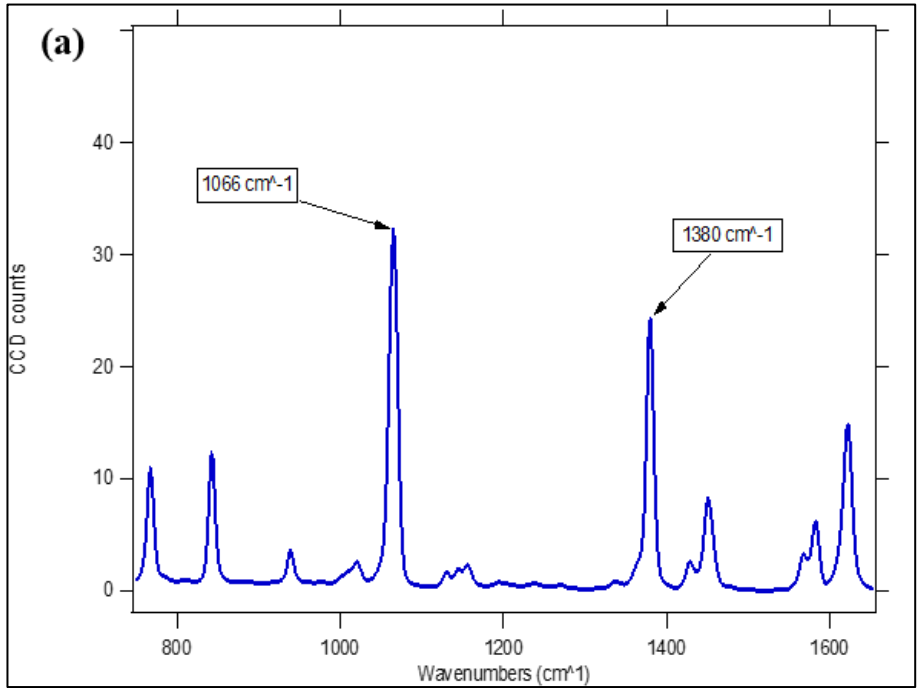
Substrate	CCD counts 1066 cm^{-1} peak	Relative deviation (%)	CCD counts 1380 cm^{-1} peak	Relative deviation (%)
<i>Silmeco Ag</i>	32252.90	17.2	24653.8	17.1
<i>Silmeco Au</i>	2767.69	16.6	2574.48	16.7
<i>Integrated Optics Ag</i>	2775.49	16.4	2042.57	17.8
<i>Integrated Optics Au</i>	1651.92	19.0	1327.78	16
<i>Horiba scientific Au</i>	737.27	20.4	782.851	19.6
<i>Diagnostic anSERS Au</i>	3785.70	49.4	4051.85	50.6

The RSD values for Raman signal intensity in Table 4.1 are the mean values across three substrates tested; i.e. the mean of 30 spectra across all substrates (10/substrate). In order to give a ‘sense’ of the variation between the substrates the intra-substrate deviation is given below in Table 4.2.

Table 4.2 Intra-substrate deviation of spot to spot Raman signal intensity

*Deviation of Raman signal from substrate to substrate, calculated from the difference of individual substrate RSD values to mean RSD of all three substrates (note: * Integrated Optics Au – only two substrates tested)*

	1066 cm⁻¹				
Substrate	1	2	3	RSD all substrates (%)	Intra-substrate deviation (%)
<i>Silmeco Ag</i>	7.88	14.89	28.92	17.2	7.8
<i>Silmeco Au</i>	20.46	18.1	11.23	16.6	3.6
<i>Integrated Optics Ag</i>	18.09	18.72	12.39	16.4	2.7
<i>Integrated Optics Au</i>	18.79	19.22	*	19.0	6.3
<i>Horiba scientific Au</i>	19.23	24.68	17.37	20.4	2.0
<i>Diagnostic anSERS Au</i>	47.1	48.17	52.89	49.4	2.3
	1380 cm⁻¹				
<i>Silmeco Ag</i>	10.95	12.41	27.98	17.1	7.2
<i>Silmeco Au</i>	17.66	20.82	11.72	16.7	3.3
<i>Integrated Optics Ag</i>	19.71	18.15	15.53	17.8	1.5
<i>Integrated Optics Au</i>	15.05	16.88	*	16	0.9
<i>Horiba scientific Au</i>	18.05	24.73	16.16	19.6	3.4
<i>Diagnostic anSERS Au</i>	47.44	48.19	56.19	50.6	3.7



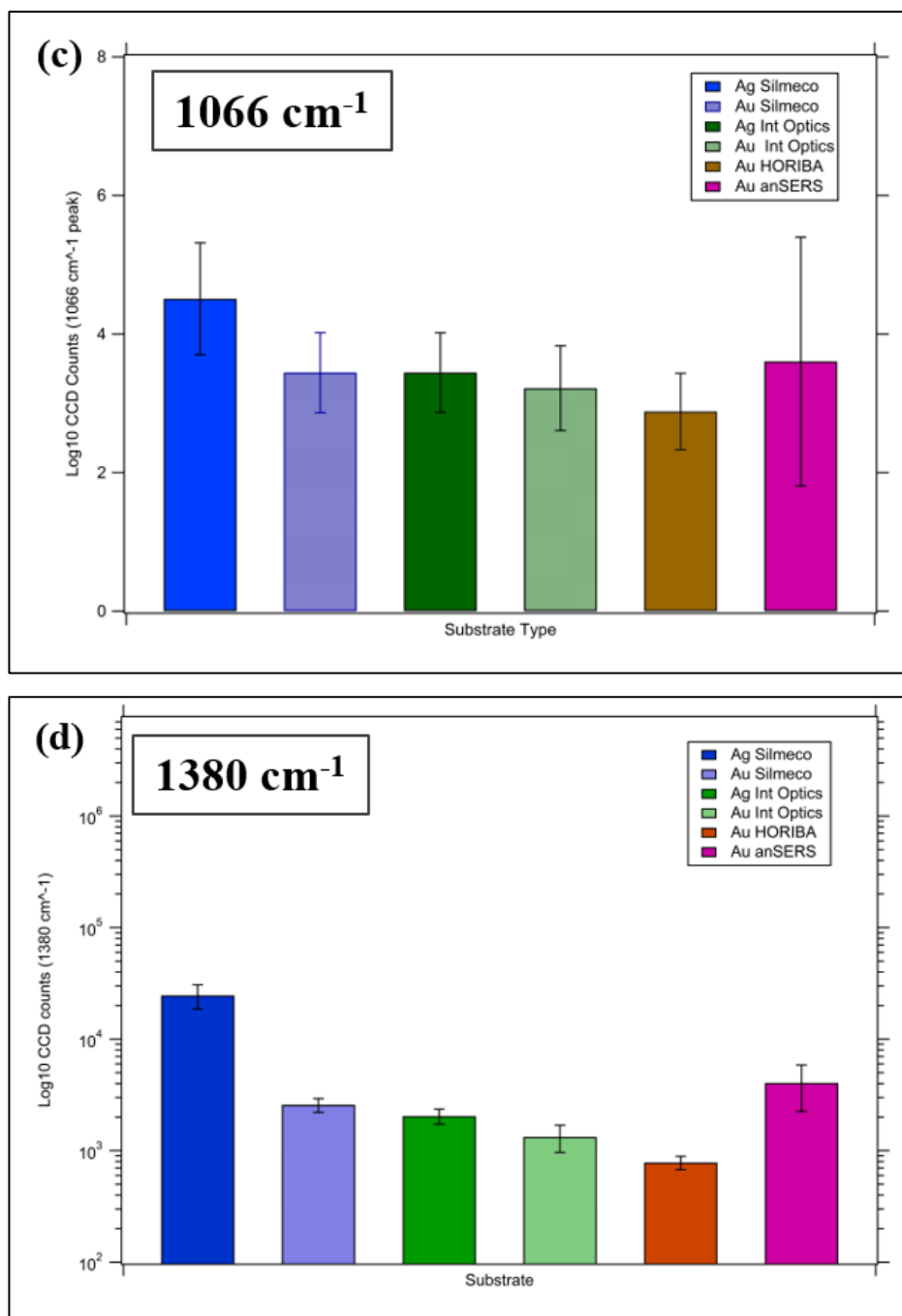
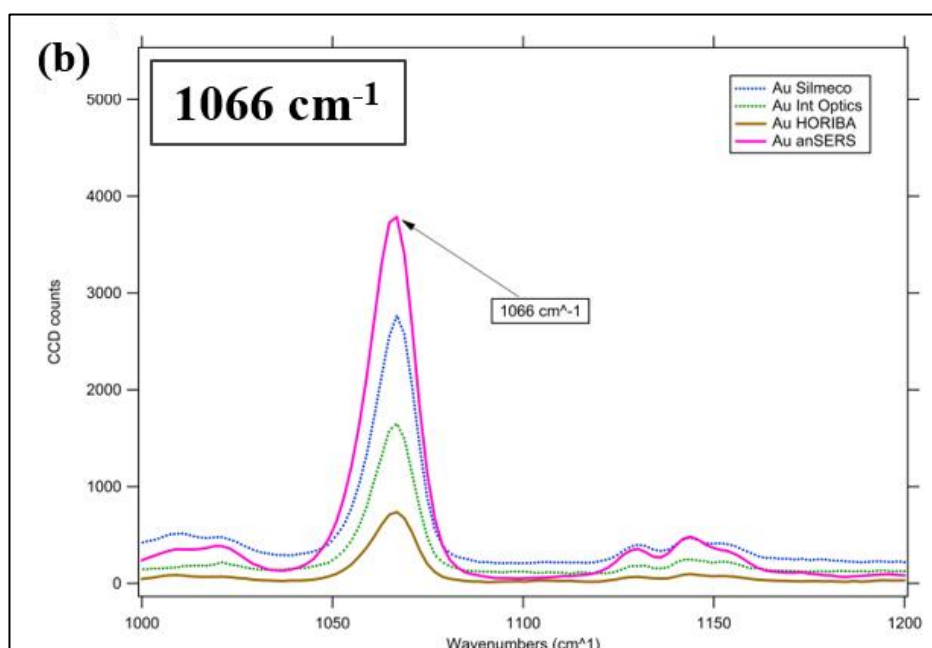
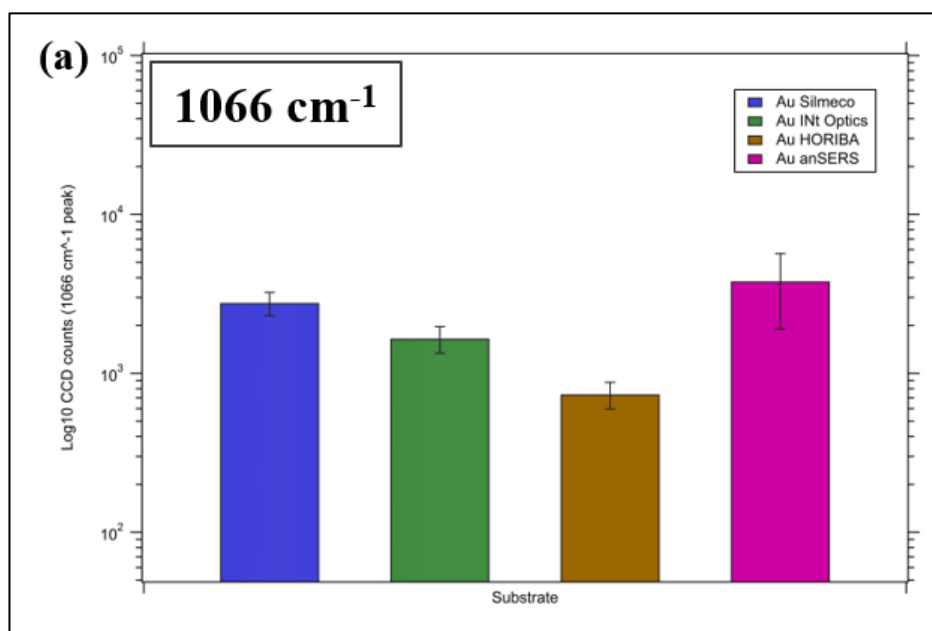


Figure 4.5 Raman characterisation; substrates functionalised with 2-Naphthalenethiol
 (a) 2-NT single spectra; 1066 & 1380 cm⁻¹ peaks labelled (b) 2-NT spectra; Inset ALL substrates with Ag Silmeco labelled. Main image, spectra from all other substrates. (c) & (d) Semi-log plots of max CCD counts at both peaks. Error bars – relative standard deviation across three substrates of type. Raman parameters (all): Laser excitation 785 nm, 0.006 mW power, 50x objective and 600 lines/mm grating.

A single spectrum from an Ag Silmeco substrate functionalised with 2-NT is shown in Figure 4.5 (a) with the prominent Raman peaks at 1066 and 1380 cm⁻¹ labelled. Both peaks are narrow and clearly defined with a high signal to noise ratio. The 2-NT spectra from all the substrates are plotted together in image (b) in the inset plot and all other spectra in the main image for visual purposes.

The SERS performance of the Ag Silmeco substrate is far superior to the others, making it difficult to distinguish the other spectra from the plot. For visual purposes a semi-log plot is used to accommodate the large difference in signal intensity (c) and (d). The anSERS inkjet substrate is the next most SERS efficient, with the C-H bending peak at 1066 cm^{-1} the most responsive in both cases.

The relative performance for the Au substrates is shown below. The anSERS inkjet substrate exhibiting the largest SERS response. The Au anSERS substrate yields a greater SERS enhancement than the Ag Integrated Optics unit (Figure 4.5 above) even though for the same substrate type Ag would give a greater SERS response than Au.



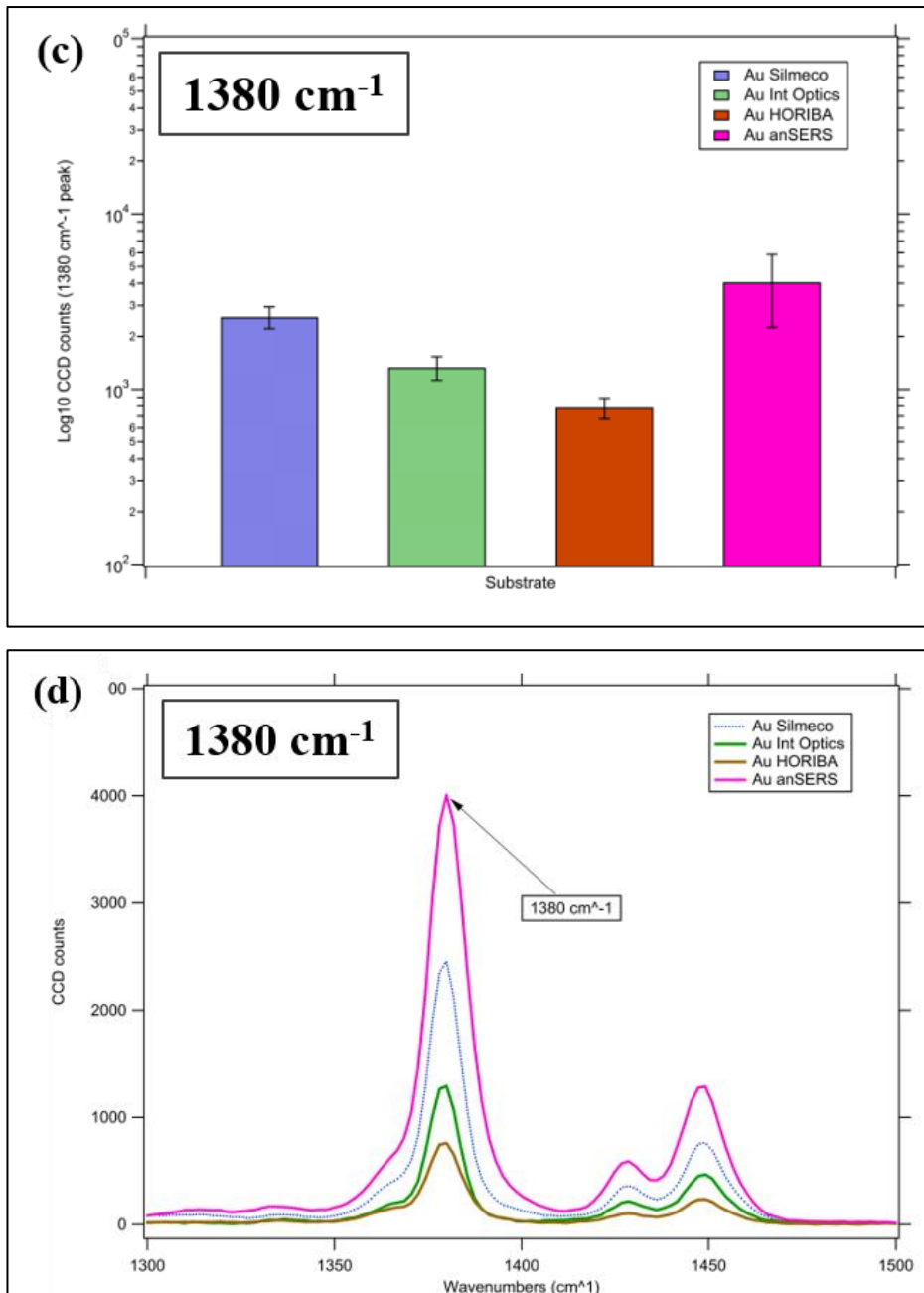
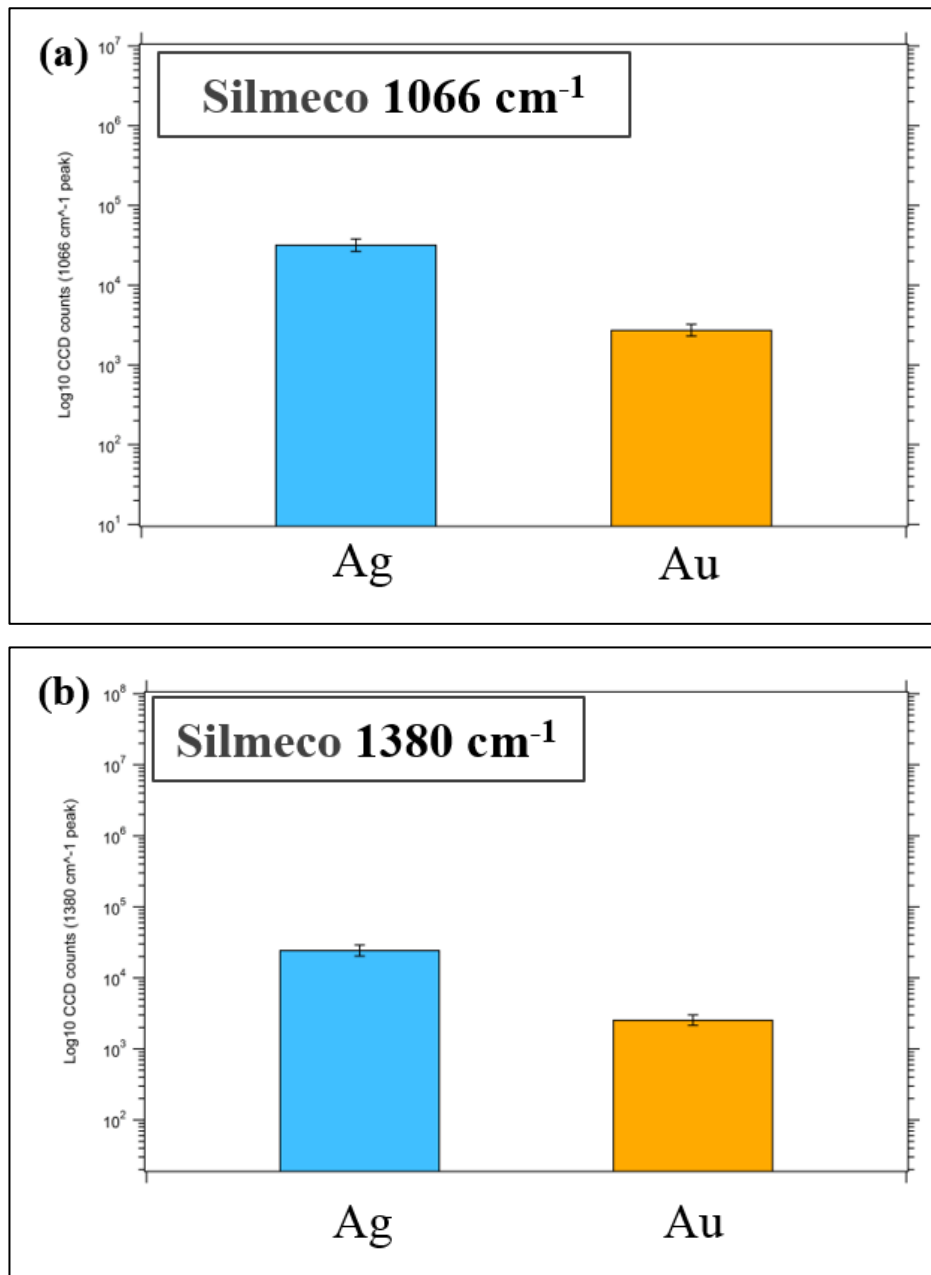


Figure 4.6 Raman comparison; Au substrates functionalised with 2-NT

The four Au substrates are compared for maximum CCD counts at both 1066 & 1380 cm⁻¹ peaks (a) & (c) Semi-Log plots of maximum intensity; error bars – relative standard deviation. (b) & (d) zoom of individual peaks. Raman parameters: Laser excitation 785 nm & 0.006 mW power, 50x objective and 600 lines/mm grating.

A comparison for Ag and Au surface layers for the same substrate type is shown in Figure 4.7 below for both the Silmecco and Integrated Optics substrates. Again, data sets for both the 1066 and 1380 cm^{-1} peaks are presented.



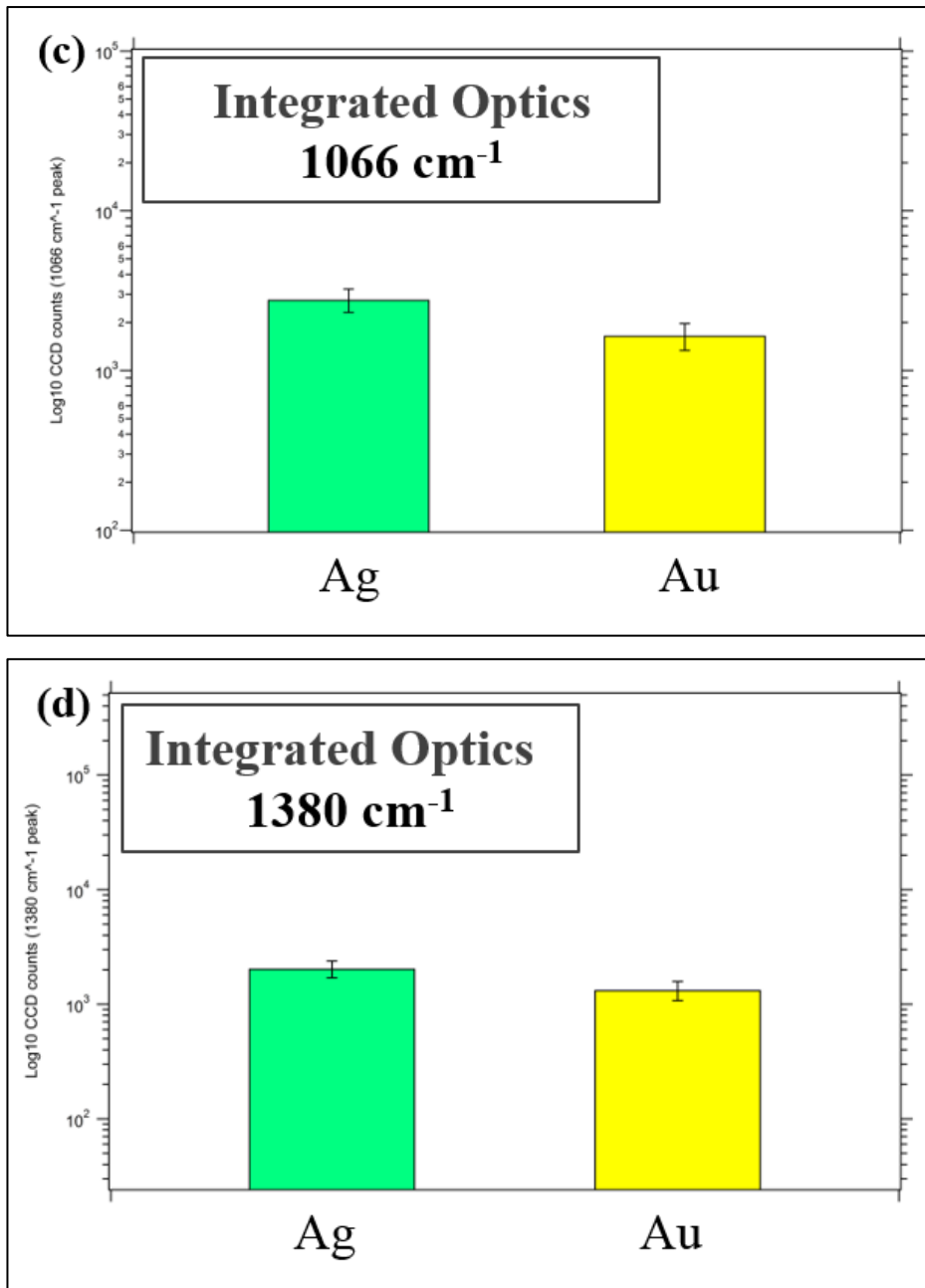


Figure 4.7 Comparison of Au & Ag surface layers

Comparison of Ag & Au surface layers at 1066 & 1380 cm⁻¹. Silmeco substrates (a) & (b) Integrated Optics (c) & (d). Raman parameters: Laser excitation 785 nm, 0.006 mW power, 50x objective and 600 lines/mm grating. Error bars – relative standard deviation.

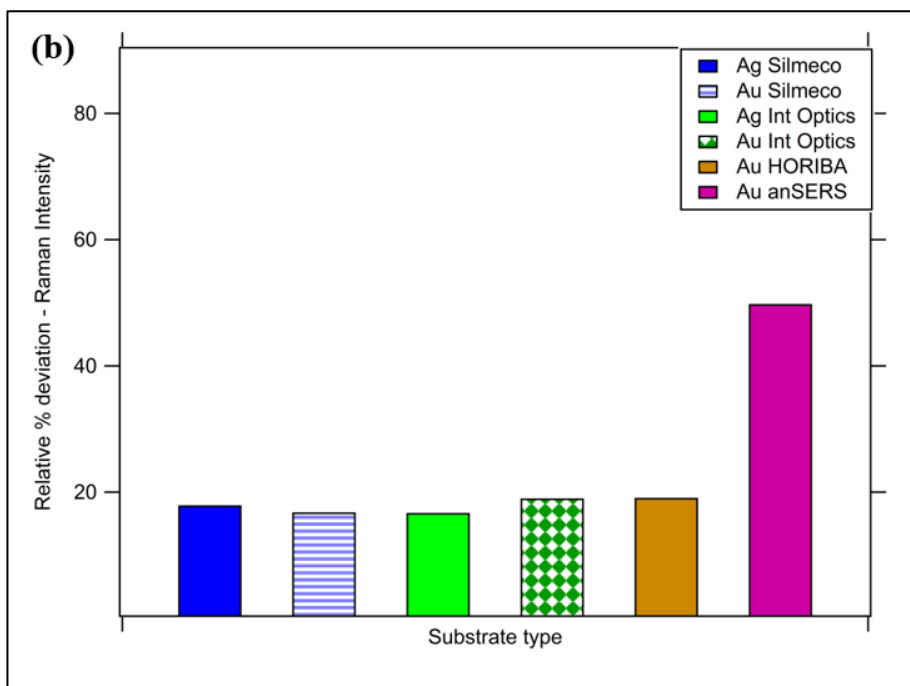
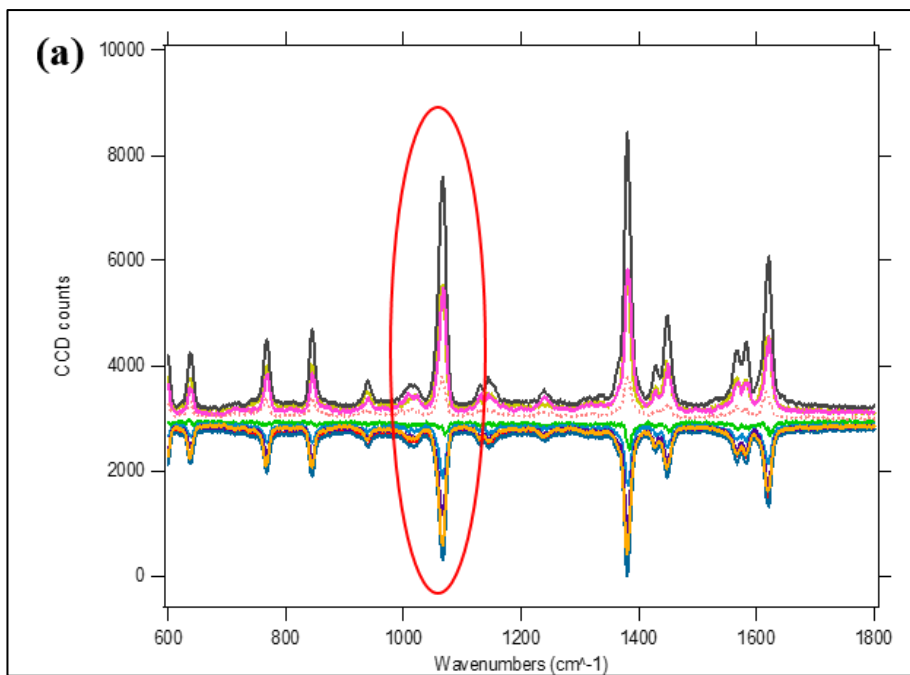
For the same substrate types and at both Raman peaks, the Ag outer layer gives a greater SERS response than the Au coating. This accords with established theoretical and experimental expectations.

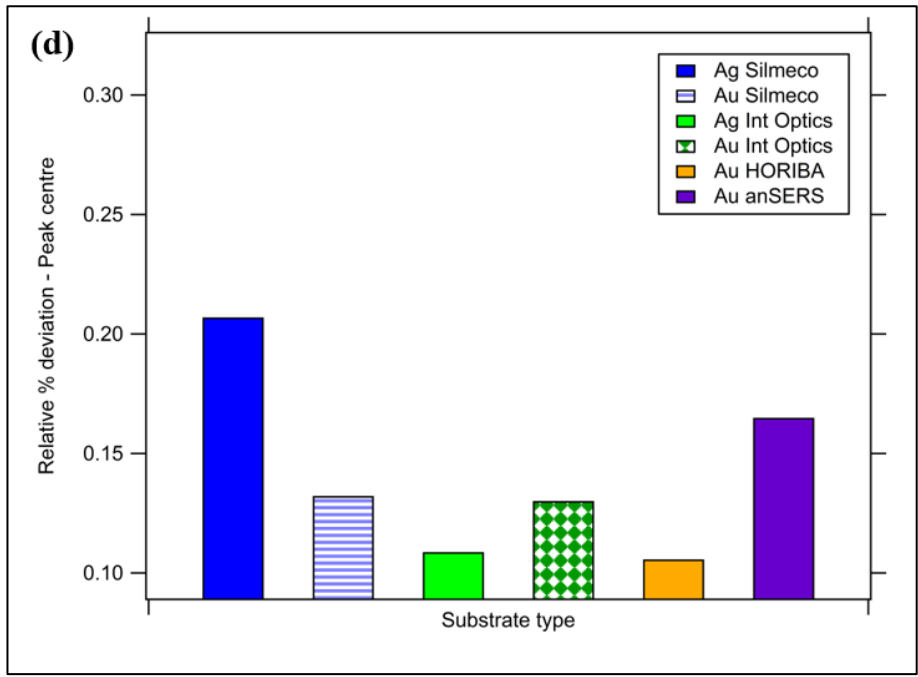
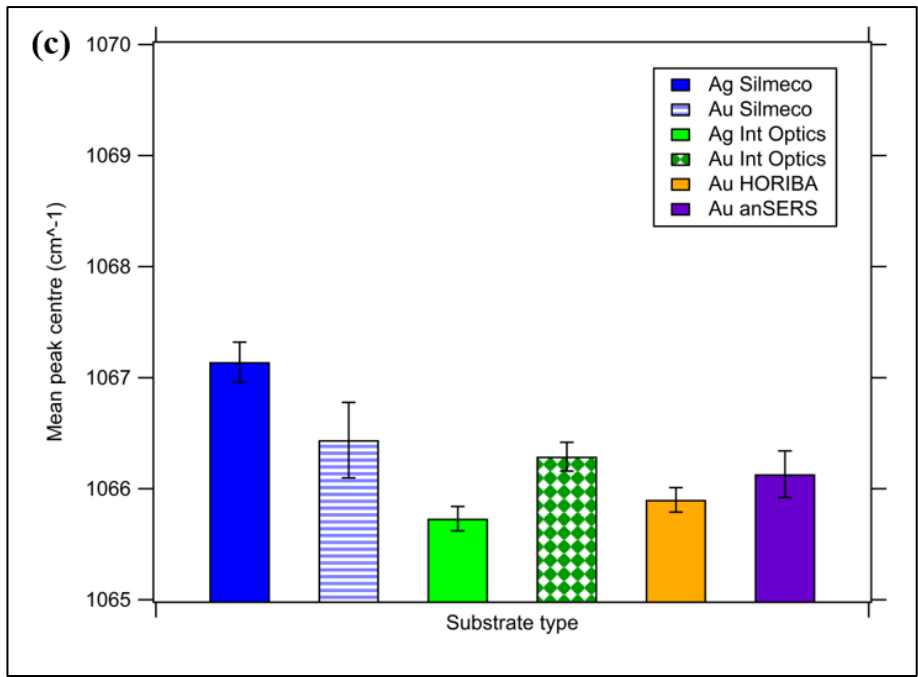
As can be seen from the above plots, the inkjet substrate generated the second largest Raman signal. However, it also demonstrated the largest deviation of Raman intensity, across its SERS active region. The high signal deviation, arises from the random nature of MNP aggregation. This highlights another important consideration regarding the performance of SERS substrates, namely the consistency and reproducibility of SERS intensity over the active area of a substrate.

In tandem with the enhancement of a signal, its spot to spot consistency is another important performance parameter for most techniques and applications. It is often the case that substrates producing a large SERS response will also have a large spot to spot signal deviation.

SERS is multivariate, with a number of parameters affecting the performance efficiency of a substrate. The consistency of the substrates can be evaluated by examining the variation from the mean of the SERS signal. The relative deviation of the (spot to spot) Raman intensity has already been calculated, with data listed in Table 4.1 above. In addition to this ‘direct’ measure of intensity variation, we will now examine both a width based parameter and peak centre deviation. A complete spectral peak contains valuable information, and the variation of parameters between spectral acquisitions will capture a sense of the consistency of a substrate. The variation to the means for 10 spectral acquisitions for the Ag Silmeco substrate is presented below in Figure 4.8 along with the RSD values for Raman signal intensity.

In order to investigate the variation of the width-based parameter and peak centre, the following approach is adopted. The mean of 10 spectra is obtained and then each individual spectra is subtracted from that mean; see Figure 4.8 (a). The spectra are normalised, curve fitted (Gaussian) and the variation of width (at FWHM) and peak position are examined. The 1066 cm^{-1} peak is chosen as it exhibited the largest signal to noise ratio of the 2-NT Raman peaks at the 785 nm excitation.





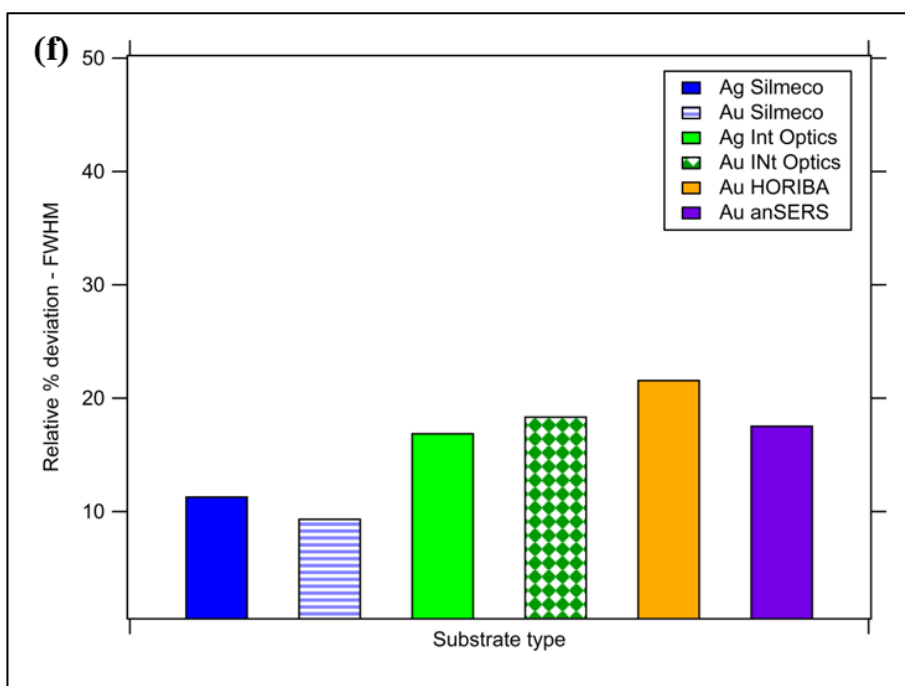
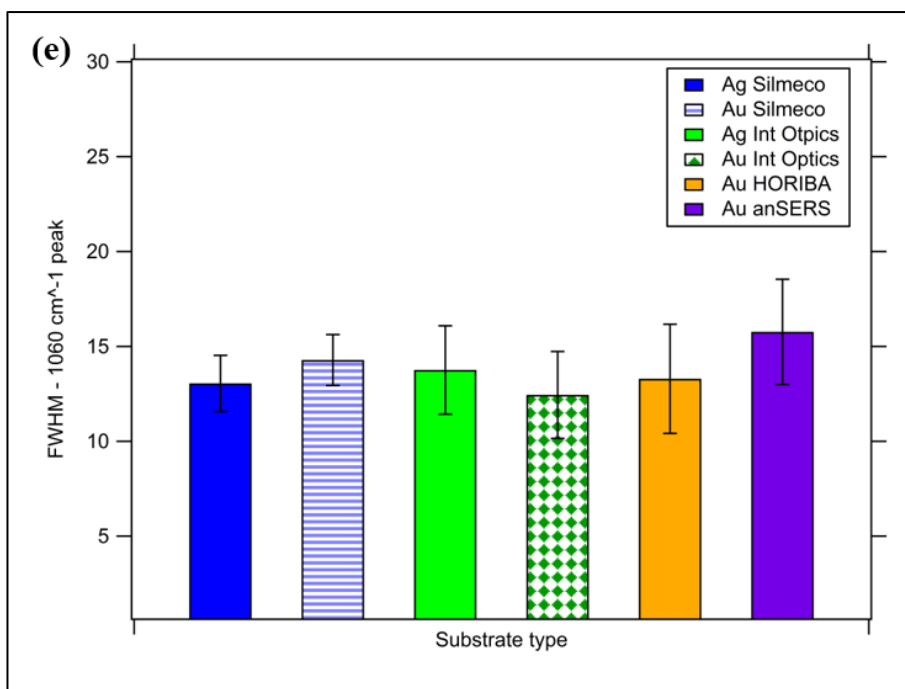


Figure 4.8 Variation to means 1066 cm⁻¹ peak for Silmeco substrate and RSD for all substrates

(a) Variation from means for 10 spectral acquisitions Ag Nanopillar substrate; 2-NT spectra, wavenumber range: 600 – 1800 cm⁻¹ (b) Relative Deviation of Raman Intensity for all substrates (c) Mean peak centre (d) Relative deviation of peak centre (e) Mean FWHM (f) Relative deviation of FWHM (b) to (f) 1066 cm⁻¹ data. Raman parameters: Laser excitation 785 nm, 0.006 mW power, 50x objective and 600 lines/mm grating.

The deviation of signal intensities presented in (b) highlight the greater variance of the inkjet substrate relative to the others. Although from this plot it is not possible to ascertain any difference between the other substrates. However, by examining the variation of the width

parameter and shift of peak centre, additional insight is gained into the consistency of each substrate. For example, plots (d) and (f).

A standard benchmark for evaluation of SERS substrates is the SERS Enhancement Factor (EF). There are a number of approaches to calculating the SERS EF, however, the following equation is the most commonly used.[187].

$$EF = \frac{\frac{I_{SERS}}{N_{SERS}}}{\frac{I_{Ref}}{N_{Ref}}} \quad \text{Equation 4.1}$$

I_{SERS} = SERS intensity; *N_{SERS}* = average number of adsorbed molecules on substrate surface;

I_{Ref} = reference Raman intensity; *N_{Ref}* = average number of molecules in the scattering volume of the reference sample.

Essentially the SERS EF calculation is the ratio between the Raman signal intensity to the number of analyte molecules within the scattering region, normalised with respect to a reference sample. In order to obtain a value for the reference Raman intensity, another experiment was performed, and is described as follows.

A 0.1M solution of 2-NT was prepared and the Raman intensity was measured from a small petri dish containing ~ 10 ml volume. Spectral measurements were obtained for the Raman parameters used in the experiments. A concentration of 0.1M (2-NT) was used rather than the 10µM used in the characterisation above. The higher concentration was chosen in order to gain a Raman signal from the solution without the aid of a SERS substrate.

Calculations for *N_{SERS}* & *N_{Ref}* are shown in appendix, page 202, with the following values obtained:

N_{SERS} = 193 molecules within the interaction volume.

N_{Ref} = 298 molecules contained within the monolayer on the substrate surface.

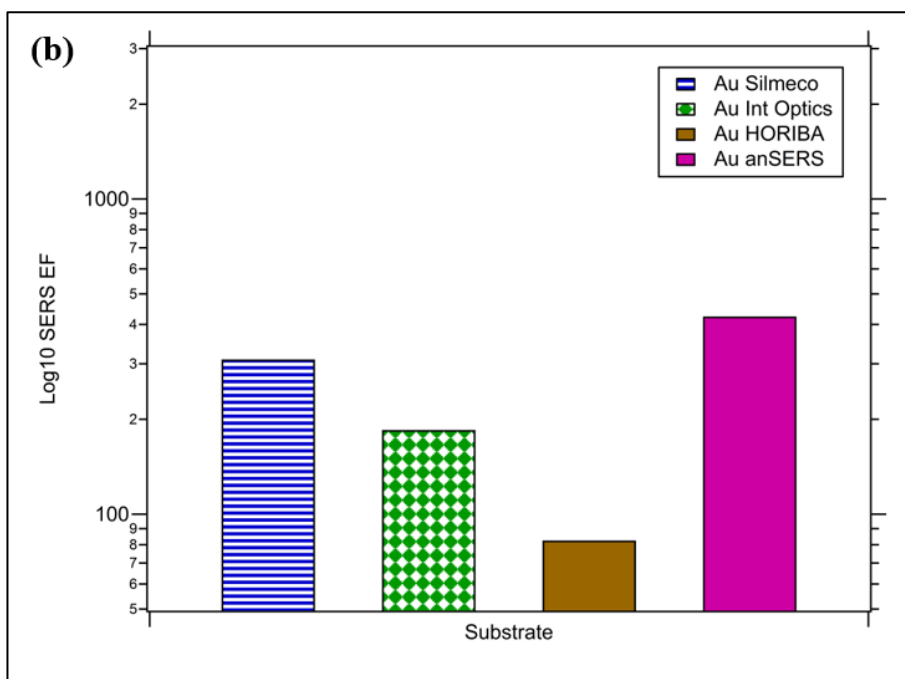
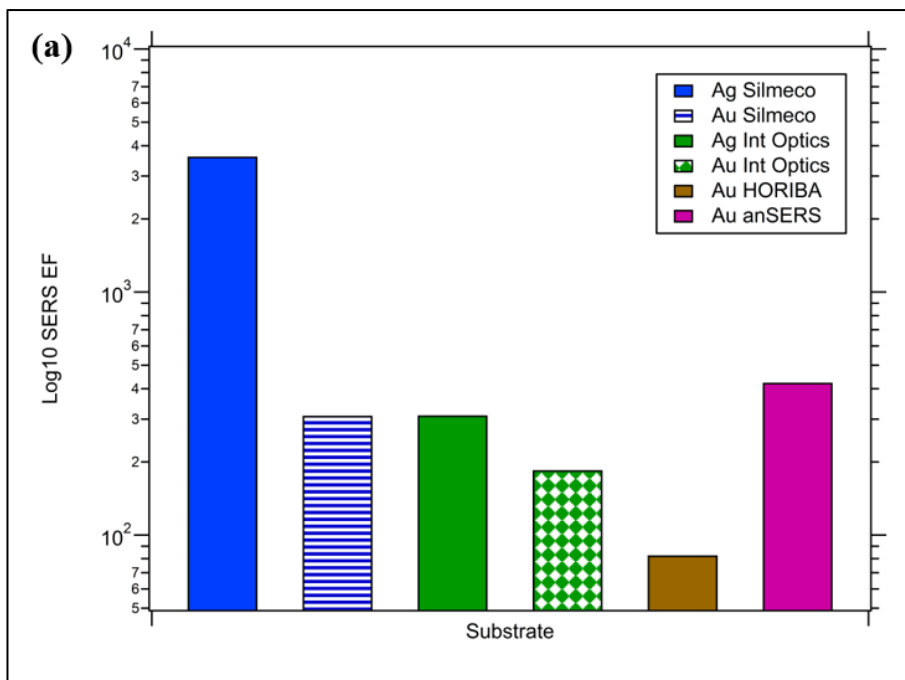


Figure 4.9 Experimental SERS enhancement factors

Semi-Log plot of SERS EF calculated from Equation 4.1 & reference signal (a) all substrates (b) Au substrates only to give better visualization of Au substrate comparison

Following on from these experimental outputs, the Ag Silmeco substrate will be the substrate of choice for the sensing of biomarkers in chapter 3. Further characterisation of these substrates is undertaken via a concentration calibration curve for 2-NT (Figure 4.10).

Serial dilutions of 2-NT were prepared for the range: 1000 – 0.001 nM. The experiment was repeated three times. The 2-NT protocol used earlier for Raman substrate comparison was also used here (page 66). The incident laser power was set at 0.006 mW which was the setting used for the substrate characterisation above.

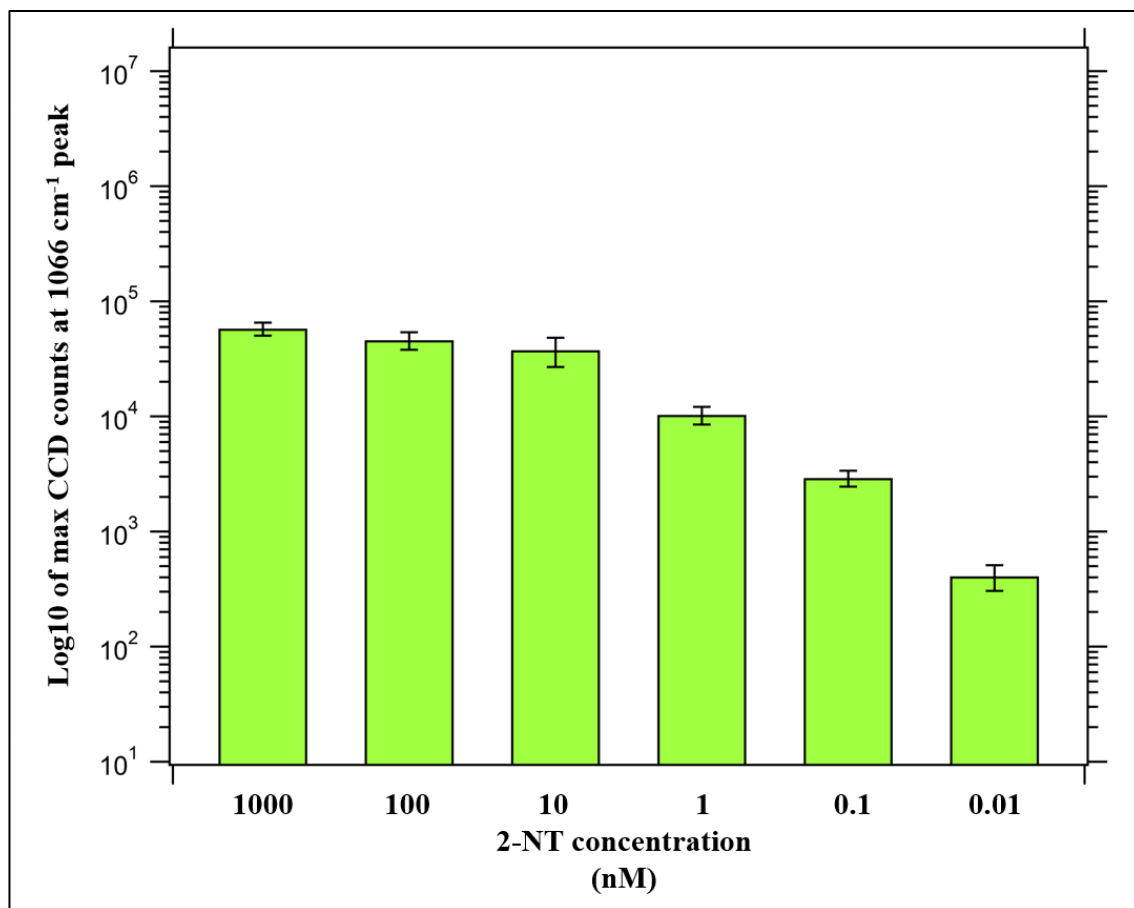


Figure 4.10 Threshold calibration curve; Ag Silmeco substrate over 1000 to 0.01 nM concentration (mean of three substrates)

Semi-log plot of calibration curve; showing lower threshold value at 0.01 nM of 2-NT. Peak data is mean of three substrates tested, error bars relative standard deviation. Laser excitation 785 nm, power 0.006 mW, 50x Objective and 600 lines/mm grating.

In order to give a measure of the variation of the signal across a single substrate, the relative deviation for six substrates across the concentration range for 10 single spectra/substrate is presented next in Table 4.3.

Table 4.3 Relative standard deviation values for one complete calibration curve

RSD values give the signal intensity variation across single substrates; 10 single spectra from random locations across the SERS-active region of each substrate; 1 μm minimum Raman acquisition separation.

2-NT concentration (nM)	1000	100	10	1	0.1	0.01
Relative standard deviation (%)	13.01	17.31	28.43	17.55	15.8	25.18

Spectra for the two lowest concentrations tested (0.1 & 0.01 nM) are presented in Figure 4.11.

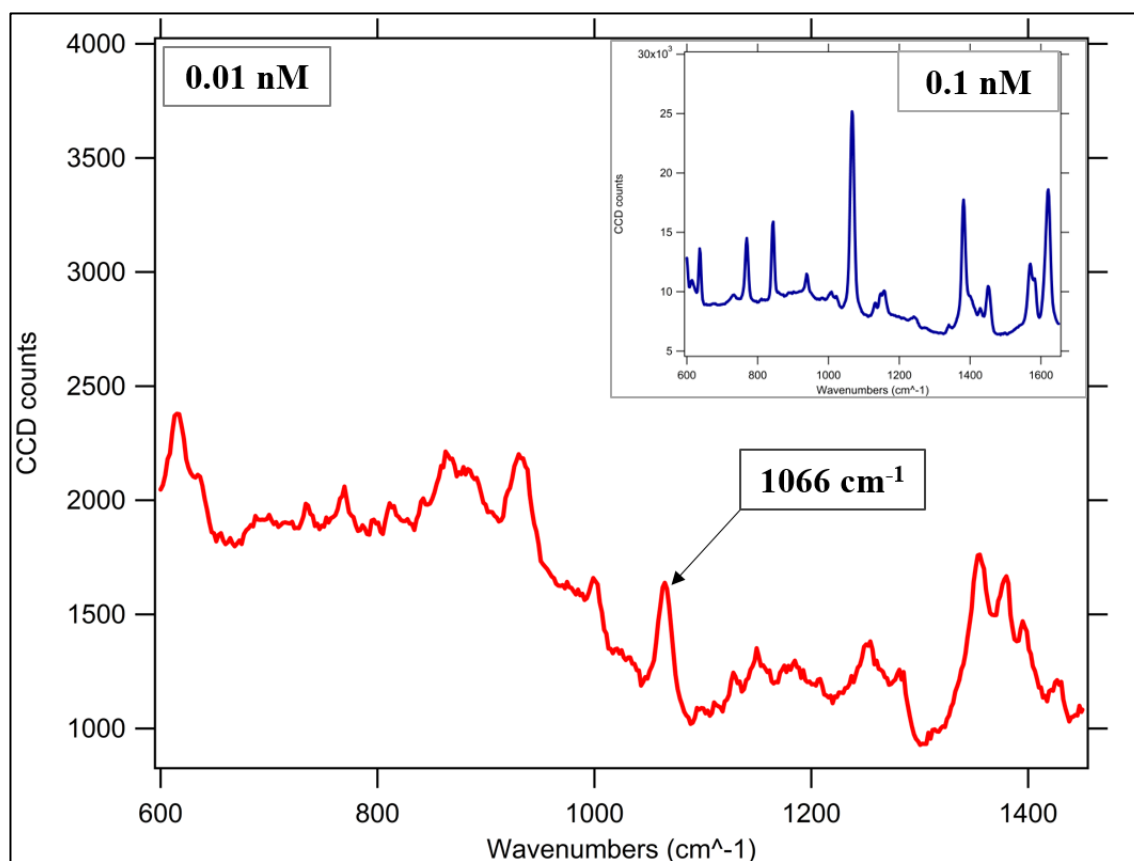


Figure 4.11 2-NT Raman spectra of low threshold (0.01 nM)

Main image; Raman spectra for low threshold limit at 0.01 nM. Signal to noise ratio $\sim 2:1$ for 1066 cm^{-1} peak which is still clearly discernible. INSET plot upper right: spectra for 0.1 nM dilution. Laser excitation 785 nm, power 0.006 mW, 50x Objective and 600 lines/mm grating

Spectral details at a concentration of 0.01 nM were still detectable at 0.006 mW laser power, however, the next serial dilution of 1 pico Molar yielded no discernible 2-NT spectra. The signal to noise ratio at the 1066 cm^{-1} peak is $\sim 2:1$.

4.3 FDTD analysis

Simulations were carried out for all the substrates characterized via Raman analysis above. The FDTD and Raman intensity outputs are plotted together (Figure 4.14) to give a qualitative appraisal of variations between the model and experimental values. Additionally, for each substrate type, simulations were carried out, with adjustments to the individual geometries made to generate an approximate uncertainty for the FDTD results.

4.3.1 FDTD & Raman comparisons

The individual simulation set up is described in Methods page 79 and following. A summary of the FDTD operational parameters is presented in Table 4.4 through to Table 4.7 and following this, plots for the FDTD and Raman intensity outputs are then presented in Figure 4.14.

Table 4.4 Simulation parameters used for Silmeco Ag & Au substrates

Source			
<i>Type</i>	<i>Wavelength range</i>	<i>Propagation</i>	<i>Polarization</i>
Total field scattered field (TFSF)	400 – 900 nm	Downward & normal to x, y	Along ‘x’
Boundary conditions			
Periodic in x, y		PML in z	
Mesh			
FDTD mesh accuracy* ¹ 3	Mesh override To cover ‘hot spot’ region between ellipse structures; dx = 0.3 & 0.5 nm for Ag & Au respectively	CMT* ² enabled ✓	
Monitors			
Profile		Point time monitors	
2		3	
Additional comments			
Disable substrate base for simulation as per reference [71]			

*¹ FDTD mesh accuracy parameters 1-8 (1-low accuracy; increased accuracy factor impacts simulation time)

*² CMT – Conformal mesh technology (page 70)

GUI images from Methods section reproduced for visual appreciation of table data.

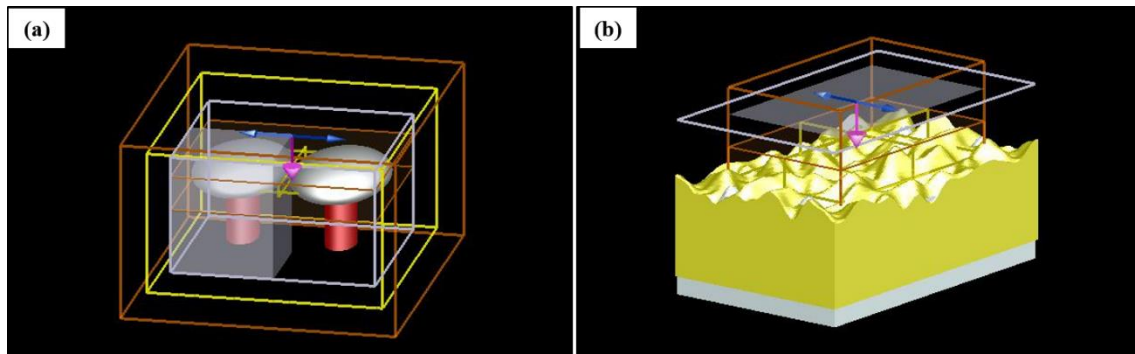


Figure 4.12 GUI images for Silmeco & Integrated Optics substrates; Table 4.4 & Table 4.5
 (a) Silmeco SERS substrate; dimer simulation objects with silicon substrate base disabled; TFSF source with symmetry option to reduce simulation time (b) Integrated Optics SERS substrate; gold surface layer 200 nm thickness; roughened surface object group.

Table 4.5 Simulation parameters used for Integrated Optics Ag & Au substrates

Source			
<i>Type</i>	<i>Wavelength range</i>	<i>Propagation</i>	<i>Polarization</i>
Plane wave	400 – 900 nm	Downward & normal to x, y	Along 'x'
Boundary conditions			
PML in x, y		PML in z	
Mesh			
FDTD mesh accuracy 4	Mesh override - Not used	CMT enabled ✓	
Monitors			
Profile		Point time monitors	
2		3	
Additional comments			
Structures continued through PML boundaries in x, y, z (lower) to prevent non-physical reflections at FDTD region boundary.			

Table 4.6 Simulation parameters used for Horiba substrate

Source			
<i>Type</i>	<i>Wavelength range</i>	<i>Propagation</i>	<i>Polarization</i>
Plane wave	400 – 900 nm	Downward & normal to x, y	Along 'x'
Boundary conditions			
Periodic in x, y		PML in z	
Mesh			
FDTD mesh accuracy 3	Mesh override Region between cylindrical structures – extends below structures into substrate and above cylinder upper surface by 10 nm; dx = 0.3 nm	CMT enabled ✓	
Monitors			
Profile		Point time monitors	
2		3	

GUI images from Methods section reproduced for visual appreciation of table data.

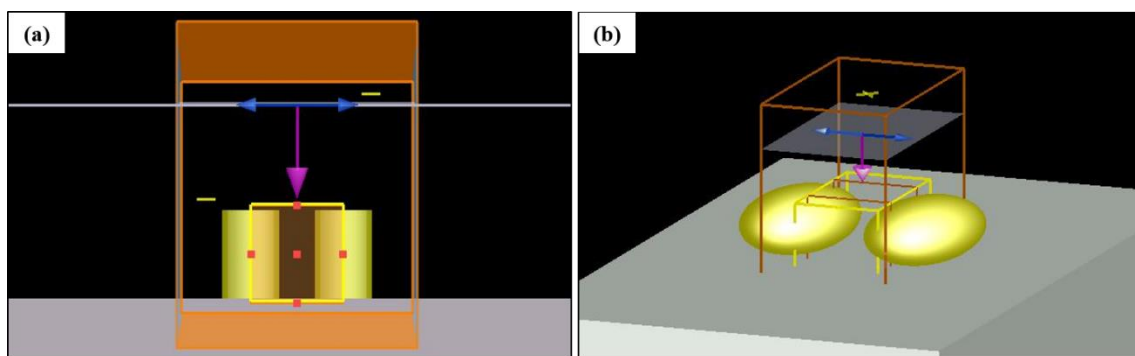
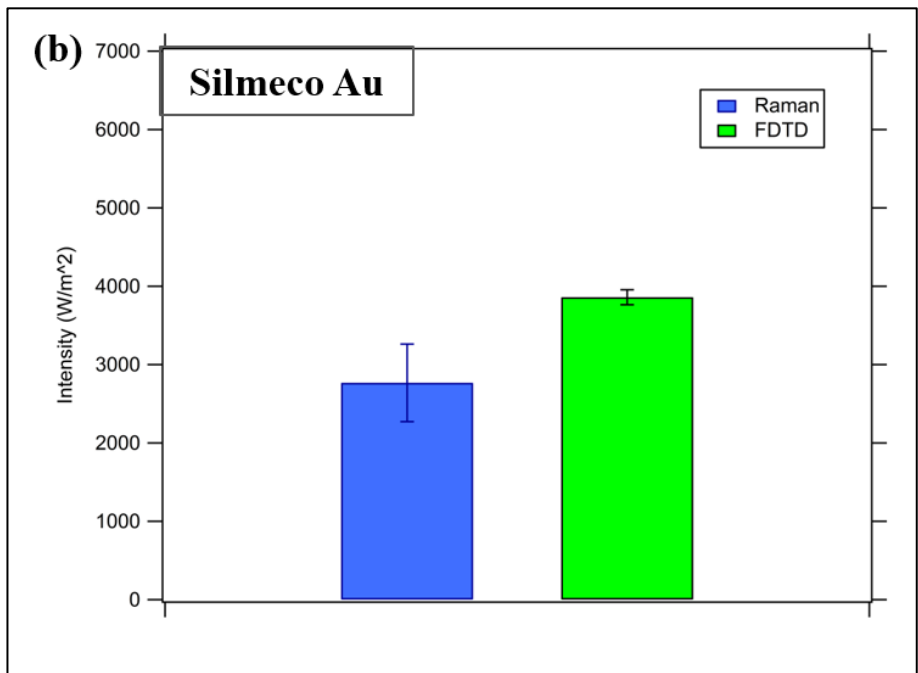
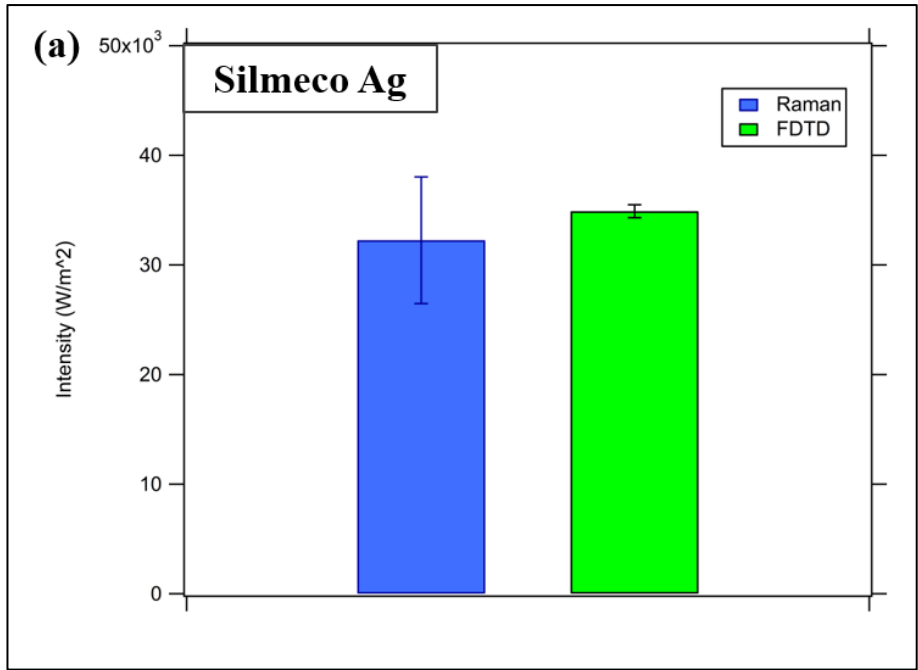


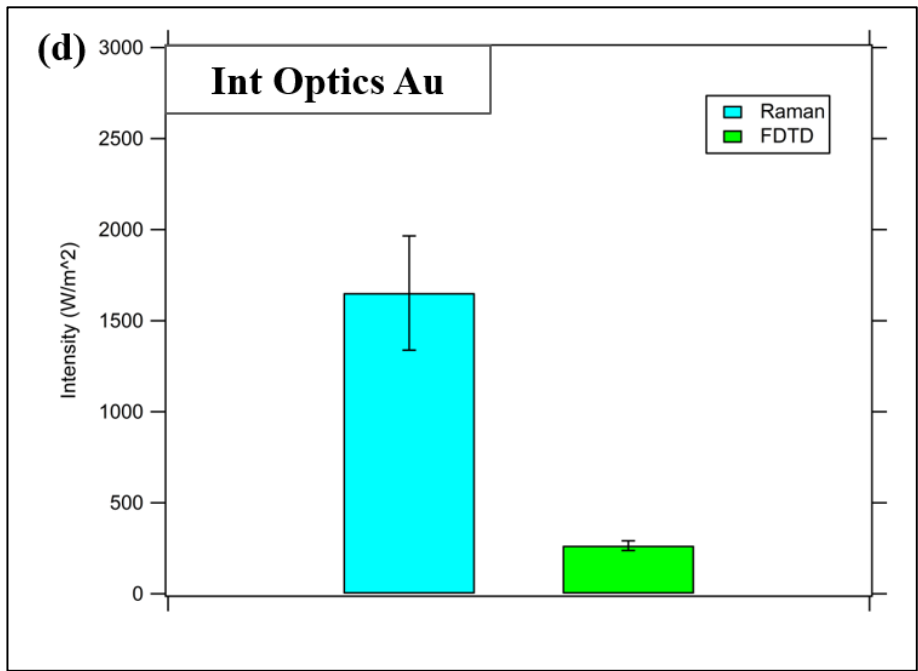
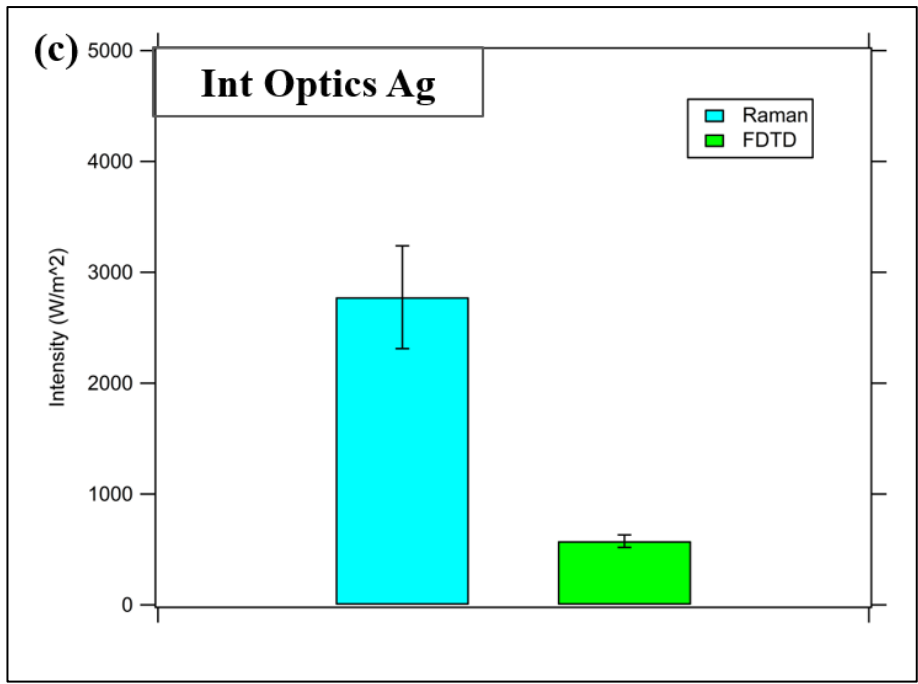
Figure 4.13 GUI images for Horiba & anSERS substrates; Table 4.6 & Table 4.7
(a) Horiba substrate; nanorod array (b) anSERS substrate; two Au nanospheres to simulate 'hot spot' region between aggregated MNP's

Table 4.7 Simulation parameters used for anSERS substrate

Source			
<i>Type</i>	<i>Wavelength range</i>	<i>Propagation</i>	<i>Polarization</i>
Plane wave	400 – 900 nm	Downward & normal to x, y	Along 'x'
Boundary conditions			
Periodic in x, y		PML in z	
Mesh			
FDTD mesh accuracy 3	Mesh override Region between the two metallic spheres – extends below structures into substrate and above spheres by 10 nm; dx = 0.3 nm	CMT enabled ✓	
Monitors			
Profile		Point time monitors	
2		3	

As mentioned above, a qualitative comparison is made between FDTD and experimental (Raman) outputs in Figure 4.14.





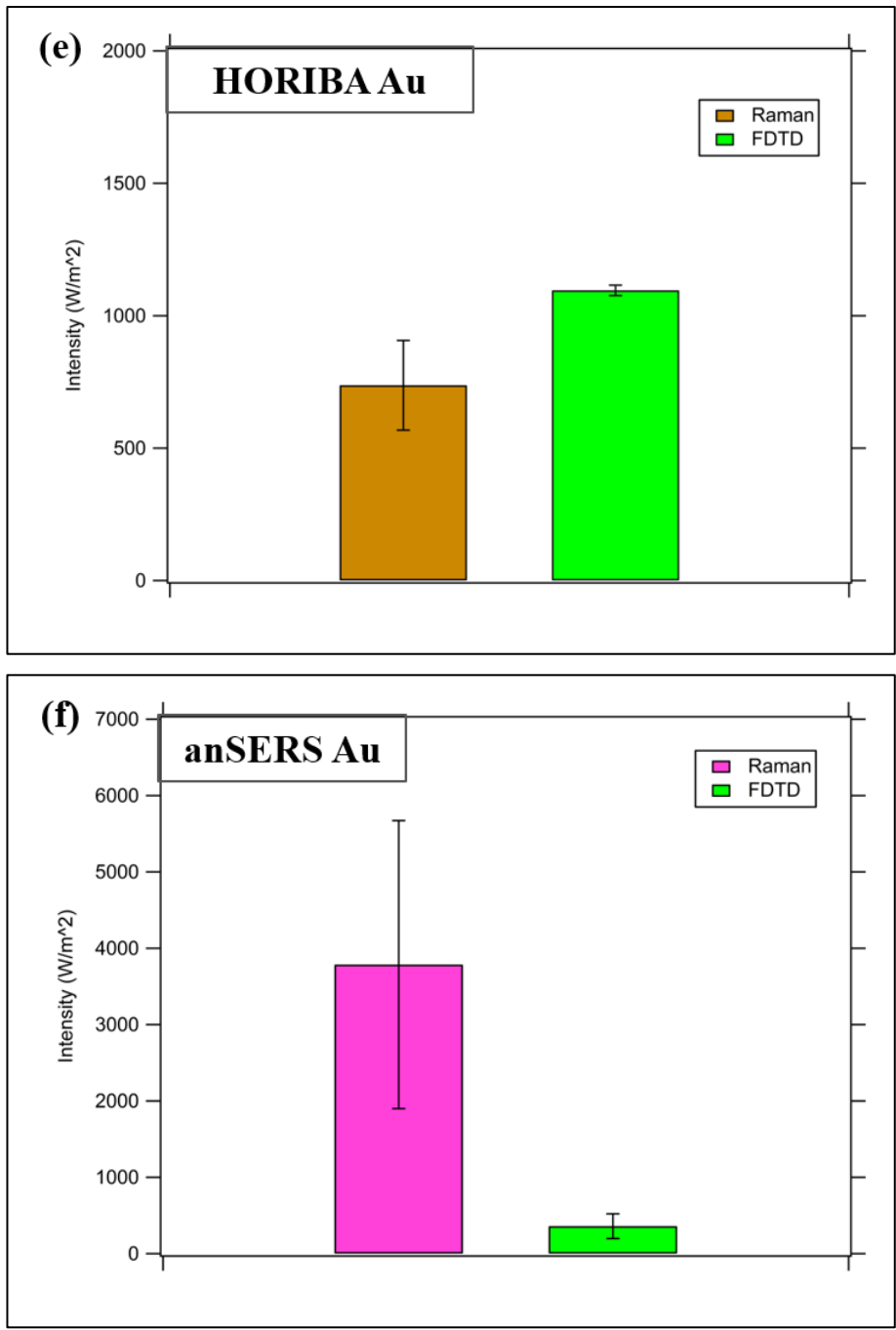


Figure 4.14 Raman/FDTD signal intensity comparison; all substrates
 (a) & (b) Silmeco substrates Ag and Au respectively (c) & (d) Integrated Optics, laser fabricated substrates, Ag and Au respectively (e) Horiba, nanorod array substrate (f) anSERS inkjet printed substrate. Error bars: Raman – relative standard deviation; FDTD – based on variation of geometric parameters (details: Methods pages 79 to 82)

The error bars for the Raman intensities are the RSD values. For the FDTD outputs, error bars are governed by variations to specific geometries. In the case of the Silmeco, Horiba and anSERS substrates the errors were determined by altering the interstructure spacing. The spacing ranges used to simulate the Silmeco, Horiba and anSERS units were: 1-4 nm, 10–20 nm, and 10-30 nm respectively. These dimensions were gained from the SEM images. In the case of the Integrated Optics laser constructs, the general roughness of the surface was varied to ascertain an ‘uncertainty’ for the FDTD outputs. The ‘roughened surface’ object used from

the FDTD object library has a ‘roughness factor’ parameter (σ). The object set up contained a ‘roughness factor’ parameter (σ). Alterations to σ result in variations to the surface geometry as illustrated; Figure 4.15.

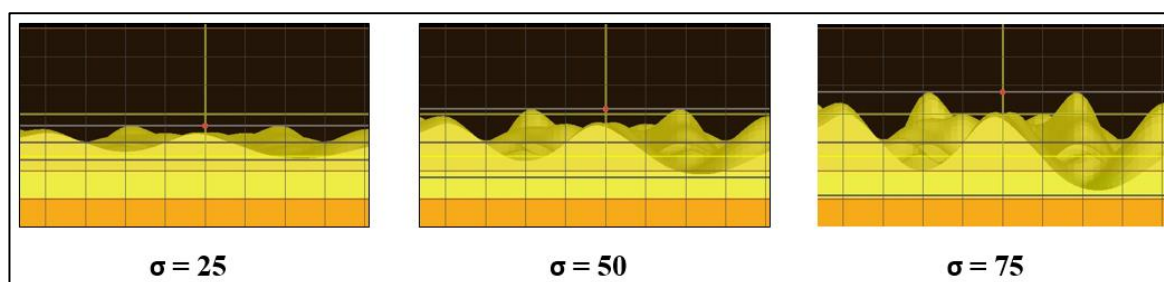


Figure 4.15 Variation in surface morphology; with ‘roughness factor’ σ ; Laser constructs
A clear change in geometry is noted with variation in σ value

A summary table of error considerations for the simulated FDTD outputs is presented in Table 4.8.

Table 4.8 Geometry variations for FDTD error estimation

Substrate	Range of interstructure spacing
Silmeco (Ag & Au)	1-4 (nm)
HORIBA	10-20 (nm)
AnSERS	10-30 (nm)
	Range of roughness factor values (σ)
Integrated Optics (Ag & Au)	25 – 50 - 75

Next, a comparison is made between the SERS enhancement factors from the experimental results (Raman) and FDTD generated values. The comparison is qualitative as two different techniques are used to calculate the EF values. The Raman SERS EF’s are calculated from Equation 4.1. The FDTD figure is achieved using the E^4 approximation; i.e. the software selects the field maxima in the simulation region and raises it to the fourth power.

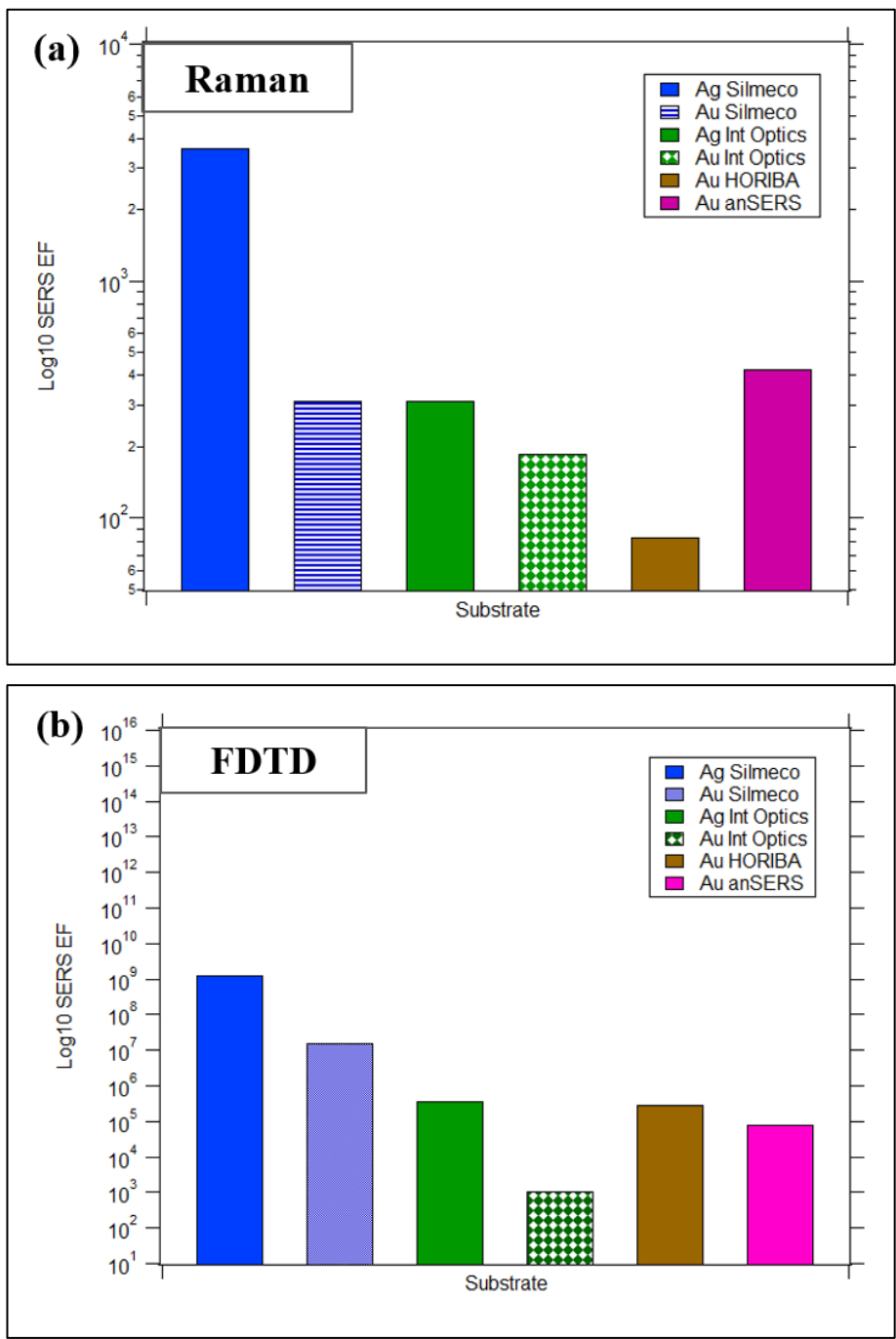


Figure 4.16 Raman/FDTD SERS EF comparison; ALL substrates
Semi-log plots both images (a) Raman-based EF calculated results (b) FDTD-based calculation

Maximum and minimum FDTD generated SERS EF values for the individual substrates are presented in Table 4.9 and calculated as per varying geometric parameters described above.

Table 4.9 Maximum and minimum FDTD generated outputs for individual substrate SERS EF's

Substrate type	SERS Enhancement Factor (<i>Max</i>)	SERS Enhancement Factor (<i>Min</i>)
Ag Nanopillar	1.2×10^9	3.5×10^5
Au Nanopillar	1.5×10^7	1.0×10^3
Ag Laser	3.3×10^5	3.2×10^3
Au Laser	7.0×10^4	6.8×10^2
Au Nanorod	1.2×10^6	3.5×10^5
Au Inkjet	1.3×10^5	7.1×10^3

4.4 Discussion

Raman, SEM and FDTD characterization of commonly available platform-based SERS substrates was carried out.

For the Raman analysis, substrates were functionalised with the Raman active molecule 2-Naphthalene thiol and the resulting spectra were examined. Two of the prominent Raman peaks in the wavenumber range: $600-1800 \text{ cm}^{-1}$ were used to compare the relative performance of each substrate type. The two key outputs obtained from the Raman characterisation, were the intensity and variation of the SERS signal. The relative standard deviation of the Raman intensity across several spectral acquisitions was calculated to give a measure of the spot to spot signal variation. The variation of FWHM and peak centre was also examined to more fully characterise substrate consistency.

A comparison between Ag and Au surface layers was also made. For two substrates of the same type/topography the Ag layer yielded a greater SERS response than Au; Figure 4.7 Values for the SERS EF were calculated from Equation 4.1 using the Raman signal from a reference sample, which is a commonly used approach [63, 187]

The substrates yielding the greatest SERS response in terms of signal enhancement were Ag Silmeco and the Au anSERS inkjet printed units. By examining the SEM images, it is noted these substrates also had the smallest values for interstructure spacing.

The second most significant SERS parameter to consider is the signal consistency. For these two substrates, the signal variations noted for the prominent 1066 cm^{-1} peak were as follows. The mean relative standard deviations (across three substrates) were 17.2% and 49.4% for the Ag Silmeco and anSERS substrates respectively. However, it was also noted that the intra-substrate variations were 7.8% and 2.3% respectively.

In order to give an estimate of the variation or uncertainty of the FDTD outputs, simulations were performed for different geometries; Table 4.8.

The FDTD analysis showed good agreement between simulated and experimental Raman parameters for the Silmeco and Horiba units. However, there was poorer agreement for the anSERS and Integrated Optics substrates; Figure 4.14. The substrate morphology for the anSERS and Integrated Optics substrates is less ‘ordered’ than that of the Silmeco and Horiba units; see SEM analysis page 94 and following.

4.5 Conclusions

We have evaluated the performance of commonly available platform-based SERS substrates, via the two key performance criteria of signal enhancement and consistency. As mentioned earlier, the electromagnetic mechanism generates most the SERS enhancement, which in turn is strongly dependent on the physical geometry of a substrate surface. Following the above characterization studies, we conclude that the key physical parameter affecting the largest SERS signal is that of the interstructure spacing. Note the high efficiency ‘leaning’ Nanopillar substrates Figure 4.1 & Figure 4.5, where structure gaps of 2-4 nm have been reported [71]. The other substrate yielding a large enhancement is the anSERS unit, where low dimension gap parameters arise from closely packed MNP’s.

Experimentally observed strong enhancements from structures in close proximity are also supported by SERS electromagnetic theory. When structures are close enough that their individual local electric fields can interact, then coupled Plasmon resonance (CPR) occurs [188, 189], which exponentially increases the SERS enhancement. This is suitably illustrated in the FDTD analysis presented in Figure 3.13.

In relation to signal deviation, the uniformity of surface nanofeatures strongly governs signal consistency. This was especially noticeable with the anSERS substrates which yielded the largest relative standard deviation of spot to spot Raman intensity. While the closely packed MNP’s of the anSERS substrates yield strong enhancements, they also exhibited a large signal deviation of ~ 50%. This arises from the random nature of MNP aggregation; Figure 4.4 (c) & (d).

In order to place the substrate characterization into the context of the literature, the discussion by M. J. Natan [33] is helpful. Natan suggests values of less than 20% for both spot to spot and substrate to substrate variation. While the consistency of the anSERS substrates with regard to signal variation across an individual substrate SERS-active region is poor, it does possess a strong enhancement. Thus making these units especially suited to trace analysis, e.g. the detection of fungicide in water [190].

We also conclude and concur with the literature that FDTD analysis is a useful characterization tool for SERS research [191, 192]. However, we have noted that in some cases the FDTD outputs will be mainly qualitative due to certain surface morphologies. This is especially a concern when the surface in question doesn’t possess consistent/regular nanostructures. A clear example of this is the FDTD analysis of the Integrated Optics substrates above. These substrates have an amorphous topography, making accurate simulation extremely challenging; see Figure 4.17 below.

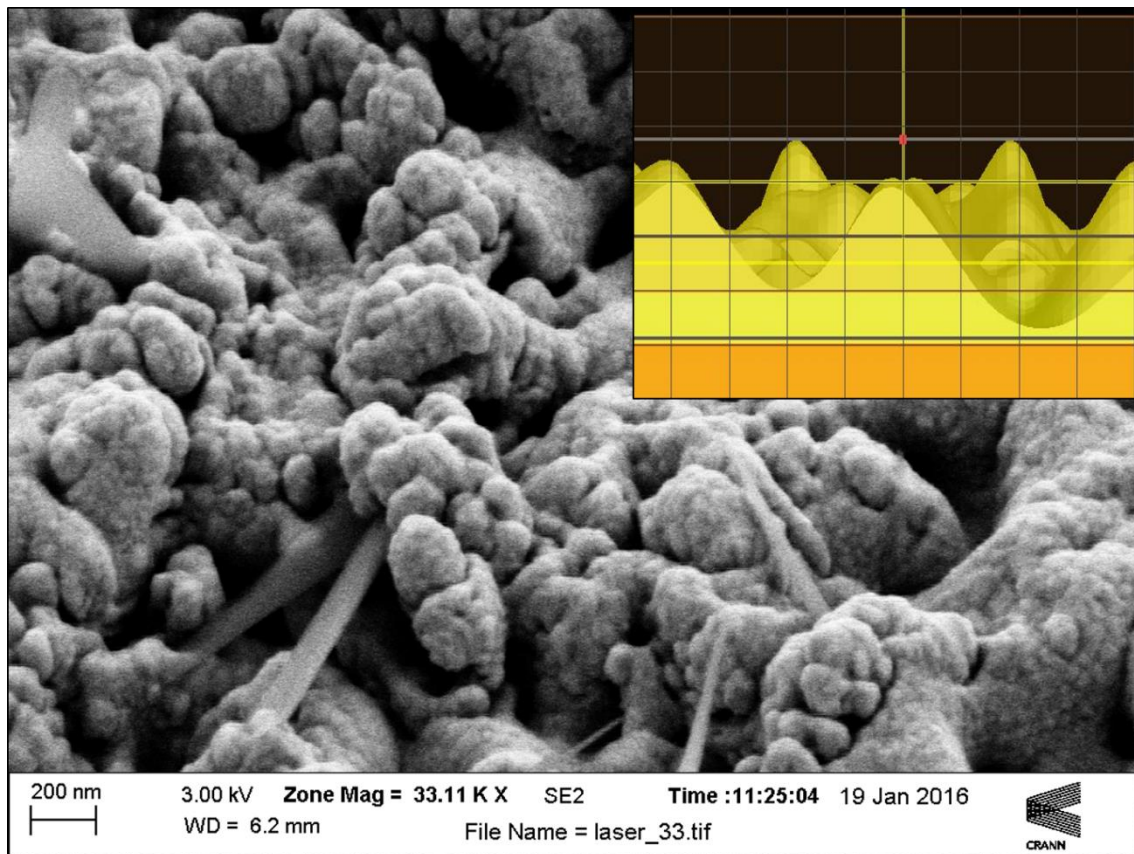


Figure 4.17 SEM image of amorphous SERS substrate geometry with FDTD GUI set up inset *Integrated Optics laser fabricated substrate. SEM image SE2 detector, Magnification 33.11 KX, 200 nm scale bar, acceleration voltage 3 kV. Inset image upper right: FDTD GUI 'set-up'. The difference between simulation object and actual surface features is clearly discernible.*

Figure 4.17 illustrates one of the challenges faced when using FDTD software to analyse the SERS response of a substrate without an ordered surface geometry. However, qualitative analysis of such substrates can still provide much useful information e.g. choice of material, thickness of outer metallic layer and a general 'sense' of SERS performance.

5 Results 2 - Design, fabrication & optimization of SERS substrates

Lithography produced substrates yield periodic structures, with excellent fabrication batch to batch consistency. The aim of the Tyndall project (NAP 370) was to develop SERS substrates with periodic nanostructures, with a view to use in ex-vivo SERS biosensing. The substrates were fabricated using state of the art Substrate Conformal Imprint Lithography (SCIL).

Initial characterisation was performed using Raman, SEM and FDTD analysis. The performance of a second substrate type, fabricated by NIL was also evaluated. These substrates were optimised via the FDTD modelling, then reworked to those specifications and re-tested by Raman analysis.

5.1 SCIL Substrates

5.1.1 Raman Analysis

The substrates were functionalized with 2NT as per the protocol used for the platform-based substrates, page 92.

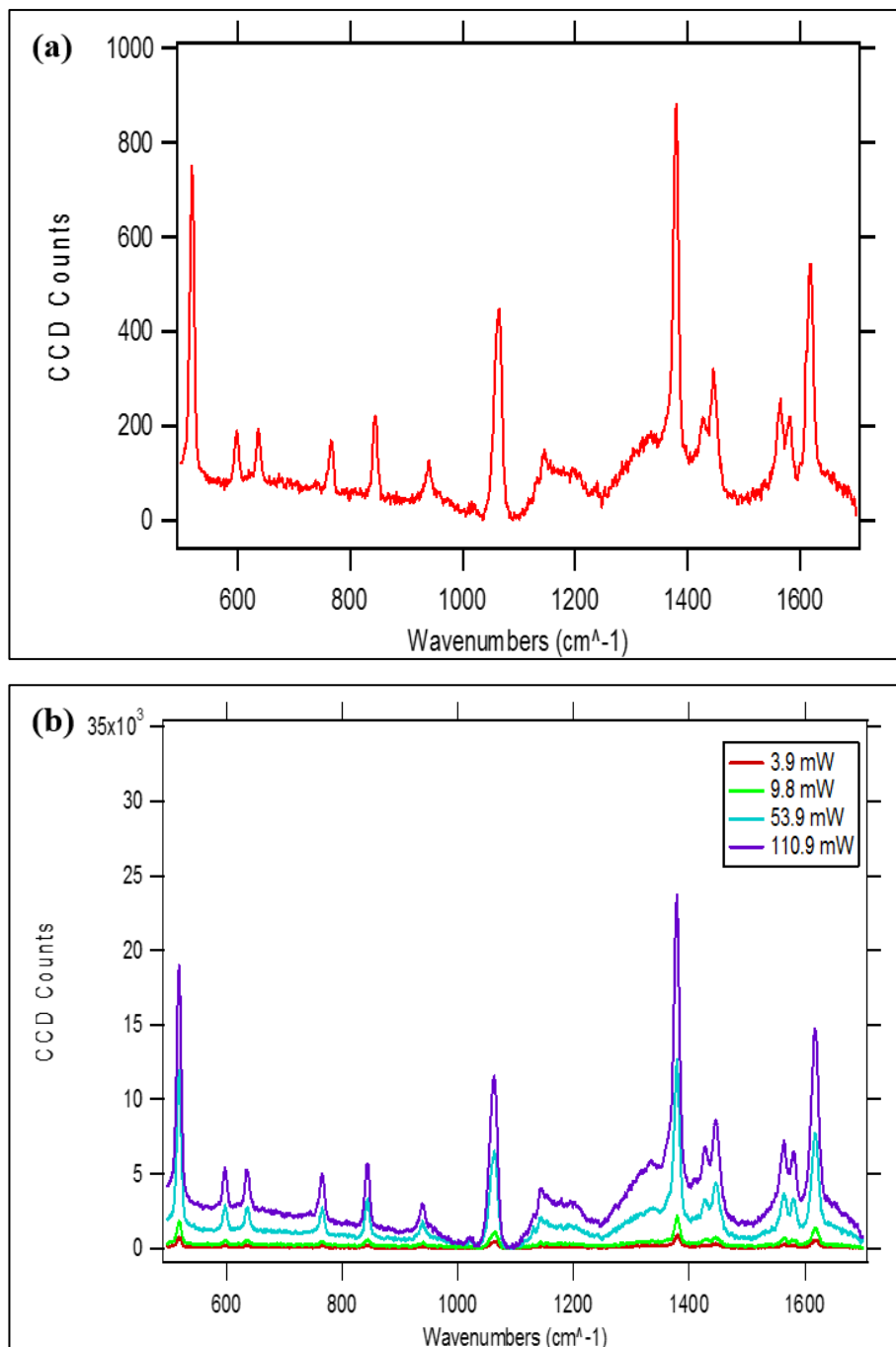


Figure 5.1 Tyndall substrate – 2NT spectra

(a) 3.9 mW laser power (b) 3.9, 9.8, 53.9 & 110.9 mW power settings, all spectra measured at 785 nm excitation, 20x objective & 600 lines/mm grating.

The Tyndall substrates exhibited minimal SERS response with an associated poor signal strength, and signal to noise ratio. Laser excitation of 3.9 mW was the minimum power required to gain a measurable Raman spectrum for the Tyndall substrates, while any setting > 0.0063 mW caused signal saturation for the commercial substrates.

Although the signal enhancement of the Tyndall units was relatively poor, the signal consistency was good. A comparison of signal consistency between the Tyndall and commercial substrates of Results chapter 1 is presented next in Table 5.1.

Table 5.1 SERS signal consistency comparison for Tyndall and commercial platform-based substrates

Raman acquisitions recorded from 10 random locations across the Tyndall substrates as per platform-based substrates

Substrate	<i>Tyndall</i>	<i>Ag Silmeco</i>	<i>Au Silmeco</i>	<i>Ag Integrated Optics</i>	<i>Au Integrated Optics</i>	<i>Au Horiba scientific</i>	<i>Au Diagnostic anSERS</i>
Mean RSD (%)	8.3	17.2	16.6	16.4	19.0	20.4	49.4
Intra-substrate deviation (%)	4.1	7.8	3.6	2.7	6.3	2.0	2.3

A comparison is made between the Tyndall and the Nanogap substrates in Figure 5.2 below, at the mutual power setting of 3.9 mW (all other Raman and experimental parameters maintained at the same value).

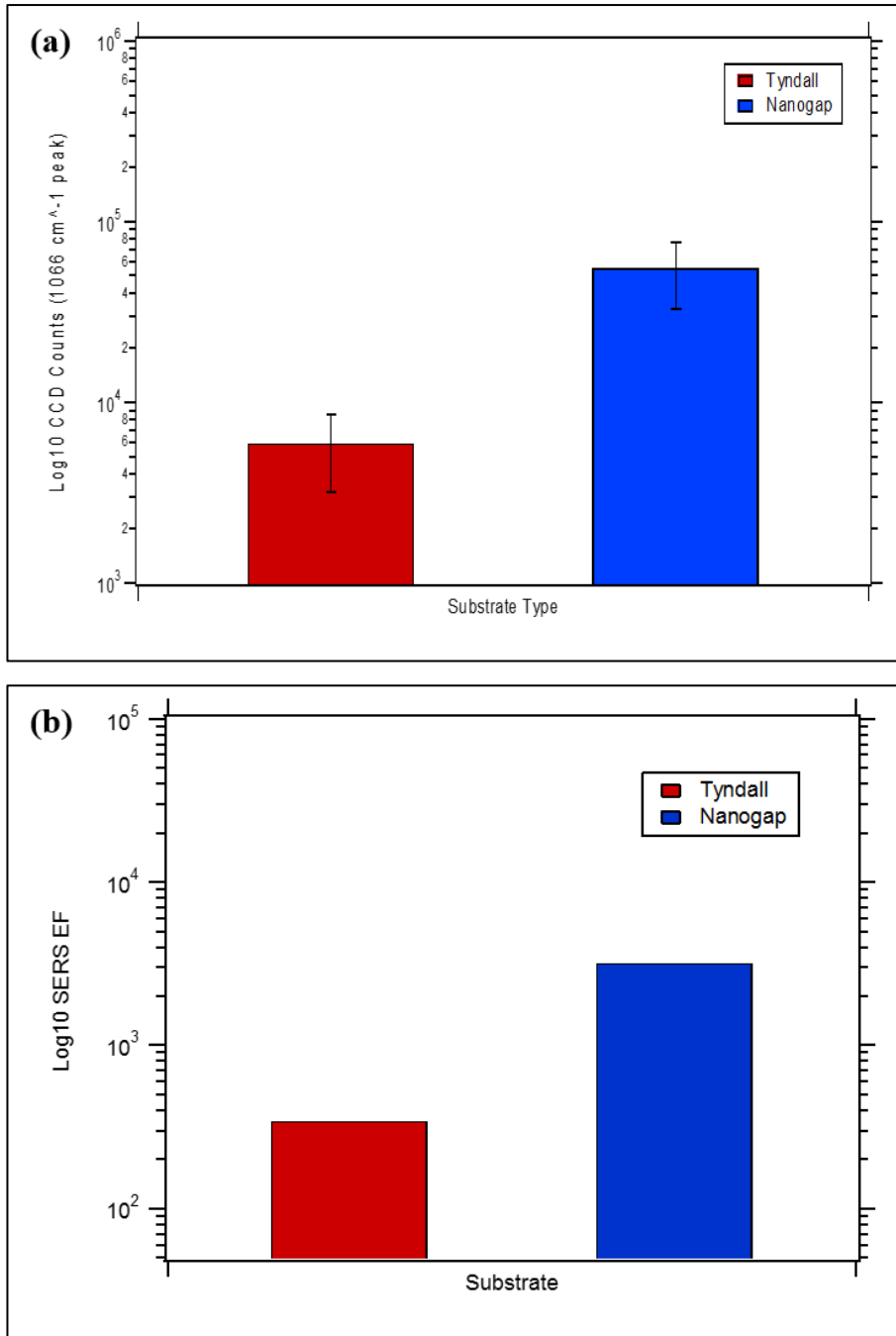


Figure 5.2 Substrate comparison; Tyndall & Nanogap

(a) Semi-Log plot of max CCD counts at 1066 cm⁻¹ peak (b) Semi-Log plot of SERS EF; calculated at 1066 cm⁻¹ peak. Raman parameters: 785 nm excitation, 3.9 mW laser power, 20x objective & 600 lines/mm grating. SERS EF calculation using Equation 4.1 as per platform-based substrates above

The SERS enhancement of the SCIL substrates was inferior to the nanogap units, the SERS EF differs by an order of magnitude; 3.4×10^2 & 3.2×10^3 for the SCIL and Nanogap substrates respectively; Figure 5.2 (b). A comparison between the Tyndall and Nanogap substrates for spot to spot signal variation is presented next in Table 5.2.

Table 5.2 SERS signal consistency comparison for Tyndall and Nanogap substrates

Raman acquisitions recorded from 10 random locations both substrates. Raman parameters: 785 nm excitation, 3.9 mW laser power, 20x objective & 600 lines/mm grating

Substrate	<i>Tyndall</i>	<i>Nanogap</i>
Mean RSD (%)	8.3	39.9
Intra-substrate deviation (%)	4.1	22.2

Again, as per comparison with commercial substrates (Table 5.1) the Tyndall units exhibit excellent spot to spot consistency of Raman signal.

Following the SEM characterisation below, the FDTD software is used to investigate and optimise the SERS performance SCIL substrates.

5.1.2 SEM characterization

In addition to the issue of poor performance, another problem was encountered during the fabrication process. The creation of the flexible SCIL mask from the EBL Master was only partially successful. The flexible mask contained 12 nanostructured regions of $\sim 70 \times 70 \mu\text{m}$, each with a different design or lattice array. However, of the 12 designs submitted for EBL patterning only 4 imprinted regions were successfully transferred to the SCIL mask, the SEM's in Figure 5.3 illustrate the problem encountered.

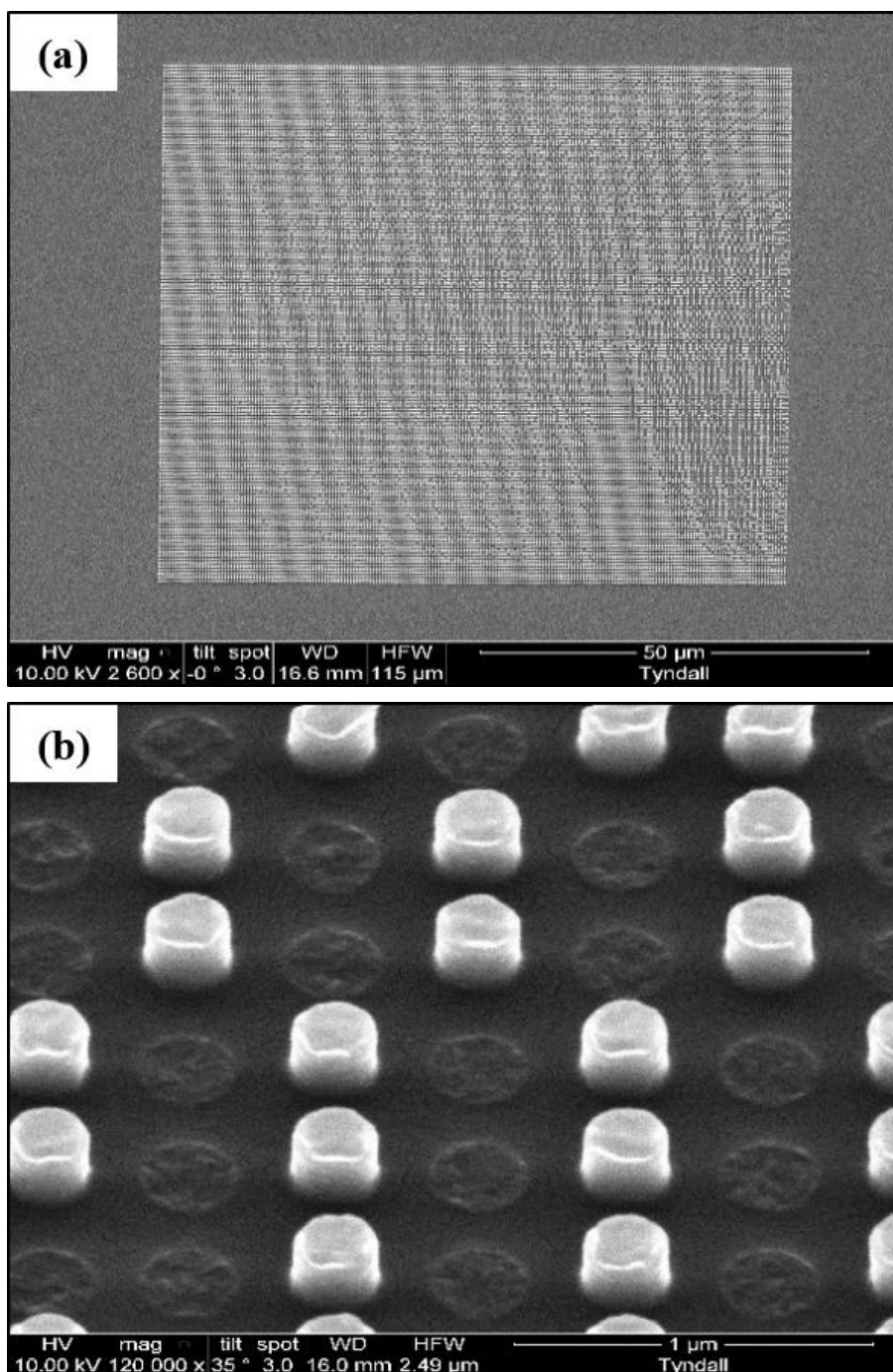
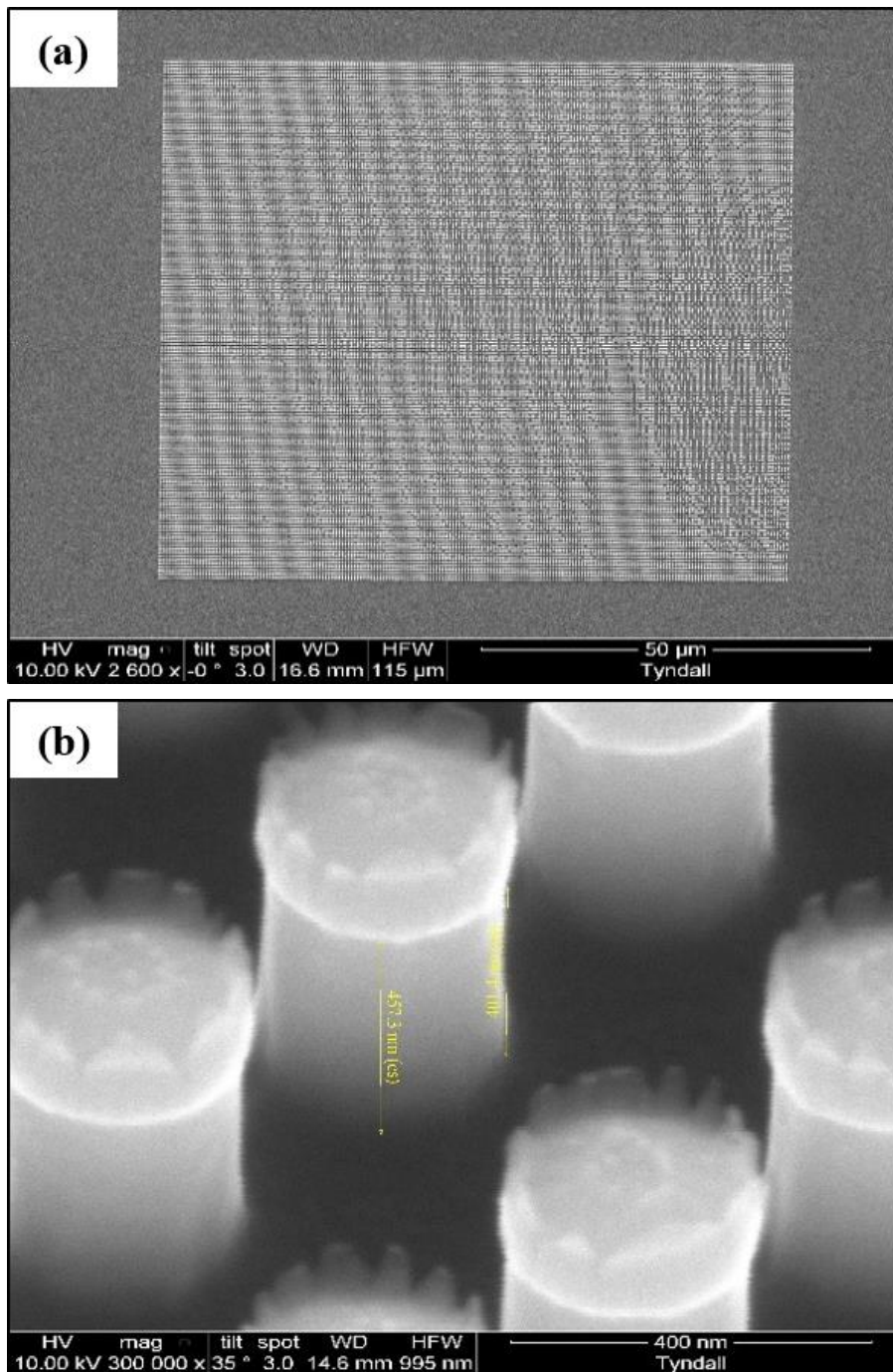


Figure 5.3 SEM's of post-imprint and CFF etching SCIL imprinted regions

Surface images showing failed imprint due to damaged SCIL mask; (a) Magnification 2.6 KX; 50 μm scale bar (b) Magnification 120 KX; 1 μm scale bar; 35° tilt. Acceleration voltages 10 kV (both images). Feature diameter pre-metallic deposition ~ 240 nm

In Figure 5.3(a) some damage to the imprinted nanostructured region is visible – the zoom image (b) shows the poor imprint quality. However, four nanostructured regions per wafer contained excellent feature coverage and were selected for the Raman analysis. As such, the impact to the NAP project was in the number of substrates available rather than the quality. For the substrates evaluated via Raman analysis, the integrity of imprinted structures was not an issue affecting the SERS performance.

The intermediate stages of the fabrication process showing structures after successful SCIL imprint and etching are given in Figure 5.4. Following CFF etching the wafers are then removed for O₂ cleaning and deposition with SiO₂ and Au.



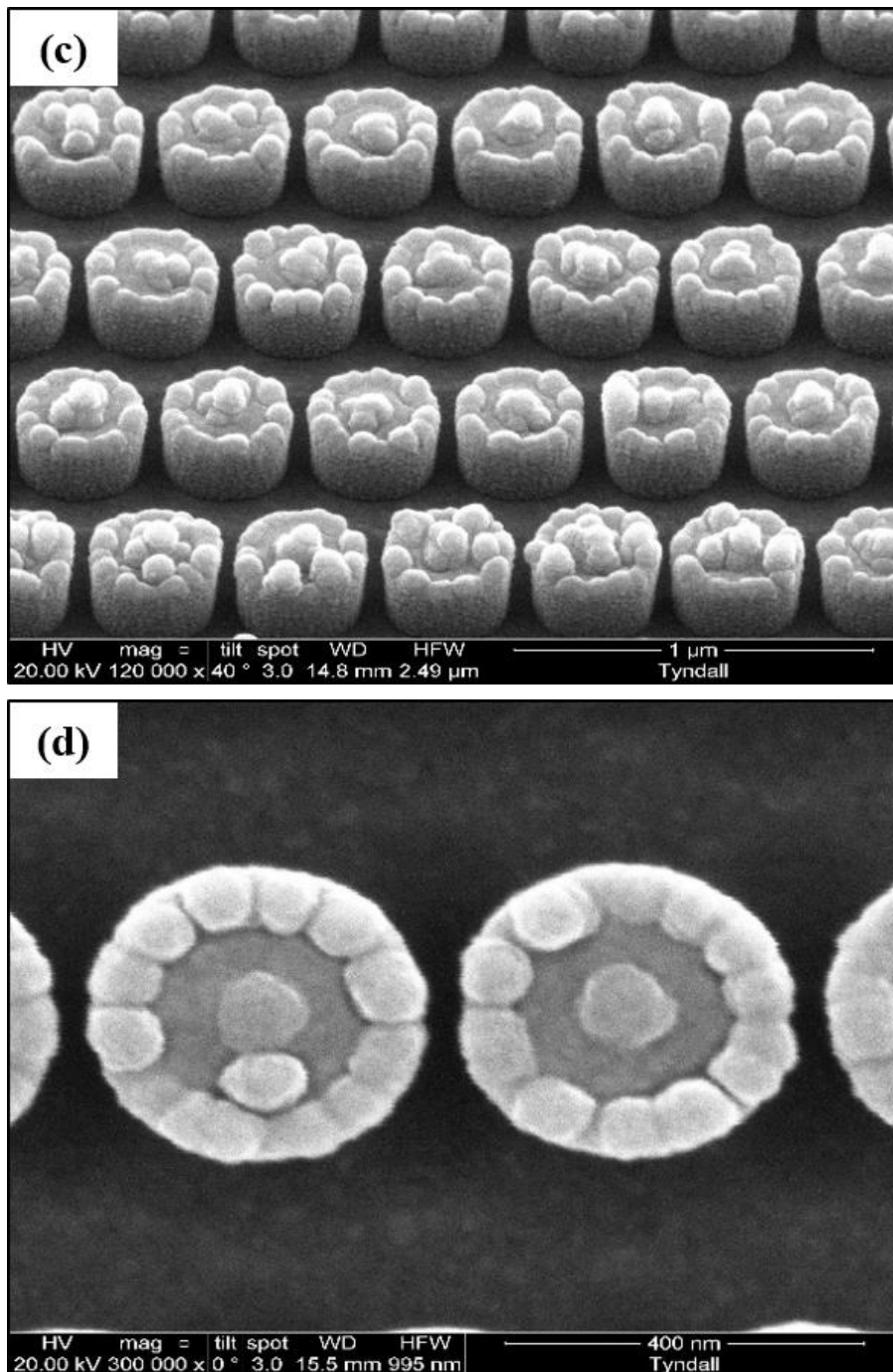
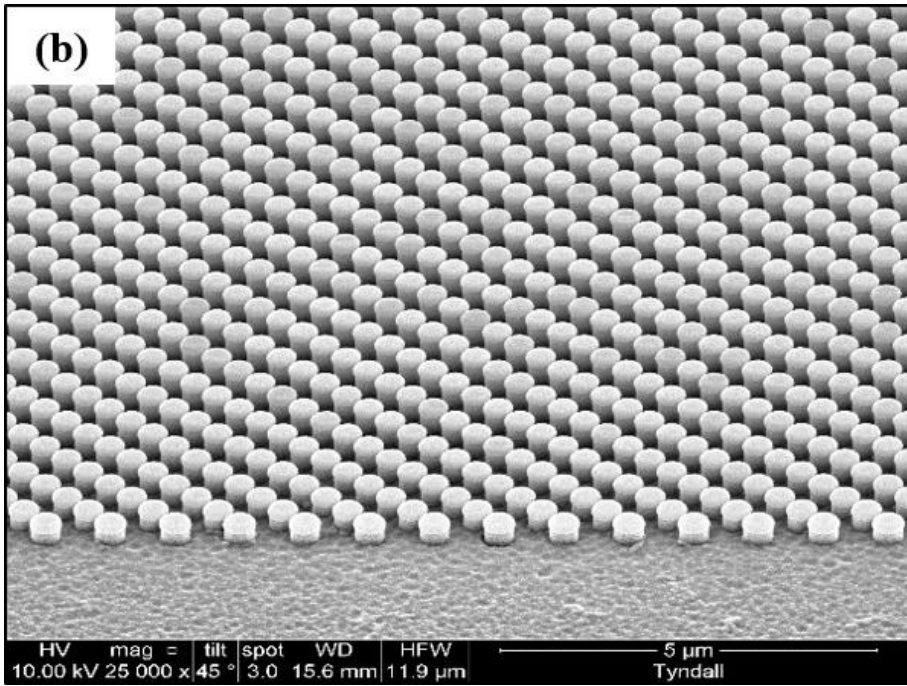
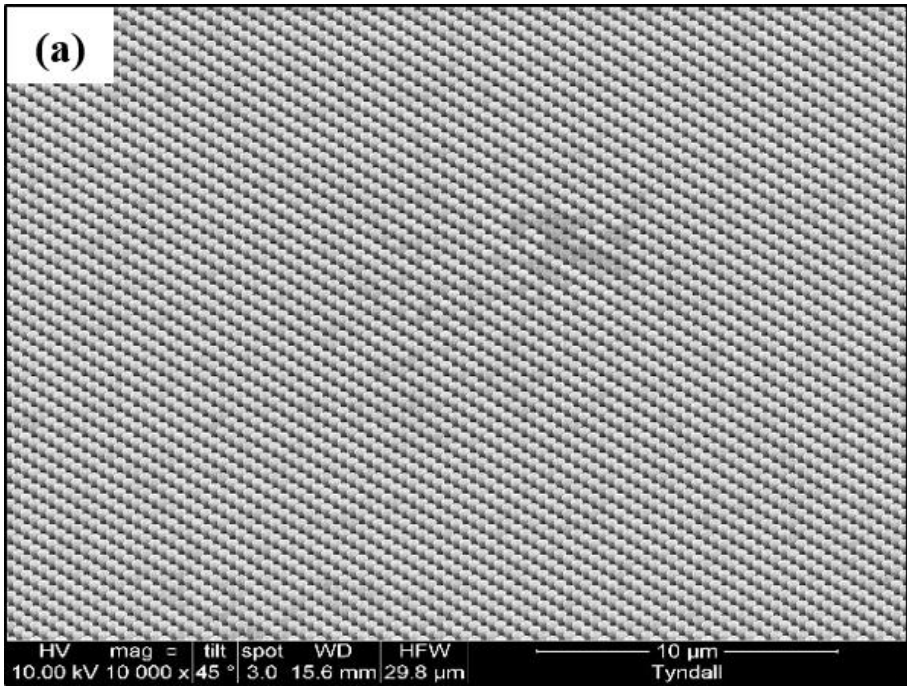


Figure 5.4 SEM's illustrating fabrication stages SCIL substrate

Nanopillar array (a) 70 x 70 μm nanostructured ROI on silicon wafer; Magnification 2.5 K X; 50 μm scale bar (b) zoom of ROI showing nanopillars post imprint & etch; Magnification 300 K X; 400 nm scale bar. Acceleration voltage 10 kV (both images) (c) Magnification 120 K X; 1 μm scale bar; 40° tilt showing nanopillar array (d) zoom image; Magnification 300 KX; 400 nm scale bar. Acceleration voltage 20 kV (both images)

Figure 5.4 (a) & (b) shows the nanostructured region post imprint and CFF etch. The imprint consistency of the pillar array's is excellent, noticeable are deposits on the face of the pillar top surface (b), (c) & (d). The most likely cause is a marking of the surface during imprint (b) which then produces preferentially deposition 'patterning'. Additional Au deposition is then carried out to further reduce the structure spacing, and is illustrated in Figure 5.5.



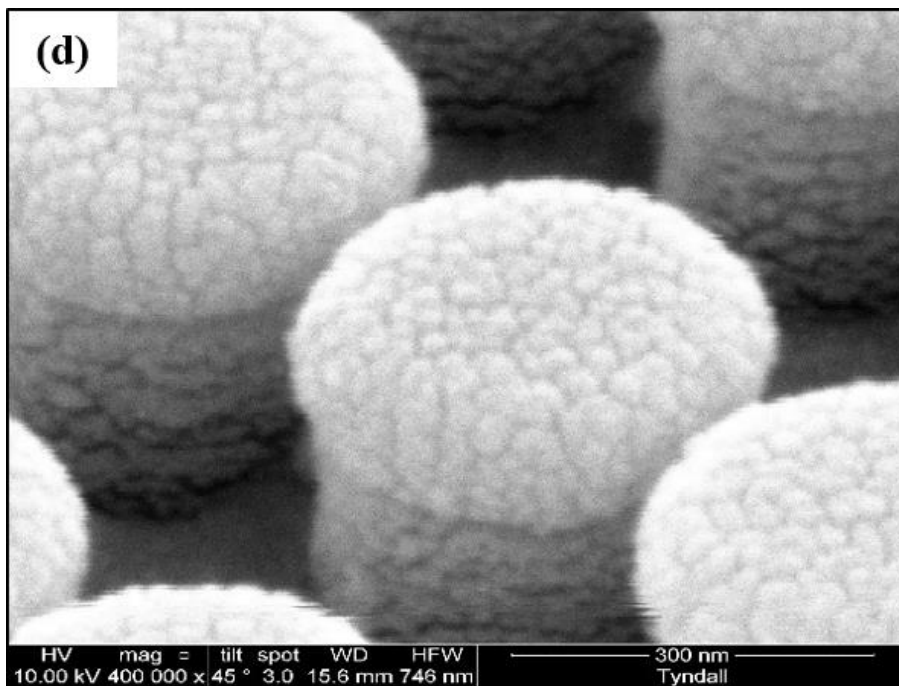
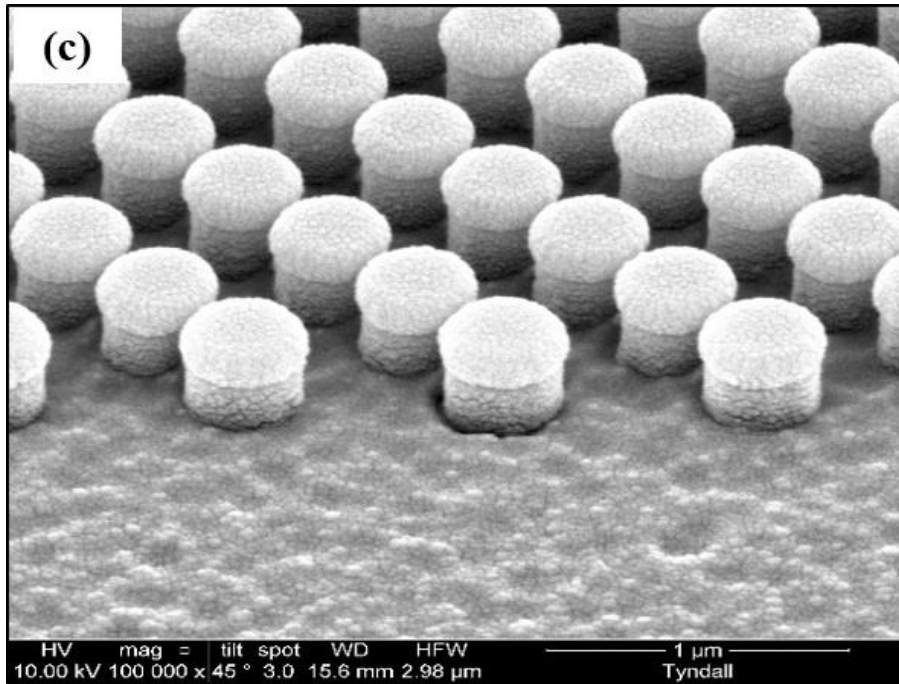


Figure 5.5 SEM's final stage Au deposition; SCIL substrate

Nanopillar array after final Au Deposition; Increasing magnification through (a) to (d) show imprinted structure quality (a) Magnification 10 K X; 10 μm scale bar (b) Magnification 25 K X; 5 μm scale bar (c) Magnification 100 K X; 1 μm scale bar (d) Magnification 400 K X; 300 nm scale bar. Acceleration voltages 10 kV, 45° tilt (ALL images)

Images (a) and (b) show imprint consistency across SERS ROI. Note in the close up images (c) and (d) the final Au deposition has covered over the 'deposits' on the pillar tops that were present after the initial deposition (Figure 5.5).

5.1.3 FDTD Analysis

FDTD modelling, is presented to investigate possible reasons for the poor experimental performance of the substrates, and also to optimise the substrate geometry for future work.

5.1.3.1 FDTD analysis of experimental performance

FDTD set up, and feature dimensions are described in methods, Figure 3.22.

The nanostructures consisted of an inner Silicon pillar, with a coating of SiO₂ and a final outer layer of Au of ~ 65 nm thickness, with pillars arranged in square, rectangular and oblique periodic arrays.

As a first step towards FDTD characterisation of the SCIL substrates, two simulations based on the ‘pre-optimised’ geometry are carried out. The relative performance of the three pillar arrays is examined, to evaluate any ‘preferred’ feature arrangement. Also, a qualitative comparison is made of Raman and FDTD intensity outputs.

An FDTD generated intensity profile is presented to show location of SERS ‘hot spots’ in the nanopillar array; Figure 5.6 and a summary table of FDTD parameters for further reference is given in Table 5.3. For more details, see Methods pages 88 and following.

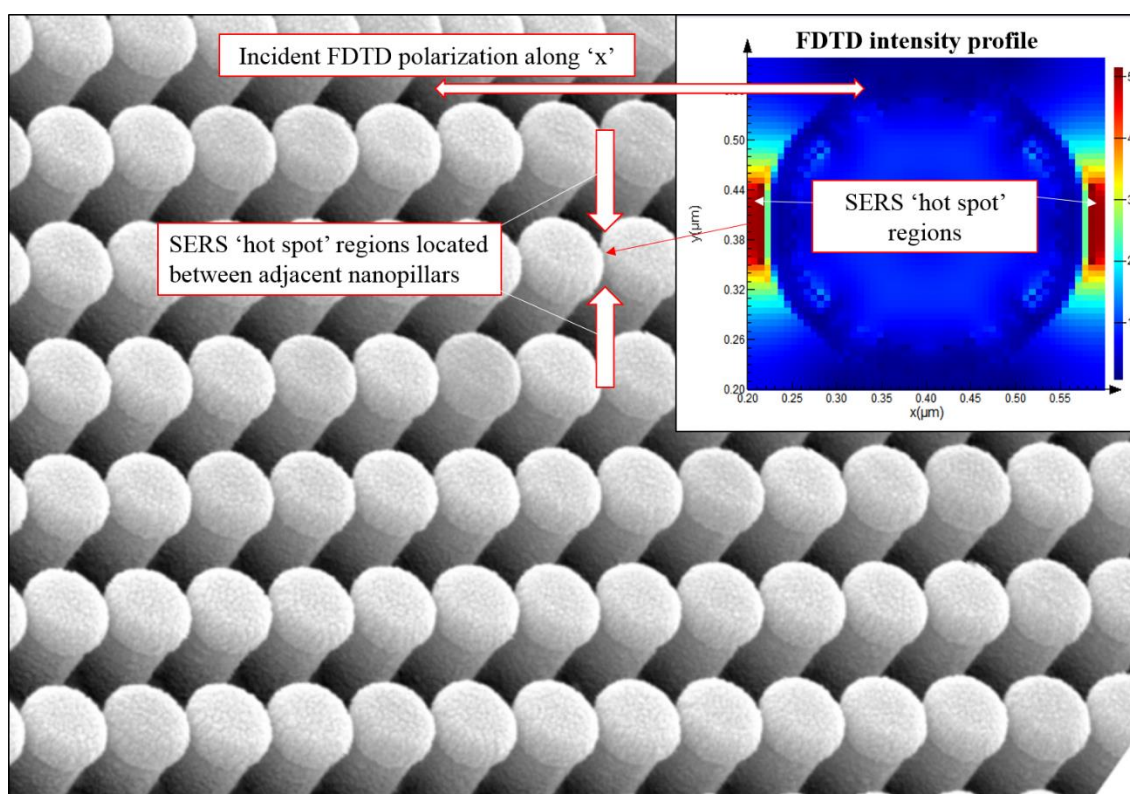


Figure 5.6 FDTD output: intensity profile showing SERS ‘hot spot’ locations

Main image: SEM zoom showing nanopillar array (Magnification 50KX; acceleration voltage 10 kV; pillar diameter 365 nm. Inset upper right: FDTD generated intensity profile in x, y showing SERS ‘hot spot’ regions at pillar edge along line through pillar centre in x. FDTD parameters; plane wave source, propagation normal to x, y and downward. Incident polarization along x. 2D x, y profile at top of pillar structures.

Table 5.3 Summary of FDTD set up parameters for Tyndall SCIL substrate

Nanopillar array 9x9 'drawn' first in GUI CAD environment. Then simulation region added to contain two pillars as a dimer. Periodic boundary conditions in x, y allow for simulation region to pass through centres of pillars.

Source			
<i>Type</i>	<i>Wavelength range</i>	<i>Propagation</i>	<i>Polarization</i>
Plane wave	400 – 900 nm	Downward & normal to x, y	Along 'x'
Boundary conditions			
Periodic in x, y		PML in z	
Mesh			
FDTD mesh accuracy* ¹ 3	Mesh override To cover 'hot spot' region between pillar structures; dx = 0.3 nm	CMT* ² enabled ✓	
Monitors			
Profile		Point time monitors	
2		3	

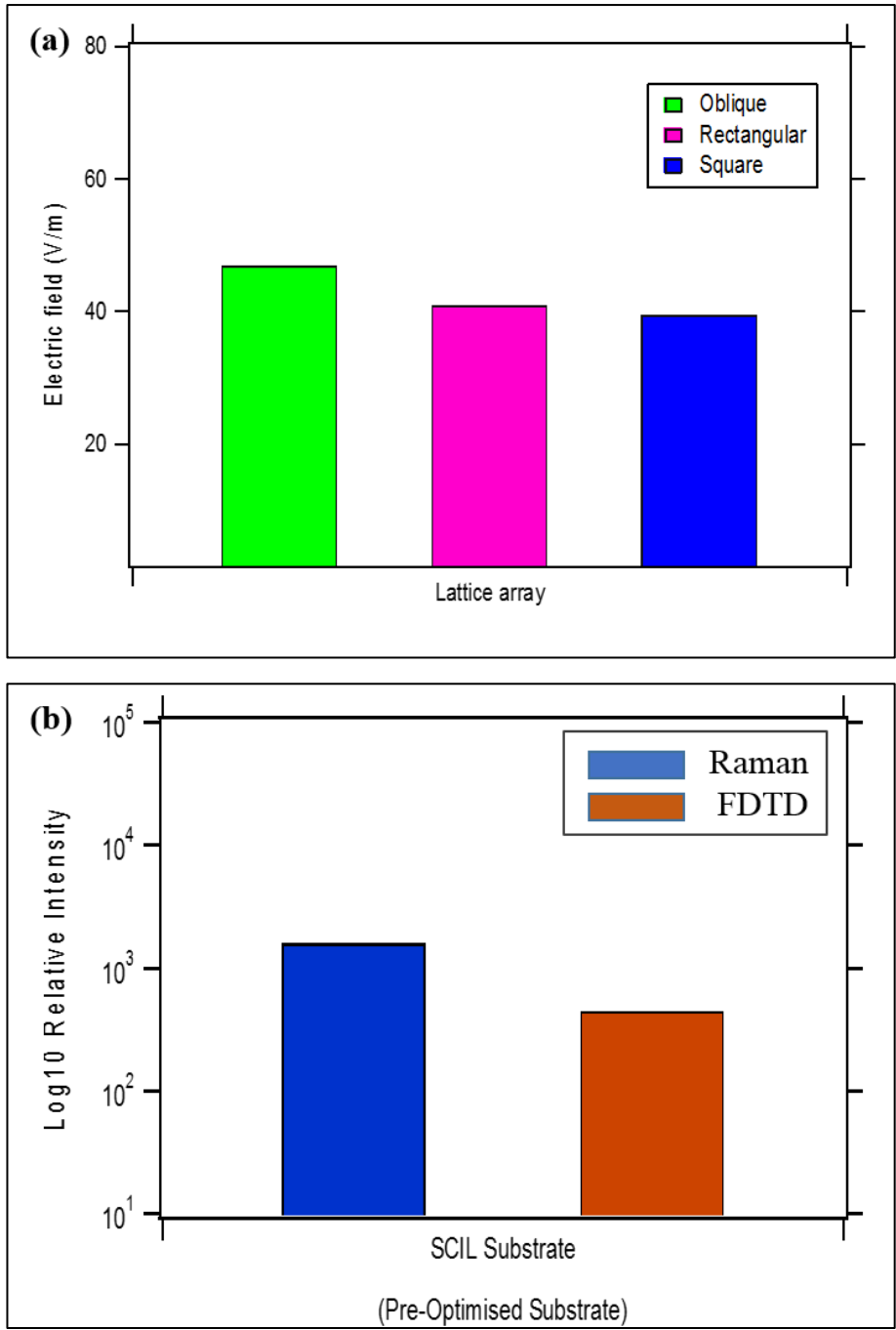


Figure 5.7 Feature geometry evaluation & FDTD/Raman comparison

(a) Electric field maxima plotted for Oblique, Rectangular and Square lattice (b) Qualitative comparison of FDTD & Raman Intensity; pre-optimised substrates. Square lattice array; FDTD parameters; plane wave source, propagation normal to x , y and downward. Incident polarization along x .

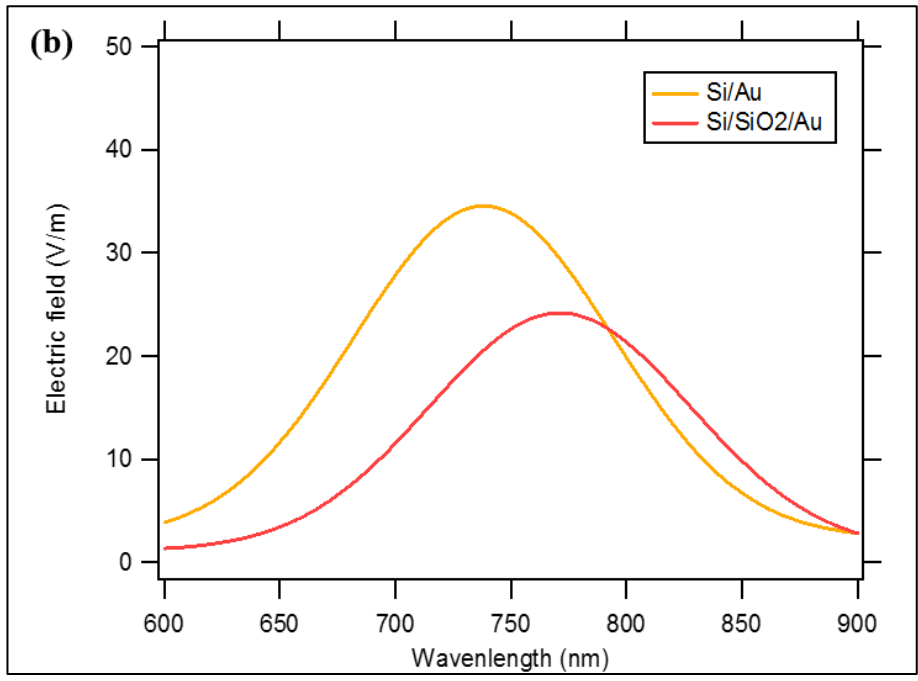
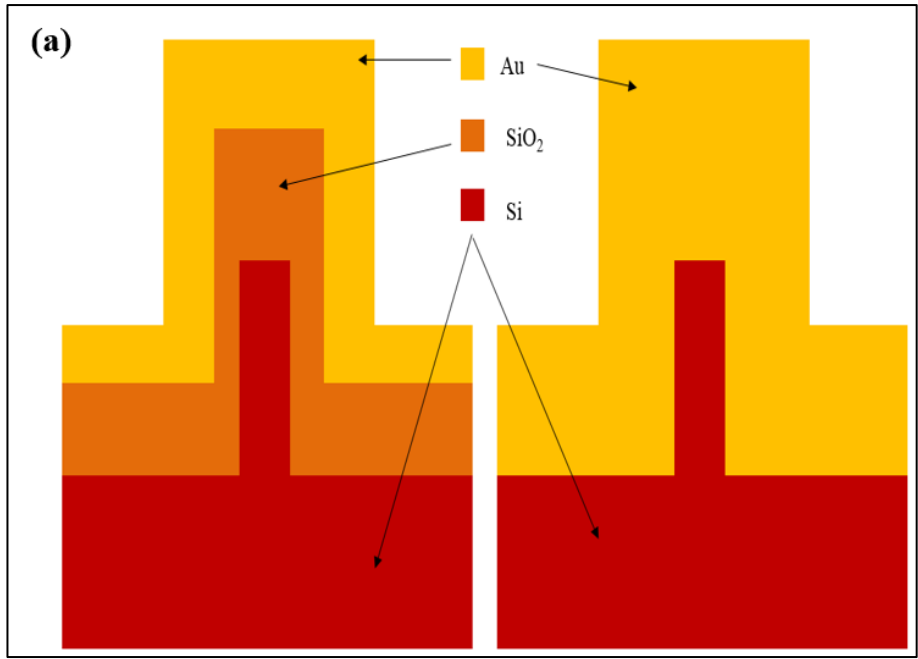
The FDTD generated electric field maxima Figure 5.7 (a) show only marginal differences between the three different arrays. The measured Raman signal for these samples also exhibited minimal variation. The FDTD intensity output in (b) is appreciably larger than the Raman intensity. Although it should be noted that the comparison is qualitative only.

Overall, the square lattice arrangement should offer a better ‘hot spot’ density, and is used below for all additional simulations. However, the FDTD simulations do indicate that the

substrate geometry alone doesn't explain the reason for the poor performance. As such, FDTD analysis is used to investigate possible causes for the poor experimental performance noted above - *Raman analysis Figure 5.1*.

Firstly, the material configuration is investigated. A material comparison is carried out to examine the difference in SERS response for the pillars, with and without the intermediate SiO₂ layer. The SiO₂ layer is used to 'bulk' out the structures prior to Au deposition. Secondly, the effect that a possible contaminant layer would be likely to have, on the SERS activity is examined. These two simulations are discussed in more detail following. The SERS response that would result from varying the interstructure spacing is examined below (page 149) in the section dealing with FDTD optimization.

In order to examine the effect that the SiO₂ layer had on the SERS response, simulations were carried out for a Silicon pillar directly overlaid with Au, and then a Si + SiO₂ + Au combination.



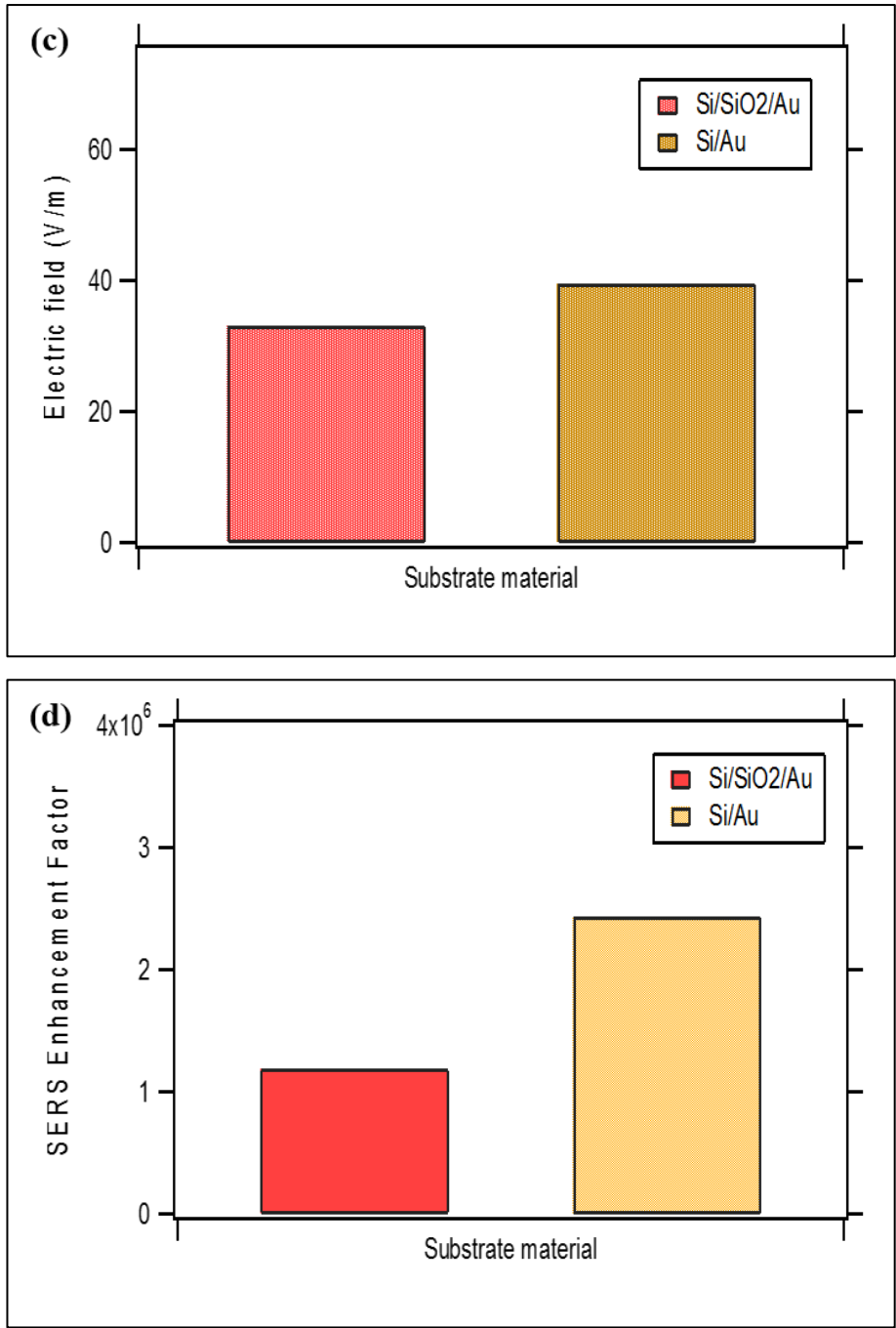


Figure 5.8 FDTD comparison of material dependent SERS response for square nanopillar array with & without SiO₂ intermediate layer

(a) Schematic; material configuration FDTD set-up; with & without SiO₂ layer (b) Electric field vs wavelength; (c) Electric field maxima (d) SERS EF. All figures: Square lattice array; simulations with & without intermediate SiO₂ layer.

The magnitude of the electric field maxima, Figure 5.8 (b) is larger for the simulation without SiO₂. Additionally, the resonance peak (SiO₂ present) is slightly red-shifted; (b) above. The FDTD generated SERS enhancement is reduced by ~ 50 %, due to the introduction of the SiO₂ layer (d). The use of SiO₂ as a material support for SERS substrates has been reported [193]. It has also been used as an intermediate layer between a Silicon ‘base’ and Ag outer film in EBL fabricated substrates [194]. However, a greater SERS response can be obtained via a metallic layer being directly overlaid on Silicon, without an intermediate SiO₂ layer.

Next, we examine the possible effect a contaminant would have on the SERS response. The SCIL imprinted wafer contained $70 \times 70 \mu\text{m}$ regions of the pillar arrays separated by $\sim 10 \text{ mm}$; Figure 5.9.

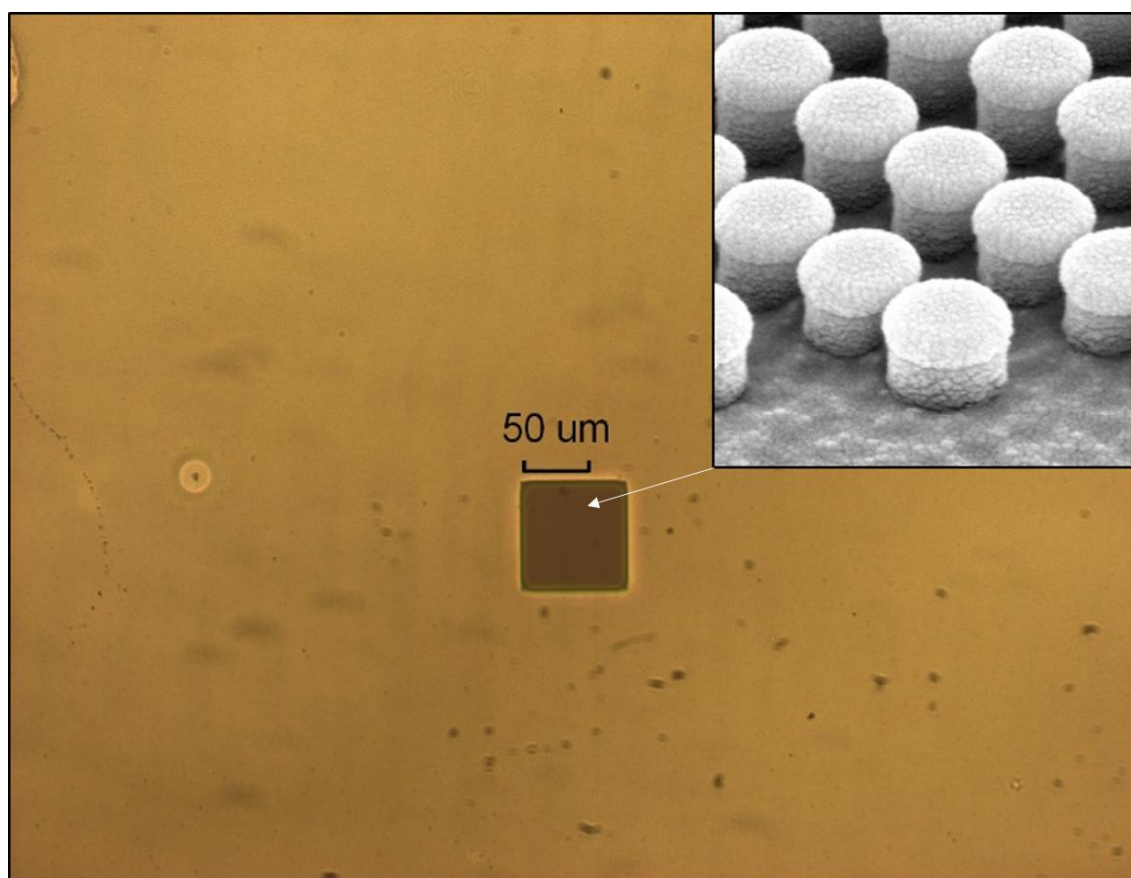


Figure 5.9 Nanostructured imprinted region on silicon wafer

Imprinted region on wafer $\sim 70 \times 70 \mu\text{m}$ with zoom of structures inset (from SEM image at 100 KX Magnification). Olympus Measuring Microscope (STM-MJS2) 40x Objective, Image acquisition with 'Infinity Analyse software' 2-C-185235

Precision dicing of the imprinted wafer was carried out in order to separate the SERS-active regions for Raman analysis. Before dicing, the wafer was first coated with a thin flexible polymer film (Polydimethylglutarimide) as a protective layer for the nanostructures. This was afterwards removed by cleaning with acetone and Isopropyl alcohol (IPA).

The possibility exists, that a thin film residue from the protective layer may have been present on the surface. Thus, a simulation was carried out to examine the 'impact' on the SERS signal, of a thin contaminant film (5 nm) present on the Au surface. The refractive index data for a polymer (PDMS) was uploaded to the FDTD material data base, and selected for the outer layer material, with simulation outputs shown below in Figure 5.10.

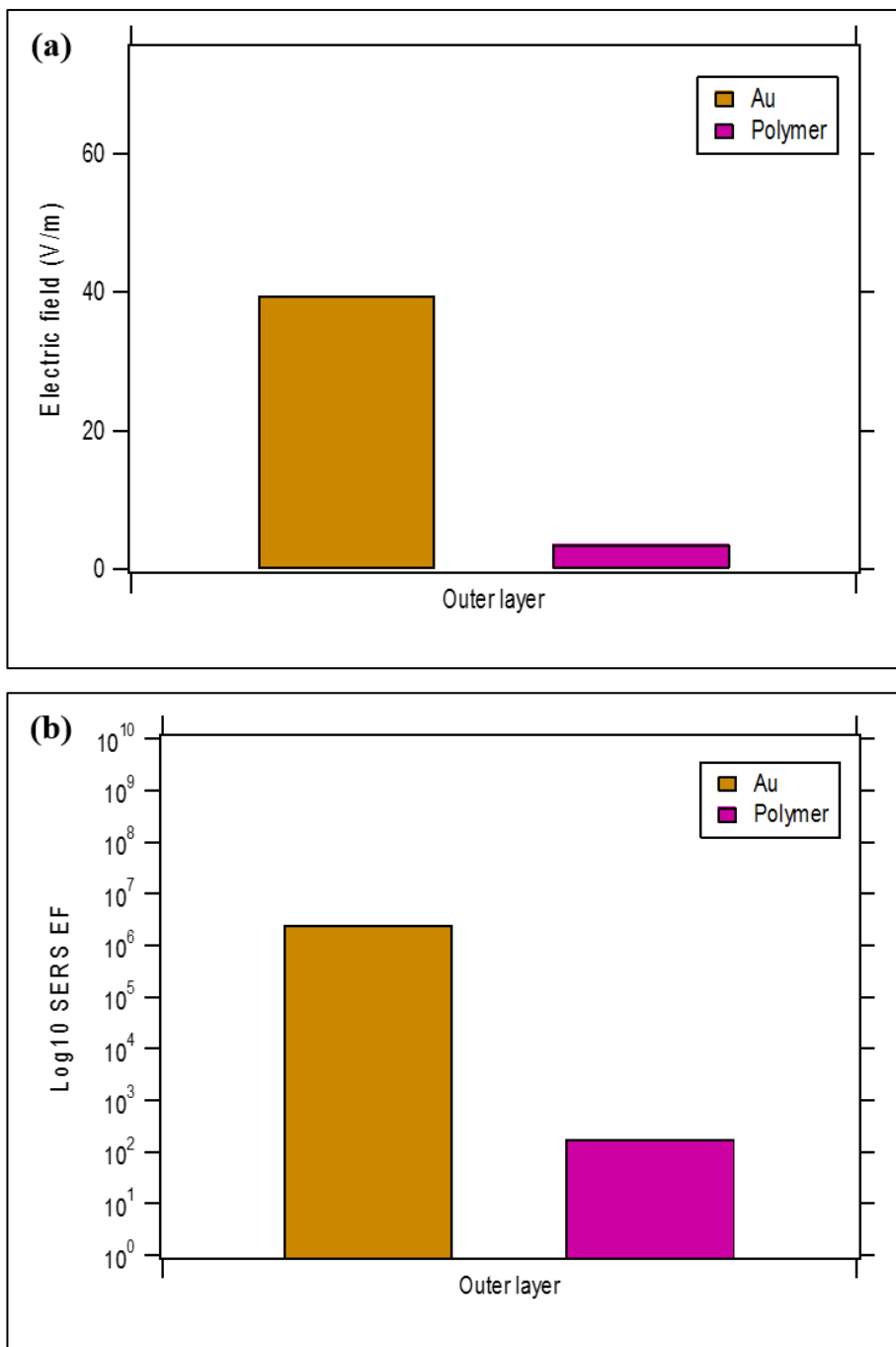


Figure 5.10 FDTD simulation for a ‘contaminant’ layer on substrate surface

Simulation for a 5 nm polymer layer contaminant (a) Electric field maxima outputs for an ‘Au’ and a polymer outer layer (b) Semi-log plot of SERS EF vs outer layer material composition. FDTD parameters; plane wave source, propagation normal to x, y and downward. Incident polarization along x.

These simulations illustrate the effect on the SERS response due to the presence of a surface contaminant. For a polymer film of only 5 nm thickness, FDTD outputs show a significant difference in SERS enhancement. There is a difference in the EF of up to four orders of magnitude; 2.4×10^6 & 1.8×10^2 respectively (FDTD EF calculation). This is illustrated in (b); semi-log plot used for visual purposes.

From the above investigation, into possible reasons for the poor SERS performance of the SCIL substrates, the following is concluded. Firstly, the presence of the SiO₂ layer, would certainly hinder the SERS enhancement. Though in itself, it would not be enough to explain the reduced levels of enhancement. However, if a contaminant layer had been present on the substrate surface, it would have had a significant impact on performance. While this is unlikely and would be detectable on the Raman spectra this simulation stresses the importance of rigorous O₂ cleaning post dicing.

A more complete understanding of the observed experimental performance can be gained by using FDTD analysis to optimise the fabrication process.

5.1.3.2 FDTD Optimisation

The fabrication feature resolution, is dictated by the resolution achievable using the e-beam patterning. Factors such as spot size and electron scattering in the resist and substrate introduce a proximity effect limit [195]. A SEM image for the resolution test is shown below which illustrates edging defects for dimensions < 100 nm. Simulations were performed with due consideration to the practical limitations imposed by the achievable fabrication parameters, e.g. Silicon pillar diameter and separation of 100 nm.

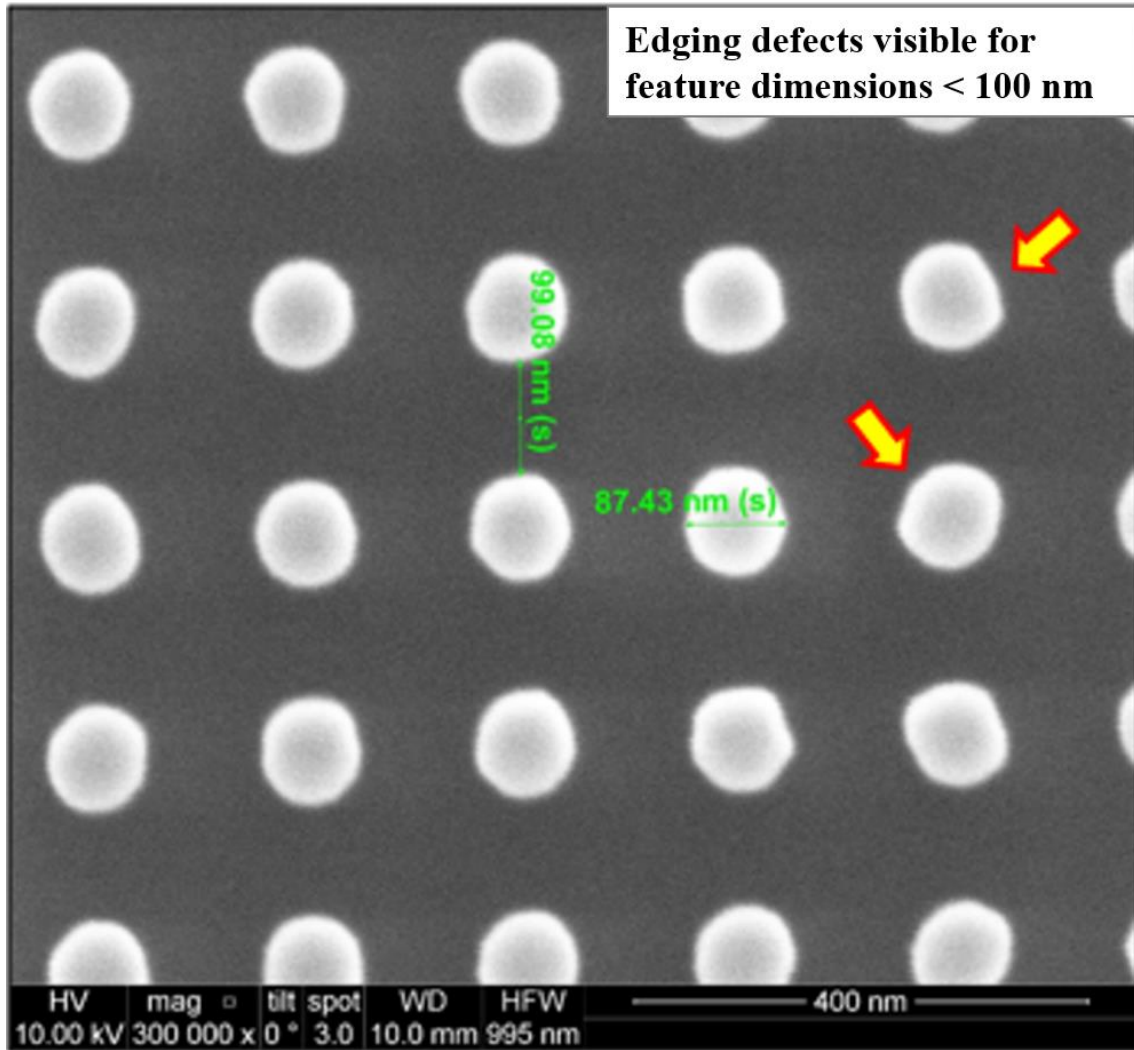


Figure 5.11 Resolution test for e-beam patterning; Tyndall substrates

Poor resolution for structure features below ~ 100 nm, edging defects illustrated upper right of image, pillar square lattice arrangement. SEM: 300 K X Magnification, 400 nm scale bar acceleration voltage 10 kV

The substrate parameters that were optimized with FDTD are as follows: diameter, height, ‘nearest neighbour’ spacing and Au layer thickness.

Table 5.4 FDTD; diameter dependent outputs

Pillar diameter (nm)	E max (V/m)	Lambda resonance (nm)	Pillar diameter (nm)	E max (V/m)	Lambda resonance (nm)
120	19.56	579	280	8.27	742
160	7.06	641	320	22.28	767
200	6.61	667	360	6.91	786
240	7.71	725	400	8.28	943

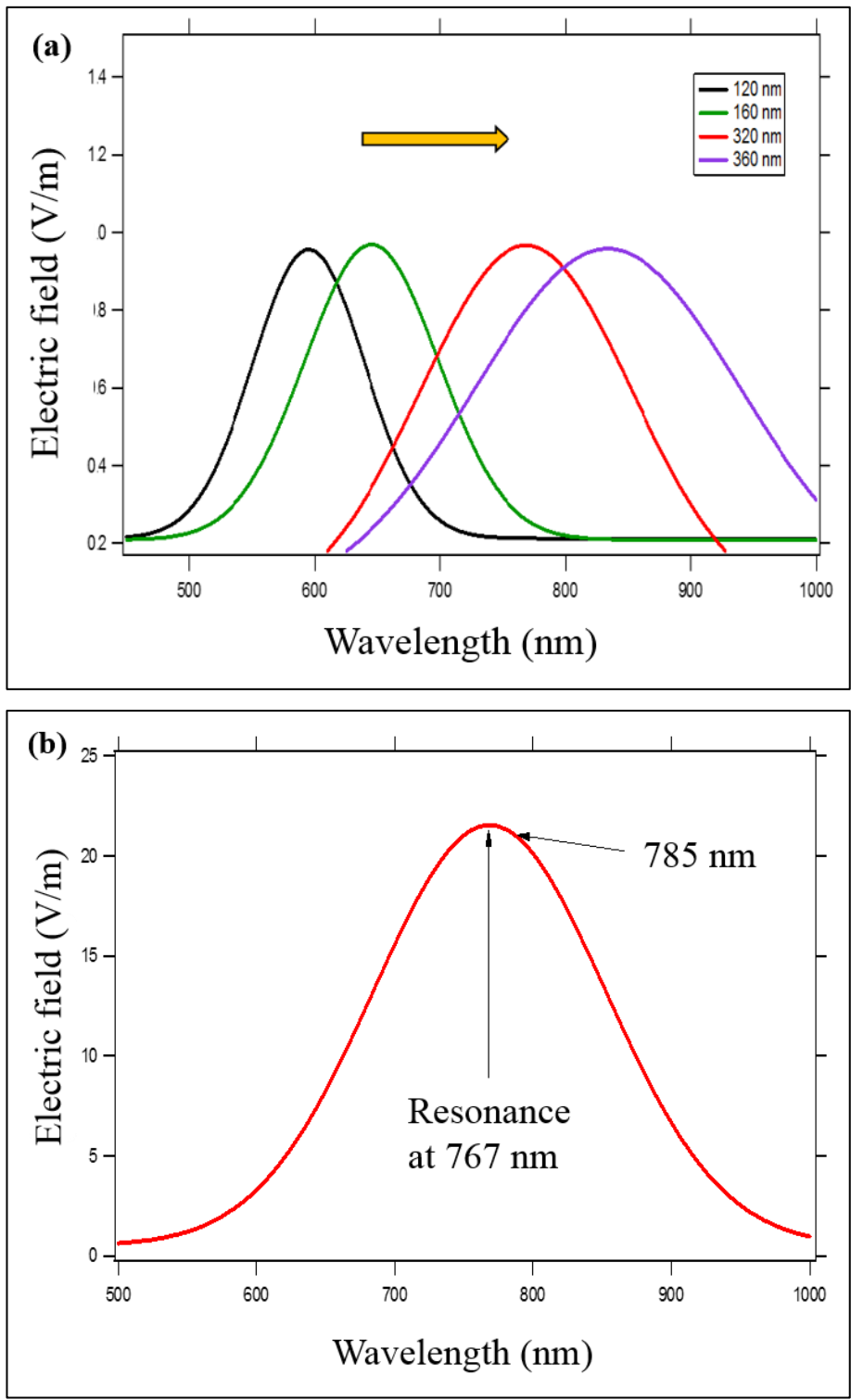


Figure 5.12 FDTD simulation for range of structure diameters. Electric field vs wavelength
 (a) Electric field vs wavelength - showing resonance peak red shifted with increasing structure diameter. Electric field data normalized and curve fitted (Gaussian) for visual purposes (b) E-field maxima vs wavelength for optimum structure diameter of 320 nm

The pillar diameters of 120 & 320 (nm) yielded the greatest SERS enhancement. However, the lambda resonance peaks were at 579 & 767 (nm) respectively. Choosing a diameter of

320 nm, will yield the largest SERS EF, and in addition will effectively ‘tune’ the substrate close to the desired 785 nm excitation wavelength.

Using the optimum structure diameter of 320 nm gained from the above simulations, a parameter sweep simulation was then carried out for structure height, with results recorded in Figure 5.13. Two parameter sweeps for structure height were carried out. The first for the range: 100 – 600 nm. The optimum height output was 350 nm, following this result, a second sweep was performed for the range: 300 – 400 nm to ‘fine tune’ the height optimisation; Figure 5.13.

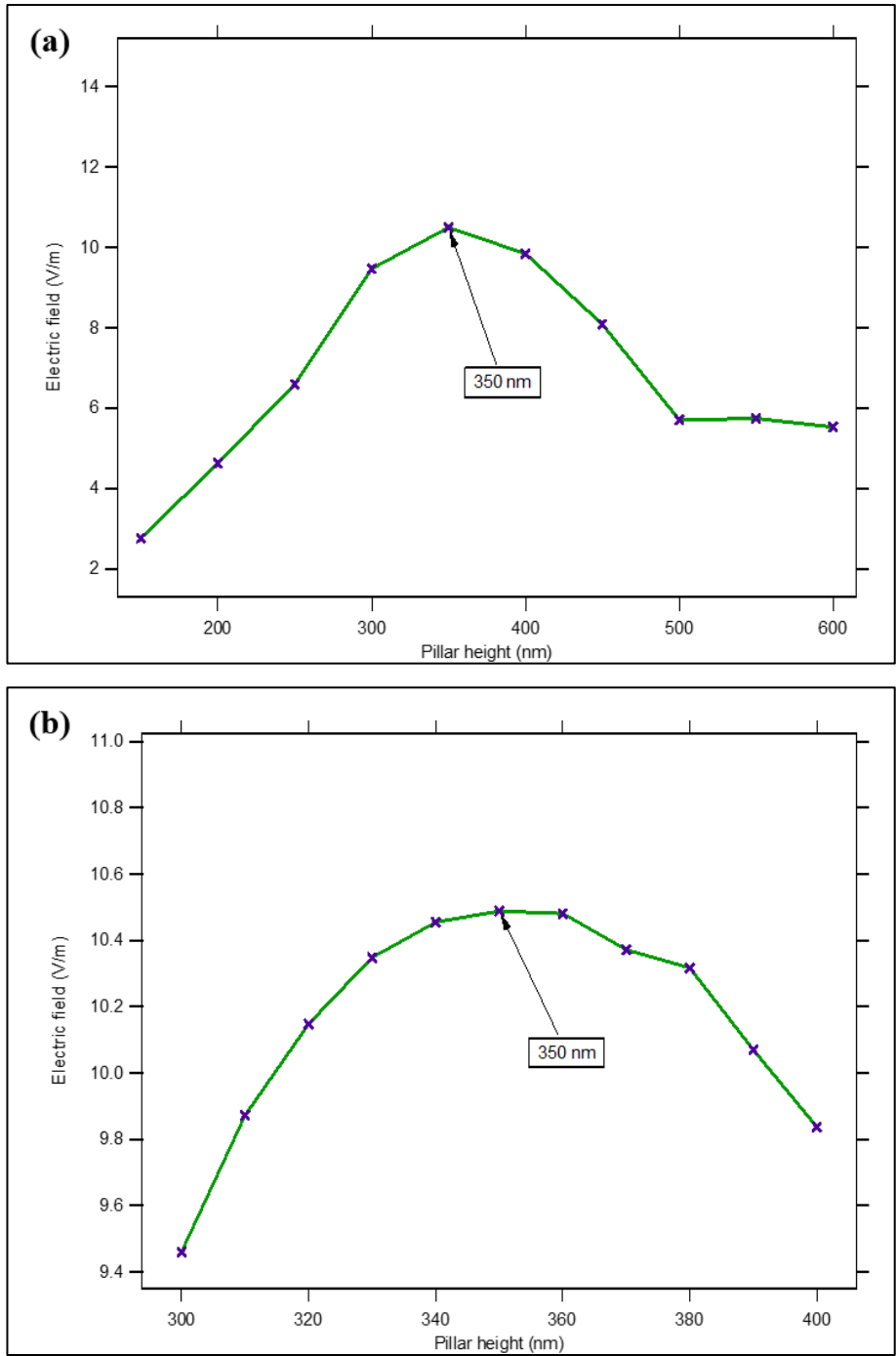


Figure 5.13 FDTD parameter sweep; pillar height. Electric field vs pillar height

Parameter sweep range: (a) 100 to 600 nm (b) 300 to 400 nm. Both plots: Maximum Electric field at 350 nm structure height. FDTD parameters; plane wave source, propagation normal to x, y and downward. Incident polarization along x.

Based on the above simulations the optimized values for Nanopillar diameter and height are: 320 & 350 (nm) respectively. These dimensions are used in the next simulations to optimize both interstructure spacing, and Au thickness.

Simulations were carried out for the following range of gaps between structures: 20, 15, 10, 5, 2.5 and '0' (nm). Note, the value at zero nm \equiv touching pillars. The final parameter

considered for optimisation, is the thickness of the Au layer. A ‘parameter sweep’ was carried out to simulate variation in electric field with Au thickness using a structure spacing of 5 nm.

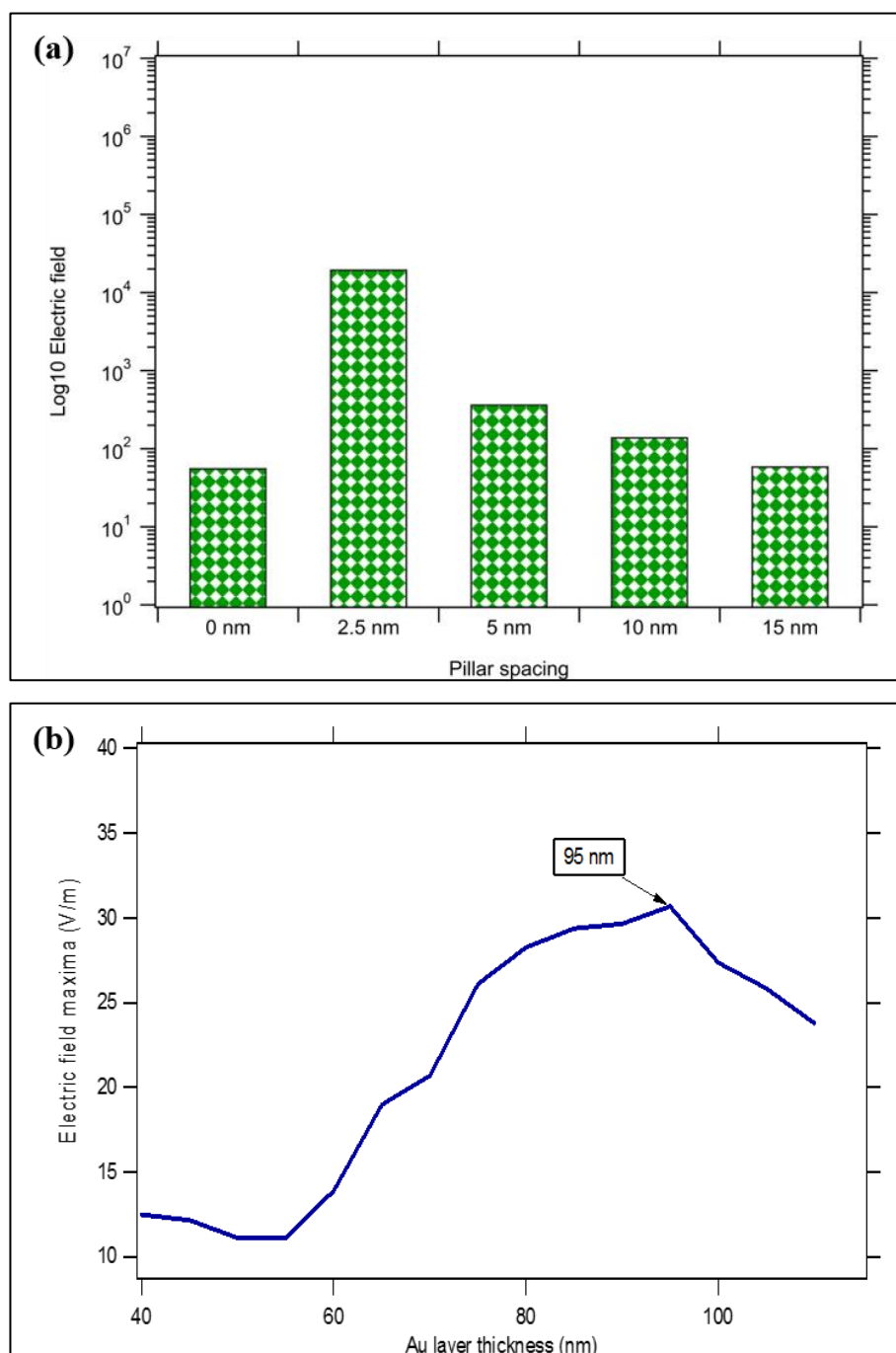


Figure 5.14 FDTD Optimised structure gap & Au thickness

(a) Semi-Log plot: Electric field vs inter-structure spacing; optimum gap value at 2.5 nm (b) Electric field maxima vs Au thickness; optimum Au layer at 95 nm. FDTD parameters; plane wave source, propagation normal to x, y and downward. Incident polarization along x.

From the data presented in Figure 5.14 (a), when the pillar spacing is at 5 nm, an excellent SERS response is achieved. As the gap decreases to 2.5 nm, there is a substantial increase to the SERS enhancement. Based on the FDTD models carried out above, a structure gap of ≤ 10 nm, should yield a significantly improved SERS response. For example, there is a difference in EF of \sim two orders of magnitude between a 10 and a 5 nm gap; $3.9e^8$ and $1.9e^{10}$

respectively. The optimum thickness of Au layer was found to be 95 nm, based on a Silicon inner pillar of 225 nm; (b).

Table 5.5 FDTD optimised parameters; summary table

FDTD Optimized Parameter	All length dimensions (nm)
Nanopillar diameter	320
Nanopillar height	350
Structure spacing	≤ 10
Material configuration	<i>Silicon/Au</i>
Au thickness	≥ 95

5.2 Nanogap substrates

The second 'in-house' samples considered were the Nanogap substrates. An array of nanoholes were imprinted using NIL. Post etching, raised structures remained leaving an array of nanogaps between them; shown in the SEM analysis below. A bi-metallic layer of Au and Ag was then deposited to generate a SERS response.

5.2.1 Raman Analysis; *Pre-Optimized*

Nanogap substrates were Raman tested after functionalization with 2NT. Raman analysis was carried out at 785 nm excitation and at two different laser power settings. A setting of 3.9 mW and 20x objective allowed for comparison with the Tyndall substrate. These Raman outputs are shown above in Figure 5.2 above (SCIL vs NIL substrate comparison). However, no comparison was made with the commercial substrates of Results 1 (page 103). This was due to the absence of a common laser power setting. The Raman analysis for the commercial substrates was carried out at 0.006 mW, with signal saturation occurring at any higher settings.

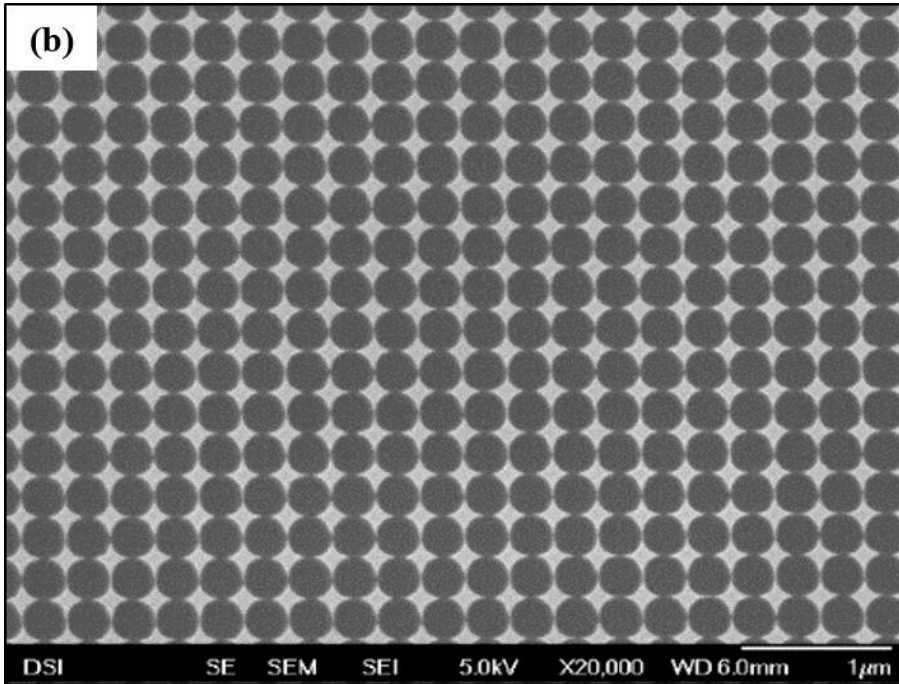
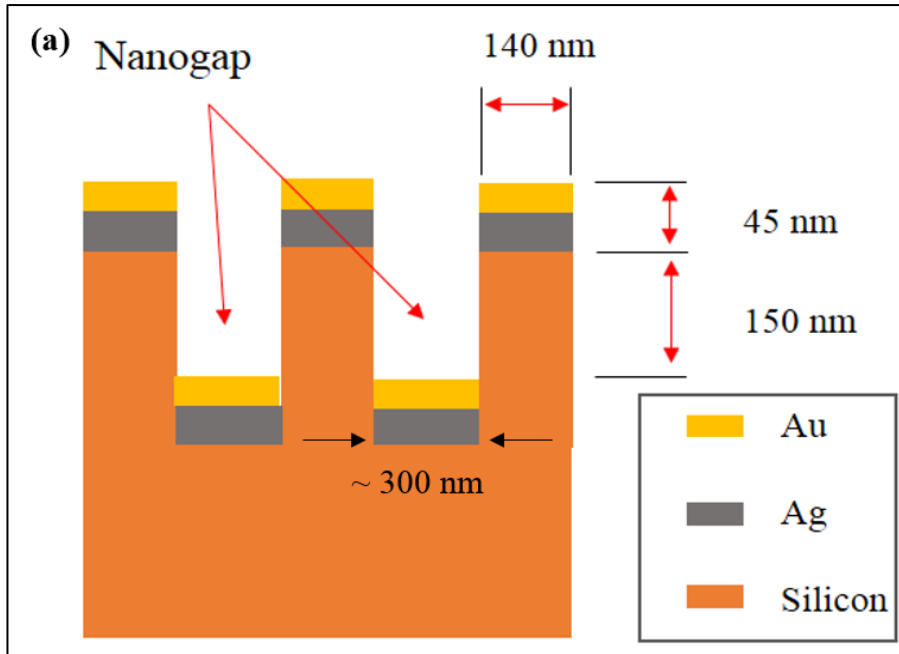
Following these initial Raman measurements, SEM and FDTD analysis was carried out in order to optimise the surface geometry of the Nanogap substrates. Raman analysis of the pre-optimised Nanogap substrates is presented with the optimised ones following optimisation.

5.2.2 SEM Characterization

SEM images for the Nanogap substrates are shown below in Figure 5.15. The array of raised structures that remain post etching on the substrate are visible in (b) with the brighter objects surrounding the darker holes. The structures are shown more clearly in the zoom image of (c). In the cross-section view (d) the bi-metallic layers at the top of the structures can be discerned, the schematic in (a) helps to illustrate the material configuration.

The benefit to using a bimetallic Ag/Au surface layer is twofold. Firstly, an Ag/Au combination yields a larger SERS EF than a purely Au layer. Also, a single Ag layer degrades much quicker than Au, thus reducing substrate shelf life. Bimetallic Ag/Au surfaces have been extensively used in SERS research [196-199]

The substrates were fabricated using deep UV photolithography, a technique also used by Fang et al. to fabricate a similar nanohole array [185].



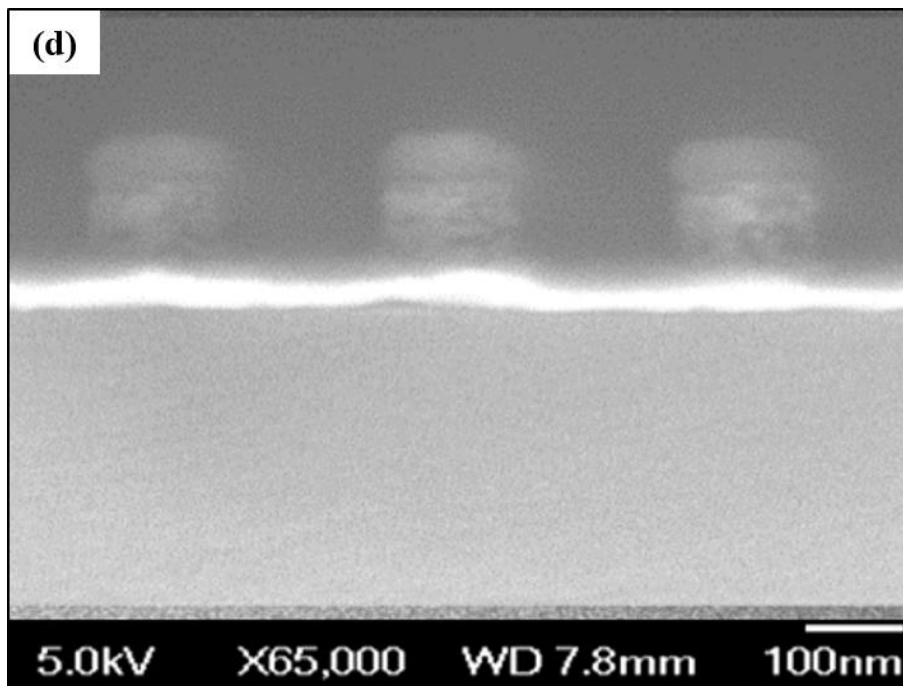
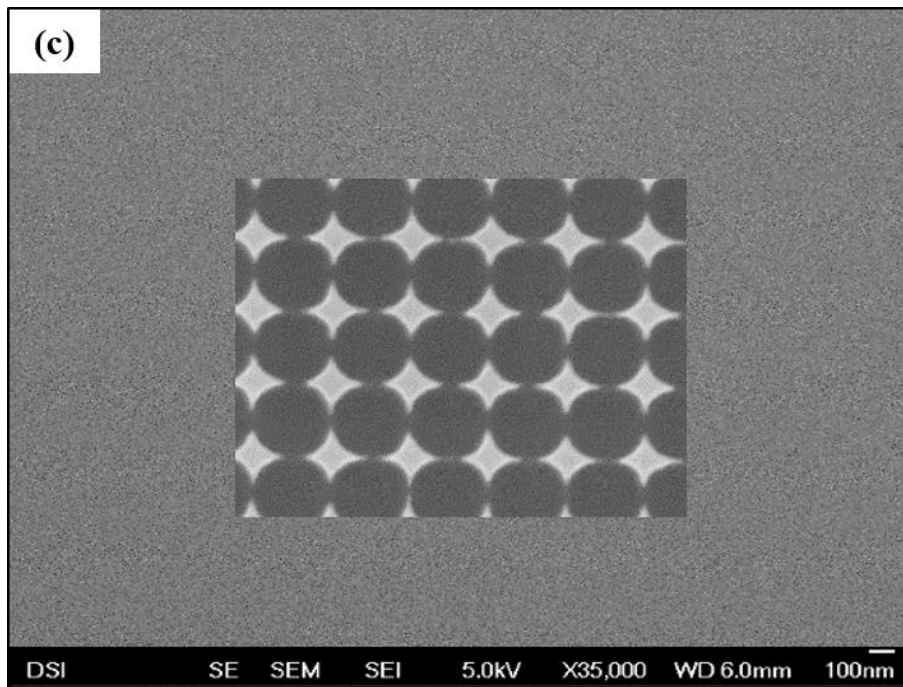


Figure 5.15 Nanogap substrates

(a) Schematic showing material configuration and structure dimensions used for FDTD simulation set up; surface bimetallic layer 45 nm thickness (Ag 35 nm + Au 10 nm). Figures (b) to (c) - SEM images (b) Large area view showing nanohole density; Magnification 20 K X, 1 μm scale bar (c) Zoom; Magnification 35 K X, 100 nm scale bar (c) Cross-section view; Magnification 65 K X, 100 nm scale bar. Acceleration voltage all SEM's 5 kV, and provided by J. Kumar A*STAR research facility, Singapore.

5.2.3 FDTD Optimization

Optimization of the nanogap substrates was performed using FDTD analysis. The main parameter affecting the SERS response that could be varied experimentally was the interstructure spacing. This was achieved via further deposition of Au layers. The simulation parameters are given in Table 5.6 and an illustration of the structure geometry is shown in Figure 5.16.

Table 5.6 Summary of FDTD set up parameters for Nanogap substrates

The marked profile region of Figure 5.16 shows structure type used for simulation

Source			
<i>Type</i>	<i>Wavelength range</i>	<i>Propagation</i>	<i>Polarization</i>
Plane wave	400 – 900 nm	Downward & normal to x, y	Along 'x'
Boundary conditions			
Periodic in x, y		PML in z	
Mesh			
FDTD mesh accuracy* ¹ 3	Mesh override To cover 'hot spot' region between 'raised' bimetallic structures; dx = 0.3 nm	CMT* ² enabled ✓	
Monitors			
Profile		Point time monitors	
2		3	

The edge of the dimer simulation objects is approximately equivalent to a pillar, as shown in Figure 5.16.

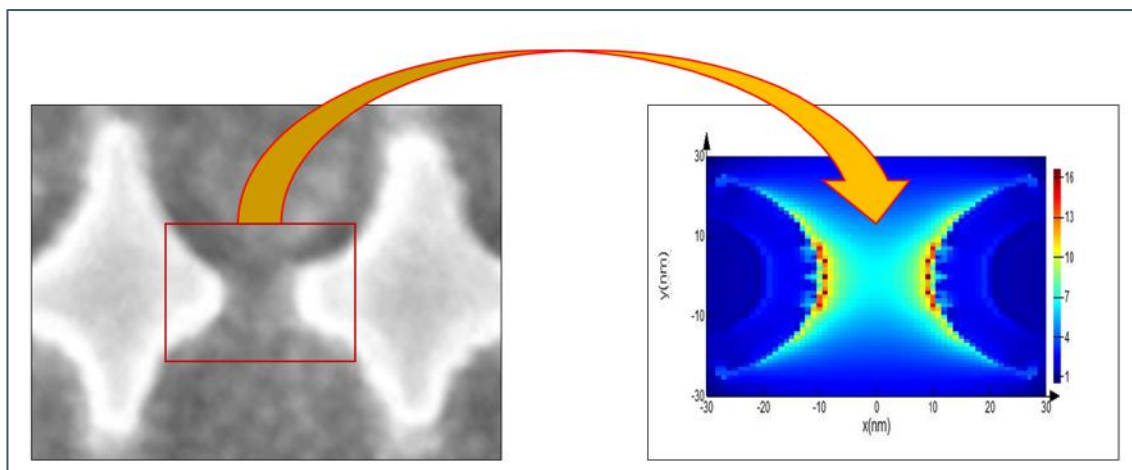


Figure 5.16 Simulation region for FDTD analysis of gap parameter

FDTD simulation shown in left image as marked 2D profile. Simulation output for electric field shown in right image. Spatial distribution of field lies within simulation region. FDTD parameters; plane wave source, propagation normal to x, y and downward. Note incident polarization along 'x'. Scale bar – electric field (V/m)

FDTD simulation region illustrated by 2D profile marked in red left image. For a source with 'x' polarisation, field maxima will be distributed about feature edges and along a line through structure centres as shown in right image.

Initial modelling revealed that for gaps > 40 nm the SERS response exhibited minimal variation. Accordingly, further simulations were carried out for a range of gap values beginning at 40 nm and decreasing to 2 nm as illustrated in Figure 5.17. The SERS EF values are presented in Table 5.7.

Table 5.7 FDTD generated SERS EF values for variation in interstructure spacing

The influence of coupled Plasmon resonance becomes more noticeable at gaps of less than 10 nm

Gap (nm)	40	30	20	10	5	2
SERS EF	2×10^6	2.1×10^6	6.2×10^6	3.2×10^7	2.3×10^8	1.6×10^{10}

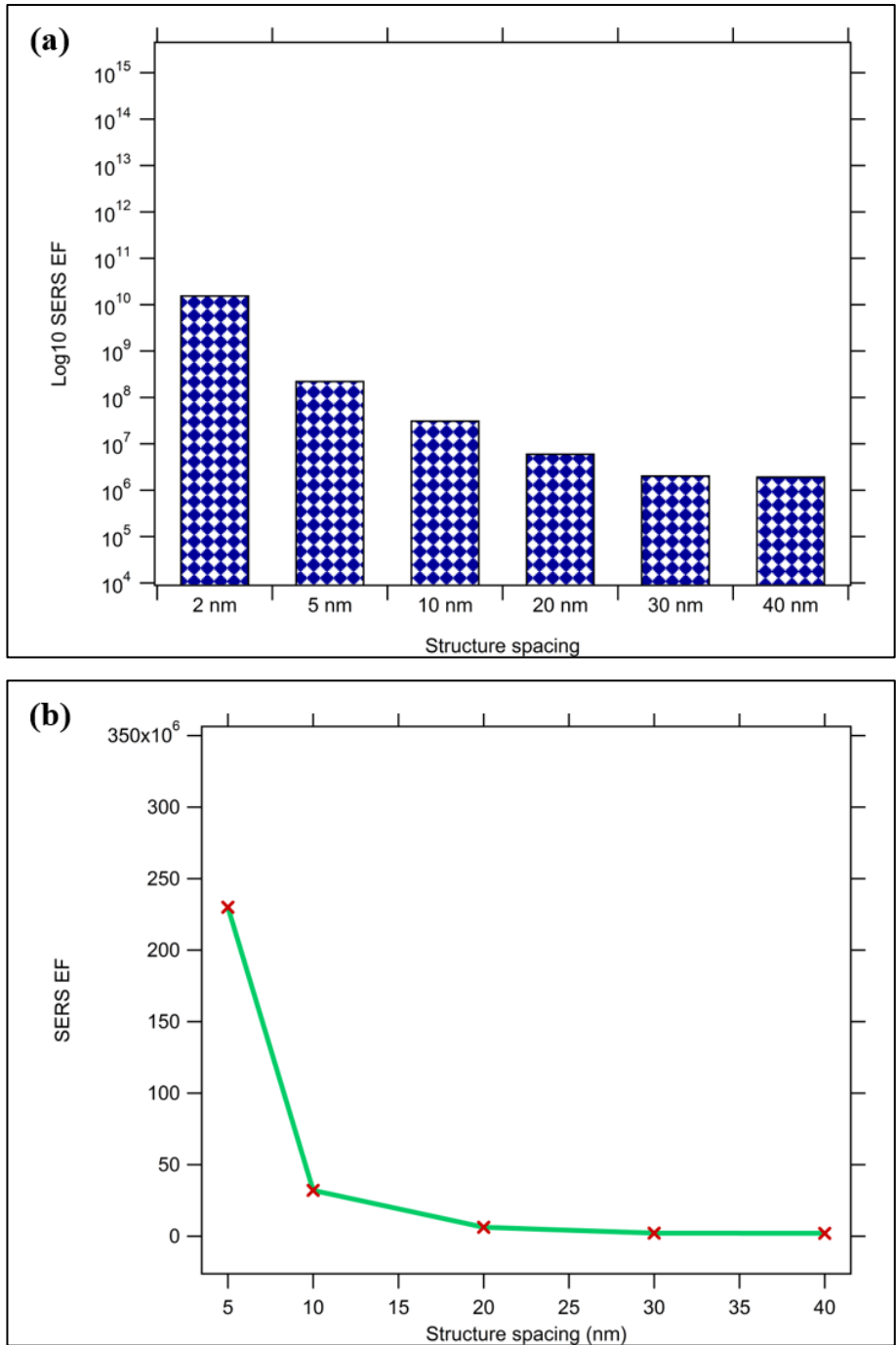
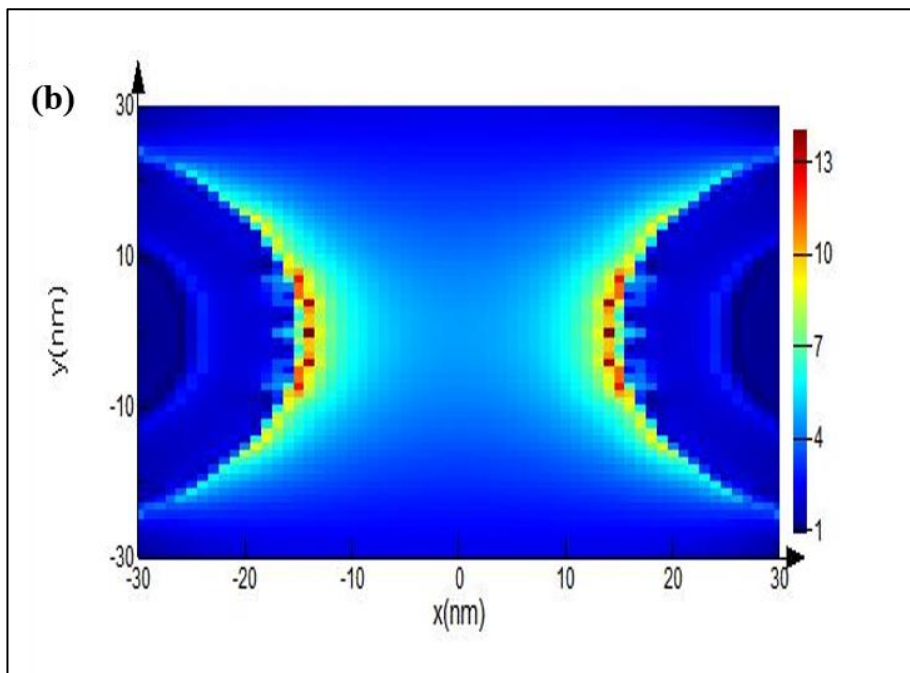
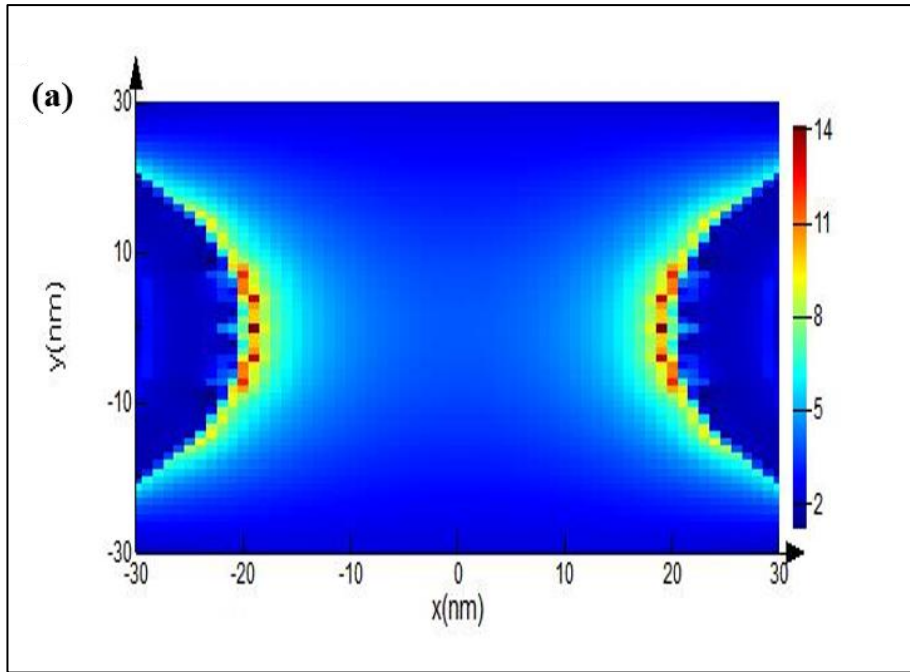
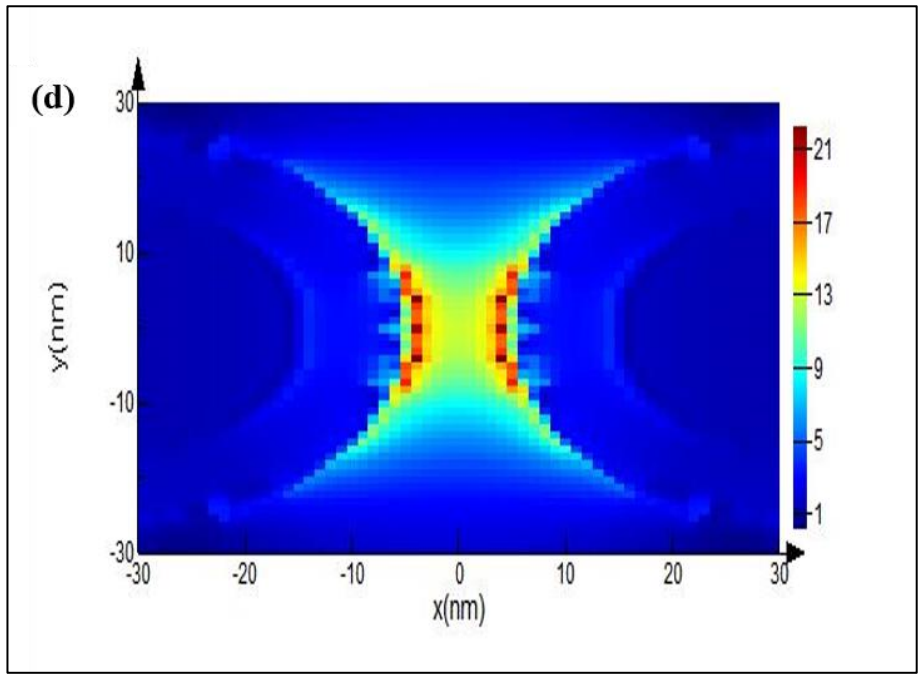
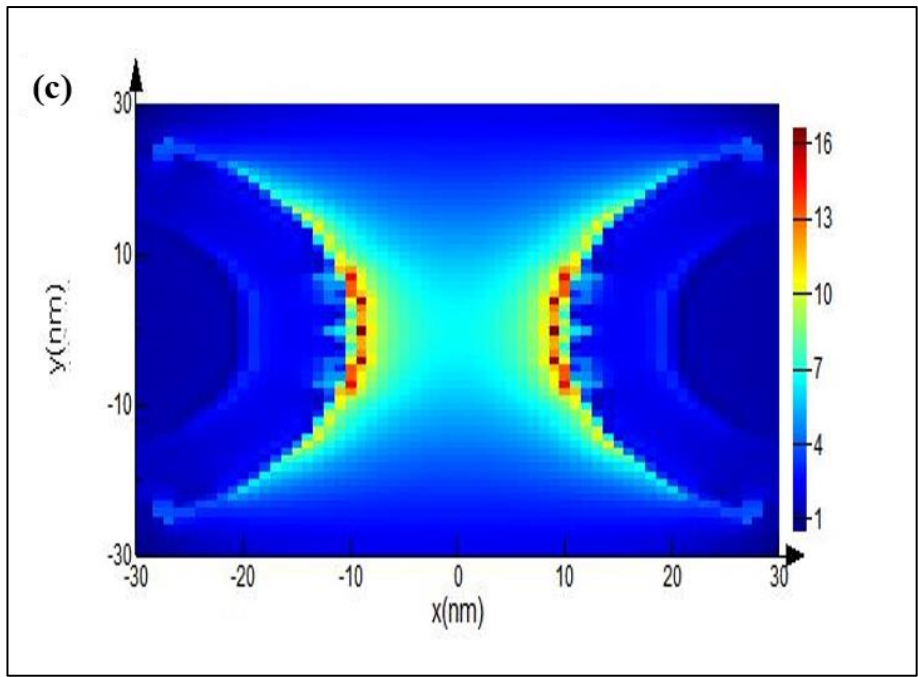


Figure 5.17 FDTD analysis; variation of SERS EF with gap dimension

(a) Semi-Log plot of SERS EF for gap range: 40-2 nm (b) SERS EF vs gap; without 2 nm data point for visual purposes; the influence of CPR is seen as gap parameter is decreased below 20 nm.

The magnitude of the SERS enhancement is strongly increased at gaps less than 20 nm. This is due to the increasing influence of coupled Plasmon resonance (CPR) as illustrated next in Figure 5.18.





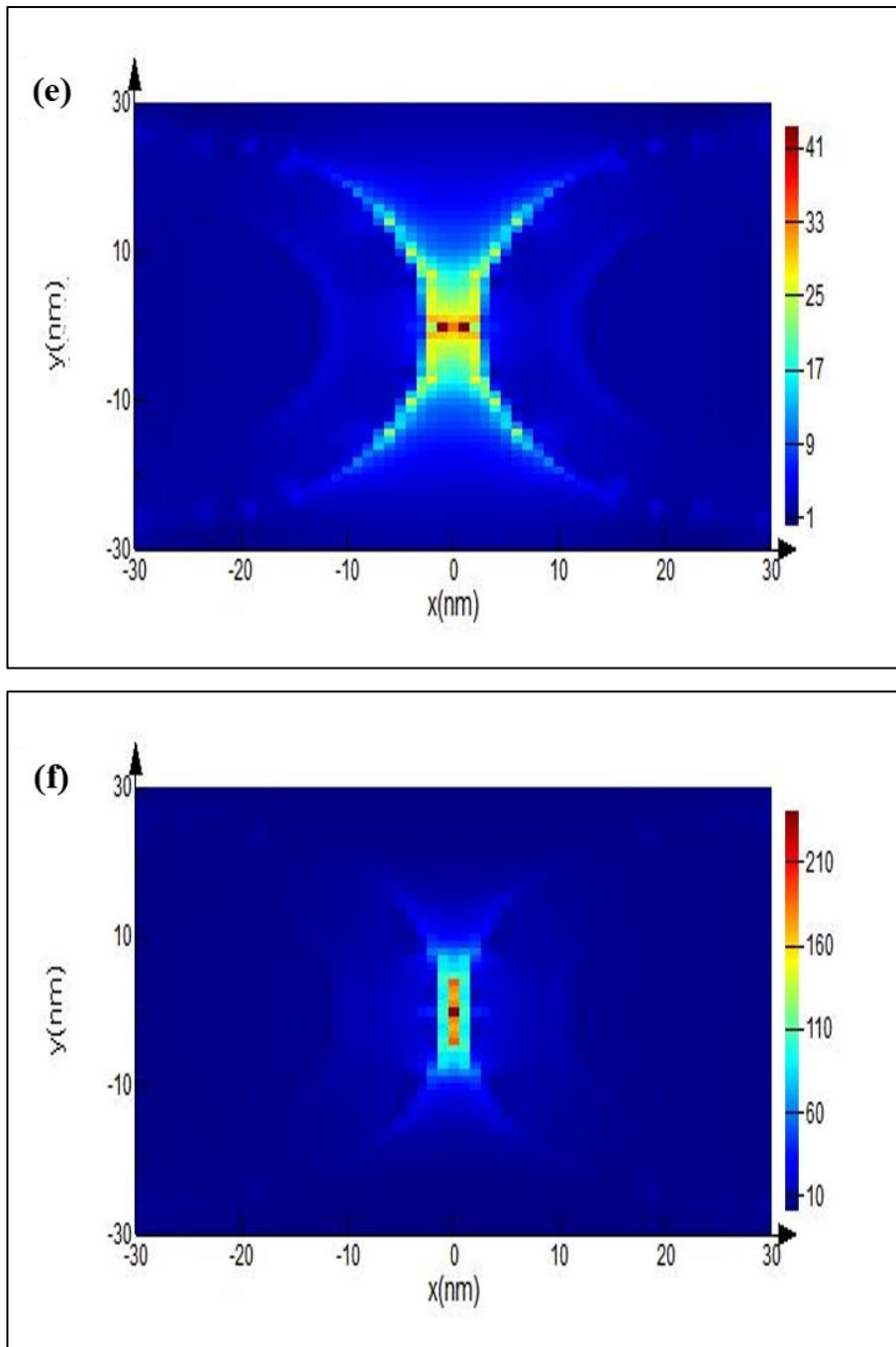


Figure 5.18 FDTD Electric field profiles for variation of gap dimensions

Simulations for variation of gap parameter shown for the range: 40-2 nm; 40; 30; 20; 10; 5; 2 nm (a) to (f) respectively. Plane wave source, Polarization along x and normal to x, y (downward). Scale bar Electric field (V/m)

As the gap decreases from 40 nm (a), the individual local electric fields begin to interact resulting in CPR, note scale bar to right of images. For example, decreasing the gap from 40 – 5 nm results in an increase in SERS enhancement of ~ three orders of magnitude. The individual field maxima are located about the edges of the structures in (a) & (b) with no CPR noted; gaps of 40 & 30 nm respectively. At 20 nm the fields can be seen to interact as CPR begins to influence the field strength and spatial distribution. As the structures are brought still closer (d) through to (f) the interacting fields generate a single ‘hot spot’ region between the structures (e) & (f).

Following the gap optimisation, the substrates were reworked to attempt to reduce the spacing between adjacent structures. Decreasing the structure spacing was achieved via further deposition, with Raman analysis presented next.

5.2.4 Raman Analysis; Optimized Substrates

Eight substrates were ‘reworked’ by further deposition of gold. After initial deposition, three substrates were removed, and a further gold layer was put down on the remaining five substrates to further reduce the gap dimension.

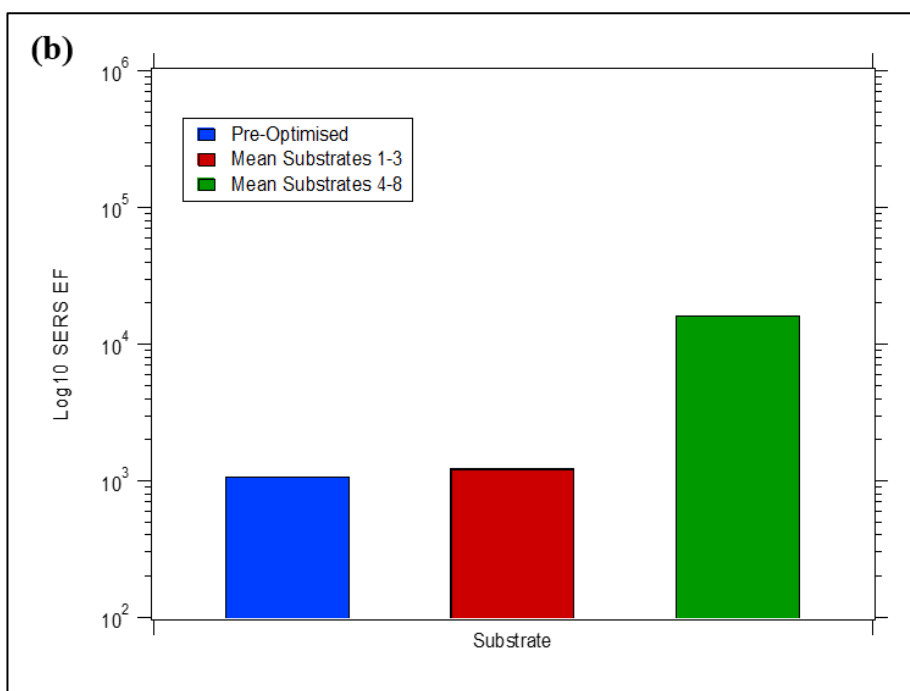
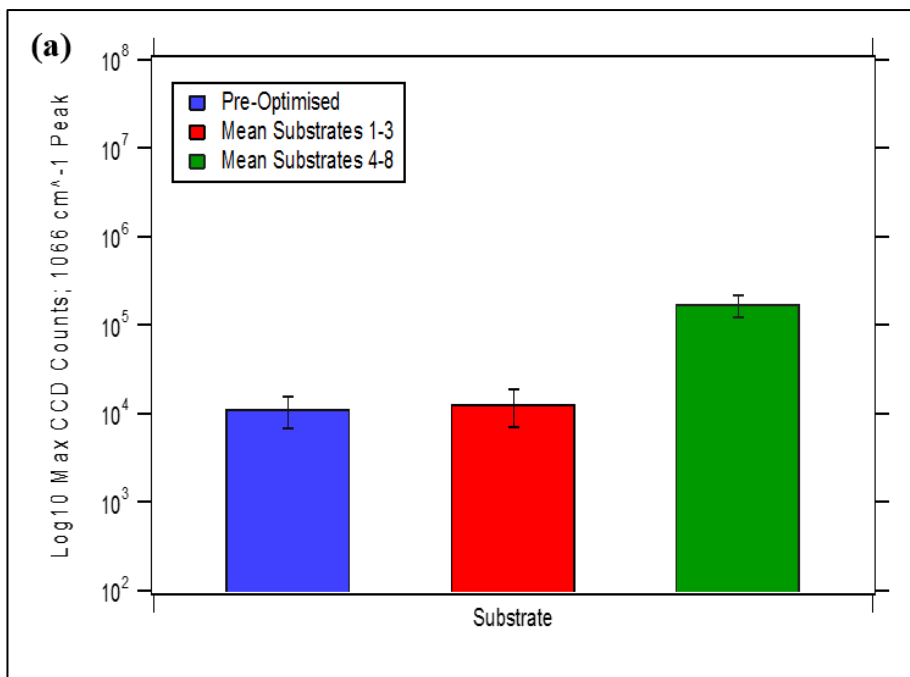
The gap dimensions achieved for the eight substrates altered by deposition, are listed below in Table 5.8.

Table 5.8 Nanogap; gap dimensions’ post deposition

Substrates 1 – 3: 1st stage deposition; Substrates 4 – 8: 2nd stage deposition

Substrate	Gap ‘x’ axis (nm)	Gap ‘y’ axis (nm)	Mean Nearest Neighbour separation (nm)	Overall mean separation (nm)
1	88	54	71	74
2	87	63	75	
3	83	67	75	
4	71	52	62	60
5	59	75	67	
6	67	75	71	
7	60	40	50	
8	56	48	52	

The optimised substrates were functionalized with 2NT as before. Raman analysis was carried out post functionalization. Comparison of relative performance at the 1066 cm⁻¹ peak is shown below in Figure 5.19; the data set for the pre-optimised substrates is included (a) & (b).



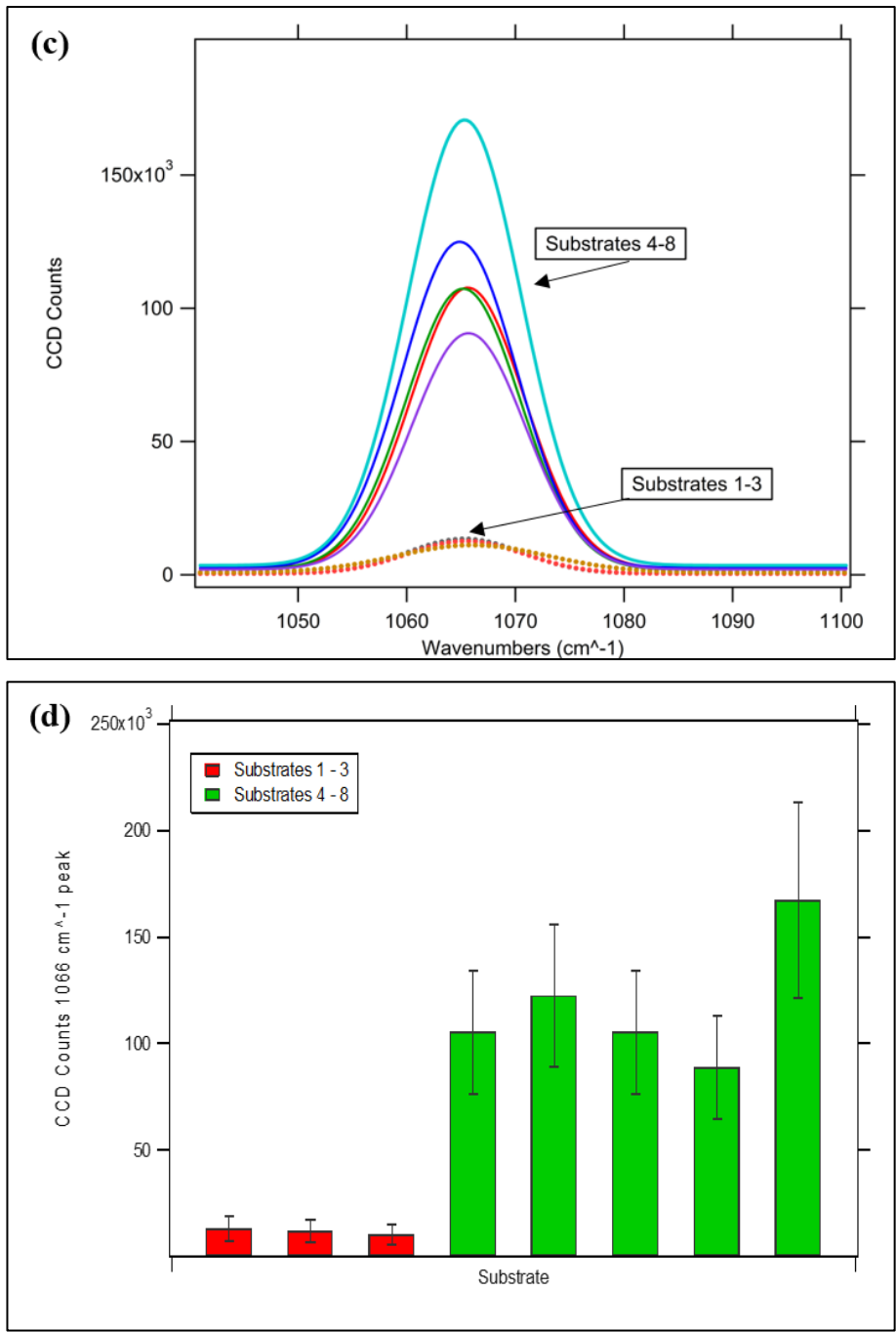


Figure 5.19 Optimized Nanogap substrates; 2NT spectra 1060 cm⁻¹ peak

Raman analysis for all substrates at 1066 cm⁻¹ Raman peak (a) & (b) Semi-Log comparisons of pre & post-optimised substrates (a) Log10 Raman intensity (b) Log10 SERS EF (calculated via Equation 4.1) (c) Raman peak intensity for post-optimised substrates, both groups; zoom of 1066 cm⁻¹ peak, curve fitted data (Gaussian) (d) Max CCD counts for post-optimized substrate batches. (All) Laser excitation at 785 nm & 0.32 mW power, 600 lines/mm grating and 50x objective. Error bars – relative standard deviation.

Both groups of optimised substrates demonstrated improved SERS performance over the pre-optimised ones. As the structure spacing is reduced, the SERS response increases (c) & (d) above. Decreasing the mean gap by ~ 15 nm (Table 5.8) between the two batches of optimised units led to an increase in EF from 1.2×10^3 to 1.6×10^4 .

(Note: SERS EF calculations presented in Figure 5.19 are with the use of Equation 4.1 and experimental values for Raman and reference intensity as described earlier; page 115).

5.3 Discussion

Two in-house SERS substrates fabricated using nanolithography techniques were evaluated using Raman, SEM and FDTD analysis. The two substrates were an Au coated substrate fabricated via Substrate Conformal Imprint Lithography (SCIL) and a bimetallic substrate via deep UV photolithography.

5.3.1 Tyndall SCIL substrates

The SCIL substrates exhibited a poor Raman enhancement, displaying very low signal to noise ratio. However, the signal consistency was excellent and was compared to the platform-based substrates of Results 1. The RSD values were: 8.3% for the SCIL units and a range of 16.4 - 49.4% for the commercial units.

FDTD analysis was carried out to optimize the Tyndall substrates for any future fabrication. A summary of the geometrical parameters suggested by the FDTD outputs is given next in Table 5.9.

Table 5.9 Summary of FDTD optimized parameters for Tyndall SCIL substrate

*Note, all length dimensions are in (nm)

Optimized parameters	Pillar diameter	Pillar height	Gap parameter	Au surface layer thickness	Material configuration
FDTD outputs*	320	350	≤ 10	≥ 95	<i>Silicon/Au</i>

An additional consideration arising from the FDTD optimization is with regard to resonance peak position. It was noted that a red shift of resonance peak occurred with increasing structure diameter; Figure 5.12. Grimault et al. have reported that for 3D FDTD simulations of nanocylinders, where increasing diameter also resulted in a red shift of the resonance peak [70]. For a pillar diameter of ~ 320 nm the substrate can effectively be ‘tuned’ close to the desired incident wavelength of 785 nm.

5.3.2 Nanogap substrates

The NIL Nanogap substrates produced a better SERS response than the SCIL substrates. However, their performance relative to the platform-based substrates characterised above was inferior. Optimisation was carried out using FDTD outputted parameters and substrates were reworked accordingly. Two stages of deposition were employed in order to reduce the structure spacing. Subsequent Raman analysis was undertaken to compare pre and post optimised structures.

The resulting Raman analysis showed that both batches of optimized substrates showed increased Raman enhancement. Additionally, the optimized substrates displayed an increase

in SERS EF from 1.2×10^3 to 1.6×10^4 for a decrease in the interstructure spacing of ~ 15 nm.

5.4 Conclusion

Both of the in-house substrates displayed poor Raman enhancement by comparison with the commercial platform-based substrates. However, the consistency of the Tyndall SCIL substrates was significantly better than all the other units tested. The mean deviation of signal (RSD) from the Tyndall substrate was 8.3%, while all the other samples tested ranged from 16.4 - 49.4% (1066 cm^{-1} peak). Although only viable as a qualitative comparison, arrays of 3D cavity Nanoantennas fabricated by Li et al. yielded an average signal deviation of 22.4% or at best 15% [75].

State of the art SCIL nanoimprinting enables the fabrication of uniform arrays of nanostructures, as shown in Figure 5.20.

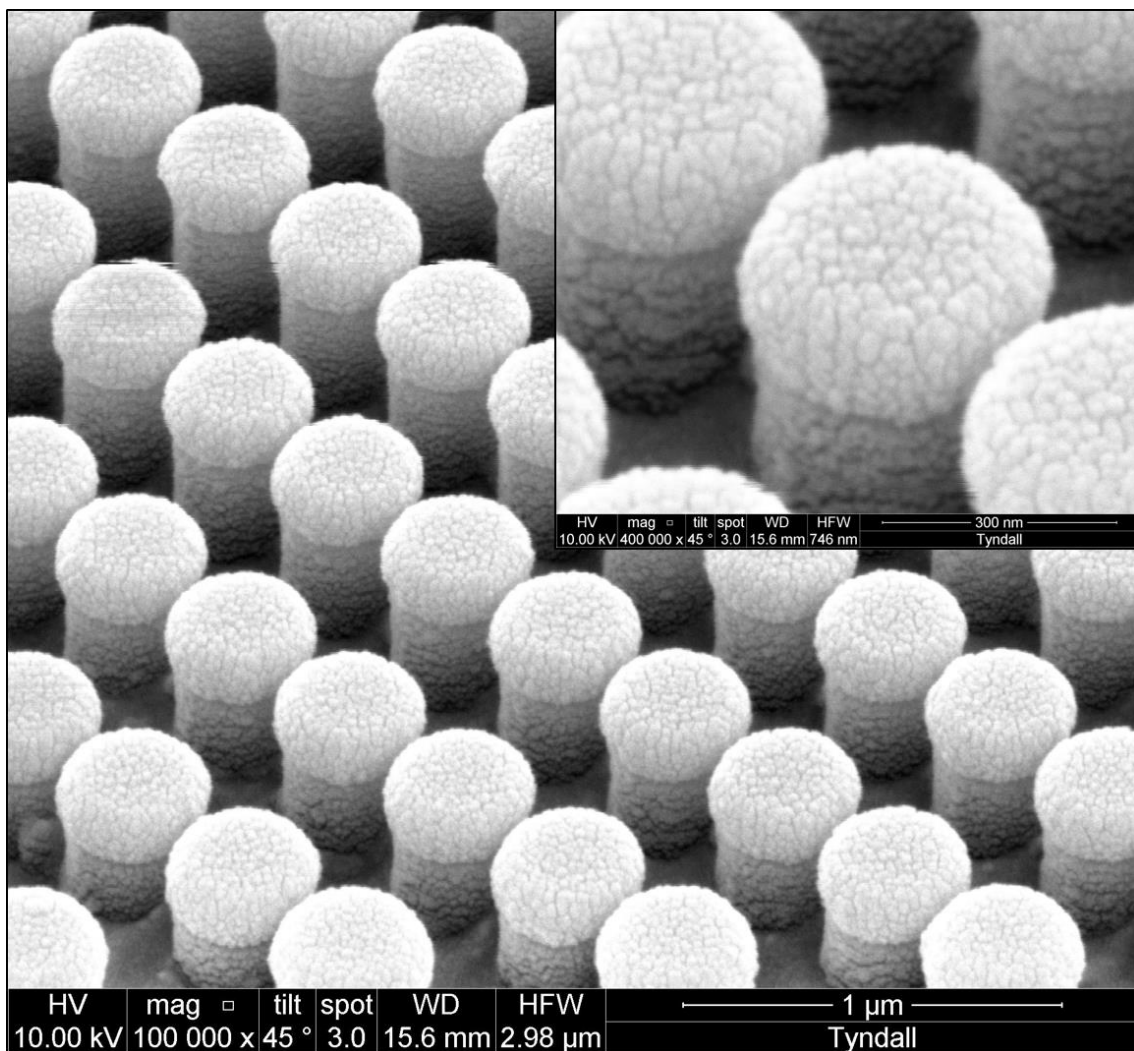


Figure 5.20 SEM showing uniform nanopillar array; Tyndall SCIL substrate
Main image; nanopillar array, Magnification 100 KX. Scale bar 1 μm. Inset zoom image; Magnification 400 KX, scale bar 300 nm. Both images, acceleration voltage 10 kV & 45° tilt.

Uniform and consistent surface nanofeatures provide excellent reproducibility of SERS response across the SERS-active region of the substrate. Additionally, the regular surface topography of substrates that is produced by SCIL imprinting allows for excellent batch to batch consistency.

Based on the FDTD analysis/optimization undertaken, the SERS enhancement for any future fabrication can be significantly improved. Thus making the SCIL nanopillar substrates more suitable for use as a SERS based sensor. A strong degree of confidence in this FDTD optimization is gained from the literature. FDTD has previously been used to optimize lithography fabricated substrates. Shioi et al. used FDTD to optimize both pitch and diameter of Au nanodisks with strong agreement to their experimental measurements [200].

A similar approach to the FDTD optimization that we performed was carried out by Dhawan et al. [76]. They also used FDTD simulations to optimized regular arrays of Au nanopillar structures, over a similar wavelength range of 500-950 nm (our experimental range: 400-900 nm; Table 5.3). We simulated interstructure gaps of 40-2 nm while Dhawan's group analysed from 20-5 nm. However, we found that the range from 20-2 to be the most significant, as CPR becomes increasingly more influential below 20 nm. An interesting point of note is the location of the SERS hot spots relative to the incident polarization. As per the FDTD outputs in Figure 3.12, Dhawan also reported that the hot spots occur between adjacent structures and parallel to the incident polarization; '*figure 1*' in their publication.

Additionally, Dhawan et al. modelled the electric field between adjacent structures by inclusion of a dimer in the simulation region for the FDTD set up to simulate a regular structural array. This was similar to the approach we adopted throughout the projects FDTD work, and is typically the method used when simulating large arrays of regular nanostructures [201, 202].

Regarding further confirmation of our approach to electric field modelling, Grimault et al. performed FDTD analysis of similar structures and found good agreement with their experimental characterization. Their work focussed on the simulation of electric fields about regular arrays of Au nanocylinders [70].

Following the simulation work carried out in Results chapters 1 & 2, a strong degree of confidence has been gained in the use of the FDTD tool. It has been helpful to understand the underlying theory/mechanisms behind the SERS phenomenon. However, we have especially confirmed the usefulness of FDTD modelling by optimizing the nanogap substrates.

Good agreement between the FDTD model and experimental outputs was noted. Increased SERS enhancement was measured experimentally following rework/fabrication according to the FDTD optimized outputs; Figure 5.19.

The topography of the nanogap substrates consist of indented regions with adjacent raised structures. FDTD simulations carried out on substrates with cavities and indented regions are also reported in the literature [75, 79].

6 Results 3 - Application – Bioanalysis

6.1 Introduction

Developing highly sensitive and rapid techniques to detect low concentration protein biomarkers in a biological environment, presents a significant challenge in nano-clinical research. The current gold standard method for detecting low levels of protein is the Enzyme-Linked Immunosorbent Assay (ELISA). ELISA diagnostic techniques generally use sensitive fluorescence based immunoassays on protein arrays, the highly specific antibody/antigen interactions are often identified via colour change.

ELISA requires lengthy and complex processes which additionally have the disadvantage of limited multiplexed detection [115]. A combination of Raman spectroscopic techniques and diagnostic protein assays may offer a competitive alternative to fluorescence-based ELISA methods.

Raman spectroscopy provides a high sensitivity and sharp label free molecular specific fingerprint that enables multiplexed detection. The use of Surface Enhanced Raman Spectroscopy (SERS) can in some cases surpass the detection sensitivity of fluorescence.

Although intrinsic Raman spectra are characteristically weak, the scattering cross-section of a target molecule can be strongly enhanced if the molecular species of interest are positioned near a nanostructured metallic surface (typically Ag or Au) [94, 203]. Detection at ultra-low concentrations of up to 10^{-13} M have been reported, and the very narrow spectral width of Raman peaks (typically 10-100 times narrower than fluorescence) has enabled greater flexibility in multiplexed analysis [204].

Combining SERS and biological assays has been reported in many varied applications. These include multimodal photodynamic and theranostic probes [204-206], Imaging [207], spectral analysis [208-210] to NIR probes capable of multiplexed detection [211, 212]

There are many different approaches that are used in SERS biosensing, but these methods generally fall into two categories; **intrinsic** and **extrinsic**.

A common **intrinsic** approach is direct labelling; where a target analyte is mixed with a colloidal dispersion of SERS optimised nanotags. The SERS nanotags act to enhance the signal of the Raman reporter [213-215] in some cases by trapping the analyte molecules within nanogaps between aggregated MNP's.

Significant progress has been made in the design and synthesis of bioconjugated nanotags. These advances have enabled the control of plasmon frequency and Raman cross-section, by optimising MNP size and geometry.

There are a number of approaches to bio-conjugating the SERS nanotags. One approach is to directly immobilise both the Raman reporter and antibody molecules onto the MNP's. While another method attaches the antibody via the use of a spacer molecule such as Polyethylene Glycol [215]. The distance to the MNP is critical and only the labelled moieties that are close enough will experience a significant SERS enhancement. This is due to the near field characteristics of SERS, i.e. there is a rapid decay of the SERS-active region with distance from the surface, typically, within 4 nm [2, 216, 217]. However, a disadvantage of this

approach is the reproducibility and quantification of the Raman responses which can be difficult.

Extrinsic SERS biosensing generally involves the use of immunoassays, that rely on the recognition of biomarkers that are conjugated to a SERS substrate via its antibody [115, 180, 218, 219]. Although direct label-free methods are more convenient than extrinsic SERS labelling, the design and synthesis of stable and well-defined metal array assemblies can still be problematical. This is especially the case with trace analysis of proteins; low concentrations of high molecular weight biomolecules have poor SERS enhancements, and selectivity can be hindered by overlapping of Raman bands [220].

A comparison of these two general approaches is given in the schematic of Figure 6.1 below.

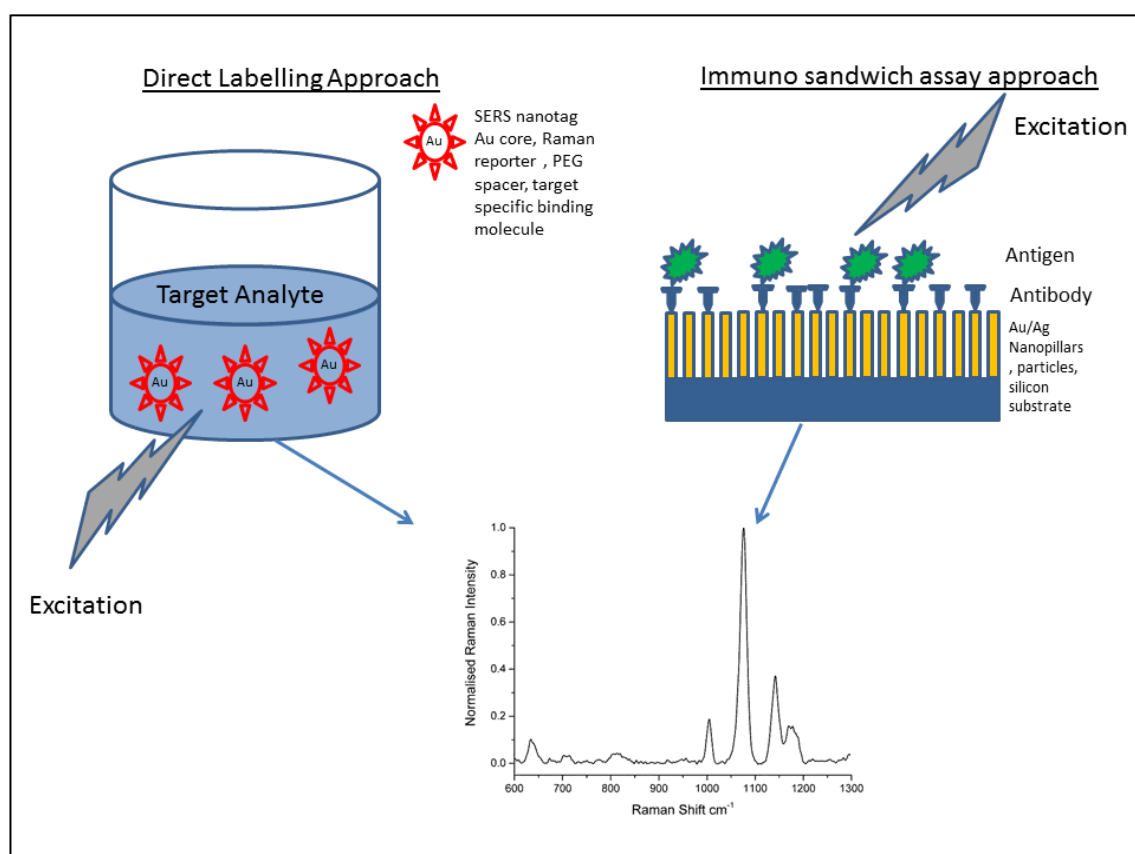


Figure 6.1 Schematic: Intrinsic & Extrinsic SERS biosensing

Direct labelling left image: Antigen bound to antibody/Raman reporter conjugated MNP's right image: SERS Immunoassay; Antigen sensed directly from the biomarker/antibody interactions

The above schematic illustrates the two general methods for generating SERS signals from analyte molecules. The *left image* displays the direct approach which uses MNP's bound to Raman reporters which themselves are bound to a specific binding molecule such as an antibody. An example of this type of direct labelling is the detection of nanoparticle uptake by cells in vitro. The *right image* shows the use of an immunolabelling approach that uses SERS to enhance the Raman signal directly from biomarker/antibody interactions.

An alternative to direct sensing of biomolecules is to use the indirect approach pursued in this work. In the indirect technique, the target analyte concentration, is now measured via frequency shifts in the Raman spectra of an underlying Raman linker molecule. The linker is

bound to the analyte via an analyte specific antibody, it has been reported that these frequency shifts are related to nano-mechanical perturbations [181, 186].

It is proposed that the Raman frequencies of an antibody conjugated Raman linker molecule, are influenced by the binding of an antigen to that antibody. The frequency shift is attributed to structural deformations at the binding site between antibody and linker molecules; which occur with variations in protein concentration. These structural distortions arise as a result of nanomechanical stress/strain on the binding site.

In essence, the Raman linker that is bound to the substrate acts as an immobiliser for the antibody. This enables the antibody to then act as an efficient Raman probe, whose signal is enhanced via the SERS effect.

The two proteins used in this project are: p53 & Epidermal Growth Factor Receptor (EGFR), which are both important biomarkers used in human cancer research.

The biomarker p53 is one of the most extensively researched DNA-binding proteins, and has been an accepted benchmark in cancer research for almost 40 years [221]. Known also as the tumour suppressor gene, the p53 protein is at the centre of the body's cellular network that defends against the spread of tumours. It is considered to be an important prognostic marker, and highly sensitive detection capability may significantly contribute to the early diagnosis of cancers [222, 223].

Epidermal Growth Factor Receptor (EGFR) is a membrane protein that facilitates cell growth, production and differentiation in multiple tissues. EGFR mutations lead to uncontrolled cell division. EGFR has been linked with several human cancers including lung and pancreatic cancer [224, 225]. An overexpression of either of these biomarkers can be an indicator of disease onset.

In this work, we aim to develop a robust technique for the indirect measurement of both of the above cancer biomarkers. The technique involves using high efficiency SERS substrates to detect the aforementioned frequency shifts in Raman linkers that occur due to subtle changes to linker/antibody binding sites. These changes arise from mechanical perturbations generated by varying concentrations of antigen that exert stress/strain influence on the linker/antibody/antigen system.

Further discussion is presented next to outline the theoretical considerations that underpin the measured Raman responses of nanomechanical stress/strain bioconjugated linker/antibody/antigen systems.

We will examine the case of a 4-ATP conjugated system in the absence of any medium.

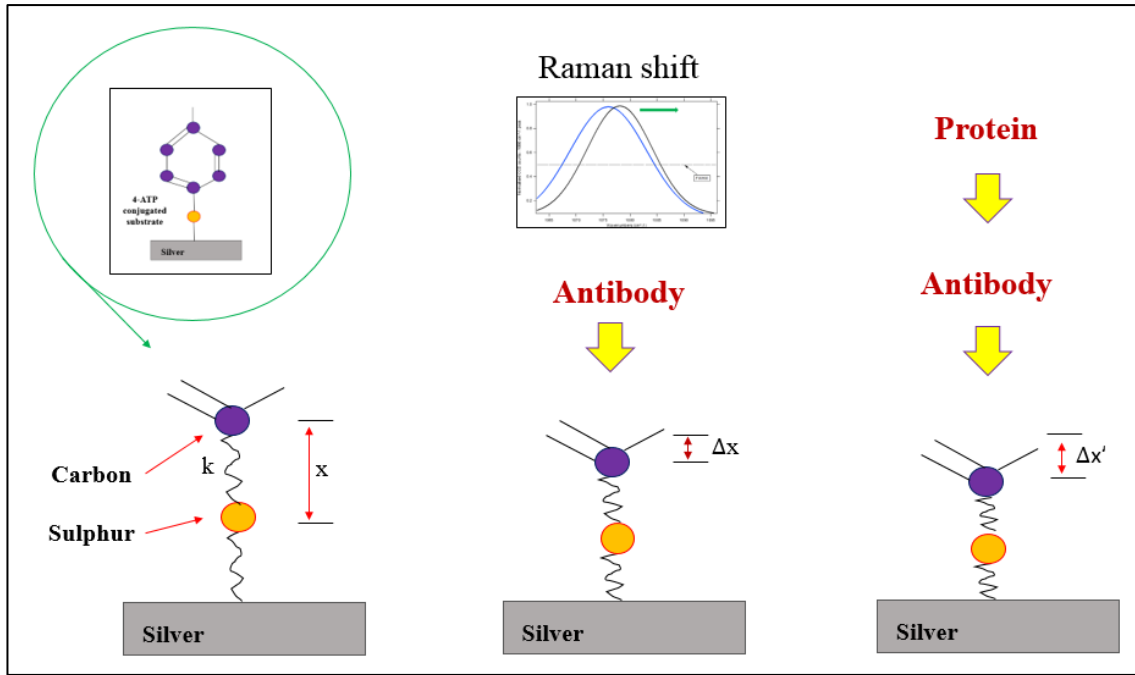


Figure 6.2 Simple nanostress response of 4-ATP conjugated SERS substrate; in the absence of any medium

Schematic showing linker/antibody binding site at substrate surface; the C-S bond is illustrated as a mechanical spring system. Spring constant 'k', with $k \equiv$ binding energy; bond length = x ; change in bond length = Δx . Note the addition of antibody and antigen alter bond length.

From a purely mechanical perspective, the CS bond can be likened to a spring, and its behaviour governed by Hooke's law. Arising from the work done on the system, the change in potential energy of the spring is generally stated as:

$$U_{elastic} = \frac{1}{2} k(\Delta x)^2 \quad \text{Equation 6.1}$$

$U_{elastic}$ = elastic potential energy; k = spring constant; Δx = displacement from equilibrium position of C-S bond

From Equation 6.1, and for the case of a purely mechanical system, we can state the following approximation:

$$\Delta x^2 \propto \Delta U \propto \Delta \nu \rightarrow \Delta FWHM$$

Where: ΔU = change in potential energy of the spring or binding energy; Δx change in spring (or bond length). For the frequency (and FWHM) measured in wavenumbers then $\Delta x^2 \propto \Delta \nu$ - i.e. the change in the vibrational frequency from equilibrium position. The change in vibrational frequency can lead to an increase in the FWHM of the peak.

This mechanical model represents the 4-ATP conjugated substrate, but the CS bond is not in isolation. It is also important to consider the Sulphur bond to the metallic substrate. This bond will also be dependent on the analyte concentration and thus influence the CS bond length. However, the two springs are effectively in series, and can be considered as one spring. In order to understand the changes to the CS bond, and the subsequent effect on the Raman peak we will consider the following.

For a two-atom system, with a bond length 'x'. The bond length will vary with the addition of antibody and subsequent protein dilutions. As x varies, so also will the potential energy, 'U' of the system.

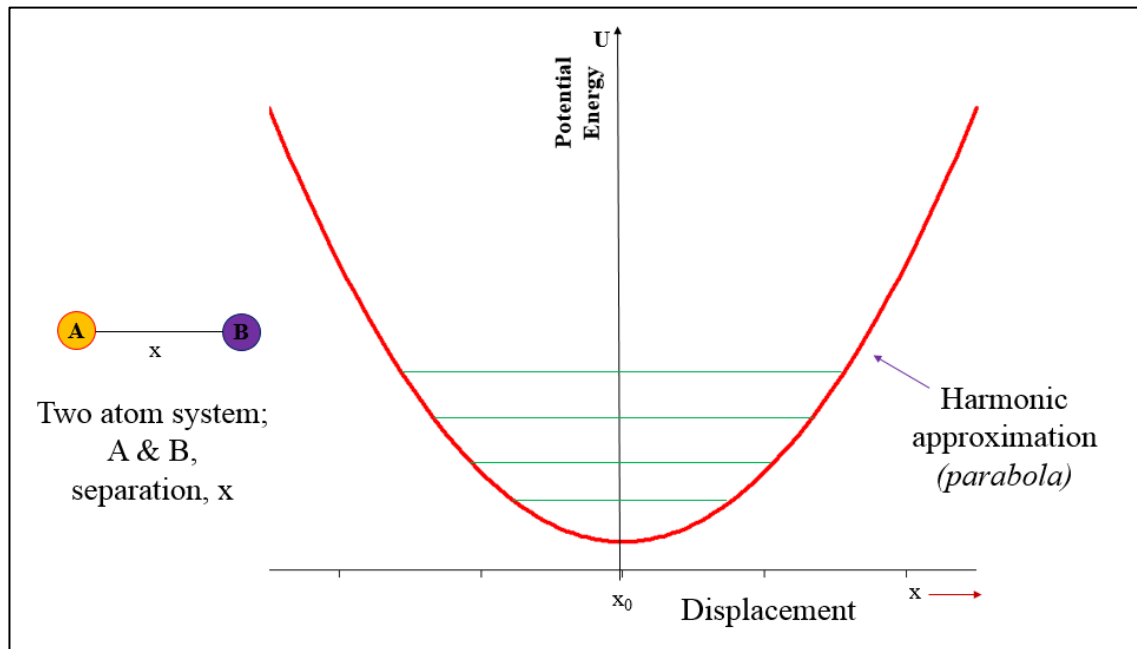


Figure 6.3 Harmonic approximation for a two-atom system

At equilibrium, the potential energy 'U' is at a minimum and the separation is given by x_0

The simplest case is considered, where only one atom 'B' can move while the other atom 'A' is fixed in position. In order to change the separation by Δx , work has to be done on the system. Thus, the potential energy has also been changed; by an amount ΔU . To a good approximation, the potential energy varies as per Equation 6.1, i.e. $\Delta U \propto \Delta x^2$. The classical harmonic approximation holds well for small displacements.

We can combine Newton's law that describes the motion of atom B, with Hooke's law and write the following.

$$\frac{d^2x}{dt^2} = -\frac{k}{m}\Delta x = -\omega^2\Delta x \quad \text{Equation 6.2}$$

With k = spring constant and m = mass; note also that the atom will oscillate at an angular frequency ω , which is given by: $\omega = \sqrt{\frac{k}{m}}$

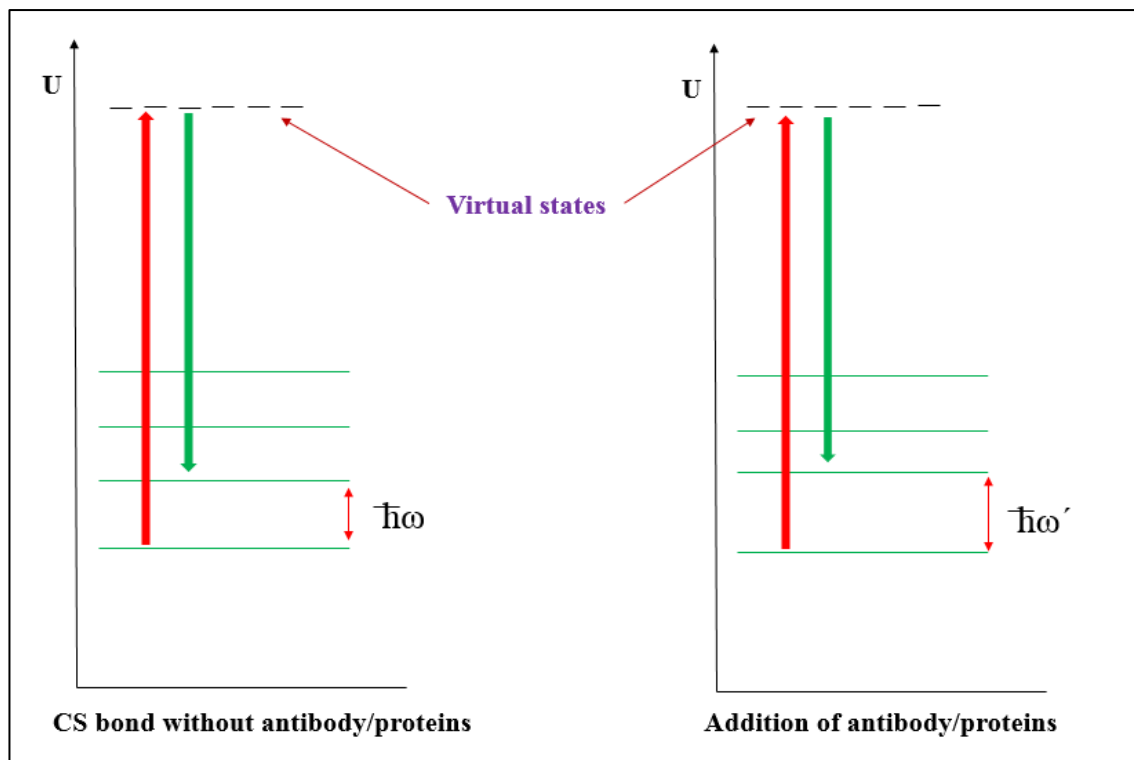


Figure 6.4 Illustration of the energy levels associated with the CS bond

Left image shows the CS bond without antibody/proteins. Right image: with addition of antibody/protein.

The energy of the Raman transition is influenced by conjugation with antibody/proteins to system, with subsequent changes to the value of ω ; see Equation 6.1.

Thus, we postulate that the quantized vibrational energy of the system will vary as antibody/proteins are added to the 4-ATP molecules. This will be governed by changes to the value of ω as the 'mass' of the system varies according to the following.

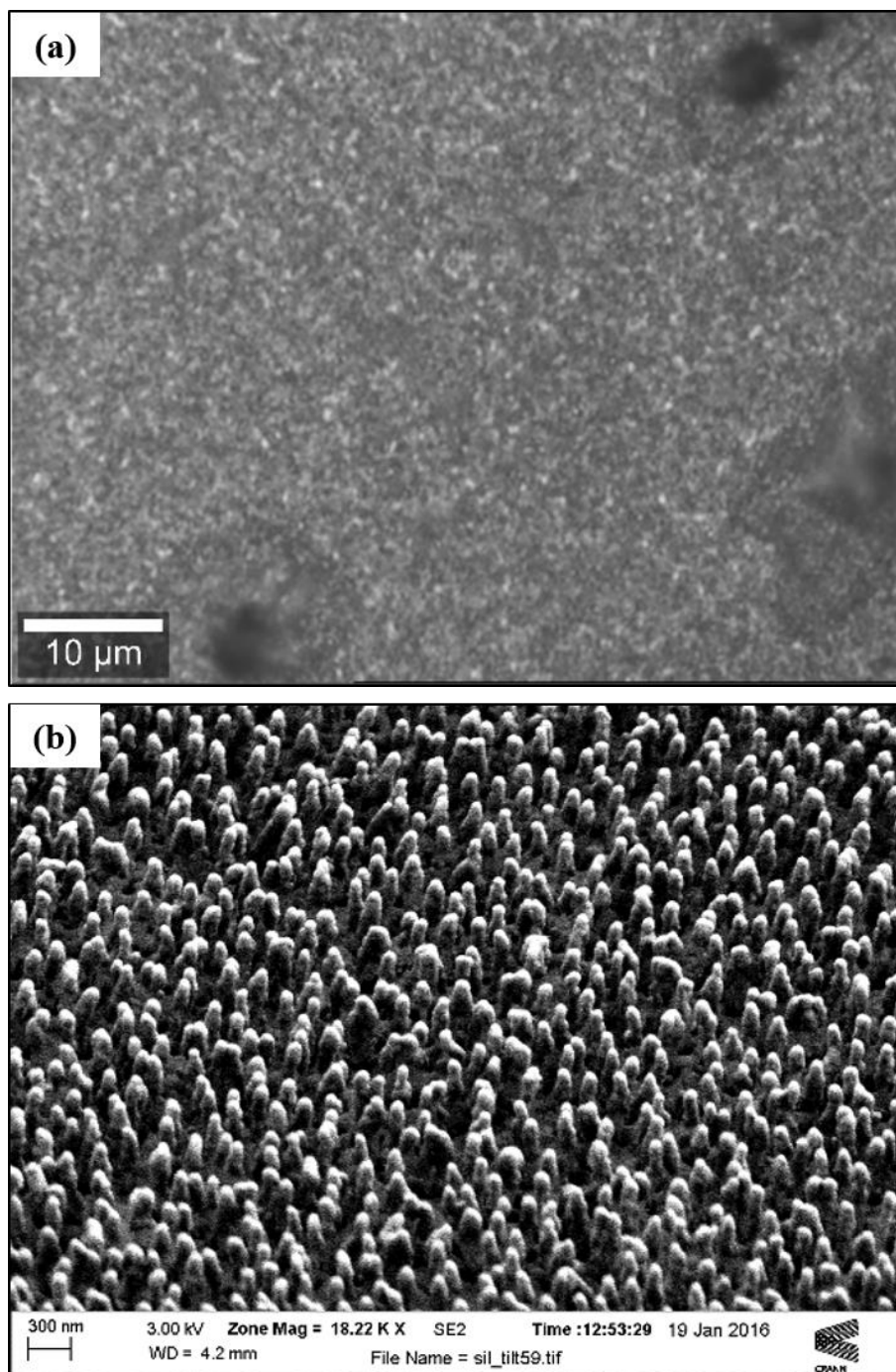
$$\omega = \sqrt{\frac{k}{m}} \text{ (initial state)} \quad \omega' = \sqrt{\frac{k}{m'}} \text{ (addition of antibody)} \quad \text{Equation 6.3}$$

[Note: the spring constant is representative of the bond strength and may also change with different protein concentrations]

6.2 Experimental; SEM & Raman analysis

In this work, we aim to develop a robust technique for the indirect measurement of both above cancer biomarkers. This will be enabled using a high sensitivity SERS substrate, with the substrate of choice being the Silmeco Ag Nanopillar; previously characterised (page 103).

Pre-and post-functionalised Silmeco substrate images shown below in Figure 6.5.



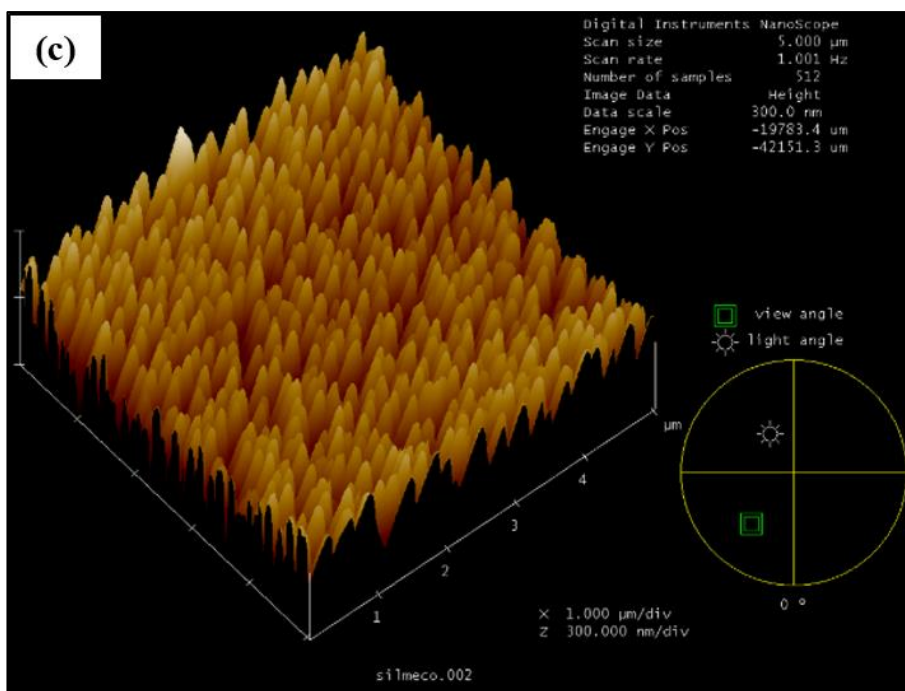


Figure 6.5 Silmeco SERS substrate functionalized with p53/antibody/4-ATP Raman linker
 (a) Silmeco substrate functionalized with p53/anti-p53/4-ATP Raman linker molecule. Reflected light image captured with 100x air objective lens (b) SEM SE2 detector top view, Magnification 18.22 KX, scale bar 300 nm, acceleration voltage 3.00 kV (c) AFM image of substrate surface topography, scale bar 5 μm with image acquisition – tapping mode. AFM image provided by P. Owens, Centre for Microscopy & Imaging, NUI Galway.

Figure 6.5 shows a range of views for a typical Silmeco nanopillar substrate. The bright spots in the reflected image (a) correlate to groupings of pillars post-functionalisation. As the liquid analyte evaporates, surface tension between Nanopillars causes adjacent pillars to lean in towards each other. The clustering of pillars with vastly reduced interpillar spacing results in strong CPR and a strongly enhanced SERS effect.

The SEM image of (b) shows a clearer view of the surface morphology before functionalisation with Raman linker and Antibody/protein. In (c) the AFM image gives a greater appreciation of the side profile.

Raman measurements are acquired from substrates functionalised with Raman linker/antibody and varying concentrations of protein; as per methods section. The Raman response to changes in protein concentration is examined, and results are presented below.

For the Raman linker 4-ATP, the 1080 cm^{-1} peak (previously assigned [226]) which corresponds to the CS stretching mode was found to be the most responsive to variations in p53 concentration. While for the 6-MP spectra the prominent thiol peak [227, 228] at 860 cm^{-1} was the most responsive to changes in EGFR concentration. The three Protein/Raman Linker model systems analysed using the Silmeco substrates are listed in Table 6.1.

Table 6.1 Raman linker/protein systems analysed

Raman linker	4-ATP	4-ATP	6-MP
Protein	p53	EGFR	EGFR

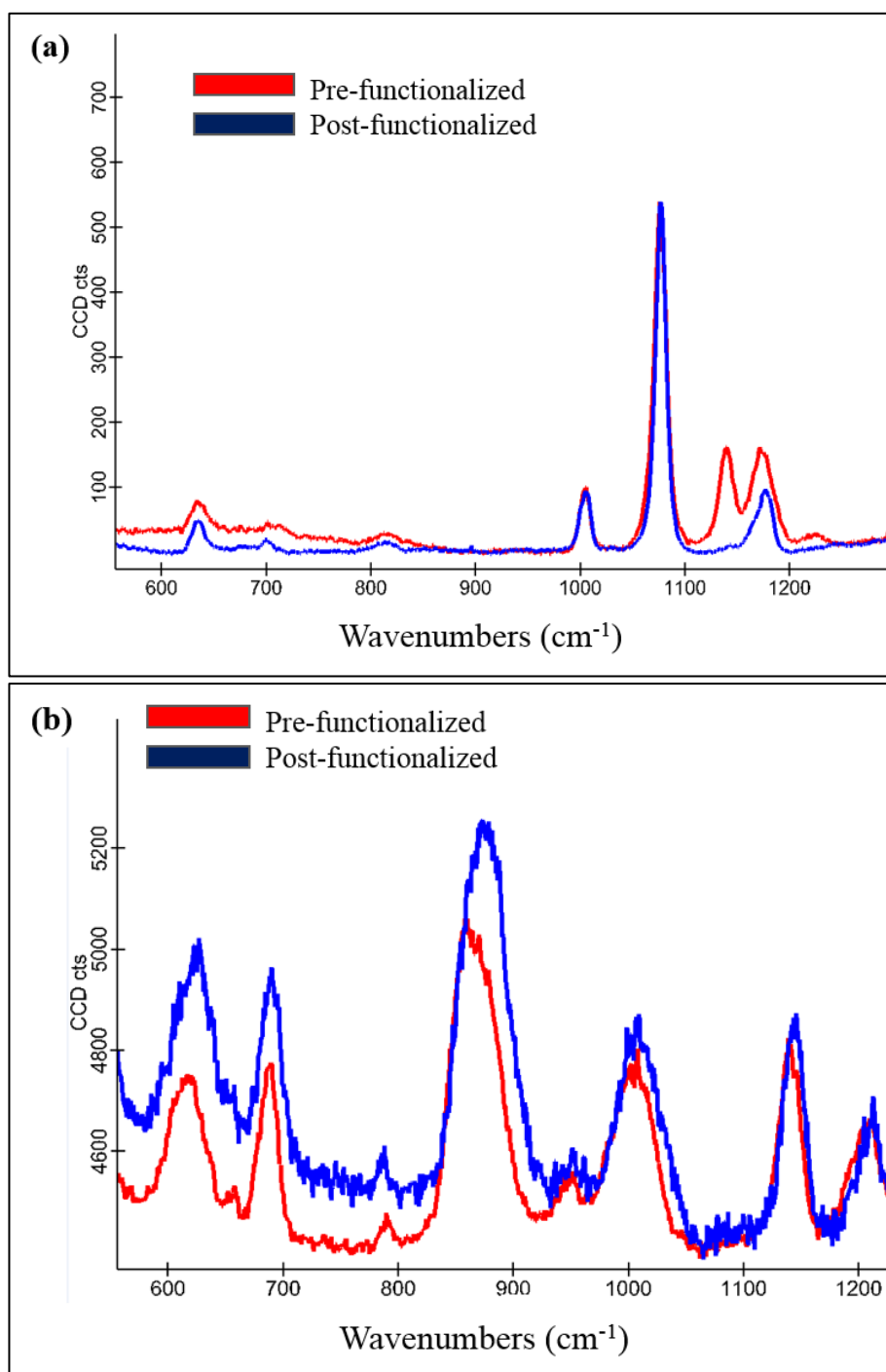


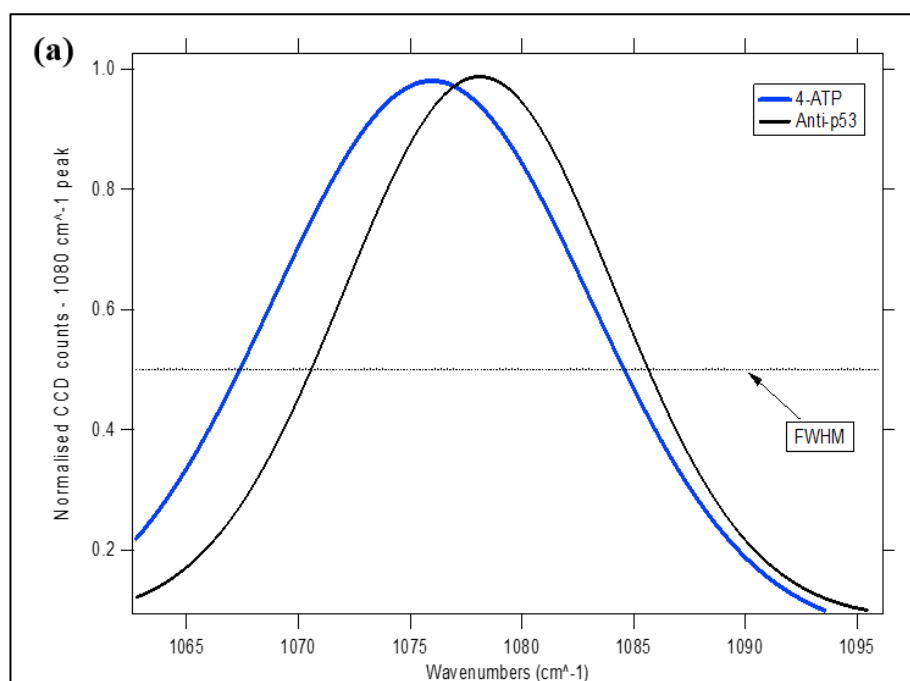
Figure 6.6 Raman Spectra for 4-ATP & 6-MP linker molecules; pre & post-functionalized Silmeco substrates: pre & post antibody/protein functionalized spectra are overlaid in both plots (a) 4-ATP Raman spectrum on p53 bound substrate (b) Raman spectrum of 6-MP on EGFR bound substrate. Raman parameters: 785 nm excitation, 100x Objective, 1200 lines/mm grating; Laser power 0.05 & 0.47 mW respectively. All spectra: 25-point acquisition, cosmic ray removal and background subtraction.

Raman spectra before and after conjugation are shown in Figure 6.6, and the plots are overlaid by cascade for visual purposes. The spectrum for 4-ATP is shown in Figure 6.6 (a). The 1080 cm^{-1} peak was found to be the most responsive to antibody/protein binding and

exhibits the greatest shift according to p53 concentration. Similarly, for the 6MP spectra, Figure 6.6 (b), the prominent thiol peak at 860 cm^{-1} was found to be the most sensitive to influences from variation in EGFR concentration. All spectra were averaged and then normalised to account for different signal intensities arising from different analyte concentrations. Spectra were normalized to the 1080 & 860 cm^{-1} peaks for the 4-ATP and 6-MP systems respectively.

Non-specific binding can interfere with the SERS signal from an analyte of interest. However, the linker molecules that are covalently bound and self-assembled onto the Ag surface prevent non-specific adsorption of molecules, thus improving Raman efficiencies; see control experiment Table 6.4 & Figure 6.13. Furthermore, by employing large area scans, statistical reliability and reproducibility of frequency changes are improved by accounting for spot to spot intensity fluctuations typically occurring for low abundance biomolecules.

In Figure 6.7 below, a close up of the 1080 cm^{-1} peak is shown to illustrate the peak response to changes in p53 concentration.



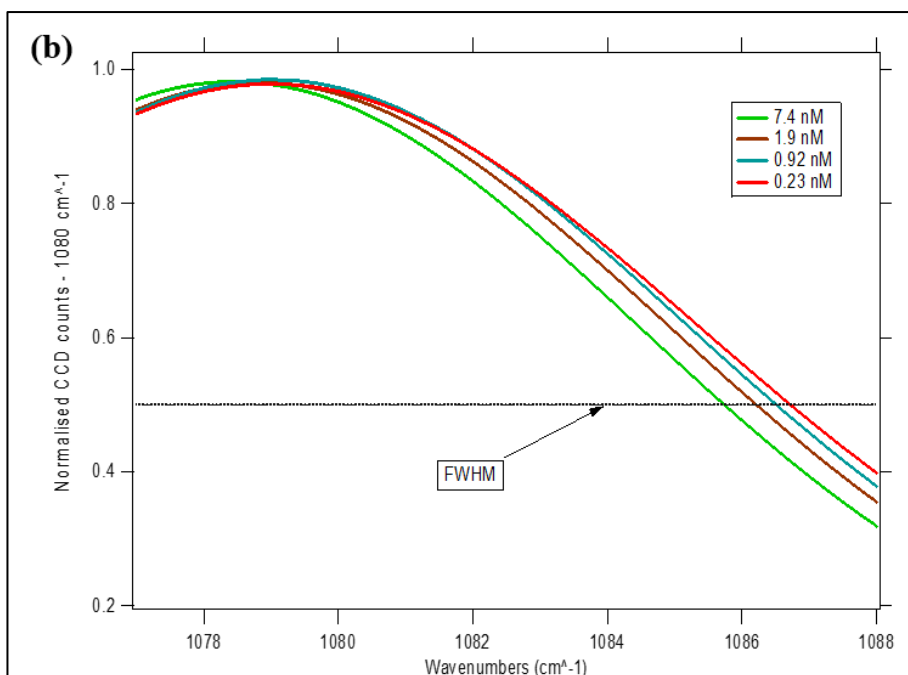


Figure 6.7 Frequency shift; 1080 cm^{-1} peak, 4-ATP/p53 Model

(a) Close up of 1080 cm^{-1} peak; showing frequency shift from 4-ATP only to 4-ATP/Anti-p53 conjugated substrate (b) zoom of leading edge; showing influence of changes in p53 concentration; subset of data removed for illustrative purposes; Raman parameters: 785 nm excitation & 0.05 mW laser power, 100x Objective, 1200 lines/mm grating (25-point average; Gaussian fitted data both plots)

A significant ‘red-shift’ (i.e. towards the higher wavenumbers) is observed from the 4-ATP only, to the 4-ATP/Antibody bound substrates; Figure 6.7 (a). In the zoom image (b), a change in the forward edge of the 1080 cm^{-1} peak can be seen. The expanded region of interest, shows frequency shifts due to the influence of p53 concentrations, with the lowest concentration at 0.23 nM exhibiting the greatest shift. While the peak shifts are non-linear and difficult to ascertain, we can qualitatively observe changes in the forward edge.

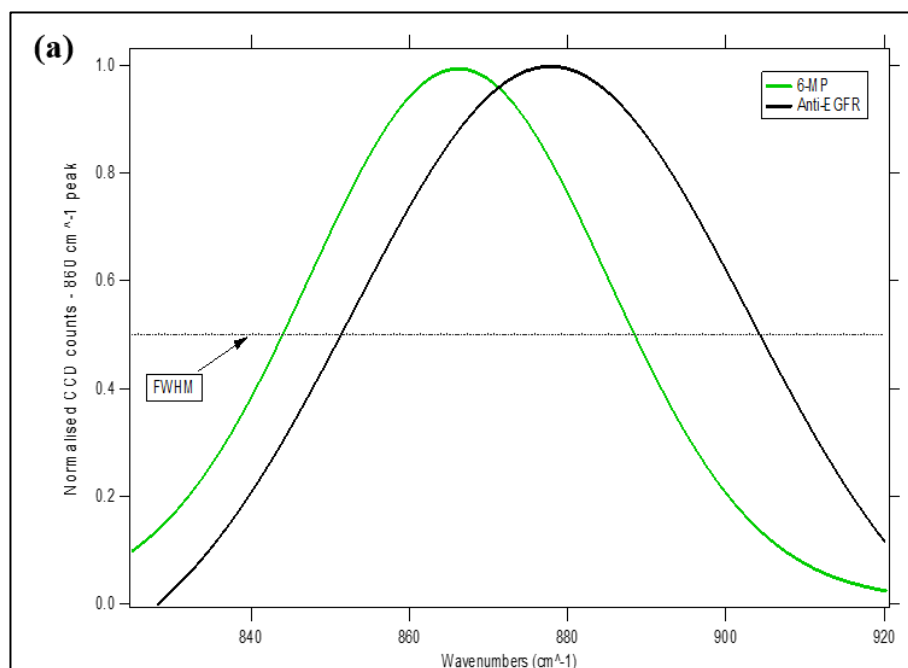
Additionally, measurement of the FWHM value of the normalised peaks shows that in parallel with the frequency shift, a peak broadening also occurs. The measurements for these changes are given in Table 6.2 below for the 4-ATP/p53 system. The peak broadening was found to be inversely proportional to protein concentration.

Table 6.2 Frequency shift and FWHM variation; 4-ATP/p53 model

Instrument uncertainty; WiTec Raman microscope $\pm 0.5 \text{ cm}^{-1}$.

Target range <i>(Note all substrates functionalised with 4-ATP)</i>	$\Delta\nu \text{ (cm}^{-1}\text{)}$	$\Delta FWHM \text{ (cm}^{-1}\text{)}$
4-ATP to Anti-p53	2.1	3.0
Anti-p53 to Low concentration p53 (0.23 nM)	1.1	0.75
Low to high concentration p53 (945 nM)	1.9	3.2

Similar frequency shifts and peak broadening were also observed for the 6-MP/Anti-EGFR/EGFR system for changes in EGFR concentration; Figure 6.8.



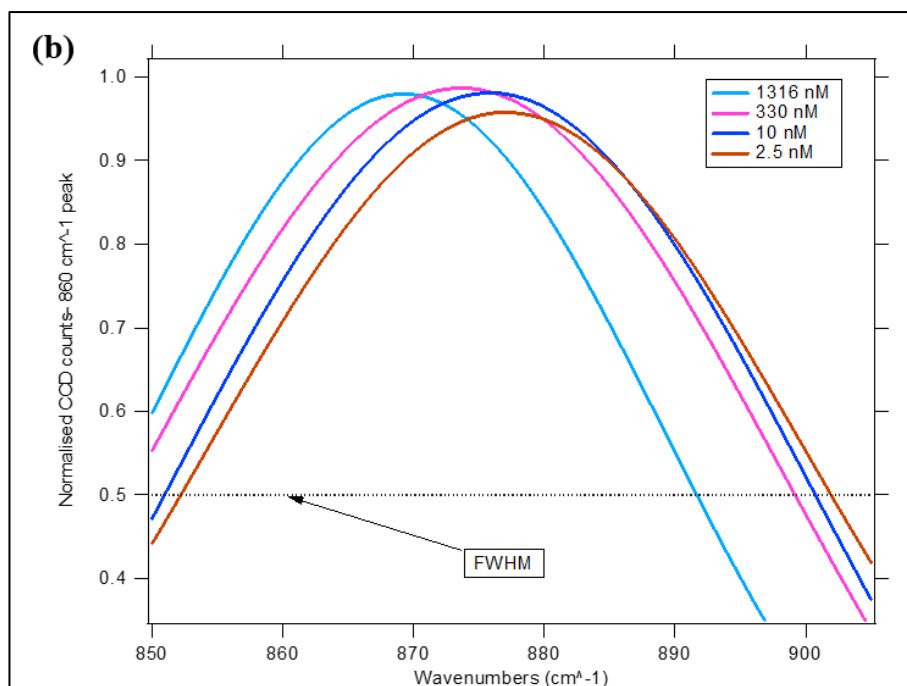


Figure 6.8 Frequency shift; 860 cm⁻¹ peak, 6-MP/EGFR model

(a) Close up of 860 cm⁻¹ peak; showing frequency shift from 6-MP to Anti-EGFR (b) Zoom of ROI showing influence of changes in EGFR concentration; subset of data removed for illustrative purposes. Raman parameters 785 nm & 0.47 mW laser power, 100x Objective, 1200 lines/mm grating (25-point average; Gaussian fitted data both plots)

As was the case for the 4-ATP/p53 model, a significant frequency shift is also observed, between the 6-MP only, to the 6-MP/Anti-EGFR bound substrates; Figure 6.8 (a). In the zoom image (b), the influence of varying protein concentration can again be seen. Values for the frequency shift and peak broadening at FWHM are given in Table 6.3 below.

Table 6.3 Frequency shift & FWHM variation; 6-MP/EGFR model

Instrument uncertainty; WiTec Raman microscope $\pm 0.5 \text{ cm}^{-1}$

Target range (Note all substrates functionalised with 6-MP)	$\Delta\nu \text{ (cm}^{-1}\text{)}$	$\Delta FWHM \text{ (cm}^{-1}\text{)}$
6-MP to Anti-EGFR	11.8	17.3
Anti-EGFR to Low concentration EGFR (2.5 nM)	1.5	10.1
Low to high concentration EGFR (5265 nM)	3.1	1.5

In Figure 6.9 FWHM and peak position variation with p53 concentration is plotted for the 4-ATP/p53 linker system.

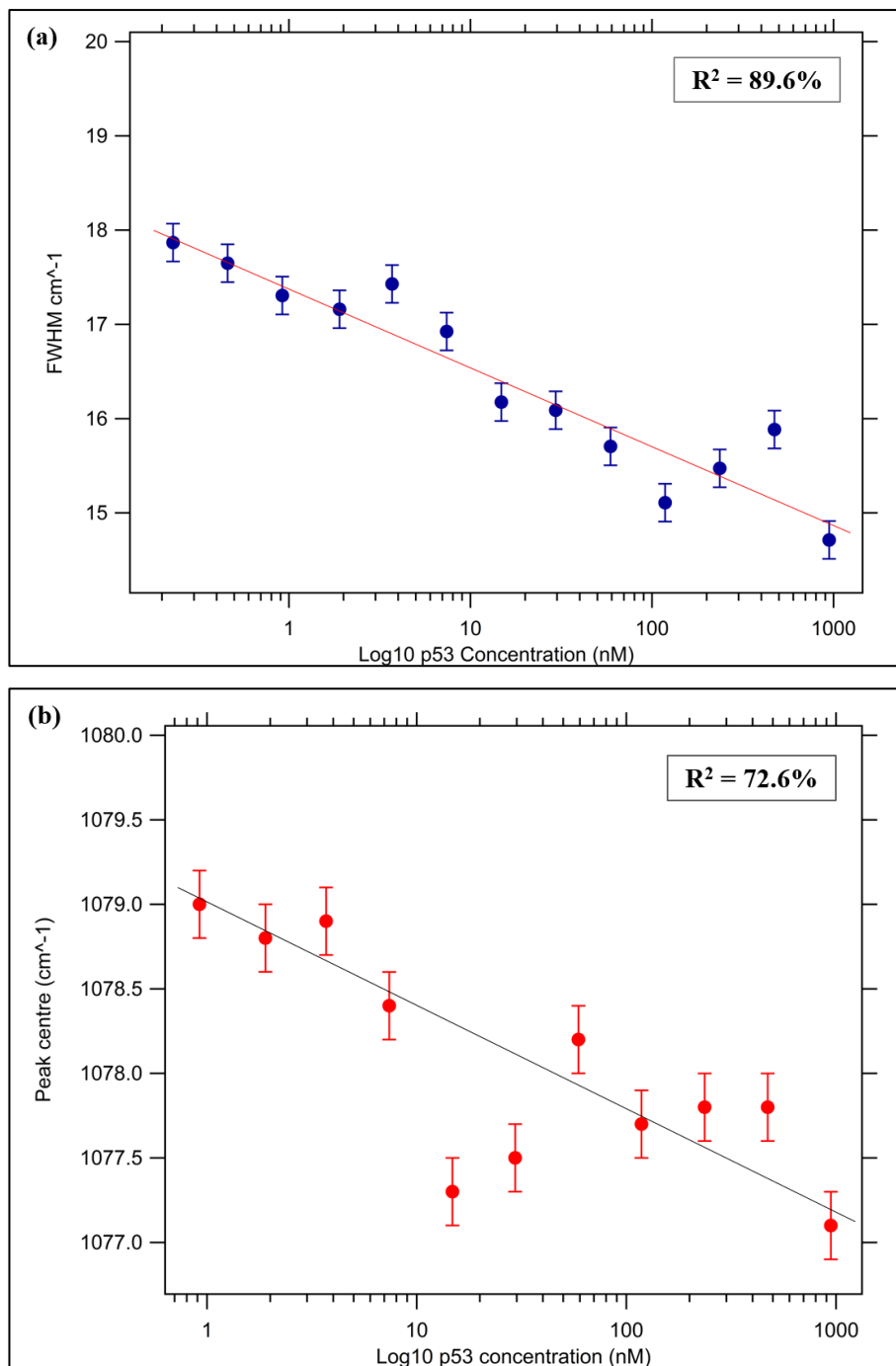


Figure 6.9 Variation in FWHM & Peak position with protein concentration for 4-ATP/p53 system

Semi-log plots for FWHM & peak position, linear regression overlaid in both plots (a) Variation of FWHM with p53 concentration; $R^2 = 89.6\%$ (b) variation in peak position with p53 concentration, $R^2 = 72.6\%$. Raman parameters both plots: 785 nm excitation wavelength, 0.47 mW laser power, 100x objective, 1200 lines/mm grating, 25-point average, Gaussian curve fitted data. Error bars ($\pm 0.2 \text{ cm}^{-1}$)

The plots of Figure 6.9 (a) & (b) are both plotted as semi-log plots (due to large variation in the range of protein concentrations). For the p53 conjugated system there is an exponential decrease over the measured range for both parameters. In order to show the trend in the data, a linear regression line is fitted, with the R^2 linear fit inset as legend. The R^2 coefficients calculated were 89.6 & 72.6 % for FWHM and peak position respectively.

We suggest that the binding between the antibody and its target protein, causes structural deformations to the protein moiety. This in turn induces a mechanical influence on the Raman linker molecules which are observable in the response of their Raman spectra, specifically, the 1080 cm^{-1} peak of the 4-ATP system.

In materials science, peak broadening and frequency shifts, have been exhibited by samples under stress. In studies relating to silicon, graphene and carbon, induced mechanical stress/strain effects have been associated with Raman peak frequency shifts and changes to FWHM [229, 230].

In our case, the peak broadening occurs at the lower protein concentrations, this indicates that the stress to the system is reduced as protein concentration decreases. A further indication, of stress variation with changes in the steric arrangement of the protein/antibody, is shown by the red shift of the peak centre.

The second of the three linker/protein models examined was 4-ATP/EGFR, spectral variations with protein concentration are presented in Figure 6.10.

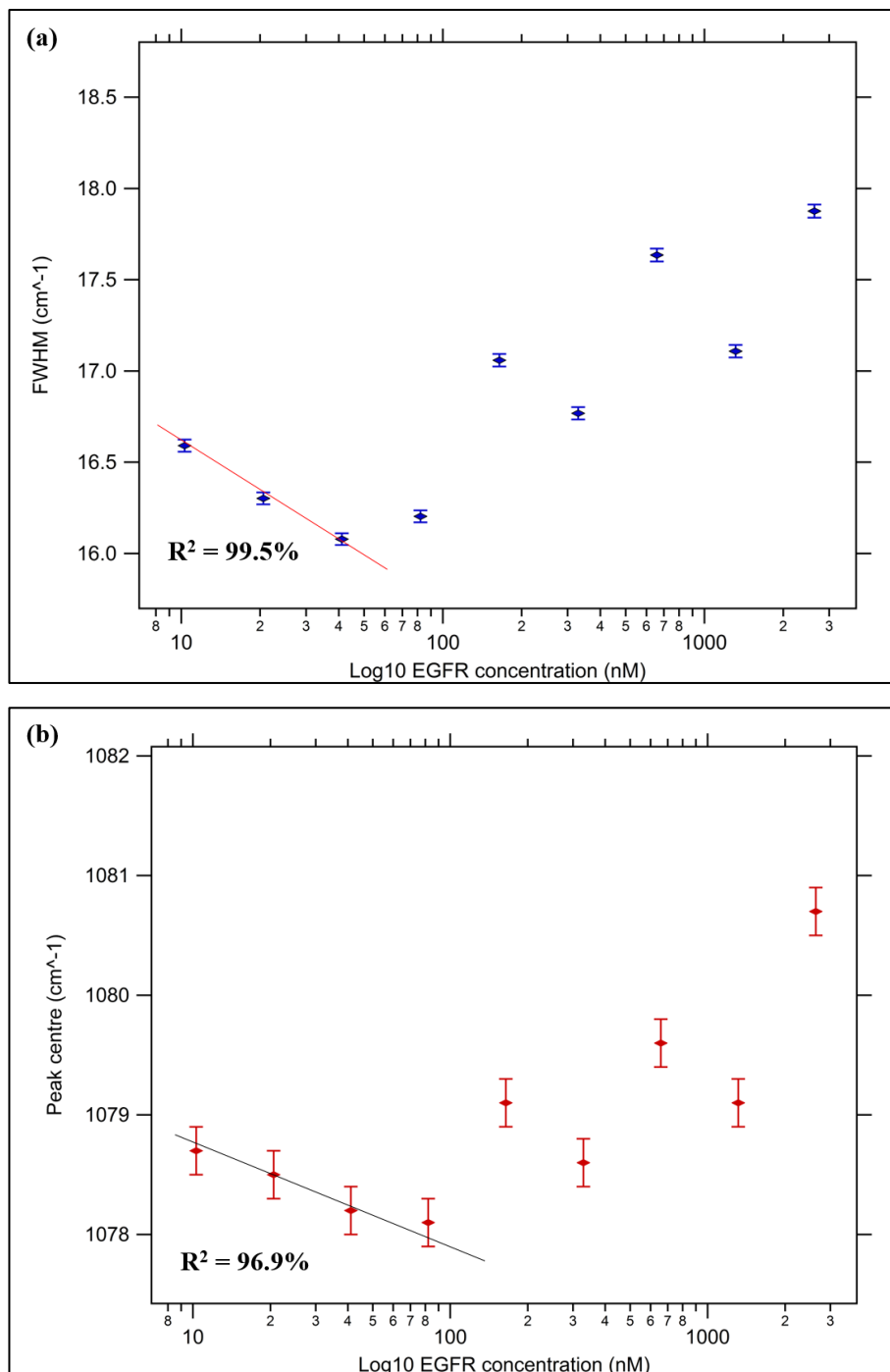


Figure 6.10 Variation in FWHM & Peak position with protein concentration for 4-ATP/EGFR system

Semi-Log plots for FWHM & peak position for 4-ATP/EGFR model, linear regression line overlaid at lower EGFR concentrations both plots (a) variation of FWHM with EGFR concentration (b) variation of peak position with EGFR concentration. Raman parameters both plots: 785 nm excitation wavelength, 0.47 mW laser power, 100x objective, 1200 lines/mm grating, 25-point average, Gaussian curve fitted data. Error bars ($\pm 0.2 \text{ cm}^{-1}$)

The observed trend for the 4-ATP/p53 system (Figure 6.9) was not witnessed for 4-ATP/EGFR (Figure 6.10) with the EGFR conjugated system exhibiting different behaviour.

For the lower EGFR concentrations, i.e. below ~ 80 nM, the system response is similar to that of the p53 model. Namely, FWHM broadening is inversely proportional to protein concentration with a concomitant red shift of peak centre position. A linear regression line is overlaid for both FWHM and peak centres - with R^2 values of 99.5 & 96.9 % respectively; Figure 6.10 (a) & (b). At a concentration of ~ 80 nM, for both FWHM and peak centre, the model behaves in an opposite manner to that observed for p53. There is a decrease in peak width and a blue shift with further increases in protein concentration.

A tentative description for the trend observed in Figure 6.10 is that at lower concentrations the 4-ATP/EGFR system exhibits stress related spectral behaviour. However, as EGFR concentration increases the plot more closely resembles a typical sigmoidal antibody/antigen binding curve. Sigmoidal curves for antibody/antigen binding are commonly reported in the literature [231, 232].

The third and final system tested was 6-MP/EGFR with plots presented in Figure 6.11.

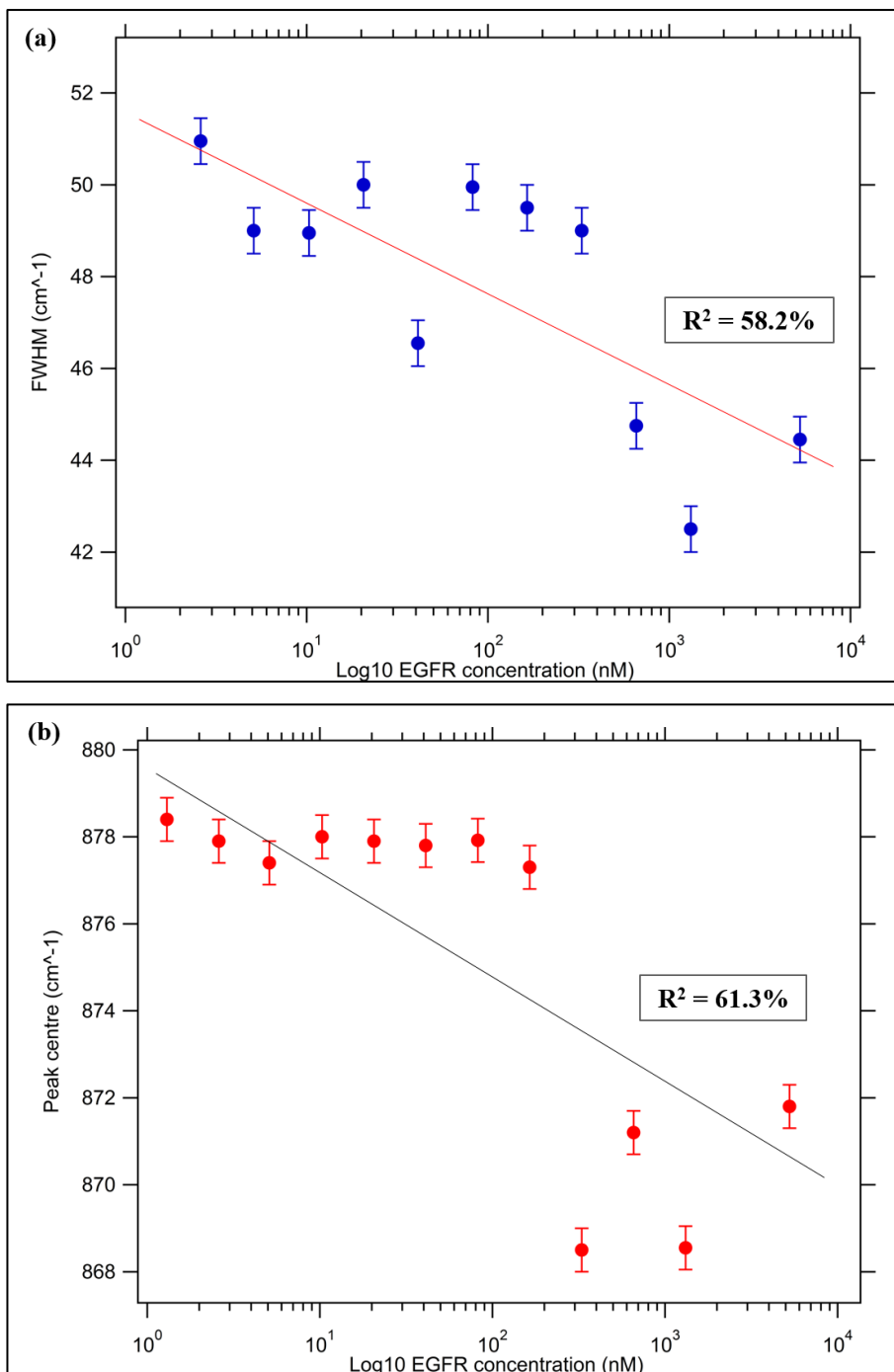


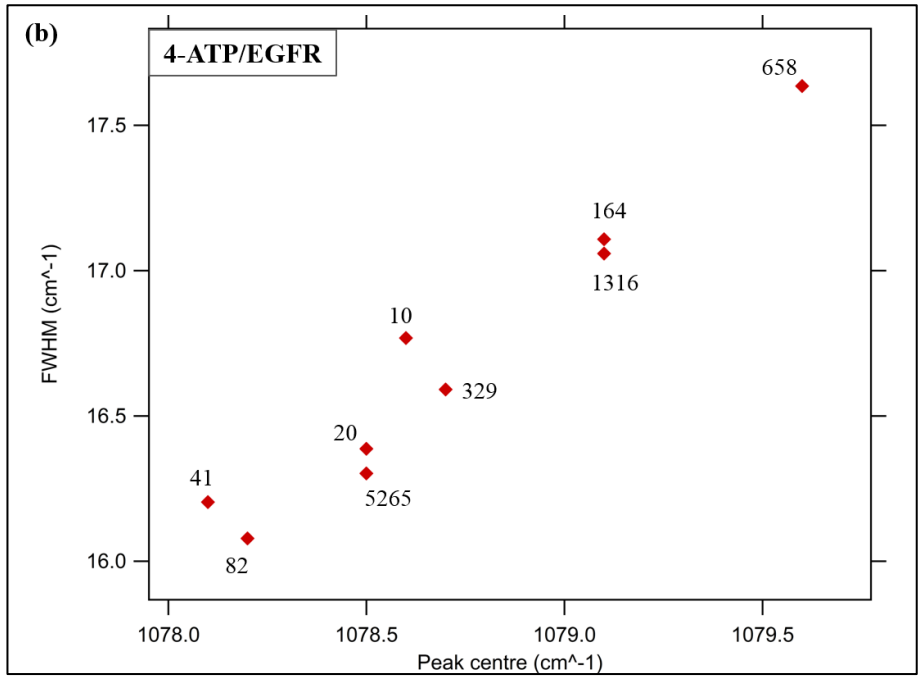
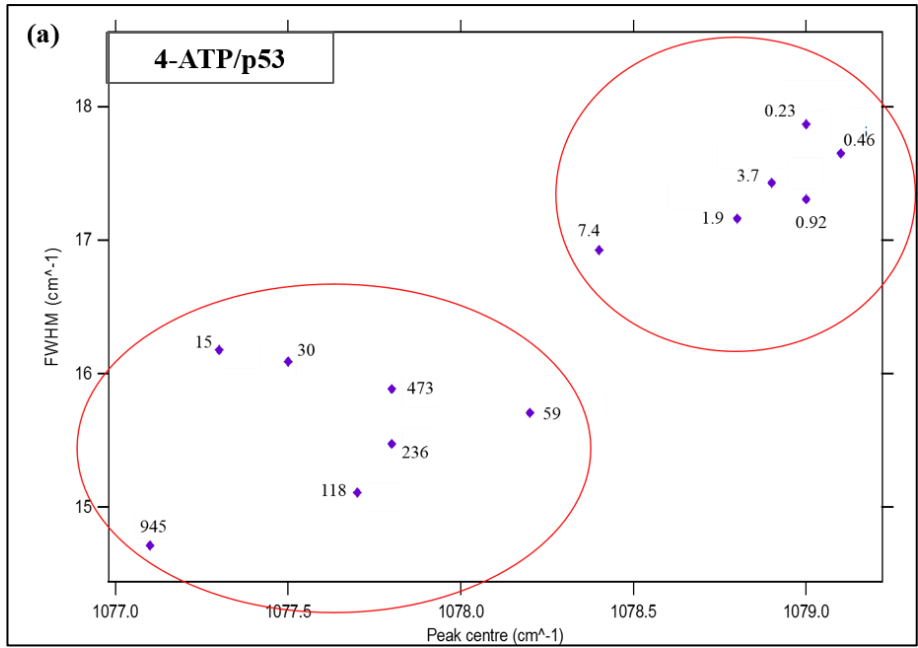
Figure 6.11 Variation in FWHM & peak position for 6-MP/EGFR system

Semi-log plots for FWHM & peak position (a) variation of FWHM with EGFR concentration, linear regression line overlaid; R² = 58.2%, (b) variation in peak position with EGFR concentration; peak centre red shifted with increasing concentration. Raman parameters both plots: 785 nm excitation wavelength, 0.47 mW laser power, 100x objective, 1200 lines/mm grating, 25-point average, Gaussian curve fitted data. Error bars (± 0.5 cm⁻¹)

For the 6-MP/EGFR system FWHM broadening occurs with decreasing protein concentration; Figure 6.11 (a). There is also a red shift in peak centre observed with increasing protein concentration. The observed spectral variations are similar to that of the 4-ATP/p53 model in Figure 6.9 above. However, the trend is not as clearly defined as the 4-ATP/p53 system. For FWHM the R^2 values are 89.6 & 58.2% for the 4-ATP & 6-MP linker systems respectively. Additionally, while a red shift of peak centre is observed in both cases, the linear fit is poor for the 6-MP/EGFR model, $R^2 = 61.3\%$; Figure 6.11 (b).

From these three systems tested, it seems that the stress response displays a degree of specificity to the linker/protein combination. The stress response observed for 4-ATP/p53 and 6-MP/EGFR was not observed for 4-ATP/p53 (except at lower concentrations).

In order to further validate the stress/strain behaviour of the 4-ATP/p53 and 6-MP/EGFR systems, correlation plots for FWHM vs peak centre are presented in Figure 6.12. It is expected that there would be a clustering of data sets at high and low concentrations for the systems exhibiting a nanostress response.



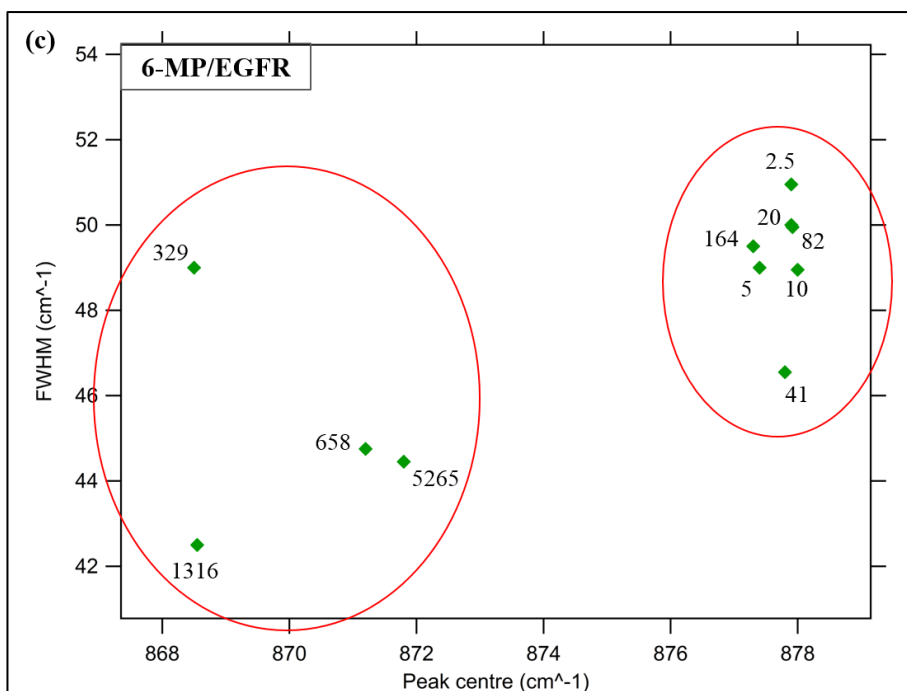


Figure 6.12 Correlation plot; FWHM & Peak centre position for 4-ATP/p53 system
 (a) 4-ATP/p53 system. Observed clear grouping of data points at high and low analyte concentrations. The antibody only data is a clear outlier - data point labels: target analyte concentration (nM) (b) 4ATP/EGFR (c) 6MP/EGFR.

The plots in Figure 6.12 (a) & (c) show clustering of the low concentration data sets, at higher wavenumbers and greater FWHM values; 4-ATP/p53 and 6-MP/EGFR respectively. The opposite is true for the high concentration measurements. However, 4-ATP/EGFR shows no particular correlation with no clear grouping of data sets at high and low concentrations; Figure 6.12 (b).

Correlation of the two key parameters of FWHM and peak position, provides direct evaluation of target analyte concentration.

It is important to ensure that there is no cross-reactivity between antibody and non-target proteins. Cross-reactivity is where the antibodies recognize or bind to interfering non-target antigens. In order to address the issue of non-specific binding events for the antibody conjugated Raman linker systems, a control experiment is performed.

Several substrates were prepared using the same protocol as above. The Raman linker/protein configurations that were examined are listed in Table 6.4 below. The analyte concentration used was 2 nM for both proteins.

Table 6.4 Control system configuration

Raman Linker	Antibody	Protein (2 nM)
4-ATP	<i>None</i>	<i>None</i>
4-ATP	Anti-p53	<i>None</i>
4-ATP	Anti-p53	EGFR
4-ATP	Anti-p53	EGFR
4-ATP	Anti-p53	EGFR
4-ATP	Anti-p53	p53
4-ATP	Anti-p53	p53
4-ATP	Anti-p53	p53
4-ATP	Anti-EGFR	<i>None</i>
4-ATP	Anti-EGFR	p53
4-ATP	Anti-EGFR	p53
4-ATP	Anti-EGFR	p53

The Raman response at FWHM of the 4-ATP 1080 cm⁻¹ peak, of the ‘control’ substrates is shown below in Figure 6.13.

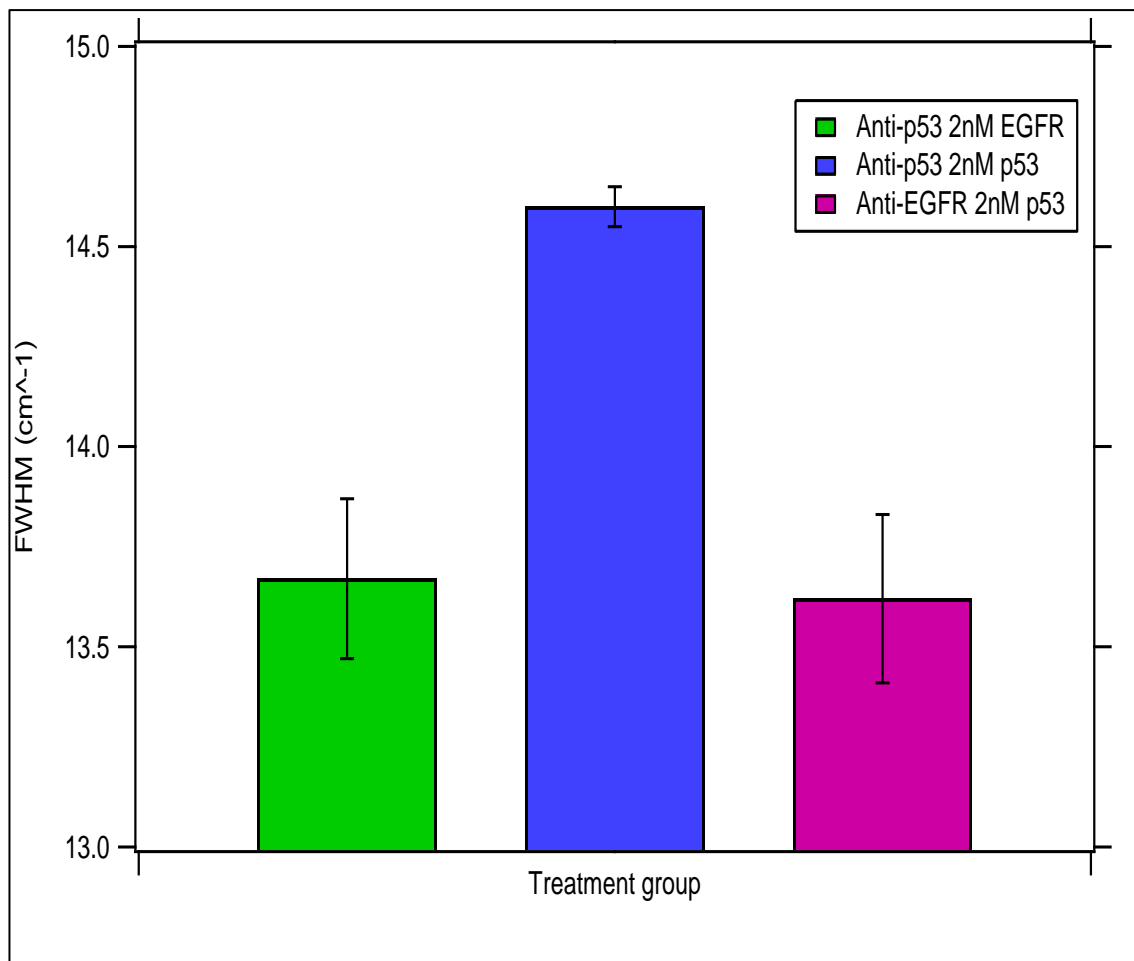


Figure 6.13 Response of control substrates at FWHM for differing system configurations
Only the anti-p53 + p53 (2nM) treatment group exhibits a FWHM broadening response

The response of the control system, demonstrates no cross-reactivity between unrelated antibody and proteins. The antibodies used are ‘manufactured’ to recognise only a specific stretch of amino acids (‘subunits’ of protein) and should not be compatible with interfering species. The control experiment confirmed this, and only the correct antibody specific protein combination (anti-p53 + p53) produced the stress response noted previously.

6.3 Discussion

We have shown that characteristics of specific peaks in the spectra of Raman active molecules vary as they are influenced by variations in protein concentration. These spectral measurements can then be used to evaluate protein concentration for certain linker/antibody/protein systems. We believe the nanomechanical responses of the systems, are demonstrated in variation to FWHM and peak position. However, it is especially the measurement of FWHM, and at lower concentrations that offers good correlation with protein concentration. A summary of which systems exhibited a nanostress response to variation in protein concentration is presented in Table 6.5.

Table 6.5 Linker/Protein systems & results

Raman Linker	Antibody	Protein	Nanostress response
4-ATP	<i>Anti-p53</i>	p53	✓
4-ATP	<i>Anti-EGFR</i>	EGFR	x
6-MP	<i>Anti-EGFR</i>	EGFR	✓

Of the three linker/protein systems analysed, it was found that the measured nanomechanical stress behaviour did not occur in each case. The 4-ATP/Anti-EGFR/EGFR system did not demonstrate a consistent Raman response to changes in protein concentration.

Reasons for this specificity arise from the complex nature of protein structural configurations and their interactions. Both p53 and EGFR comprise of electron rich aromatic lateral chains, and are different in both structural size, weight and the nature of their binding sites. The molecular weight of p53 is 53 kDa, while EGFR is 97 kDa; their antibodies are both ~ 150 kDa. These differences between the proteins, influence the efficiency of the Raman linker/antibody/protein to substrate binding.

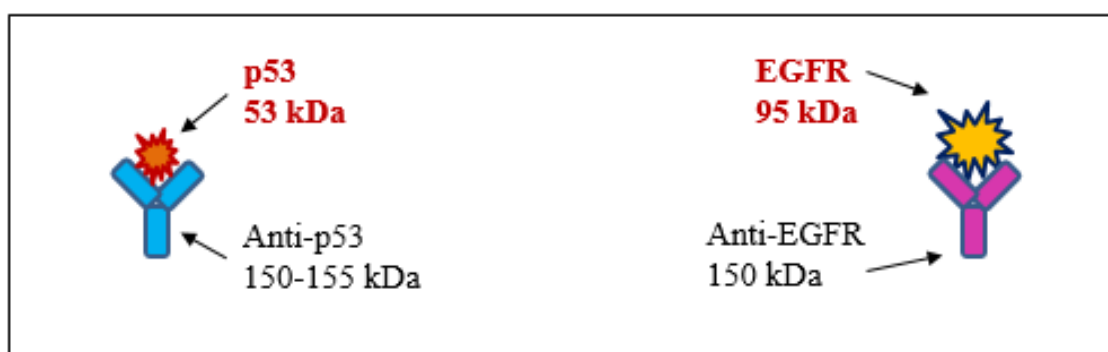


Figure 6.14 Schematic showing molecular weight for p53 and EGFR biomarkers
Commercial IgG antibodies used for both p53 and EGFR

The molecular weights of the antibodies are significantly larger than the associated antigens for both p53 and EGFR. For the antibodies ~ 150 kDa in both cases while the antigens are 53 kDa and 95 kDa for p53 and EGFR respectively. If the stress response most accurately describes the observed spectral variations, then it is expected that the molecular weight will be the dominant factor involved in the stress response of the system. Thus, it is also expected

that the greatest frequency shifts and FWHM variations should be observed from Raman linker only to Raman linker/Antibody functionalised substrates. This is the case for both the 4-ATP and 6-MP linkers; Table 6.2 & Table 6.3.

With regard to the nanostress response of these systems, a summary of the spectral changes measured is as follows.

The 4-ATP/p53 model displayed a FWHM broadening inversely proportional to protein concentration, and red shift of peak centre with increasing concentration. The linear relation had R^2 values of 89.6 & 72.6% for FWHM and peak shift respectively.

Compared to 4-ATP/p53 system, the 6-MP/EGFR model portrayed weaker Raman scattering with associated reduction in the signal to noise ratio. However, it was still possible to detect the effects of nanomechanical stress/strain as it was for the 4-ATP/p53 system. This was due to the sensitivity of the SERS substrates used, which enabled the detection of subtle influences of variations in protein concentration; Figure 4.5.

Finally, the 4-ATP/EGFR model displayed a possible nanostress response at lower concentrations. However, as concentration increases beyond ~ 80 nM the curve more closely resembles a sigmoidal response exhibited by a typical antibody/antigen binding event [233]

In addition to mechanical effects, other influences on the system will arise from the electrostatic properties of the protein molecules. Protein electrostatic affinity and general binding efficiency can be described by the K_D value. The K_D value for p53 is 1.5×10^{-9} M [234] and for EGFR 1.9×10^{-11} M. The equilibrium dissociation constant or K_D value is a quantification of the strength of a biomolecular interaction. The binding strength or affinity of an antibody/antigen reaction is inversely proportional to the K_D value i.e. the lower the K_D value the higher the affinity [235, 236].

In the case of the two biomarkers used in this project, EGFR has a stronger affinity to its antibody than p53. This may in part explain why the p53 system demonstrated a more dominant mechanical/stress response.

We believe that for the p53 model, which has a larger K_D value than EGFR, the mechanical nanostress influence was the primary factor affecting Raman spectral variations. However, for EGFR systems, the lower K_D value meant that the binding affinity became a more significant factor. This is especially the case for 4-ATP/EGFR as concentration increased. Where possible nanostress behaviour was observed at low concentrations only; Figure 6.10.

Correlation plots for the two key indicators of FWHM and peak centre shift were also plotted. Separate clustering of data points at high and low concentration were observed for the 4-ATP/p53 and 6-MP/EGFR models offering further endorsement of the stress/sensor model. A similar correlation at high and low concentrations was not observed for the 4-ATP/EGFR model.

A control experiment was also performed to confirm that no cross-reactivity would occur between antibodies and non-target antigens. The results verified that the antibodies for the two biomarkers used were specific to their target antigens.

6.4 Conclusions

We have shown that variations in protein concentration affect the Raman spectra of certain Raman linker/antibody/protein combinations when measured using highly sensitive SERS substrates. The influence of protein concentration on specific spectral peaks was noted to particularly affect the FWHM and peak centre position.

We believe that the dominant mechanism involved in the observed changes to the Raman spectra is a 'physical' effect. This mechanism is essentially an induced mechanical nanostress/strain on the binding site between Raman linker and antibody which varies with protein concentration. This nanostress/strain occurs as the change in antigen concentration produces structural modifications to the protein moiety. This was especially noticeable for the 4-ATP/p53 and 6-MP/EGFR models.

In addition to our experimental observations, other important verification for the nanomechanical stress model are found in the literature.

The possibility of other chemical effects that may occur, after linker/antibody/antigen binding was investigated by Moulin et al. [237]. They concluded that no post-binding influence on Raman frequency shifts would arise from linker and antibody molecules that were not attached to each other.

Some other key conclusions from the work by Kho et al. [186] are listed as follows.

The work by Kho et al. involved the Raman linkers 4-ATP and 6-MP with the biomarkers H1 and p53 respectively. Their studies ruled out any non-mechanical influence of the antibodies on the frequency shifts of the linker spectra. They concluded this from comparisons between the antibody and 4-ATP spectra, where it was found that the intensities recorded from the antibody spectra were ten times weaker than that of the linker spectra. Thus, the antibody has only negligible influence on the frequency shifts.

Additionally, as mentioned above, the antibody is ~ 12 nm in length which means that the location of its paratope is well outside the SERS near field region. This in turn places any antigens that attach to the antibody/antigen binding site also outside the SERS near field. Thus, the effect of antigen concentration on linker/antibody binding sites will predominantly be of a mechanical nature.

Another key consideration is the possible effect on the pH levels of any non-conjugated linker molecules 'adjacent' to antibody conjugated molecules, and the subsequent effect on Raman spectra. Kho et al. measured pure 4-ATP spectra at different pH levels and compared them to 4-ATP/antibody spectra, by contrasting peak intensity ratios of the 4-ATP 1007 & 1620 cm^{-1} peaks. They found that the different pH levels did not cause a peak shift as observed for antibody/antigen conjugated systems.

Finally, in further confirmation of the mechanical model to explain the observed effects of varying protein concentration on Raman linker spectra, Kho et al. performed an experiment using polystyrene microspheres. A thin film of microspheres was placed onto a linker/antibody conjugated SERS substrate in order to directly exert a mechanical stress to the system. It was found that a red shift of peak centres occurred from this purely mechanical influence. In other work by Domenici et al. [115] involving SERS biosensing of p53, they also noted red shifted peak positions resulting from increasing concentration.

The conclusion we make from our experimental work, is that quantifiable measurement of protein concentration is possible using the technique detailed above. This is especially the case at low concentrations. This low concentration sensitivity makes the technique especially suited to SERS bioanalysis where the Raman signal to noise ratio is characteristically low. We also believe that the recorded Raman data was immune to system-based intensity fluctuations.

However, we also noted that the Raman linker/antibody/protein models are very specific and that only certain combinations will result in quantifiable changes to the Raman peaks of interest.

Regarding future work, we suggest that experimental plots of frequency shifts and peak broadening are examined for different molecular weight proteins. Thus, the mechanical stress sensor model can be analysed to see how closely it mirrors the experimental outputs for each biomarker. It is expected that the nanostress model will differ to some degree from experimental results. This will result from at least two other contributing factors, with the most significant being electrostatic.

The electrostatic properties and interactions of proteins are complex. However, to some degree the properties are size dependent. For proteins, it has been reported that smaller surface areas contain a greater density of charged and polar groups than larger surface areas [238]. Thus, the relative sizes of individual biomarkers along with KD values could be a convenient way to relate the influence of electrostatic properties to the system response.

The antibodies act as ‘receptors’ for the target antigen. As the protein concentration increases, a saturation threshold of antibody receptors should be achieved. As such, future studies should also investigate the saturation behaviour at the upper concentration threshold. At the upper threshold, it is expected that no further frequency shifts would be observed due to saturation of the antibody active binding sites. This has been reported in the literature for studies on a nanostress 4-ATP/H1 antibody/antigen sensor [181].

A suitable range of suggested biomarkers that can be used for future work are given in Table 6.6.

Table 6.6 Biomarker & antibody molecular weights

Commercial antibodies generally used with PSA, CA15-3 & CA125 are IgG which comprise of two heavy chains of ~ 55 kDa and two lighter chains of ~ 25 kDa; overall $M_w \approx 160$ kDa

Biomarker type	M_w – Protein (kDa)	M_w – Antibody (kDa)	Cancer type
Prostate specific antigen (PSA)	28	160	Prostate cancer
p53	53	150	Breast, colorectal, lung, liver & ovarian cancers
Cancer antigen 15-3 (CA15-3)	122	160	Breast cancer
Cancer antigen 125 (CA125)	1,519	160	Ovarian cancer

7 Concluding Discussion & Future work

7.1 SERS sensing platforms

To date, SERS analysis has brought numerous advantages to the varied applications that it has been used for. However, the degree to which SERS can realize its full potential, is ultimately governed by the quality of the substrates that can be fabricated. We have examined several different types of platform-based SERS substrates for relative performance. One conclusion gained is that the use of state of the art nanofabrication techniques is no guarantee of achieving high efficiency substrates. The governing factor relating to signal enhancement that drives substrate fabrication is the geometrical parameter associated with a strong SERS enhancement. Most notably, ultra-small structure spacing between adjacent nanostructures is required to achieve large SERS enhancements. However, this must ideally be achieved in conjunction with good signal consistency across the SERS-active region.

From the characterisation above, it was found that the most efficient SERS platform was the Ag ‘leaning’ Nanopillar surface array. It possessed exceptionally strong enhancements along with reasonable consistency. It is of interest to note how this substrate achieves the ultra-low gap dimensionality required for such high levels of performance. Structure spacing of ~ 2 nm are achieved post fabrication. This circumvents the challenges of directly fabricating such dimensions with existing nanofabrication techniques.

The choice of SERS sensing platforms depends very much on whether the application is for ‘high sensitivity total solution’ or ‘trace detection/field use’. We have shown that the detection of ultra-low concentrations of proteins is possible using high efficiency substrates, in conjunction with research grade Raman spectrometers [1]. The substrates have also been used to characterise complex biological samples such as diphenylalanine nanotube-folic acid conjugates [71, 239]. However, while substrates such as the inkjet printed units lack the sensitivity of the ‘leaning’ Nanopillars, they can still generate strong SERS signals. Thus, substrates such as the inkjet test strips do not require the use of high end spectrometers and are ideally suited to trace detection field use [190, 240].

The SCIL technique is typically used for applications such as: Photonic crystal patterning (i.e. LED manufacture) [241]; micro-optical elements [242]; and printed electronics (e.g. RFID’s) [243]. However, SCIL can easily produce arrays of high quality periodic nanostructures. This makes it possible to fabricate SERS substrates with moderate enhancement and excellent consistency for both individual substrates and batch to batch reproducibility. The SCIL process can potentially provide SERS substrates that fulfil these two performance criteria. Provided the recommended optimization is carried out for any future fabrication. The SCIL process utilizes a reusable flexible mask during fabrication. This has the additional advantage of significant cost savings in the case of a large volume production run. In the literature it is reported that up to 3000 imprints from a single flexible stamp are achievable [241].

7.2 SERS Nanostress biosensing

In this work, our aim was to develop a robust technique for measurement of biomarker concentration using high efficiency SERS substrates. An indirect approach to the measurement of protein concentration was adopted. Quantitative measurements were acquired for changes in analyte concentration by measuring both frequency shifts and peak broadening. We propose that our method for measurement of these changes is immune to system based intensity fluctuations. This is especially advantageous at the lower end of the concentration range, where intensity fluctuations typically occur for low abundance biomolecules.

The lowest concentrations measured in this work are comparable to the sensitivity achieved in previous work using nanostress sensors [181, 186]. Measurements of 0.23 and 1.3 nM were obtained for the lower threshold concentrations of p53 and EGFR respectively.

Future work should aim to develop a better understanding of the processes involved in generating the nanostress response. Additionally, the suitability of other linker/protein combinations for use as nanostress biosensing systems should be examined. The sensitivity thresholds should be evaluated and compared to current ELISA-based methods.

During our work, it was also noted that the assays are specific to certain combinations of linker/antibodies. The difference in the characteristic behaviour of various nanostress systems can be exploited, in order to enable multiplexed sensing of antigens. The ability to detect multiple combinations of biomarkers from a single sample, will give a more certain prognosis of disease presence.

Multiplexed detection using SERS nanostress biosensing has been reported. For example, Kho et al. [186] functionalised two separate Raman linker/antibody systems in a two-step process. During the initial step, the first linker formed self-assembled Nanoislands. This left the regions between these domains free, for the second linker to bind to, creating a mixed monolayer of linker molecules.

Similar work was undertaken by Tang et al. [244] where a multiplexed frequency shift SERS immunoassay was investigated for liver cancer biomarkers. Their work takes further steps to ensure more clearly differentiated Raman linker domains on the platform surface. This was carried out via the use of micro-contact printing, with a PDMS stamp generating square 2 x 2 μm regions. However, much work remains to be done in the area of multiplexed analysis. While the substrates were 'multi' functionalized, the proteins had to be individually tested on separate substrates, in order to gain the required frequency shifts.

It is envisaged that this type of nanostress sensor, could be used to test for the presence and concentration of specific cancer biomarkers present in any bio fluid. This would enable the eventual use of nanostress SERS biosensing, as a point of care clinical diagnostic technique. Elevated levels of p53 have been reported as indicators of the presence of both prostate [245] and breast cancer, while EGFR has been linked to lung cancer [246]. Many other biomarker examples are: cytokeratin 19 fragment Cyfra21-1; tissue polypeptide antigen; and cancer antigen 125 which are reported to be present in the saliva of patients with oral [247] and ovarian cancer [248].

The combination of sensitive multiplexed detection, with rapid readout capability of SERS biosensing, is a very promising research in the field of cancer research. With suitable development, it promises to be an excellent companion or alternative to the current gold standard methods that are available such as ELSIA.

8 Appendix

8.1 Commercial SERS substrates; fabrication techniques

Commercially available SERS substrates were purchased and characterized in Results 1 - Evaluation of Platform-based SERS substrates. A brief account of the fabrication techniques used by the commercial suppliers of these platform-based substrates is described as follows.

8.1.1 Silmeco ltd.

The Silmeco ‘leaning nanopillar’ substrates were manufactured using a four-stage procedure as described in the publication by Wu et al. [63] and is described briefly as follows.

1. Silicon Nanopillar structures are formed on a standard four-inch Silicon wafer using Reactive Ion Etching (RIE)
2. Impurities and contaminants from step 1 are removed by O₂ plasma cleaning
3. A preparatory adhesion layer of Cr is evaporated onto the nanostructures to ready the substrate for the final metallic deposition
4. A metallic thin film (‘Ag’ or ‘Au’) is then deposited onto the nanopillars via e-beam evaporation

8.1.2 Integrated optics

The Integrated optics substrates were fabricated via laser processing, and overlaid with either Ag or Au.

1. Laser ablation of soda lime glass to produce amorphous surface features of nanoscale geometry
2. A metallic thin film of ~ 200 nm thickness is then deposited to gain a SERS response from the substrate.

8.1.3 Horiba scientific

The Horiba substrates consisted of an Au array of nanorods realized by a two-stage oblique angled deposition (OAD)

1. First stage dynamic oblique deposition: to achieve a SiO₂ master pattern of nanorods
2. Second stage dynamic oblique deposition: Au deposition to achieve a SERS-active surface

The resulting nanogeometry is anisotropic and substrates are marked for correct alignment in Raman analysis.

8.1.4 Diagnostic anSERS

The inkjet printed substrates were manufactured by Diagnostic anSERS Inc.

The fabrication involves ‘printing’ Au nanostructures onto cellulose paper using a commercial piezo-based inkjet printer and Au nanoparticles (~ 50 nm). The steps involved in making these substrates are detailed in the publications by Hoppmann [190], Wei & White [249, 250] and summarized as follows.

1. A highly concentrated solution of Au Nanoparticles (NP) is made by centrifuging a gold colloid and suspending the supernatant in water.

2. A 'gold ink' is then created by adding glycerol and ethanol to the concentrated Au nanoparticles.
3. The gold ink is then injected into previously unused printer cartridges, and printed onto unprocessed chromatography paper. In order to increase the density of nanoparticles on the SERS active region the printing is repeated a further three times

A summary is given in Table 8.1 for the performance, signal deviation and purchase cost of the platform-based substrates.

Table 8.1 Summary; Platform-based substrate Raman comparison

Relative Deviation calculated at 1066 cm⁻¹ peak

Substrate Type	Metallic outer layer	SERS response	Relative Deviation (1066 cm⁻¹peak)	Purchase cost	Supplier
<i>'Leaning' Nanopillar</i>	Ag	Exceptionally High	17.9	Medium	<i>Silmeco ltd., Denmark</i>
<i>'Leaning' Nanopillar</i>	Au	High	16.8	Medium	<i>Silmeco ltd., Denmark</i>
<i>Laser fabricated</i>	Ag	High	16.7	Medium	<i>Integrated Optics, Lithuania</i>
<i>Laser fabricated</i>	Au	Moderate - High	19	Medium	<i>Integrated Optics, Lithuania</i>
<i>Nanorod array</i>	Au	Poor-Moderate	19.1	High	<i>Horiba Scientific</i>
<i>Inkjet</i>	Au	High	49.8	Low	<i>Diagnostic anSERS Inc., U.S.</i>

8.2 SERS EF calculations

SERS EF calculations as per Equation 4.1, with values for N_{SERS} & N_{Ref} obtained using the following:

Number of 2-NT molecules/nm² = 2; based on dimension of molecule as ≈ 0.76 nm reported by Zareie et al. [251].

For 50x lens, laser spot area = 0.882 μm^2 ; reduce by 2/3 to account for surface topography, laser spot area = 0.147 μm^2

$N_{\text{SERS}} = 193$ molecules

Sphere volume = 1.177 μm^3 => reduce by 30% to account for beam shape =>

Interaction volume = 0.392 μm^3 . Number of molecules in scattering volume ~ 298

$N_{\text{Ref}} = 298$ molecules.

The experimental values for I_{Ref} are listed below in Table 8.2

Table 8.2 Reference Raman Intensities

CCC Counts; background subtracted data

Objective lens	Raman Laser Power (mW)	CCD counts (1066 cm ⁻¹ peak)
20x	3.9	26.60
50x	0.32	13.17
50x	0.006	13.80

8.3 General calculations

Molarity calculations given by:

Mass (g) = Concentration (mol/L) * Volume (L) * Molecular Weight (g/mol)

Relative standard deviation (RSD) given by:

$$RSD = \frac{SDev}{Mean} \times 100\% \quad \text{Equation 8.1}$$

Laser spot diameter (d) given by:

$$d = \frac{(1.22) \times \lambda}{NA} \quad \text{Equation 8.2}$$

Wavelength (λ), Numerical Aperture (NA)

Table 8.3 Laser spot size; Renishaw Raman microscope

Objective	NA	Radius (μm)
20x	0.4	1.2
50x	0.75	0.65

8.4 Molecular structures & EDC reaction scheme

8.4.1 Molecular structures Raman reporter molecules

The molecular structures for the SERS probes are included in this section.

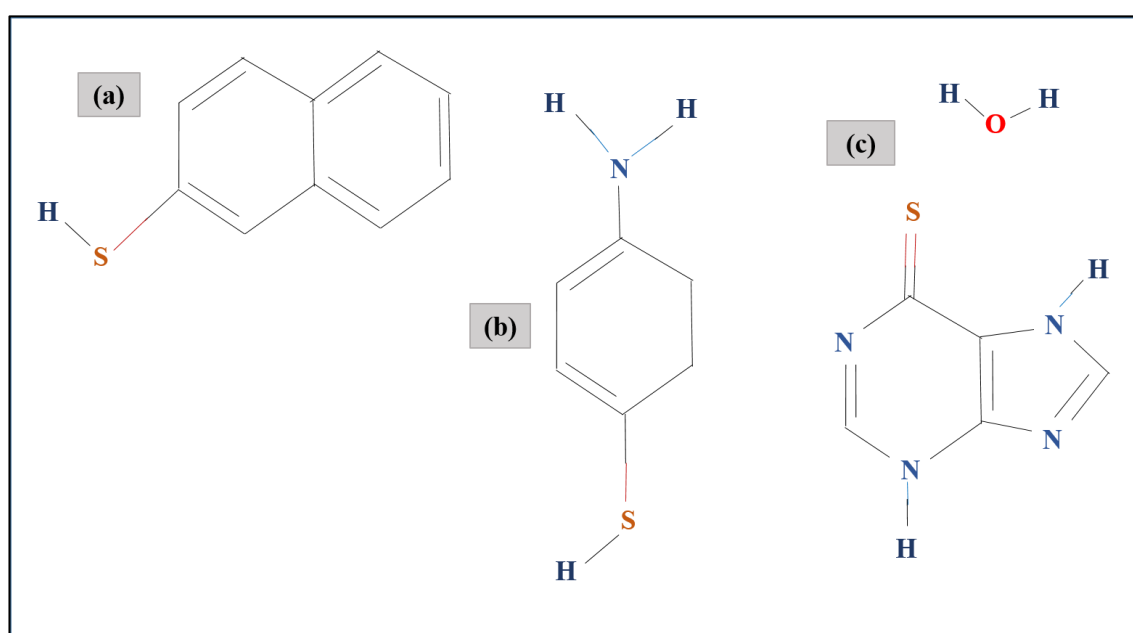


Figure 8.1 Molecular structure for SERS probes used in experimental work

(a) 2-Naphthalenethiol (2-NT) (b) 4-Aminothiophenol (4-ATP) (c) 6-Mercaptopurine Monohydrate (6-MP)

Molecular formula & molecular weights (M_w) are as follows:

2-Naphthalenethiol:

Molecular formula: $C_{10}H_8S$; $M_w = 160.24$ g/mol

4-Aminothiophenol:

Molecular formula: C_6H_7NS ; $M_w = 125.19$ g/mol

6-Mercaptopurine: Molecular formula:

$C_5H_4N_4S$; $M_w = 152.175$ g/mol

6-Mercaptopurine Monohydrate:

Molecular formula: $C_5H_4N_4S \cdot H_2O$; $M_w = 170.19$ g/mol

8.4.2 EDC reaction scheme

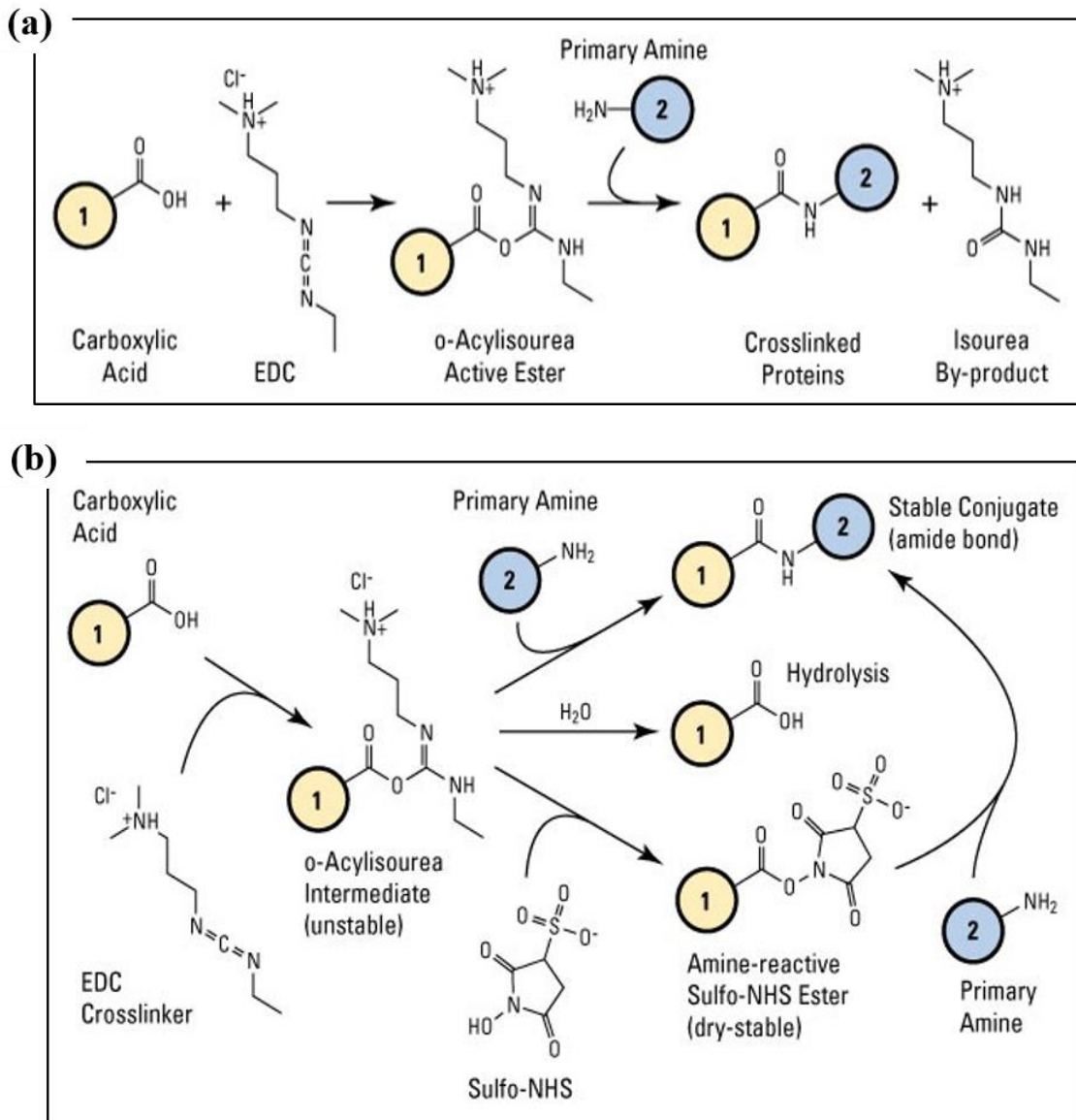
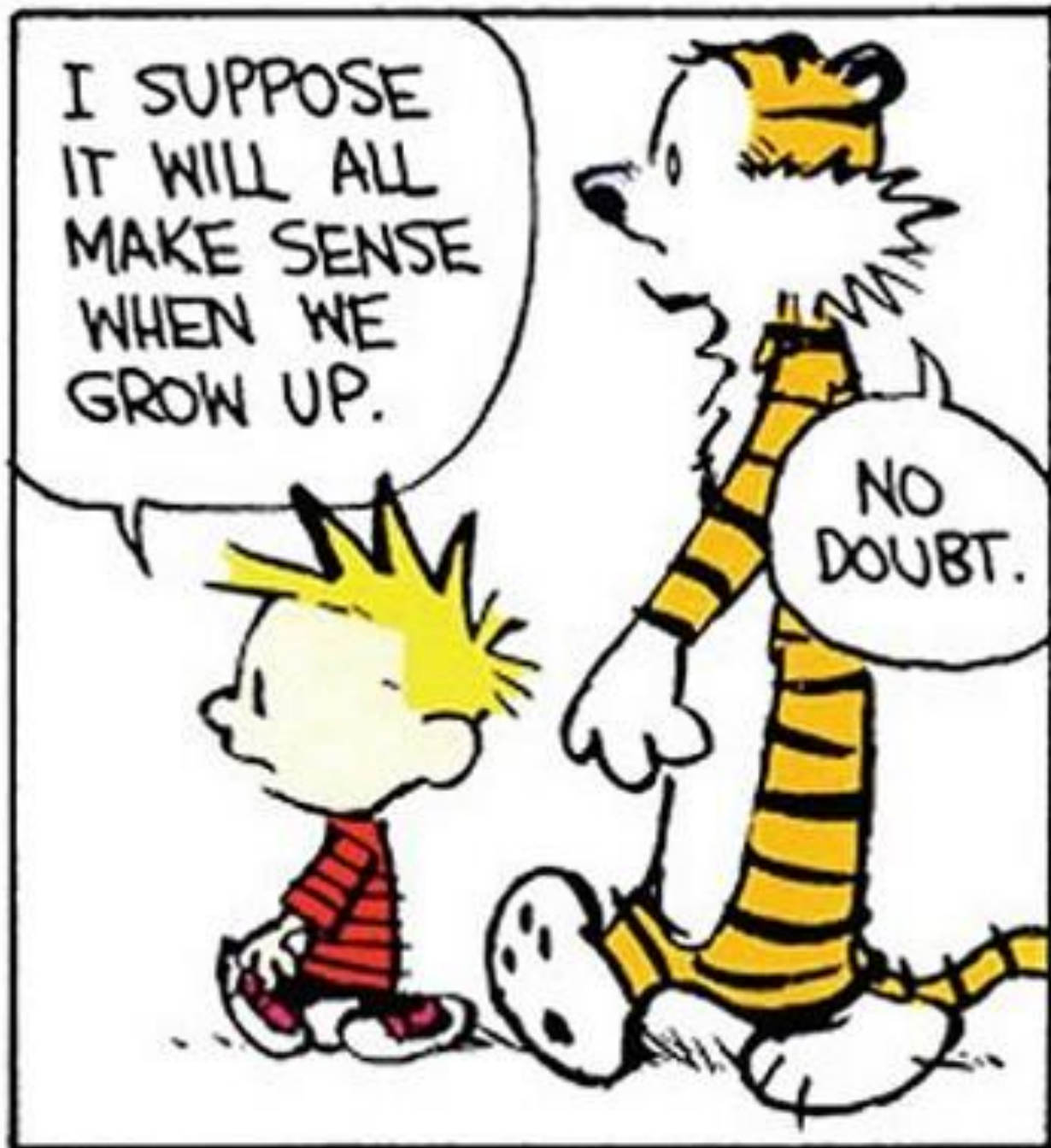


Figure 8.2 EDC reaction scheme

(a) EDC Carboxyl to amine crosslinking reaction scheme (b) EDC/NHS crosslinking reaction scheme

8.5 General references

- Funding for SCIL fabrication of nanostructured silicon wafers at Tyndall; acquired under the National Access Programme (NAP); *project number NAP370*
- NCBES (AFM image): *The authors acknowledge the facilities and scientific and technical assistance of the NCBES Microscopy unit within the Centre for Microscopy & Imaging at the National University of Ireland Galway, a facility that is funded by NUIG and the Irish Government's Programme for Research in Third Level Institutions, Cycles 4 and 5, National Development Plan 2007-2013*
- CRANN Advanced Microscopy Laboratory (AML); SEM images: *The authors acknowledge the facilities, scientific and technical assistance of the AML Microscopy unit, Trinity, Dublin*
- SERS Ag Nanopillar substrates supplied without cost by Tomas Rindzevicius, Silmeco ltd. under a Non-Disclosure Agreement (NDA) with NUIGalway.
- Protocol for Raman characterisation with 2NT; A*STAR research facility, Singapore
- SEM's for the following figure were received courtesy of J. Perumal, A*STAR research facility, Singapore: Figure 5.15
- Figure 2.7. *Authors:* Etchegoin PG, Le Ru EC. *Editor:* Schlücker S. *Title:* Surface Enhanced Raman Spectroscopy; Analytical, Biophysical & Life Science Applications. *Page 3. Publication year:* 2011. © Wiley-VCH Verlag GmbH & Co. KGaA. Reproduced with permission. [10]
- 'Calvin & Hobbes' image; page 208. Sourced from Andrews McMeel Syndication (*Universal*), accessed 1/9/2016. Reproduced with permission.
https://www.google.ie/search?q=images+calvin+and+hobbes&rlz=1C1NNVC_enIE495IE495&tbm=isch&tbo=u&source=univ&sa=X&ved=0ahUKEwik4ZDRre7OAhWmKsAKHWSuDKEQ7AkINw&biw=1366&bih=683#imgrc=SjJPqgpUcON-LM%3A
- Figure 8.2 Sourced from: Life Sciences Solutions, Thermo Fisher Scientific, Paisley PA4 9RF; accessed 23/1/2017. Reproduced with permission.
<https://www.thermofisher.com/ie/en/home/life-science/protein-biology/protein-biology-learning-center/protein-biology-resource-library/pierce-protein-methods/carbodiimide-crosslinker-chemistry.html>



9 Bibliography

1. Owens P, Phillipson N, Perumal J, O'Connor GM, Olivo M. Sensing of p53 and EGFR Biomarkers Using High Efficiency SERS Substrates. *Biosensors*. 2015;5(4):664-77.
2. Haynes C, McFarland A, Van Duyne R. *Surface-Enhanced Raman Spectroscopy*. 2005.
3. Kneipp K. *Surface-enhanced Raman scattering*. 2007.
4. McQuillan AJ. *Recollection. The discovery of surface-enhanced Raman scattering. Notes and Records of the Royal Society*. 2009;63(2):209-.
5. Kneipp K, Wang Y, Kneipp H, Perelman LT, Itzkan I, Dasari RR, et al. Single molecule detection using surface-enhanced Raman scattering (SERS). *Physical review letters*. 1997;78(9):1667.
6. Hahn DW. *Raman scattering theory. Department of Mechanical and Aerospace Engineering, University of Florida*. 2007.
7. Raman C, Krishnan K. Polarisation of scattered light-quanta. *Nature*. 1928;122:169.
8. Schatz GC, Van Duyne RP. *Electromagnetic mechanism of surface-enhanced spectroscopy. Handbook of vibrational spectroscopy*. 2002.
9. Valley N, Greeneltch N, Van Duyne RP, Schatz GC. A look at the origin and magnitude of the chemical contribution to the enhancement mechanism of surface-enhanced Raman spectroscopy (SERS): Theory and experiment. *The Journal of Physical Chemistry Letters*. 2013;4(16):2599-604.
10. Etchegoin PG, Le Ru EC. *Basic electromagnetic theory of SERS. Surface Enhanced Raman Spectroscopy: analytical, biophysical and life science applications*. 2011:1-38.
11. Willets KA, Van Duyne RP. *Localized surface plasmon resonance spectroscopy and sensing. Annu Rev Phys Chem*. 2007;58:267-97.
12. Kiefer W, Schlücker S. *Surface enhanced Raman spectroscopy: analytical, biophysical and life science applications: John Wiley & Sons*; 2011.
13. Sharma B, Cardinal MF, Kleinman SL, Greeneltch NG, Frontiera RR, Blaber MG, et al. *High-performance SERS substrates: Advances and challenges. MRS bulletin*. 2013;38(08):615-24.
14. Yang Z-L, Li Q-H, Ren B, Tian Z-Q. *Tunable SERS from aluminium nanohole arrays in the ultraviolet region. Chem Commun*. 2011;47(13):3909-11.
15. Jennings C, Aroca R, Hor AM, Loutfy RO. *Surface-enhanced Raman scattering from copper and zinc phthalocyanine complexes by silver and indium island films. Analytical chemistry*. 1984;56(12):2033-5.
16. Abdelsalam ME, Mahajan S, Bartlett PN, Baumberg JJ, Russell AE. *SERS at structured palladium and platinum surfaces. Journal of the American Chemical Society*. 2007;129(23):7399-406.
17. Albrecht MG, Creighton JA. *Anomalously intense Raman spectra of pyridine at a silver electrode. Journal of the American Chemical Society*. 1977;99(15):5215-7.
18. Haynes CL, Van Duyne RP. *Plasmon-sampled surface-enhanced Raman excitation spectroscopy. The Journal of Physical Chemistry B*. 2003;107(30):7426-33.

19. Shafer-Peltier KE, Haynes CL, Glucksberg MR, Van Duyne RP. Toward a glucose biosensor based on surface-enhanced Raman scattering. *Journal of the American Chemical Society*. 2003;125(2):588-93.
20. Zhang X, Young MA, Lyandres O, Van Duyne RP. Rapid detection of an anthrax biomarker by surface-enhanced Raman spectroscopy. *Journal of the American Chemical Society*. 2005;127(12):4484-9.
21. Xia L, Yang Z, Yin S, Guo W, Li S, Xie W, et al. Surface enhanced Raman scattering substrate with metallic nanogap array fabricated by etching the assembled polystyrene spheres array. *Optics Express*. 2013;21(9):11349-55.
22. Fan M, Andrade GF, Brolo AG. A review on the fabrication of substrates for surface enhanced Raman spectroscopy and their applications in analytical chemistry. *Analytica chimica acta*. 2011;693(1):7-25.
23. Kneipp K, Kneipp H, Manoharan R, Hanlon EB, Itzkan I, Dasari RR, et al. Extremely large enhancement factors in surface-enhanced Raman scattering for molecules on colloidal gold clusters. *Applied spectroscopy*. 1998;52(12):1493-7.
24. Yan B, Thubagere A, Premasiri WR, Ziegler LD, Dal Negro L, Reinhard BM. Engineered SERS substrates with multiscale signal enhancement: Nanoparticle cluster arrays. *ACS nano*. 2009;3(5):1190-202.
25. Kumar GVP. Plasmonic nano-architectures for surface enhanced Raman scattering: a review. *Journal of Nanophotonics*. 2012;6:064503.
26. Kreibig U. Electronic properties of small silver particles: the optical constants and their temperature dependence. *Journal of Physics F: Metal Physics*. 1974;4(7):999.
27. Lane LA, Qian X, Nie S. SERS nanoparticles in medicine: from label-free detection to spectroscopic tagging. *Chemical Reviews*. 2015;115(19):10489-529.
28. Ciou S-H, Cao Y-W, Huang H-C, Su D-Y, Huang C-L. SERS enhancement factors studies of silver nanoprism and spherical nanoparticle colloids in the presence of bromide ions. *The Journal of Physical Chemistry C*. 2009;113(22):9520-5.
29. Lin XM, Cui Y, Xu YH, Ren B, Tian ZQ. Surface-enhanced Raman spectroscopy: substrate-related issues. *Analytical and bioanalytical chemistry*. 2009;394(7):1729-45.
30. Tang X-L, Jiang P, Ge G-L, Tsuji M, Xie S-S, Guo Y-J. Poly (N-vinyl-2-pyrrolidone)(PVP)-capped dendritic gold nanoparticles by a one-step hydrothermal route and their high SERS effect. *Langmuir*. 2008;24(5):1763-8.
31. Jena BK, Raj CR. Seedless, surfactantless room temperature synthesis of single crystalline fluorescent gold nanoflowers with pronounced SERS and electrocatalytic activity. *Chemistry of Materials*. 2008;20(11):3546-8.
32. Seo D, Park JC, Song H. Polyhedral gold nanocrystals with Oh symmetry: From octahedra to cubes. *Journal of the American Chemical Society*. 2006;128(46):14863-70.
33. Natan MJ. Concluding remarks surface enhanced Raman scattering. *Faraday Discussions*. 2006;132:321-8.
34. Jiang Z, Jiang X, Su S, Wei X, Lee S, He Y. Silicon-based reproducible and active surface-enhanced Raman scattering substrates for sensitive, specific, and multiplex DNA detection. *Applied Physics Letters*. 2012;100(20):203104--4.

35. Castillo F, De la Rosa E, Pérez E. Gold aggregates on silica templates and decorated silica arrays for SERS applications. *European Physical Journal D-Atomic MolecularOptical and Plasma Physics*. 2011;63(2):301.
36. Seniutinas G, Gervinskas G, Verma R, Gupta BD, Lapierre F, Stoddart PR, et al. Versatile SERS sensing based on black silicon. *Optics Express*. 2015;23(5):6763-72.
37. Deng Y-L, Juang Y-J. Black silicon SERS substrate: Effect of surface morphology on SERS detection and application of single algal cell analysis. *Biosensors and Bioelectronics*. 2014;53:37-42.
38. Chursanova M, Germash L, Yukhymchuk V, Dzhagan V, Khodasevich I, Cojoc D. Optimization of porous silicon preparation technology for SERS applications. *Applied surface science*. 2010;256(11):3369-73.
39. Chan S, Kwon S, Koo TW, Lee LP, Berlin AA. Surface-Enhanced Raman Scattering of Small Molecules from Silver-Coated Silicon Nanopores. *Advanced Materials*. 2003;15(19):1595-8.
40. Ma L, Zhou Y, Jiang N, Lu X, Shao J, Lu W, et al. Wide-band "black silicon" based on porous silicon. *Applied Physics Letters*. 2006;88(17):171907.
41. Talian I, Mogensen KB, Oriňák A, Kaniansky D, Hübner J. Surface-enhanced Raman spectroscopy on novel black silicon-based nanostructured surfaces. *Journal of Raman Spectroscopy*. 2009;40(8):982-6.
42. Zasadzinski J, Viswanathan R, Madsen L, Garnæs J, Schwartz D. Langmuir-blodgett films. *Science-AAAS-Weekly Paper Edition-including Guide to Scientific Information*. 1994;263(5154):1726-38.
43. Lin X-M, Cui Y, Xu Y-H, Ren B, Tian Z-Q. Surface-enhanced Raman spectroscopy: substrate-related issues. *Analytical and bioanalytical chemistry*. 2009;394(7):1729-45.
44. Tao A, Kim F, Hess C, Goldberger J, He R, Sun Y, et al. Langmuir-Blodgett silver nanowire monolayers for molecular sensing using surface-enhanced Raman spectroscopy. *Nano letters*. 2003;3(9):1229-33.
45. Kleinman SL, Sharma B, Blaber MG, Henry A-I, Valley N, Freeman RG, et al. Structure enhancement factor relationships in single gold nanoantennas by surface-enhanced Raman excitation spectroscopy. *Journal of the American Chemical Society*. 2012;135(1):301-8.
46. Du Y, Shi L, He T, Sun X, Mo Y. SERS enhancement dependence on the diameter and aspect ratio of silver-nanowire array fabricated by anodic aluminium oxide template. *Applied surface science*. 2008;255(5):1901-5.
47. Korte F, Serbin J, Koch J, Egbert A, Fallnich C, Ostendorf A, et al. Towards nanostructuring with femtosecond laser pulses. *Applied Physics A: Materials Science & Processing*. 2003;77(2):229-35.
48. Bjerneld EJ, Svedberg F, Käll M. Laser-induced growth and deposition of noble-metal nanoparticles for surface-enhanced Raman scattering. *Nano letters*. 2003;3(5):593-6.
49. Agarwal N, Fazio E, Neri F, Trusso S, Castiglioni C, Lucotti A, et al. Ag and Au nanoparticles for SERS substrates produced by pulsed laser ablation. *Crystal Research and Technology*. 2011;46(8):836-40.

50. Diebold ED, Mack NH, Doorn SK, Mazur E. Femtosecond laser-nanostructured substrates for surface-enhanced Raman scattering. *Langmuir*. 2009;25(3):1790-4.
51. Hamdorf A, Olson M, Lin CH, Jiang L, Zhou J, Xiao H, et al. Femtosecond and nanosecond laser fabricated substrate for surface-enhanced Raman scattering. *Optics letters*. 2011;36(17):3353-5.
52. Alvarez-Puebla R, Cui B, Bravo-Vasquez J-P, Veres T, Fenniri H. Nanoimprinted SERS-active substrates with tunable surface plasmon resonances. *The Journal of Physical Chemistry C*. 2007;111(18):6720-3.
53. Hamouda F, Barbillon G, Held S, Agnus G, Gogol P, Maroutian T, et al. Nanoholes by soft UV nanoimprint lithography applied to study of membrane proteins. *Microelectronic Engineering*. 2009;86(4):583-5.
54. Cottat M, Lidgi-Guigui N, Tijunelyte I, Barbillon G, Hamouda F, Gogol P, et al. Soft UV nanoimprint lithography-designed highly sensitive substrates for SERS detection. *Nanoscale research letters*. 2014;9(1):1-6.
55. Haynes CL, Van Duyne RP. Nanosphere lithography: a versatile nanofabrication tool for studies of size-dependent nanoparticle optics. *The Journal of Physical Chemistry B*. 2001;105(24):5599-611.
56. Sweetenham CS, Nottingher I. Combined atomic force microscopy-Raman mapping of electric field enhancement and surface-enhanced Raman scattering hot-spots for nanosphere lithography substrates. *Journal of Nanophotonics*. 2011;5:059504.
57. Nunns A, Gwyther J, Manners I. Inorganic block copolymer lithography. *Polymer*. 2013;54(4):1269-84.
58. Hawker CJ, Russell TP. Block copolymer lithography: Merging “bottom-up” with “top-down” processes. *MRS bulletin*. 2005;30(12):952-66.
59. Zhang J, Gao Y, Alvarez-Puebla RA, Buriak JM, Fenniri H. Synthesis and SERS properties of nanocrystalline gold octahedra generated from thermal decomposition of HAuCl₄ in block copolymers. *Advanced Materials*. 2006;18(24):3233-7.
60. Lin Y-Y, Liao J-D, Ju Y-H, Chang C-W, Shiau A-L. Focused ion beam-fabricated Au micro/nanostructures used as a surface enhanced Raman scattering-active substrate for trace detection of molecules and influenza virus. *Nanotechnology*. 2011;22(18):185308.
61. Sivashanmugan K, Liao J-D, Liu BH, Yao C-K. Focused-ion-beam-fabricated Au nanorods coupled with Ag nanoparticles used as surface-enhanced Raman scattering-active substrate for analyzing trace melamine constituents in solution. *Analytica chimica acta*. 2013;800:56-64.
62. Schmidt MS, Hübner J, Boisen A. Large Area Fabrication of Leaning Silicon Nanopillars for Surface Enhanced Raman Spectroscopy. *Advanced Materials*. 2012.
63. Wu K, Rindzevicius T, Schmidt MS, Mogensen KB, Hakonen A, Boisen A. Wafer-Scale Leaning Silver Nanopillars for Molecular Detection at Ultra-Low Concentrations. *The Journal of Physical Chemistry C*. 2015;119(4):2053-62.
64. Zhang R, Xu B-B, Liu X-Q, Zhang Y-L, Xu Y, Chen Q-D, et al. Highly efficient SERS test strips. *Chemical Communications*. 2012;48(47):5913-5.

65. Li B, Zhang W, Chen L, Lin B. A fast and low-cost spray method for prototyping and depositing surface-enhanced Raman scattering arrays on microfluidic paper based device. *Electrophoresis*. 2013;34(15):2162-8.
66. Zhang W, Li B, Chen L, Wang Y, Gao D, Ma X, et al. Brushing, a simple way to fabricate SERS active paper substrates. *Analytical Methods*. 2014;6(7):2066-71.
67. Yu C-C, Chou S-Y, Tseng Y-C, Tseng S-C, Yen Y-T, Chen H-L. Single-shot laser treatment provides quasi-three-dimensional paper-based substrates for SERS with attomolar sensitivity. *Nanoscale*. 2015;7(5):1667-77.
68. Liu Y-J, Chu HY, Zhao Y-P. Silver nanorod array substrates fabricated by oblique angle deposition: morphological, optical, and SERS characterizations. *The Journal of Physical Chemistry C*. 2010;114(18):8176-83.
69. Driskell JD, Shanmukh S, Liu Y, Chaney SB, Tang X-J, Zhao Y-P, et al. The use of aligned silver nanorod arrays prepared by oblique angle deposition as surface enhanced Raman scattering substrates. *The Journal of Physical Chemistry C*. 2008;112(4):895-901.
70. Grimault AS, Vial A, Lamy de La Chapelle M. Modeling of regular gold nanostructures arrays for SERS applications using a 3D FDTD method. *Applied Physics B: Lasers and Optics*. 2006;84(1):111-5.
71. Wu K, Rindzevicius T, Schmidt MS, Mogensen KB, Xiao S, Boisen A. Plasmon resonances of Ag capped Si nanopillars fabricated using mask-less lithography. *Optics Express*. 2015;23(10):12965-78.
72. Oo SZ, Charlton MDB, Pollard M, Pearce S, Chen R, editors. 3D analysis of surface plasmon dispersion for SERS sensor based on inverted pyramid nanostructures. 2012.
73. Kim K, Choi J-Y, Lee HB, Shin KS. Raman scattering of 4-aminobenzenethiol sandwiched between Ag nanoparticle and macroscopically smooth Au substrate: Effects of size of Ag nanoparticles and the excitation wavelength. *The Journal of chemical physics*. 2011;135(12):124705.
74. Shen HX, Zou WJ, Yang ZL, Yuan YX, Xu MM, Yao JL, et al. Surface-enhanced Raman spectroscopy on single Fe₂O₃@ Au spindle nanoparticle: polarization dependence and FDTD simulation. *Journal of Optics*. 2015;17(11):114014.
75. Li W-D, Ding F, Hu J, Chou SY. Three-dimensional cavity nanoantenna coupled plasmonic nanodots for ultrahigh and uniform surface-enhanced Raman scattering over large area. *Optics Express*. 2011;19(5):3925-36.
76. Dhawan A, Gerhold M, Vo-Dinh T. Theoretical simulation and focused ion beam fabrication of gold nanostructures for surface-enhanced Raman scattering (SERS). *Nanobiotechnology*. 2007;3(3):164-71.
77. Ye J, Wen F, Sobhani H, Lassiter JB, Dorpe PV, Nordlander P, et al. Plasmonic nanoclusters: near field properties of the Fano resonance interrogated with SERS. *Nano letters*. 2012;12(3):1660-7.
78. Zeng Z, Liu Y, Wei J. Recent advances in surface-enhanced raman spectroscopy (SERS): Finite-difference time-domain (FDTD) method for SERS and sensing applications. *TrAC Trends in Analytical Chemistry*. 2016;75:162-73.
79. Xu Z, Wu HY, Ali SU, Jiang J, Cunningham BT, Liu GL. Nanoreplicated positive and inverted submicrometer polymer pyramid array for surface-enhanced Raman spectroscopy. *Journal of Nanophotonics*. 2011;5:3526.

80. Yee K. Numerical solution of initial boundary value problems involving Maxwell's equations in isotropic media. *Antennas and Propagation, IEEE Transactions on*. 1966;14(3):302-7.
81. Taflove A. Application of the finite-difference time-domain method to sinusoidal steady-state electromagnetic-penetration problems. *Electromagnetic Compatibility, IEEE Transactions on*. 1980(3):191-202.
82. Lin M, He L, Awika J, Yang L, Ledoux DR, Li Ha, et al. Detection of melamine in gluten, chicken feed, and processed foods using surface enhanced Raman spectroscopy and HPLC. *Journal of food science*. 2008;73(8):T129-T34.
83. Inscore F, Shende C, Sengupta A, Huang H, Farquharson S. Detection of drugs of abuse in saliva by Surface-Enhanced Raman Spectroscopy (SERS). *Applied spectroscopy*. 2011;65(9):1004-8.
84. Boyd S, Bertino MF, Ye D, White LS, Seashols SJ. Highly sensitive detection of blood by surface enhanced Raman scattering. *Journal of forensic sciences*. 2013;58(3):753-6.
85. Halvorson RA, Vikesland PJ. Surface-enhanced Raman spectroscopy (SERS) for environmental analyses. *Environmental science & technology*. 2010;44(20):7749-55.
86. Mulvihill M, Tao A, Benjauthrit K, Arnold J, Yang P. Surface-enhanced Raman spectroscopy for trace arsenic detection in contaminated water. *Angewandte Chemie*. 2008;120(34):6556-60.
87. Hakonen A, Andersson PO, Schmidt MS, Rindzevicius T, Käll M. Explosive and chemical threat detection by surface-enhanced Raman scattering: A review. *Analytica chimica acta*. 2015;893:1-13.
88. Chen K, Leona M, Vo-Dinh KC, Yan F, Wabuyele MB, Vo-Dinh T. Application of surface-enhanced Raman scattering (SERS) for the identification of anthraquinone dyes used in works of art. *Journal of Raman Spectroscopy*. 2006;37(4):520-7.
89. Ropret P, Madariaga JM. Applications of Raman spectroscopy in art and archaeology. *Journal of Raman Spectroscopy*. 2014;45(11-12):985-92.
90. Cui Y, Hegde RS, Phang IY, Lee HK, Ling XY. Encoding molecular information in plasmonic nanostructures for anti-counterfeiting applications. *Nanoscale*. 2014;6(1):282-8.
91. Anker JN, Hall WP, Lyandres O, Shah NC, Zhao J, Van Duyne RP. Biosensing with plasmonic nanosensors. *Nature materials*. 2008;7(6):442-53.
92. Kho KW, Qing KZM, Shen ZX, Ahmad IB, Lim SSC, Mhaisalkar S, et al. Polymer-based microfluidics with surface-enhanced Raman-spectroscopy-active periodic metal nanostructures for biofluid analysis. *Journal of biomedical optics*. 2008;13:054026.
93. Zhang X, Shah NC, Van Duyne RP. Sensitive and selective chem/bio sensing based on surface-enhanced Raman spectroscopy (SERS). *Vibrational Spectroscopy*. 2006;42(1):2-8.
94. Bantz KC, Meyer AF, Wittenberg NJ, Im H, Kurtuluş Ö, Lee SH, et al. Recent progress in SERS biosensing. *Physical Chemistry Chemical Physics*. 2011;13(24):11551-67.
95. Feng S, Chen R, Lin J, Pan J, Chen G, Li Y, et al. Nasopharyngeal cancer detection based on blood plasma surface-enhanced Raman spectroscopy and multivariate analysis. *Biosensors and Bioelectronics*. 2010;25(11):2414-9.
96. Kudelski A. Analytical applications of Raman spectroscopy. *Talanta*. 2008;76(1):1-8.

97. De S, Pal A, Jana NR, Pal T. Anion effect in linear silver nanoparticle aggregation as evidenced by efficient fluorescence quenching and SERS enhancement. *Journal of Photochemistry and Photobiology A: Chemistry*. 2000;131(1):111-23.
98. Faulds K, Stevenson R, Graham D. Quantitative DNA analysis using surface enhanced resonance raman scattering. 2010.
99. Graham D, Stevenson R, Thompson DG, Barrett L, Dalton C, Faulds K. Combining functionalised nanoparticles and SERS for the detection of DNA relating to disease. *Faraday Discussions*. 2011;149:291-9.
100. Linacre A, Graham D. Role of molecular diagnostics in forensic science. *Expert review of molecular diagnostics*. 2002;2(4):346-53.
101. von Maltzahn G, Centrone A, Park JH, Ramanathan R, Sailor MJ, Hatton TA, et al. SERS-coded gold nanorods as a multifunctional platform for densely multiplexed near-infrared imaging and photothermal heating. *Advanced Materials*. 2009;21(31):3175-80.
102. Keren S, Zavaleta C, Cheng Z, de La Zerda A, Gheysens O, Gambhir S. Noninvasive molecular imaging of small living subjects using Raman spectroscopy. *Proceedings of the National Academy of Sciences*. 2008;105(15):5844-9.
103. Yigit MV, Medarova Z. In vivo and ex vivo applications of gold nanoparticles for biomedical SERS imaging. *Am J Nucl Med Mol Imaging*. 2012;2(2):232-41.
104. Yuan H, Liu Y, Fales AM, Li YL, Liu J, Vo-Dinh T. Quantitative surface-enhanced resonant Raman scattering multiplexing of biocompatible gold nanostars for in vitro and ex vivo detection. *Analytical chemistry*. 2012;85(1):208-12.
105. Kah JCY, Kho KW, Lee CGL, Richard CJ. Early diagnosis of oral cancer based on the surface plasmon resonance of gold nanoparticles. *International journal of nanomedicine*. 2007;2(4):785.
106. Stuart DA, Yuen JM, Shah N, Lyandres O, Yonzon CR, Glucksberg MR, et al. In vivo glucose measurement by surface-enhanced Raman spectroscopy. *Analytical chemistry*. 2006;78(20):7211-5.
107. Cash KJ, Clark HA. Nanosensors and nanomaterials for monitoring glucose in diabetes. *Trends in molecular medicine*. 2010;16(12):584-93.
108. Wang H, Malvadkar N, Koytek S, Bylander J, Reeves WB, Demirel MC. Quantitative analysis of creatinine in urine by metalized nanostructured parylene. *Journal of biomedical optics*. 2010;15:027004.
109. Hennigan SL, Driskell JD, Dluhy RA, Zhao Y, Tripp RA, Waites KB, et al. Detection of *Mycoplasma pneumoniae* in Simulated and True Clinical Throat Swab Specimens by Nanorod Array-Surface-Enhanced Raman Spectroscopy. *PLoS One*. 2010;5(10):e13633.
110. Kho KW, Fu CY, Dinish U, Olivo M. Clinical SERS: are we there yet? *Journal of Biophotonics*. 2011.
111. Sharma B, Frontiera RR, Henry A-I, Ringe E, Van Duyne RP. SERS: materials, applications, and the future. *Materials Today*. 2012;15(1):16-25.
112. Premasiri W, Moir D, Klempner M, Krieger N, Jones G, Ziegler L. Characterization of the surface enhanced Raman scattering (SERS) of bacteria. *The Journal of Physical Chemistry B*. 2005;109(1):312-20.

113. Wang T-L, Chiang HK, Lu H-H, Peng F-Y. Semi-quantitative surface enhanced Raman scattering spectroscopic creatinine measurement in human urine samples. *Optical and quantum electronics*. 2005;37(13):1415-22.
114. Waites KB, Balish MF, Atkinson TP. New insights into the pathogenesis and detection of *Mycoplasma pneumoniae* infections. *Future microbiology*. 2008;3(6):635-48.
115. Domenici F, Bizzarri AR, Cannistraro S. SERS-based nanobiosensing for ultrasensitive detection of the p53 tumor suppressor. *International journal of nanomedicine*. 2011;6:2033.
116. Lin J, Chen R, Feng S, Pan J, Li Y, Chen G, et al. A Novel Blood Plasma Analysis Technique Combining Membrane Electrophoresis with Silver Nanoparticle Based SERS Spectroscopy for Potential Applications in Non-invasive Cancer Detection. *Nanomedicine: Nanotechnology, Biology and Medicine*. 2011.
117. Jun B-H, Kim J-H, Park H, Kim J-S, Yu K-N, Lee S-M, et al. Surface-enhanced Raman spectroscopic-encoded beads for multiplex immunoassay. *Journal of combinatorial chemistry*. 2007;9(2):237-44.
118. Chon H, Lee S, Son SW, Oh CH, Choo J. Highly sensitive immunoassay of lung cancer marker carcinoembryonic antigen using surface-enhanced Raman scattering of hollow gold nanospheres. *Analytical chemistry*. 2009;81(8):3029-34.
119. Fletcher RH. Carcinoembryonic antigen. *Annals of internal medicine*. 1986;104(1):66-73.
120. Liu GL, Rosa-Bauza YT, Salisbury CM, Craik C, Ellman JA, Chen FF, et al. Peptide-nanoparticle hybrid SERS probes for optical detection of protease activity. *Journal of nanoscience and nanotechnology*. 2007;7(7):2323-30.
121. Lee M, Lee K, Kim KH, Oh KW, Choo J. SERS-based immunoassay using a gold array-embedded gradient microfluidic chip. *Lab on a Chip*. 2012;12(19):3720-7.
122. Lee S, Kim S, Choo J, Shin SY, Lee YH, Choi HY, et al. Biological imaging of HEK293 cells expressing PLC γ 1 using surface-enhanced Raman microscopy. *Analytical chemistry*. 2007;79(3):916-22.
123. Jokerst JV, Miao Z, Zavaleta C, Cheng Z, Gambhir SS. Affibody-functionalized gold-silica nanoparticles for Raman molecular imaging of the epidermal growth factor receptor. *Small*. 2011;7(5):625-33.
124. Qian X, Peng X-H, Ansari DO, Yin-Goen Q, Chen GZ, Shin DM, et al. In vivo tumor targeting and spectroscopic detection with surface-enhanced Raman nanoparticle tags. *Nature biotechnology*. 2008;26(1):83-90.
125. Bro R, Smilde AK. Principal component analysis. *Analytical Methods*. 2014;6(9):2812-31.
126. Virkler K, Lednev IK. Forensic body fluid identification: the Raman spectroscopic signature of saliva. *Analyst*. 2010;135(3):512-7.
127. Sikirzhyski V, Virkler K, Lednev IK. Discriminant analysis of Raman spectra for body fluid identification for forensic purposes. *Sensors*. 2010;10(4):2869-84.
128. Ni J, Lipert RJ, Dawson GB, Porter MD. Immunoassay readout method using extrinsic Raman labels adsorbed on immunogold colloids. *Analytical chemistry*. 1999;71(21):4903-8.

129. Chen J-W, Lei Y, Liu X-J, Jiang J-H, Shen G-L, Yu R-Q. Immunoassay using surface-enhanced Raman scattering based on aggregation of reporter-labeled immunogold nanoparticles. *Analytical and bioanalytical chemistry*. 2008;392(1-2):187-93.
130. Wang H-N, Vo-Dinh T. Multiplex detection of breast cancer biomarkers using plasmonic molecular sentinel nanoprobe. *Nanotechnology*. 2009;20(6):065101.
131. Cialla D, März A, Böhme R, Theil F, Weber K, Schmitt M, et al. Surface-enhanced Raman spectroscopy (SERS): progress and trends. *Analytical and bioanalytical chemistry*. 2012;403(1):27-54.
132. Mukhopadhyay R. Microfluidics: on the slope of enlightenment. *Analytical chemistry*. 2009;81(11):4169-73.
133. Lim C, Hong J, Chung BG, Choo J. Optofluidic platforms based on surface-enhanced Raman scattering. *Analyst*. 2010;135(5):837-44.
134. Chakraborty. *Microfluidics and Microfabrication* 2010.
135. Gupta R, Bastani B, Goddard N, Grieve B. Absorption spectroscopy in microfluidic flow cells using a metal clad leaky waveguide device with a porous gel waveguide layer. *Analyst*. 2013;138(1):307-14.
136. Mogensen KB, Klank H, Kutter JP. Recent developments in detection for microfluidic systems. *Electrophoresis*. 2004;25(21-22):3498-512.
137. Nguyen NT, Wu Z. Micromixers—a review. *Journal of Micromechanics and Microengineering*. 2005;15:R1.
138. Stroock AD, Dertinger SKW, Ajdari A, Mezić I, Stone HA, Whitesides GM. Chaotic mixer for microchannels. *Science*. 2002;295(5555):647.
139. Hudson SD, Chumanov G. Bioanalytical applications of SERS (surface-enhanced Raman spectroscopy). *Analytical and bioanalytical chemistry*. 2009;394(3):679-86.
140. Efremov EV, Ariese F, Gooijer C. Achievements in resonance Raman spectroscopy: Review of a technique with a distinct analytical chemistry potential. *Analytica chimica acta*. 2008;606(2):119-34.
141. Chrimes AF, Khoshmanesh K, Stoddart PR, Mitchell A, Kalantar-zadeh K. Microfluidics and Raman microscopy: current applications and future challenges. *Chemical Society Reviews*. 2013;42(13):5880-906.
142. Robert B. Resonance Raman spectroscopy. *Photosynthesis research*. 2009;101(2-3):147-55.
143. Munro C, Smith W, Garner M, Clarkson J, White P. Characterization of the surface of a citrate-reduced colloid optimized for use as a substrate for surface-enhanced resonance Raman scattering. *Langmuir*. 1995;11(10):3712-20.
144. Roy S, Gord JR, Patnaik AK. Recent advances in coherent anti-Stokes Raman scattering spectroscopy: Fundamental developments and applications in reacting flows. *Progress in Energy and Combustion Science*. 2010;36(2):280-306.
145. Beyrau F, Bräuer A, Seeger T, Leipertz A. Gas-phase temperature measurement in the vaporizing spray of a gasoline direct-injection injector by use of pure rotational coherent anti-Stokes Raman scattering. *Optics letters*. 2004;29(3):247-9.

146. Rinia HA, Burger KN, Bonn M, Müller M. Quantitative label-free imaging of lipid composition and packing of individual cellular lipid droplets using multiplex CARS microscopy. *Biophysical journal*. 2008;95(10):4908-14.
147. Eckhardt G, Hellwarth R, McClung F, Schwarz S, Weiner D, Woodbury E. Stimulated Raman scattering from organic liquids. *Physical review letters*. 1962;9(11):455.
148. Freudiger CW, Min W, Saar BG, Lu S, Holtom GR, He C, et al. Label-free biomedical imaging with high sensitivity by stimulated Raman scattering microscopy. *Science*. 2008;322(5909):1857-61.
149. Saar BG, Zeng Y, Freudiger CW, Liu YS, Himmel ME, Xie XS, et al. Label-Free, Real-Time Monitoring of Biomass Processing with Stimulated Raman Scattering Microscopy. *Angewandte Chemie International Edition*. 2010;49(32):5476-9.
150. Saar BG, Freudiger CW, Reichman J, Stanley CM, Holtom GR, Xie XS. Video-rate molecular imaging in vivo with stimulated Raman scattering. *Science*. 2010;330(6009):1368-70.
151. Carron KT, Kennedy BJ. Molecular-specific chromatographic detector using modified SERS substrates. *Analytical chemistry*. 1995;67(18):3353-6.
152. Pettinger B, Ren B, Picardi G, Schuster R, Ertl G. Nanoscale probing of adsorbed species by tip-enhanced Raman spectroscopy. *Physical review letters*. 2004;92(9):096101.
153. Stadler J, Schmid T, Zenobi R. Developments in and practical guidelines for tip-enhanced Raman spectroscopy. *Nanoscale*. 2012;4(6):1856-70.
154. Anderson N, Hartschuh A, Cronin S, Novotny L. Nanoscale vibrational analysis of single-walled carbon nanotubes. *Journal of the American Chemical Society*. 2005;127(8):2533-7.
155. Ichimura T, Fujii S, Verma P, Yano T, Inouye Y, Kawata S. Subnanometric near-field Raman investigation in the vicinity of a metallic nanostructure. *Physical review letters*. 2009;102(18):186101.
156. Zhang R, Zhang Y, Dong Z, Jiang S, Zhang C, Chen L, et al. Chemical mapping of a single molecule by plasmon-enhanced Raman scattering. *Nature*. 2013;498(7452):82-6.
157. Zhang W, Srichan N, Chrimes AF, Taylor M, Berean KJ, Ou JZ, et al. Sonication synthesis of micro-sized silver nanoparticle/oleic acid liquid marbles: A novel SERS sensing platform. *Sensors and Actuators B: Chemical*. 2016;223:52-8.
158. Yang M, Alvarez-Puebla R, Kim H-S, Aldeanueva-Potel P, Liz-Marzán LM, Kotov NA. SERS-active gold lace nanoshells with built-in hotspots. *Nano letters*. 2010;10(10):4013-9.
159. Song J, Duan B, Wang C, Zhou J, Pu L, Fang Z, et al. SERS-encoded nanogapped plasmonic nanoparticles: growth of metallic nanoshell by templating redox-active polymer brushes. *Journal of the American Chemical Society*. 2014;136(19):6838-41.
160. Yim D, Kang H, Jeon S-J, Kim H-I, Yang J-K, Kang TW, et al. Graphene oxide-encoded Ag nanoshells with single-particle detection sensitivity towards cancer cell imaging based on SERRS. *Analyst*. 2015;140(10):3362-7.
161. Bedics MA, Kearns H, Cox JM, Mabbott S, Ali F, Shand NC, et al. Extreme red shifted SERS nanotags. *Chemical Science*. 2015;6(4):2302-6.

162. Jun BH, Noh MS, Kim J, Kim G, Kang H, Kim MS, et al. Multifunctional Silver-Embedded Magnetic Nanoparticles as SERS Nanoprobes and Their Applications. *Small*. 2010;6(1):119-25.
163. Guo Q-H, Zhang C-J, Wei C, Xu M-M, Yuan Y-X, Gu R-A, et al. Controlling dynamic SERS hot spots on a monolayer film of Fe₃O₄@ Au nanoparticles by a magnetic field. *Spectrochimica Acta Part A: Molecular and Biomolecular Spectroscopy*. 2016;152:336-42.
164. Frontiera RR, Mathies RA. Femtosecond stimulated Raman spectroscopy. *Laser & Photonics Reviews*. 2011;5(1):102-13.
165. Kukura P, McCamant DW, Mathies RA. Femtosecond stimulated Raman spectroscopy. *Annu Rev Phys Chem*. 2007;58:461-88.
166. Frontiera RR, Henry A-I, Gruenke NL, Van Duyne RP. Surface-enhanced femtosecond stimulated Raman spectroscopy. *The Journal of Physical Chemistry Letters*. 2011;2(10):1199-203.
167. Keller EL, Brandt NC, Cassabaum AA, Frontiera RR. Ultrafast surface-enhanced Raman spectroscopy. *Analyst*. 2015;140(15):4922-31.
168. Tong L, Wei H, Zhang S, Xu H. Recent advances in plasmonic sensors. *Sensors*. 2014;14(5):7959-73.
169. Sun M, Zhang Z, Zheng H, Xu H. In-situ plasmon-driven chemical reactions revealed by high vacuum tip-enhanced Raman spectroscopy. *Scientific reports*. 2012;2:647.
170. Pozzi EA, Sonntag MD, Jiang N, Chiang N, Seideman T, Hersam MC, et al. Ultrahigh vacuum tip-enhanced Raman spectroscopy with picosecond excitation. *The Journal of Physical Chemistry Letters*. 2014;5(15):2657-61.
171. Fan W, Lee YH, Pedireddy S, Zhang Q, Liu T, Ling XY. Graphene oxide and shape-controlled silver nanoparticle hybrids for ultrasensitive single-particle surface-enhanced Raman scattering (SERS) sensing. *Nanoscale*. 2014;6(9):4843-51.
172. Khurgin JB. How to deal with the loss in plasmonics and metamaterials. *Nature nanotechnology*. 2015;10(1):2-6.
173. Boltasseva A, Atwater HA. Low-loss plasmonic metamaterials. *Science*. 2011;331(6015):290-1.
174. Taton TA, Mucic RC, Mirkin CA, Letsinger RL. The DNA-mediated formation of supramolecular mono- and multilayered nanoparticle structures. *Journal of the American Chemical Society*. 2000;122(26):6305-6.
175. Young KL, Ross MB, Blaber MG, Rycenga M, Jones MR, Zhang C, et al. Using DNA to design plasmonic metamaterials with tunable optical properties. *Advanced Materials*. 2014;26(4):653-9.
176. Dieringer JA, Wustholz KL, Masiello DJ, Camden JP, Kleinman SL, Schatz GC, et al. Surface-enhanced Raman excitation spectroscopy of a single rhodamine 6G molecule. *Journal of the American Chemical Society*. 2008;131(2):849-54.
177. Ma W, Sun M, Xu L, Wang L, Kuang H, Xu C. A SERS active gold nanostar dimer for mercury ion detection. *Chemical Communications*. 2013;49(44):4989-91.
178. März A, Mönch B, Rösch P, Kiehnopf M, Henkel T, Popp J. Detection of thiopurine methyltransferase activity in lysed red blood cells by means of lab-on-a-chip surface

- enhanced Raman spectroscopy (LOC-SERS). *Analytical and bioanalytical chemistry*. 2011;400(9):2755-61.
179. Aroca RF, Goulet PJ, dos Santos DS, Alvarez-Puebla RA, Oliveira ON. Silver nanowire layer-by-layer films as substrates for surface-enhanced Raman scattering. *Analytical chemistry*. 2005;77(2):378-82.
180. Dinish U, Yaw FC, Agarwal A, Olivo M. Development of highly reproducible nanogap SERS substrates: Comparative performance analysis and its application for glucose sensing. *Biosensors and Bioelectronics*. 2011;26(5):1987-92.
181. Perumal J, Kong KV, Dinish U, Bakker RM, Olivo M. Design and fabrication of random silver films as substrate for SERS based nano-stress sensing of proteins. *RSC Advances*. 2014;4(25):12995-3000.
182. Fabritius T, Saarela J, Myllyla R, editors. Determination of the refractive index of paper with clearing agents. *International Conference on Lasers, Applications, and Technologies 2005: High-Power Lasers and Applications; 2006: International Society for Optics and Photonics*.
183. Rivas L, Sanchez-Cortes S, Garcia-Ramos J, Morcillo G. Mixed silver/gold colloids: a study of their formation, morphology, and surface-enhanced Raman activity. *Langmuir*. 2000;16(25):9722-8.
184. Hunyadi SE, Murphy CJ. Bimetallic silver–gold nanowires: fabrication and use in surface-enhanced Raman scattering. *Journal of Materials Chemistry*. 2006;16(40):3929-35.
185. Fang C, Agarwal A, Buddharaju KD, Khalid NM, Salim SM, Widjaja E, et al. DNA detection using nanostructured SERS substrates with Rhodamine B as Raman label. *Biosensors and Bioelectronics*. 2008;24(2):216-21.
186. Kho KW, Dinish U, Kumar A, Olivo M. Frequency shifts in SERS for biosensing. *ACS nano*. 2012;6(6):4892-902.
187. Le Ru E, Blackie E, Meyer M, Etchegoin PG. Surface enhanced Raman scattering enhancement factors: a comprehensive study. *The Journal of Physical Chemistry C*. 2007;111(37):13794-803.
188. Prokes S, Glembocki O, Rendell R, Ancona M. Enhanced plasmon coupling in crossed dielectric/metal nanowire composite geometries and applications to surface-enhanced Raman spectroscopy. DTIC Document, 2007.
189. Etchegoin PG, Galloway C, Le Ru E. Polarization-dependent effects in surface-enhanced Raman scattering (SERS). *Physical Chemistry Chemical Physics*. 2006;8(22):2624-8.
190. Hoppmann EP, Wei WY, White IM. Highly sensitive and flexible inkjet printed SERS sensors on paper. *Methods*. 2013;63(3):219-24.
191. Liao Y-J, Huang J-N, Guo J-Y, Jiang S-J. Realistic FDTD Simulations of Plasmonic Properties on Ag Columnar Thin Films as SERS Biosensor. *Nano*. 2016;11(10):1650113.
192. Kurouski D, Large N, Chiang N, Greeneltch N, Carron KT, Seideman T, et al. Unraveling near-field and far-field relationships for 3D SERS substrates—a combined experimental and theoretical analysis. *Analyst*. 2016;141(5):1779-88.

193. Muniz-Miranda M. SERS-active Ag/SiO₂ colloids: photoreduction mechanism of the silver ions and catalytic activity of the colloidal nanoparticles. *Journal of Raman Spectroscopy*. 2004;35(10):839-42.
194. Gunnarsson L, Bjerneld E, Xu H, Petronis S, Kasemo B, Käll M. Interparticle coupling effects in nanofabricated substrates for surface-enhanced Raman scattering. *Applied Physics Letters*. 2001;78(6):802-4.
195. Manfrinato VR, Zhang L, Su D, Duan H, Hobbs RG, Stach EA, et al. Resolution limits of electron-beam lithography toward the atomic scale. *Nano letters*. 2013;13(4):1555-8.
196. Xu S, Zhao B, Xu W, Fan Y. Preparation of Au–Ag coreshell nanoparticles and application of bimetallic sandwich in surface-enhanced Raman scattering (SERS). *Colloids and Surfaces A: Physicochemical and Engineering Aspects*. 2005;257:313-7.
197. Fu CY, Kho KW, Dinish U, Koh ZY, Malini O. Enhancement in SERS intensity with hierarchical nanostructures by bimetallic deposition approach. *Journal of Raman Spectroscopy*. 2012;43(8):977-85.
198. Fan M, Lai F-J, Chou H-L, Lu W-T, Hwang B-J, Brolo AG. Surface-enhanced Raman scattering (SERS) from Au: Ag bimetallic nanoparticles: the effect of the molecular probe. *Chemical Science*. 2013;4(1):509-15.
199. Rodríguez-González B, Burrows A, Watanabe M, Kiely CJ, Marzán LML. Multishell bimetallic AuAg nanoparticles: synthesis, structure and optical properties. *Journal of Materials Chemistry*. 2005;15(17):1755-9.
200. Shioi M, Jans H, Lodewijks K, Van Dorpe P, Lagae L, Kawamura T. Tuning the interaction between propagating and localized surface plasmons for surface enhanced Raman scattering in water for biomedical and environmental applications. *Applied Physics Letters*. 2014;104(24):243102.
201. Gabudean A, Biro D, Astilean S. Localized surface plasmon resonance (LSPR) and surface-enhanced Raman scattering (SERS) studies of 4-aminothiophenol adsorption on gold nanorods. *Journal of Molecular Structure*. 2011;993(1):420-4.
202. Pavaskar P, Theiss J, Cronin SB, editors. Exploring optimized configurations of plasmonic nanoparticles. *SPIE NanoScience+ Engineering*; 2010: International Society for Optics and Photonics.
203. Chan J, Fore S, Wachsmann-Hogiu S, Huser T. Raman spectroscopy and microscopy of individual cells and cellular components. *Laser & Photonics Reviews*. 2008;2(5):325-49.
204. Vendrell M, Maiti KK, Dhaliwal K, Chang Y-T. Surface-enhanced Raman scattering in cancer detection and imaging. *Trends in biotechnology*. 2013;31(4):249-57.
205. Fales AM, Yuan H, Vo-Dinh T. Cell-penetrating peptide enhanced intracellular Raman imaging and photodynamic therapy. *Molecular pharmaceutics*. 2013;10(6):2291-8.
206. Tu Q, Chang C. Diagnostic applications of Raman spectroscopy. *Nanomedicine: Nanotechnology, Biology and Medicine*. 2012;8(5):545-58.
207. Lucas L, Chen XK, Smith A, Korbelik M, Zeng H, Lee PWK, et al., editors. Imaging EGFR distribution using surface-enhanced Raman spectroscopy. 7192; 2009; 2009.
208. Li X, Yang T, Lin J. Spectral analysis of human saliva for detection of lung cancer using surface-enhanced Raman spectroscopy. *J Biomed Opt*. 2012;17(3):0370031-5.

209. Inscore F, Shende C, Sengupta A, Huang H, Farquharson S. Detection of Drugs of Abuse in Saliva by Surface-Enhanced Raman Spectroscopy (SERS). *Appl Spectrosc.* 2011;65(9):1004-8.
210. Farquharson S, Gift AD, Shende C, Maksymiuk P, Inscore FE, Murran J. Detection of 5-fluorouracil in saliva using surface-enhanced Raman spectroscopy. *Vib Spectrosc.* 2005;38(1-2):79-84.
211. Maiti KK, Dinish US, Samanta A, Vendrell M, Soh KS, Park SJ, et al. Multiplex targeted in vivo cancer detection using sensitive near-infrared SERS nanotags. *Nano Today.* 2012;7(2):85-93.
212. Samanta A, Maiti KK, Soh KS, Liao X, Vendrell M, Dinish US, et al. Ultrasensitive Near-Infrared Raman Reporters for SERS-Based In Vivo Cancer Detection. *Angew Chem-Int Edit.* 2011;50(27):6089-92.
213. Antonio KA, Schultz ZD. Advances in biomedical Raman microscopy. *Analytical chemistry.* 2013;86(1):30-46.
214. Maiti KK, Dinish U, Fu CY, Lee J-J, Soh K-S, Yun S-W, et al. Development of biocompatible SERS nanotag with increased stability by chemisorption of reporter molecule for in vivo cancer detection. *Biosensors and Bioelectronics.* 2010;26(2):398-403.
215. Wang Y, Schlücker S. Rational design and synthesis of SERS labels. *Analyst.* 2013;138(8):2224-38.
216. Kennedy B, Spaeth S, Dickey M, Carron K. Determination of the distance dependence and experimental effects for modified SERS substrates based on self-assembled monolayers formed using alkanethiols. *The Journal of Physical Chemistry B.* 1999;103(18):3640-6.
217. Dieringer JA, McFarland AD, Shah NC, Stuart DA, Whitney AV, Yonzon CR, et al. Surface enhanced Raman spectroscopy: new materials, concepts, characterization tools, and applications. *Faraday Discuss.* 2006;132(9):26.
218. Perumal J, Balasundaram G, Mahyuddin AP, Choolani M, Olivo M. sers-based quantitative detection of ovarian cancer prognostic factor haptoglobin. *International journal of nanomedicine.* 2015;10:1831.
219. Girish CM, Iyer S, Thankappan K, Rani VD, Gowd GS, Menon D, et al. Rapid detection of oral cancer using Ag-TiO₂ nanostructured surface-enhanced Raman spectroscopic substrates. *Journal of Materials Chemistry B.* 2014;2(8):989-98.
220. Han XX, Ozaki Y, Zhao B. Label-free detection in biological applications of surface-enhanced Raman scattering. *TrAC Trends in Analytical Chemistry.* 2012;38:67-78.
221. Greenblatt M, Bennett W, Hollstein M, Harris C. Mutations in the p53 tumor suppressor gene: clues to cancer etiology and molecular pathogenesis. *Cancer research.* 1994;54(18):4855-78.
222. Vousden KH, Ryan KM. p53 and metabolism. *Nature Reviews Cancer.* 2009;9(10):691-700.
223. Vousden KH, Prives C. Blinded by the light: the growing complexity of p53. *Cell.* 2009;137(3):413-31.

224. Paez JG, Jänne PA, Lee JC, Tracy S, Greulich H, Gabriel S, et al. EGFR mutations in lung cancer: correlation with clinical response to gefitinib therapy. *Science*. 2004;304(5676):1497-500.
225. Aggarwal S, Yadav S, Gupta S. EGFR targeted PLGA nanoparticles using gemcitabine for treatment of pancreatic cancer. *Journal of biomedical nanotechnology*. 2011;7(1):137-8.
226. Hong S, Li X. Optimal size of gold nanoparticles for surface-enhanced Raman spectroscopy under different conditions. *Journal of Nanomaterials*. 2013;2013:49.
227. Szeghalmi A, Leopold L, Pinzaru S, Chis V, Silaghi-Dumitrescu I, Schmitt M, et al. Adsorption of 6-mercaptapurine and 6-mercaptapurine-riboside on silver colloid: A pH-dependent surface-enhanced Raman spectroscopy and density functional theory study. II. 6-mercaptapurine-riboside. *Biopolymers*. 2005;78(6):298-310.
228. Han G, Liu R, Han M-Y, Jiang C, Wang J, Du S, et al. Label-Free Surface-Enhanced Raman Scattering Imaging to Monitor the Metabolism of Antitumor Drug 6-Mercaptopurine in Living Cells. *Analytical chemistry*. 2014;86(23):11503-7.
229. Zabel J, Nair RR, Ott A, Georgiou T, Geim AK, Novoselov KS, et al. Raman spectroscopy of graphene and bilayer under biaxial strain: bubbles and balloons. *Nano letters*. 2012;12(2):617-21.
230. Dieing T, Ibach W. Software requirements and data analysis in confocal Raman microscopy. *Confocal Raman Microscopy*: Springer; 2011. p. 61-89.
231. Magang S, Qin M, ETTORE JMW, Renke D, Baillie TA, Rushmore TH. Sigmoidal kinetic model for two co-operative substrate-binding sites in a cytochrome P450 3A4 active site: an example of the metabolism of diazepam and its derivatives. *Biochemical Journal*. 1999;340(3):845-53.
232. DeLean A, Munson P, Rodbard D. Simultaneous analysis of families of sigmoidal curves: application to bioassay, radioligand assay, and physiological dose-response curves. *American Journal of Physiology-Gastrointestinal and Liver Physiology*. 1978;235(2):G97-102.
233. Wienken CJ, Baaske P, Rothbauer U, Braun D, Duhr S. Protein-binding assays in biological liquids using microscale thermophoresis. *Nature communications*. 2010;1:100.
234. Heffler MA, Walters RD. Using electrophoretic mobility shift assays to measure equilibrium dissociation constants: GAL4-p53 binding DNA as a model system. *Biochemistry and Molecular Biology Education*. 2012;40(6):383-7.
235. Uitert LGV, Haas CG. Studies on coordination compounds. I. A method for determining thermodynamic equilibrium constants in mixed solvents1, 2. *Journal of the American Chemical Society*. 1953;75(2):451-5.
236. Friguet B, Chaffotte AF, Djavadi-Ohanian L, Goldberg ME. Measurements of the true affinity constant in solution of antigen-antibody complexes by enzyme-linked immunosorbent assay. *Journal of immunological methods*. 1985;77(2):305-19.
237. Moulin A, O'shea S, Badley R, Doyle P, Welland M. Measuring surface-induced conformational changes in proteins. *Langmuir*. 1999;15(26):8776-9.
238. Bélanger A, Van Halbeek H, Graves HC, Grandbois K, Stamey TA, Huang L, et al. Molecular mass and carbohydrate structure of prostate specific antigen: studies for establishment of an international PSA standard. *The Prostate*. 1995;27(4):187-97.

239. Castillo JJ, Rindzevicius T, Wu K, Schmidt MS, Janik KA, Boisen A, et al. Synthesis and characterization of covalent diphenylalanine nanotube-folic acid conjugates. *Journal of Nanoparticle Research*. 2014;16(7):1-8.
240. Wei WY, White IM. A simple filter-based approach to surface enhanced Raman spectroscopy for trace chemical detection. *Analyst*. 2012;137(5):1168-73.
241. Ji R, Hornung M, Verschuuren MA, van de Laar R, van Eekelen J, Plachetka U, et al. UV enhanced substrate conformal imprint lithography (UV-SCIL) technique for photonic crystals patterning in LED manufacturing. *Microelectronic Engineering*. 2010;87(5):963-7.
242. Fader R, Landwehr J, Rumler M, Rommel M, Bauer A, Frey L, et al. Functional epoxy polymer for direct nano-imprinting of micro-optical elements. *Microelectronic Engineering*. 2013;110:90-3.
243. Moonen PF, Yakimets I, Huskens J. Fabrication of transistors on flexible substrates: from mass-printing to high-resolution alternative lithography strategies. *Advanced Materials*. 2012;24(41):5526-41.
244. Tang B, Wang J, Hutchison JA, Ma L, Zhang N, Guo H, et al. Ultrasensitive, Multiplex Raman Frequency Shift Immunoassay of Liver Cancer Biomarkers in Physiological Media. *ACS nano*. 2016.
245. Bauer JJ, Sesterhenn IA, Mostofi F, McLeod DG, Srivastava S, Moul JW. Elevated levels of apoptosis regulator proteins p53 and bcl-2 are independent prognostic biomarkers in surgically treated clinically localized prostate cancer. *The Journal of urology*. 1996;156(4):1511-6.
246. Rekhtman N, Paik PK, Arcila ME, Tafe LJ, Oxnard GR, Moreira AL, et al. Clarifying the spectrum of driver oncogene mutations in biomarker-verified squamous carcinoma of lung: lack of EGFR/KRAS and presence of PIK3CA/AKT1 mutations. *Clinical Cancer Research*. 2012;18(4):1167-76.
247. Hu S, Arellano M, Boontheung P, Wang J, Zhou H, Jiang J, et al. Salivary proteomics for oral cancer biomarker discovery. *Clinical Cancer Research*. 2008;14(19):6246-52.
248. Bhatt AN, Mathur R, Farooque A, Verma A, Dwarakanath B. Cancer biomarkers- Current perspectives. 2010.
249. Wei WY, White IM. Inkjet-printed paper-based SERS dipsticks and swabs for trace chemical detection. *Analyst*. 2013;138(4):1020-5.
250. Wei WY, White IM. Chromatographic separation and detection of target analytes from complex samples using inkjet printed SERS substrates. *Analyst*. 2013;138(13):3679-86.
251. Zareie MH, Barber J, McDonagh AM. Structural changes in self-assembled monolayers initiated by ultraviolet light. *The Journal of Physical Chemistry B*. 2006;110(32):15951-4.